The Dynamics & Evolution of Martian Ices:

Implications for Present-Day Liquid Water

by

Aditya R. Khuller

A Dissertation Presented in Partial Fulfillment
of the Requirements for the Degree
Doctor of Philosophy

Approved February 2023 by the
Graduate Supervisory Committee:

Philip R. Christensen, Chair
Steven W. Ruff
Kelin X. Whipple
Thomas G. Sharp
Sang-Heon Shim

ARIZONA STATE UNIVERSITY

May 2023

ABSTRACT

The presence of ices (H_2O and CO_2) and liquid water is key to the evolution of martian geology, with implications for the potential for past or extant life, and the future of robotic and human exploration on Mars.

In this dissertation, I present the first direct evidence that the smooth deposits covering mid-latitude, martian pole-facing slopes are composed of shallow dusty H_2O ice covered by desiccated material. To analyze this H_2O ice, I developed the first validated radiative transfer model for dusty martian snow and glacier ice. I found that these ice exposures have < 1% dust in them, and discovered the lowest latitude detection of H_2O ice on Mars, at 32.9°S. After observing the ice disappear, and new gully channels form, I proposed a model for gully formation. In this model, dusty ice gets exposed by slumping, leading to melting in the subsurface and channels eroding within the ice and the wall rock beneath. Access to liquid water within this ice could provide potential abodes for any extant life.

Next, I developed novel methodology to search for CO_2 frosts within the entire Thermal Emission Imaging System (THEMIS) infrared dataset and found that about half of all gullies overlap with CO_2 frost detections. I also used the Thermal Emission Spectrometer (TES) water vapor retrievals to assess the formation and distribution of H_2O frosts on Mars.

Additionally, I used radar data from the Mars Advanced Radar for Subsurface and Ionospheric Sounding (MARSIS) instrument to investigate Mars' ice-rich South Polar

Layered Deposits (SPLD). I discovered radar signals similar to those proposed to be caused by a subglacial lake throughout the martian SPLD.

Finally, I mapped martian polygonal ridge networks thought to represent fossilized remnants of ancient groundwater near the Perseverance rover landing site with the help of citizen scientists across a fifth of Mars' total surface area and analyzed their thermophysical properties.

All these studies highlight the key role that ices and liquid water have played in shaping Mars' landscape through time, and provide an intriguing path forward in martian exploration and the search for alien life.

ACKNOWLEDGMENTS

This entire dissertation, and my introduction to the wonderful world(s) of planetary science began almost seven and a half years ago, when I met a wholly remarkable individual, Phil Christensen. I had just come from India, wanting to study astronomy, but majoring in Aerospace Engineering because I'd heard that "You'd have to become a professor to support your astronomy research", which I wasn't sure I wanted to do at the time.

As an Aerospace Engineering major, I had a choice. I could either take the rather bland sounding 'Introduction to Engineering' course that all engineers took, or I could take Phil's class on an 'Introduction to Exploration'. After enjoying the opportunity to explore four continents with my mother growing up, the choice was easy. Listening to Phil talk about the challenges of building a NASA instrument two doors away from where we were seated in class seemed incomprehensible. I just wanted to be like him, and learn from him. I began joining the queue of people wanting to ask him questions after class. Sometimes I already knew the answers to my questions, but I would ask them anyway, just to be able to talk to him. Eventually, I asked him what I needed to do to work for him. He just smiled and said, "Just get good grades, and keep bugging me." So that's what I did.

Phil ended up hiring me at the Mars Space Flight Facility my first summer in Arizona. He told me he'd written a paper about a decade ago, on how these smooth deposits on mid-latitude, martian slopes were covered with snow that could melt to form

gullies. I was to prove him wrong, and see him at the end of that summer. Seven and a half years later, and I think he's right.

Phil has taught me the key tenets of being a scientist- to be open, humble, and understanding of all ideas and people. I have learned a tremendous amount from him, and I will forever be grateful for his generosity and kindness.

Gary Clow and Steve Warren, who I consider the world's experts on snow and ice, have helped me on innumerable occasions to piece together the puzzle that the ices on Mars represent; I hope to continue learning from, and working with them.

I have also been fortunate enough to learn from three other incredible scientists: Laura Kerber, Serina Diniega and Jeff Plaut at NASA's Jet Propulsion Laboratory. Laura gave me such an incredible wealth of diverse, interesting, and fun experiences, ranging from helping build basalt walls for lunar rovers to drive down to simulating winds in Antarctica. She has always been there for me when I need any help or advice. Working with Serina taught me a lot about how to work with scientists with opposing views and remember that we are all striving toward the same goal: unraveling mysteries on other worlds. Jeff's immense experience and careful approach have shown me how to better discern the truth in what might look like a "muddy" scene.

My excellent PhD committee of Steve Ruff, Kelin Whipple, Tom Sharp and Dan Shim, has provided me with very helpful feedback and advice throughout my time here. Steve, in particular, has taught me a lot about piecing together scientific reasoning and arguments, and I am grateful that he is always willing to talk to me when I walk into his office at odd hours.

Thank you to all my true friends- Alejandro, Deolu, Sarah R., Arnav, Heather, Leann and Sarah B., for always being there for me when I needed your help; when I was sad, feeling alone. or planning petty larceny. I will always be by your side. I owe thanks also to Jay, Alex, and Saira for being there to discuss ideas with, and always providing fantastic feedback.

My love for science and physics began a long time ago, with my late grandfather, Amrit, and the wonderful books that my parents bought for me when I was a kid. In school, physics was always my favorite subject (except for classical mechanics), which led me to smuggle myself into my friends' physics classes whenever I could, without Geetanjali Ma'am or Rahul Sir noticing.

Alejandro, Anmol, Gil Speyer, Ben Barrowes and Scott Dickenshied have helped me tremendously in trying to learn how to navigate the treacherous lands of computer programming, from the archaic, but all-powerful Fortran-77, to the slithering snake, Python.

Lastly, I cannot put into words how much help my mother has given me over the last twenty-five years. Her indefatigable love and sacrifices help fuel my determination, and I am forever indebted to her. I am immensely thankful to her, my father, and the rest of my family for all their incredibly helpful advice, and patiently listening to me describe the latest developments on martian ices to them for the 42nd time.

The journey is the reward.

TABLE OF CONTENTS

Page

CHAPTER Page

LIST OF TABLES

LIST OF FIGURES

Figure Page

Figure Page

Chapter 1

INTRODUCTION

The presence of ices (H_2O and CO_2) and liquid water is key to the evolution of martian geology, with implications for the potential for past or extant life, and the future of robotic and human exploration on Mars.

1.1. Background

The obliquity of Mars is thought to have oscillated over recent timescales (10^5–10^6 years), leading to the cycling of H_2O ice from the poles to the mid-latitudes. Today, the poles contain the largest known reservoirs of ices (H_2O and CO_2) on Mars, and about a third of Mars' surface has H_2O ice buried below $<\sim$1 m of desiccated material. These H_2O and CO_2 ice reservoirs hold key records of Mars' climate history, and understanding the state and evolution of ices can provide insights into past and present-day processes on Mars.

Like on Earth, water in the form of ice and liquid has played a key role in shaping the martian landscape. Over the last 50 years, we have obtained a plethora of evidence for ancient rivers, channels, deltas, alluvial fans, and lakes littered across the martian surface. Further evidence for the substantial role that ices have played on Mars is provided by features formed in Mars' more recent geologic history, such as the polar layered deposits, buried glaciers, rampart craters and gullies.

Excitingly, observations over the last two decades have shown that Mars is an active planet. Landforms like gullies are still forming and being modified, likely by a

combination of ices and the generation of near-surface liquid water by ice melting in the subsurface.

In this dissertation, I explore how martian ices and liquid water evolve over time, through a combination of remote sensing data (visible/near-infrared, thermal infrared and radar) analysis, numerical modeling and geologic mapping. One of the key goals of this dissertation is to help better constrain the conditions under which H_2O ice can melt on Mars. If martian H_2O ice is melting, access to liquid water produced within the ice might provide abodes for any extant martian life. Locations of potentially melting H_2O ice should therefore represent key targets for future robotic and human missions to Mars.

1.2. Chapter 1: Evidence of Exposed Dusty Water Ice within Martian Gullies

In the first chapter, I present the first direct evidence that the mid-latitude, martian pole-facing slopes that are covered by smooth deposits ("mantles") are composed of shallow, buried dusty H_2O ice covered by desiccated material. I found that this buried dusty H_2O ice often gets exposed when the overlying desiccated material slumps down within martian gullies. To analyze these dusty H_2O ice exposures, I developed a dusty martian snow radiative transfer model. This radiative transfer modeling shows that these ice exposures have less than 1% dust in it, and they represent the lowest latitude detection of dusty water ice on Mars at 33°S.

Repeat-imagery of these ice exposures show the ice disappearing over the course of multiple Mars Years (one Mars Year is roughly 668 Earth days), and new gully channels forming. Based on these observations and similar mid-latitude gullies formed in bedrock and ice on Mars, I propose a model for gully formation based on Christensen

(2003a), where dusty ice gets exposed within these mantles by slumping, leading to the ice melting in the subsurface and eroding channels within the ice. If sufficient meltwater is available at the base of the ice layer, channels can be eroded into the wall rock beneath. Numerical models show that H_2O snow on Mars melts only when it contains small amounts of dust. The observed exposure of dusty ice provides a mechanism for it to melt under some conditions and form some gullies. Access to liquid water within this ice could provide potential abodes for any extant life.

1.3. Chapter 2: Spectral Albedo of Dusty Martian H_2O Snow and Ice

In the second chapter, I expand on the dusty martian snow radiative transfer modeling work by developing the first radiative transfer model for dusty martian snow and glacier ice validated against in-situ measurements on Mars and Earth. On Earth, fresh snow (with grain radius 50– 100 μm) quickly metamorphoses due to vapor diffusion and grain-boundary diffusion (Kaempfer & Schneebeli, 2007); surface snow grains can grow to radii of several hundred μm. The density also increases, in three stages by three different mechanisms (grain-boundary sliding, mechanical deformation, and bubble shrinkage): (a) In snow, densification proceeds by grain-boundary sliding, up to 550 kg/m^3. This is the maximum density obtainable for snow at the surface. (b) In subsurface firn, density can increase by mechanical deformation up to 830 kg/m^3; at this density, the air becomes closed off into bubbles, becoming “glacier ice.” (c) Overburden pressure in glacier ice causes the air bubbles to shrink, further increasing the density to approach that of pure ice, 917 kg/m^3 (Cuffey & Paterson, 2010).

Using this model, I show that < 1% of martian dust can lower the albedo of H_2O ice from ~1.0 to ~0.1 at visible wavelengths. Additionally, I show that dusty (>0.01% dust) firn and glacier ice have a lower albedo than pure dust, making them difficult to distinguish at visible wavelengths. Finally, I show that the only in-situ observations of martian H_2O ice at the Mars Phoenix landing site are matched by modeled 350-μm snow grains with 0.015% dust, indicating that this snow has not yet metamorphosed into glacier ice. These results can be used to characterize orbital observations of martian H_2O ice and refine climate-model predictions of ice stability.

1.4. Chapter 3: The Distribution of Frosts on Mars: Links to Present-Day Gully Activity

Numerous types of activity in mid-latitude martian gullies have been observed over the last decade. Some activity has been constrained to occur in the coldest times of year, suggesting that frosts (H_2O and CO_2) that form seasonally and diurnally might play a key role in this activity. In the third chapter, I analyze the distribution and effects of frosts on Mars. To do so, I developed novel methodology to search for CO_2 frosts globally within the entire Mars Odyssey Thermal Emission Imaging System (THEMIS) infrared dataset. To analyze the distribution of H_2O frosts, I used Mars Global Surveyor Thermal Emission Spectrometer (TES) infrared water vapor retrieval data. I found that CO_2 frost detections are observed at all latitudes and are strongly correlated with dusty, low thermal inertia regions near the equator. While it is difficult to accurately detect the formation of H_2O frost, the global H_2O frost point distribution generally follows water vapor column abundance and is weakly correlated with surface pressure.

I found that most global CO_2 frost detections do not contain gullies, but 47% of all gullies, and 73% of active gullies (76% in the south, and 25% in the north) do overlap with CO_2 frost detections. Based on these observations and my thermal modeling, I predict that the conditions necessary for significant present-day gully activity include a few centimeters of CO_2 frost within loose, unconsolidated sediments ($I \sim 300$ J m^{-2} K^{-1} $s^{-0.5}$) on relatively steep (>20°) slopes. Additionally, it could be possible for small amounts of H_2O frosts to play a role in present-day equatorial mass wasting events. However, whether present-day gully activity is representative of gully formation is still open to debate, because it seems unlikely that frosts can erode channels into rocky substrates– even considering geologic timescales.

1.5. Chapter 4: Characteristics of the Basal Interface of the Martian South Polar Layered Deposits

In the fourth chapter, I used radar data from the Mars Express Mars Advanced Radar for Subsurface and Ionospheric Sounding (MARSIS) instrument to investigate the properties of materials lying below the surface of Mars' south polar regions (South Polar Layered Deposits; "SPLD"). The SPLD are several kilometer-thick stacks of layered H_2O ice-rich deposits extending outward from the martian south pole.

Using MARSIS radar data, I created new, detailed (~40,000 points) maps of the basal surface ("interface") underneath the SPLD. Using these maps, I derived the thickness (ranging from 0 to 3.7 km) and volume of the SPLD ($\sim 1.60 \times 10^6$ km^3).

Additionally, I found that there are multiple areas throughout the south polar region where the energy reflected from the basal interface is unexpectedly higher than

that of the surface. Previous analyses of one such region in Ultimi Scopuli suggested that these stronger reflections could be caused by the presence of subglacial water underneath the SPLD. While the cause of the relatively high basal echo power values is uncertain, my observations suggest that this behavior is widespread, and not unique to Ultimi Scopuli.

1.6. Chapter 5: Irregular Polygonal Ridge Networks in Arabia Terra, Nili Fossae and Nilosyrtis

In the fifth chapter, I mapped polygonal ridge networks thought to represent fossilized remnants of ancient groundwater near the Mars Perseverance rover landing site across an area of 2.8×10^7 km^2. Of these ridge networks, 864 out of 952 (91%) are confined to Noachian-aged 'etched', 'dissected' or 'cratered' terrain, suggesting that they represent ancient records of crustal fracture and fill processes.

Previous spectral analyses of selected ridges in Nili Fossae revealed that both the ridges and their host units are phyllosilicate (clay)-rich, but found that the ridges might have larger grain sizes in comparison with their host units. My thermophysical analysis of seven ridge networks studied previously using spectral data indicates that the ridges typically have lower average thermal inertias (409 ± 120 J m^{-2} K^{-1} s$^{-0.5}$) than their host units (477 ± 138 J m^{-2} K^{-1} s$^{-0.5}$). These lower ridge thermal inertias are contrary to what is expected and could be due to sub-pixel mixing with nearby detrital material.

While it is not possible to determine the precise formation mechanism of these polygonal ridge networks from our new data, their formation can be assessed in terms of three possibly separate processes: (1) polygonal fracture formation, (2) fracture filling

and (3) exhumation. I find that polygonal fracture formation by impact cratering and/or desiccation of sedimentary host deposits is consistent with my results and previous spectral studies. Once the polygonal fractures have formed, fracture filling by clastic dikes and/or mineral precipitation from aqueous circulation is most consistent with my results. Exhumation, probably by aeolian processes that eroded much of these ancient Noachian terrains where the ridges are present caused the filled fractures to lie in relief as ridges today. If these ridge networks represent ancient, fossilized remnants of aqueous circulation, then my new results suggest that groundwater processes were widespread across Noachian terrain. In-situ studies by the Perseverance rover in these regions will better constrain the formation mechanisms and histories of these ridge networks and help shed light on this potential former groundwater activity.

1.7. Looking Beyond

The culmination of the work presented in this dissertation have provided a framework for my work to continue studying ices and liquid water on Mars, Earth and other bodies on the solar system. I will discuss future directions and ongoing work in the conclusions chapter of this dissertation.

Chapter 2

EVIDENCE OF EXPOSED DUSTY WATER ICE WITHIN MARTIAN GULLIES

Aditya. R. Khuller[1], Philip. R. Christensen[1]

[1]School of Earth and Space Exploration, Arizona State University, Tempe, AZ 85281.

Citation: Khuller, A.R. and Christensen, P.R., (2021). Evidence of Exposed Dusty Water Ice within Martian Gullies. *Journal of Geophysical Research: Planets*.

Key Points:

- We present new evidence of the lowest latitude detections of dusty water ice on Mars, within gullies carved in mantle units.
- Gullies eroded into mantle and wall rock materials seem unlikely to be eroded by CO_2 frost and H_2O ice sublimation models.
- A H_2O ice melt model can explain gullies eroded into the mantle and wall rock, and could provide potential abodes for any extant life.

Abstract

Mid-latitude slopes on Mars are mantled by deposits proposed to contain H_2O ice and dust, overlaid by a desiccated lag. However, direct evidence of their volatile content is lacking. Here we present novel evidence of light-toned materials within mid-latitude gully alcoves eroded into these mantles. The appearance and Lambert albedo of these materials suggests that they are either dust or H_2O ice. We interpret them to be H_2O ice because it is unlikely for a short-term, localized dust deposit to form only within the mantle walls. The temperatures are generally too warm (> ~240 K) for the ice to be a frost in equilibrium. Therefore, this ice is likely similar to the dusty ice documented within mid-latitude scarps, but with more dust, and exposed in smaller patches by slumping. It has been proposed that CO_2 frosts remove the overlying lag, causing the exposed H_2O ice to sublimate, liberate dust within the ice for transport, and erode gullies in the mantle. But we observe gullies eroded in wall rock that continue into the mantle, implying that the same process erodes both substrates. H_2O ice melt can explain gullies eroded in the wall rock and the mantle. Numerical models show that relatively dense H_2O snow on Mars melts only when it contains small amounts of dust. The observed exposure of dusty ice provides a mechanism for it to melt under some conditions and form some gullies. Access to liquid water within this ice could provide potential abodes for any extant life.

2.1. Background

2.1.1. H_2O Ice on Mars

The presence of H_2O ice and liquid water are key to the evolution of martian geology, with implications for the potential for past or extant life, and the future of robotic and human exploration on Mars. H_2O ice reservoirs hold key records of Mars' climate history, and understanding the state and evolution of subsurface ice can provide insight on past and present-day processes on Mars.

The obliquity of Mars is thought to have oscillated over recent timescales (10^5 to 10^6 years), leading to the cycling of H_2O ice from the poles to the mid-latitudes (Jakosky et al., 1995; Head et al., 2003). The poles contain the largest known reservoirs (~2.6×10^6 km^3) of ice (Smith et al., 2001a; Byrne, 2009). The seasonal polar caps are composed mostly of CO_2 ice, and are present at the surface of each pole during the winter (Leighton & Murray, 1966; Kieffer, 1979). During the summer, the retreating seasonal caps reveal underlying perennial ice caps. The northern perennial ice cap is composed of H_2O ice (Farmer et al., 1976; Kieffer et al., 1976), and is the principal source and sink of water vapor on Mars (Smith, 2004). The southern perennial cap consists of a ~10 m thick CO_2 ice layer over H_2O ice (Kieffer et al., 2000; Titus et al., 2003; Bibring et al., 2004; Byrne, 2009). Stacks of layered H_2O ice deposits that are several kilometers thick extend outwards from each pole. Like the perennial caps, these polar layered deposits also show hemispherical differences in morphology and structure, representing their different ages and formation histories (Byrne, 2009).

Ice is also present at the mid-latitudes, but it is usually within the subsurface. Models of ice stability predicted that water ice is stable below < ~1 m of desiccated material poleward of ~50° in either hemisphere for flat ground (Leighton & Murray, 1966; Mellon & Jakosky, 1995; Mellon et al., 2004; Schorghofer & Aharonson, 2005). This prediction was supported by data from the Mars Odyssey Neutron Spectrometer, High Energy Neutron Detector, and Gamma Ray instruments (Feldman et al., 2002; Mitrofanov et al., 2002; Boynton et al., 2004), that showed high water-equivalent hydrogen in the top ~1 m of the surface, poleward of ~50° in both hemispheres. In-situ evidence of this shallow, subsurface ice was provided by the Phoenix lander at ~68°N (Smith et al., 2009).

Geomorphic evidence for ice-rich materials has been documented through much of the mid-latitudes, ranging from viscous flow features (Milliken et al., 2003), lobate debris aprons (Squyres, 1979; Mangold, 2003; Pierce & Crown, 2003; Head et al., 2005), concentric crater fill (Squyres & Carr, 1986; Dickson et al., 2010; Levy et al., 2010), lineated valley fill (Levy et al., 2007; Dickson et al., 2012), scalloped depressions (e.g., Zanetti et al., 2010), expanded craters (e.g., Viola & McEwen, 2018) and thermal contraction polygons (Levy et al., 2009a). Subsurface radar measurements have detected H_2O ice within some of these landforms (e.g., lobate-debris aprons; Holt et al., 2008; Plaut et al., 2009) and large regions of Utopia and Arcadia Planitiae (Bramson et al., 2015; Stuurman et al., 2016). Additionally, a 1–10 m thick mantling unit thought to contain H_2O ice and dust over much of the mid-latitudes has been observed (Mustard et al., 2001). This unit covers > 23% of Mars (Kreslavsky & Head, 2002), representing an

ice reservoir of ~1.5–6 × 10^4 km^3 with very few craters, suggesting a young age between 0.15–10 Ma (Mustard et al., 2001). Regional layering of this mantling unit has been observed and inferred to be due to multiple cycles of emplacement (Schon et al., 2009).

Numerous examples of 'pasted-on', smooth mantles are observed on pole-facing, mid-latitude slopes (Carr, 2001; Christensen, 2003a; Conway & Balme, 2014). These mantling units have been found to increase in thickness towards the pole in both hemispheres (from a mean of ~10 m at 30° to ~40 m at 60° latitude; Conway et al., 2018). Often, a raised curvilinear edge marks the upslope boundary of these mantles; this edge can be present at varying heights on the same slope (Carr, 2001; Christensen, 2003a; Bleamaster III & Crown, 2005). At some locations, arcuate, moraine-like ridges are present downslope of the mantles (Arfstrom & Hartmann, 2005; Berman et al., 2005; Conway et al., 2018). While ice stability models for flat ground predict near-surface ice poleward of ~50° in both hemispheres, near-surface ice is expected to be stable on cold, pole-facing slopes poleward of ~30° (Aharonson & Schorghofer, 2006; Vincendon et al., 2010b). Indirect, morphometric measurements have suggested that these mantles contain 46–95% H_2O ice (Conway & Balme, 2014; Gulick et al., 2019), but no direct evidence of their ice content exists at present.

2.1.2. Characteristics of Martian Gullies

Martian gullies typically consist of a head alcove, main, secondary channels and depositional aprons; they are found on various slopes including crater walls, channel walls and isolated knobs (Malin & Edgett, 2000). Gullies are distributed in both hemispheres poleward of ~30°, although they are more sparsely distributed in the

northern hemisphere (Heldmann & Mellon, 2004; Balme et al., 2006; Dickson et al., 2007; Heldmann et al., 2007; Harrison et al., 2015). While 55% of gullies are found on pole-facing slopes, gullies transition to equator-facing slopes at higher latitudes (~45°S and ~40°N; Harrison et al., 2015). These gullies exhibit a variety of morphologies, and are eroded into substrates such as sand dunes, crater wall materials and pasted-on mantles thought to be ice-rich (Malin & Edgett, 2000; Christensen, 2003a; Heldmann & Mellon, 2004; Harrison et al., 2015; Dundas et al., 2019). A host of mechanisms have been proposed for their formation, for example: release of liquid water/brine from aquifers (Heldmann & Mellon, 2004), liquid CO_2 aquifers (Musselwhite et al., 2001), melting of pore ice (Costard et al., 2002), melting within snow deposits (Christensen, 2003a; Williams et al., 2008), melting of seasonal H_2O frost (Kossacki & Markiewicz, 2004), and CO_2-gas/frost mechanisms (Hoffman, 2002; Dundas et al., 2019).

A wide variety of gully activity has been observed over the last two decades, with constrained activity occurring during winter and spring (Harrison et al., 2009; Diniega et al., 2010; Dundas et al., 2010; Dundas et al., 2012; Dundas et al., 2015b; Dundas et al., 2019). The often-contemporaneous presence of seasonal/diurnal frosts has led to some authors (Diniega et al., 2010; Dundas et al., 2010; Dundas et al., 2012; Dundas et al., 2015; Dundas et al., 2019) suggesting that these frosts might play a key role in this present-day activity. Most of this activity has been observed to take place on crater walls and sand dunes. However, the coarse, decameter-sized to bedrock materials (hereafter referred to as wall rock) and ice-rich units often present on crater walls may not be able to be eroded by frost sublimation processes alone (Dundas et al., 2019).

2.2. Evidence for Dusty H_2O Snow and Ice on Mars

While there is a plethora of evidence for H_2O ice at the mid-latitudes, the nature and origin of this ice is unclear. Although other theories (e.g., Fisher, 2005; Sizemore et al., 2015) have been proposed, two primary contrasting theories of widespread ice deposition at the mid-latitudes exist: (1) ice deposition into soil pores by the diffusion of water vapor (Mellon & Jakosky, 1995; Mellon et al., 2004) and (2) ice deposition by precipitation as dusty snow (Jakosky & Carr, 1985; Jakosky et al., 1995; Christensen, 2003a; Madeleine et al., 2014).

To date, evidence for H_2O ice (~50 vol%) within soil pore spaces has only been observed at the Phoenix landing site (Smith et al., 2009; Cull et al., 2010b). However, despite pore-filling ice dominating volumetrically at the Phoenix landing site (Mellon et al., 2009), evidence for H_2O ice exceeding the soil pore space has been found at numerous locations throughout the mid-latitudes. For example, ice exposed by impact craters (Byrne et al., 2009), at Phoenix (Smith et al., 2009; Cull et al., 2010b) and in the form of large-scale erosional scarps (Dundas et al., 2018) is composed of about 99% ice and 1% dust/sediment. These observations indicate that they represent exposures of dusty ice (< 1% dust), rather than icy regolith (< ~25% ice). Therefore, the mid-latitude mantle units are likely composed of dusty ice, with dissected portions of the mantle (Mustard et al., 2001) representing ice-rich units whose upper few meters have been desiccated (Christensen, 2003a). Although variability in the precise ice contents at each location is expected, smooth, pasted-on mantles on pole-facing slopes are likely also remnants of this once widespread, continuous mantle composed of dusty ice stable under a layer of

desiccated sediment (Christensen, 2003a; Schon et al., 2009; Conway & Balme, 2014). In this paper, we present evidence of this dusty ice currently being exhumed in mid-latitude gully alcoves.

2.3. Theory and Models of H_2O Snow and Ice

2.3.1. Snow Metamorphism on Mars

Freshly fallen snow typically changes its physical state due to water vapor diffusion, overburden pressure, and the formation of liquid water. These effects cause snow grains to grow, thereby reducing the air between grains and increasing the bulk density of the snow. When individual snow grains are no longer distinct, the snow has transformed into glacier ice (Cuffey & Paterson, 2010). While it is difficult to accurately determine the rates of snow metamorphism on Mars, estimates of martian snow metamorphism rates imply timescales of decades/centuries (Clow, 1987; Kieffer, 1990) to millions of years (Bramson et al., 2017) for fresh snow ($\leq$ ~50 kg/m^3 bulk density) to transform into solid, glacier ice (~917 kg/m^3 bulk density). The significantly longer timescales predicted by Bramson et al. (2017) are likely due to an underestimation of temperature gradients caused by radiative heating within exposed snow (see Sections 2.3.2 and 2.3.3). However, when snow is buried by a dust lag, the relatively low thermal conductivity of the overlying dust will reduce the temperatures of the snow underneath, leading to lower rates of snow metamorphism. Thus, the true rates of metamorphism are likely to vary through the snow's lifetime, and will depend greatly on local atmospheric and thermal conditions. Nevertheless, analysis of the only current in-situ data of martian excess ice at Phoenix (~68°N) suggests average grain radii of ~1–1.3 mm (Gyalay et al.,

2019). This average grain radius corresponds to coarse-grained snow (not glacier ice), and similar results have been obtained in the northern mid-latitudes (~38–52°N), where modeled ice densities of ~640 kg/m^3 (coarse-grained snow) match radar measurements (Bramson et al., 2017). In the absence of knowledge of the exact physical properties of martian ice, we review the theoretical behavior of pure snow, dusty snow and dense ice on Mars in the following sections.

2.3.2. Behavior of Pure H_2O Snow on Mars

Pure H_2O snow at the surface of Mars sublimates and cannot melt. For melting to occur, the snow must be at or above the melting point temperature (273 K) and there must be sufficient energy to replace the latent heat lost from vapor diffusion (Ingersoll, 1970; Farmer, 1976; Clow, 1987). Radiative heating can contribute towards satisfying the latent heat requirements for melting to occur. In the solar spectrum (~0.2–2.5 μm), for clean H_2O snow (with no dust), the absorption coefficients of ice are very high for wavelengths > 1.4 μm (Warren & Brandt, 2008). This absorption leads to near-surface (top few mm) heating rates that are higher than at visible wavelengths ($0.4 < \lambda > 0.75$ μm) by over an order of magnitude, despite only 15% of the incident flux occurring for λ > 1.4 μm (Clow, 1987). However, for visible wavelengths (accounting for ~50% of the incident flux), although radiation can penetrate the snow very deeply (few tens of cm), the majority (~ 99%) is scattered back out (Clow, 1987; Warren & Brandt, 2008). This means that despite accounting for radiative heating rates, there is insufficient energy available to melt clean H_2O snow at any surface pressure below 600 mbar, even at

temperatures above the triple point (Ingersoll, 1970; Clow, 1987; Mellon & Phillips, 2001; Dundas & Byrne, 2010).

2.3.3. Behavior of Dusty H_2O Snow on Mars and Issues with Martian Ice Models

Exposed snow/ice on Mars is not clean and typically contains < ~1% of dust in it (Byrne et al., 2009; Dundas et al., 2018). The presence of these small amounts of dust within snow (< 1%) increases the energy absorbed at visible wavelengths by 3–4 orders of magnitude, resulting in enhanced radiative heating at depth by a factor of up to 10 (Warren & Wiscombe, 1980; Clow, 1987; Dang et al., 2015). Larger snow grains (1–4 mm grain radius; 400–500 kg/m^3 density) also increase the likelihood of photon absorption (Dang et al., 2015), which leads to greater radiative heating at depth, more than offsetting conductive losses (Mellon & Phillips, 2001) to the surface (Clow, 1987). Thus, the latent heat energy required to melt dusty snow is provided by increased radiative heating at depth caused by the presence of dust within relatively coarse-grained snow.

However, the critical role of dust within ice has not been explicitly accounted for in most models of ice on Mars (e.g., Ingersoll, 1970; Mellon & Phillips, 2001; Hecht, 2002; Dundas & Byrne, 2010; Schorghofer, 2010; Schorghofer & Forget, 2012; Bramson et al., 2017), despite being included in Earth ice models for decades (e.g., Warren, 1984; Dozier et al., 2009). The failure to account for absorption by dust within ice leads to an underestimation of heating rates at depth, and therefore insufficient energy for melting to occur. Additionally, Kite et al. (2011) point out that it is possible that the latent heat losses predicted by these kinds of models are overestimates (particularly at the scale of

martian snowpacks, when the effects of atmospheric circulation and near-surface air resistance are explicitly accounted for; Clow & Haberle, 1990; Clow & Haberle, 1991), which also leads to less energy available for melting to occur.

Models that do explicitly account for radiative heating effects (Clow, 1987; Williams et al., 2008) predict that a dust content of only 0.1% is sufficient for melting to occur for a wide range of snow properties and atmospheric pressures. Melting is expected to occur 10–20 cm below the surface, despite surface temperatures far below the freezing point of water (Clow, 1987; Christensen, 2003a). However, for liquid water to be stable, the local H_2O partial pressure must be at, or above the triple point pressure (611 Pa), which is much greater than the average martian H_2O partial pressure of 1 Pa at the surface. How is this subsurface liquid water stable? Within the snow, the gas within the pores is saturated with water vapor (Neumann et al., 2009), and overlying snow/ice and dust can act as barriers against vapor diffusion to the atmosphere (Farmer, 1976; Clow, 1987; Hecht, 2002; Christensen, 2003a; Richardson & Mischna, 2005; Hudson et al., 2007). Thus, despite evaporative latent heat losses, subsurface temperatures can reach the melting point (273 K), where the local H_2O partial pressure is saturated at 611 Pa, allowing liquid water to be stable. As a result, exposed, coarse-grained dusty snow can melt and sublimate in the mid-latitudes today under these conditions (Clow, 1987; Christensen, 2003a; Williams et al., 2008).

2.3.4. Behavior of Denser H_2O Ice

As noted in Sections 2.3.2 and 2.3.3, the heating rates in snow are governed by the balance between incoming solar radiation being absorbed at depth and conductive

heat losses. These heating rates can change when the density of snow increases through metamorphism. In particular, snow metamorphism causes the thermal conductivity (also dependent on temperature) to rise, leading to greater conductive losses (Text 2.S1 in the supporting information). For example, at temperatures between 200–220 K, the thermal conductivity of 550 kg/m^3 snow is about half (~1.2–1.5 W/m · K) that of glacier ice (~2.8–3.1 W/m · K; Fig. 2.S1). However, between ~255–273 K, the thermal conductivity of 550 kg/m^3 snow (~2.2–4 W/m · K) is essentially equal to, or greater than that of glacier ice because of vapor diffusion/latent heat contributions present in snow that diminish in solid glacier ice (Clow, 1987; Williams et al., 2008), whose conductivity drops from ~2.29 to 2 W/m · K in this temperature range. But despite the elevated thermal conductivity of coarse-grained, 550 kg/m^3 snow, models predict that it can melt under current martian summer conditions at the mid-latitudes (e.g., Clow, 1987; Williams et al., 2008). This result suggests that when ground surface temperatures exceed ~250 K (e.g., at the mid-latitudes during summer), snow with densities > 550 kg/m^3 (and glacier ice) can also melt, because denser snow (and glacier ice) has a lower thermal conductivity than less dense snow at these temperatures (Fig. 2.S1), meaning less heat is lost to conduction and more energy is available for melting.

An increase in snow density is also accompanied by a greater penetration depth for solar radiation, due to denser ice's significantly lower extinction coefficient at visible wavelengths, leading to radiative heating occurring deeper (~1–5 m) in glacier ice than in snow (10–20 cm) (Schwerdtfeger & Weller, 1967; Schwerdtfeger, 1969; Weller, 1969; Brandt & Warren, 1993; Chinnery et al., 2020). The magnitude of this radiative heating is

enhanced for denser ice because of its lower albedo (discussed in Section 2.3.5). Because the radiative heating occurs deeper for ice than in snow, conductive heat transfer to the surface is less efficient in removing heat, resulting in greater amounts of energy being available for melting (Brandt & Warren, 1993; Liston & Winther, 2005). The presence of small amounts of dust (< 1%) within the ice can further increase subsurface solar heating rates (as summarized in Section 2.3.3). Although there are currently no models of martian glacier ice that explicitly account for the key radiative effects outlined above, these results suggest that if martian snow has metamorphosed into glacier ice, it can melt a few meters below the exposed ice surface, at temperatures well below freezing (Brandt & Warren, 1993; Liston et al., 1999; Liston & Winther, 2005).

2.3.5. Albedo of Dusty H_2O Snow and Ice

The spectral reflectivity, albedo and appearance of snow can vary tremendously with grain radius, structure and the incorporation of dust (Kayetha et al., 2007; Dozier et al., 2009). Larger H_2O ice grains cause greater forward scattering and are more absorptive. Thus, the spectral albedo of snow decreases at all wavelengths as ice grain radii (and bulk densities) increase toward becoming glacier ice (Wiscombe & Warren, 1980; Dang et al., 2015; Warren, 2019). We computed the spectral variation of ice-dust mixtures between wavelengths of 0.5–1.5 μm (see Text 2.S2 for details) using Mie theory (Matzler, 2002), a delta-Eddington radiative transfer model (Warren & Wiscombe, 1980; Dang et al., 2015) and refractive index data for H_2O ice (Warren & Brandt, 2008) and martian dust (Wolff et al., 2009). Figure 2.1 shows that the inclusion of very small amounts of dust (< 1%) within snow results in a reduction in albedo by about 50% at

visible wavelengths. The addition of greater amounts of dust (> 1%) can make dusty snow essentially indistinguishable from pure dust at visible wavelengths (Fig. 2.S2; Dang et al., 2015).

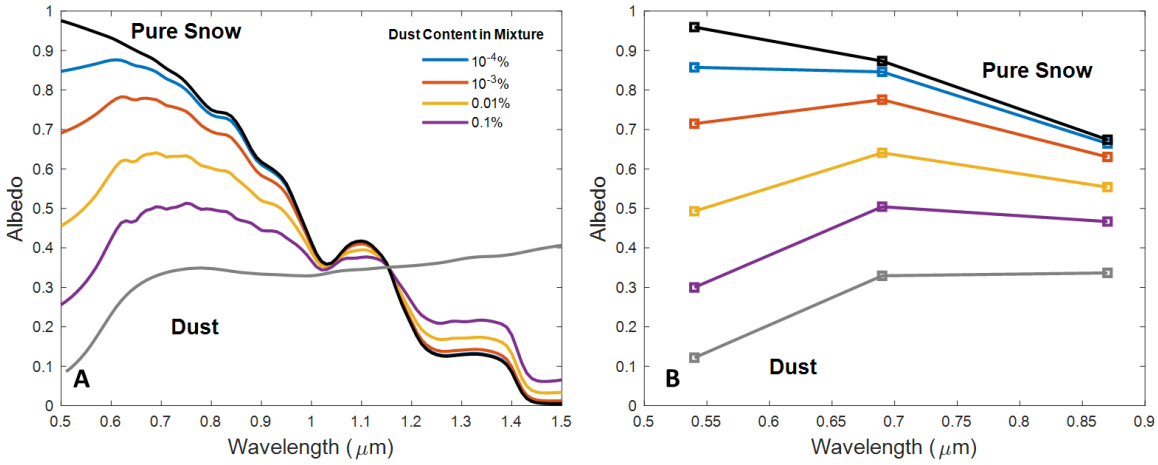

Figure 2.1. The effect of dust (gray) on the spectral albedo of pure snow (black) a) between 0.5–1.5 µm wavelengths and b) sampled at HiRISE color filter center wavelengths. These computations are for a semi-infinite, 550 kg/m^3 (40% porosity) snowpack with snow and dust grain radii of 1000 and 1.8 µm, respectively, and a solar zenith angle of 49.5°.

2.4. Methods

In order to search for potential occurrences of exposed, dusty ice we examined visible image data (~30 images) that had overlapping 1-km-wide central color swaths from the High Resolution Imaging Experiment (HiRISE; McEwen et al., 2007a) onboard the Mars Reconnaissance Orbiter during local spring/summer seasons at gully locations (Harrison et al., 2015) using JMARS (Christensen et al., 2009a). At the Gully 1 location (Table 2.S1), we also examined available Context Camera (CTX; Malin et al., 2007) data

to document the behavior of the light-toned materials with time. The HiRISE (~0.25 m/pixel) filters are centered at 536, 694 and 874 nm (McEwen et al., 2007a), whereas the CTX (~6 m/pixel) filter is centered at 611 nm (Malin et al., 2007). At each location, we analyzed available images, calculated the Lambert albedo of the light-toned materials to assess their brightness as described below, and made qualitative comparisons with known ice (Brown et al., 2008; Byrne et al., 2009; Dundas et al., 2018; Table 2.S2) and dust (e.g., Dundas, 2020; Table 2.S3) exposures on Mars. In addition, Thermal Emission Imaging System (THEMIS; Christensen et al., 2004) infrared (~100 m/pixel) images (Table 2.S4) were analyzed at all light-toned material gully locations to check for the potential presence of frosts near the time of HiRISE/CTX observations.

HiRISE radiometrically calibrated, map-projected Reduced Data Records (RDRs) were converted to I/F (measured intensity divided by solar flux at the top of the atmosphere) by applying scale factors to pixel values (Delamere et al., 2010). CTX Experiment Data Records (EDRs) were processed and radiometrically calibrated to I/F values using ISIS3 (Gaddis et al., 1997; Bell III et al., 2013). I/F values were then converted to Lambert albedo by dividing by the cosine of the incidence angle over the entire image (Hapke, 2012). This assumes that the surface is Lambertian (Soderblom et al., 2006; Bell III et al., 2013; Rice et al., 2018). For each region of interest (known ice exposure/light-toned material/dust) in HiRISE Infrared-Red-Blue (IRB) products, averaged pixel data from 5 × 5 pixel boxes (as shown in HiView (http://www.uahirise.org/hiview/) were used. Albedo values are not topographic slope-corrected but only pixels near light-toned regions with similar slope characteristics were

used for comparisons. No atmospheric correction or ratios were performed on the Lambertian albedo data.

The estimated uncertainty of HiRISE's absolute calibration is ±20%, with a spectral calibration uncertainty of ~5% (Milazzo et al., 2015). The uncertainty in CTX measurements ranges from 10–20% (Bell III et al., 2013). In addition to the instrument calibration uncertainties, changing dust cover, standard image noise filtering, differences in viewing geometry and atmospheric conditions can cause variations in inferred Lambert albedo (Bell III et al., 2008; Daubar et al., 2016). However, despite these potential effects, HiRISE and CTX albedo estimates have been found to agree within 15% of measurements made in-situ at the surface of Mars, suggesting that their radiometric calibration is validated (Rice et al., 2018). Additionally, our use of 25-pixel averages for HiRISE albedo values improves the signal to noise and reduces the probability of random noise effects. Regardless, we interpret all albedo estimates as approximate, and do not draw precise quantitative conclusions from the albedo data alone.

2.5. Observations

2.5.1. Gully/Mantle Morphology

Pasted-on mantles are present at a variety of heights from the top of the slope wall and often appear relatively smooth (Fig. 2.2). The surface of these materials often contain blocks interpreted to be boulders (McEwen et al., 2007b; Dundas et al., 2018). The upslope boundary is typically curvilinear, and can appear lobate. Often, at the edges of the mantle, a depression within the wall rock is observed, suggesting that the pasted-on

material lies in a shallow depression that has been eroded into the underlying substrate (Fig. 2.2).

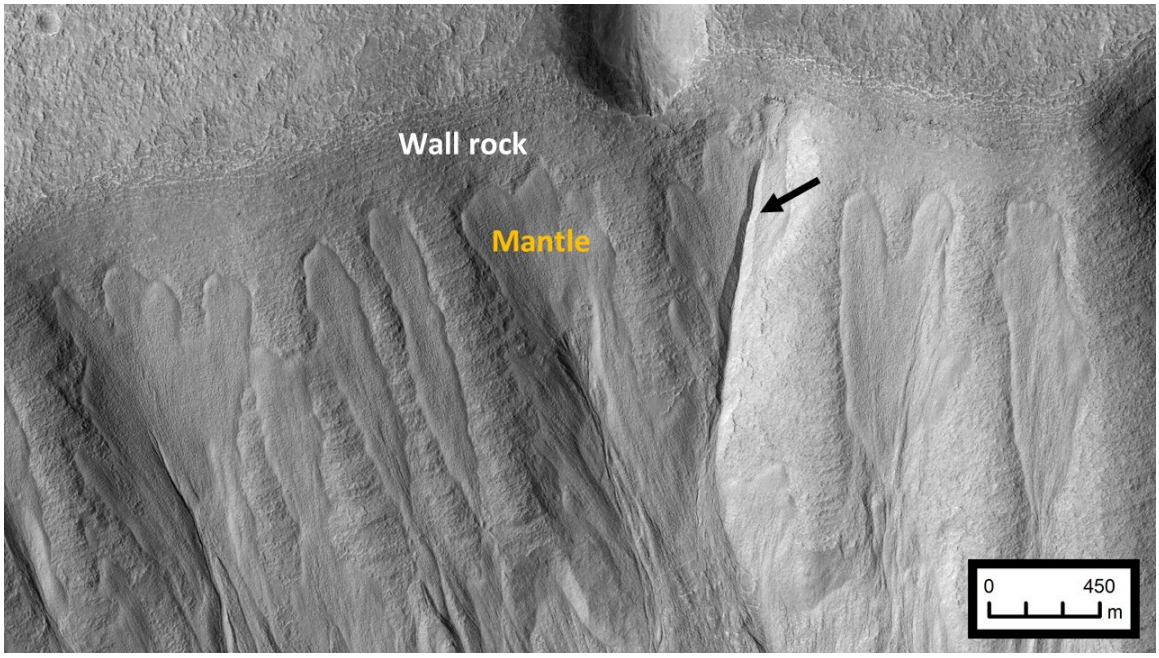

Figure 2.2. Pasted-on mantles in Dao Valles (32.8°S, 93.3°E). Distinct, curvilinear upper boundaries of the mantle are observed at this location, in addition to a V-shaped gully incision (black arrow) within the mantle. HiRISE image ESP_020926_1470. North is towards the top, illumination is from the left and latitudes are planetocentric in all figures. Grayscale HiRISE image figures show 694 nm filter data.

Gullies are formed in the mantle material in some cases (Fig. 2.3), and if the mantles are indeed volatile-rich, then little true erosion (i.e., weathering and transport) would be required; the gullies could form simply by the sublimation of icy material (i.e., transport by vapor diffusion). However, gullies are also observed to have formed in the underlying wall rock (Figs. 2.3b and 2.3d; note the transition from the mottled, rockier material above the mantle, referred to as 'texturally altered bedrock' by Conway et al.

(2018), to the relatively smooth mantle downslope). Gullies eroded in wall rock materials appear shallower, and their U-shape is consistent with erosion into equally resistant topsoil (wall rock) and subsoil (wall rock) (Weidelt, 1976). Gullies eroded in the mantle are often V-shaped (Figs. 2.2 and 2.3), consistent with a subsoil (wall rock) that is more resistant than the topsoil (mantle) (Weidelt, 1976; Conway et al., 2018). This observation is especially pronounced in smaller, earlier-stage gullies, before gully alcoves grow into broader, more developed alcoves (Fig. 2.4). These channels that are eroded into the wall rock can be seen continuing into the mantle (see Figure 14 in Harrison et al. (2015) for additional examples of similar wall rock-mantle gullies), implying that the same process eroded the wall rock and the mantle (Fig. 2.3).

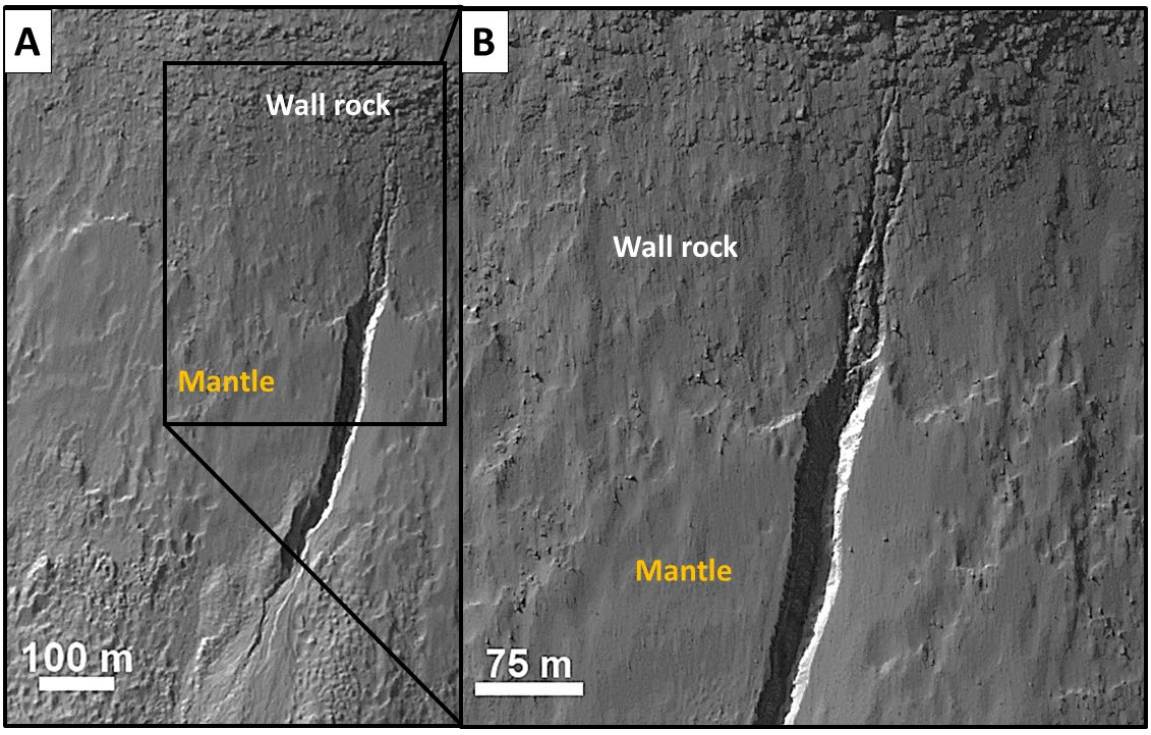

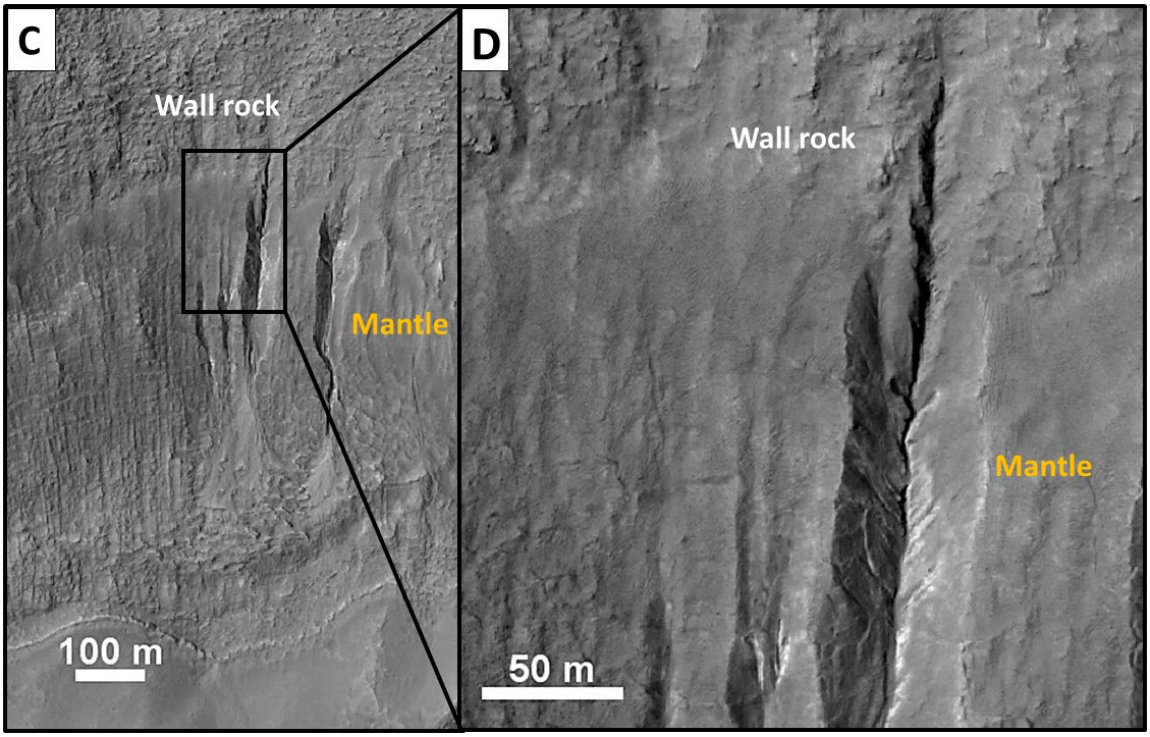

Figure 2.3. Channels that erode the bedrock extend downslope into the pasted-on mantle. Erosion within the wall rock is significantly narrower than in pasted-on materials, likely due to the difference in mechanical strength between the two materials. (A and B) HiRISE image PSP_007526_1435, centered at 36.3°S, 178.6°E. (C and D) HiRISE image ESP_014329_1435, centered at 36°S, 199.4°E.

2.5.2. Context for Light-toned Material

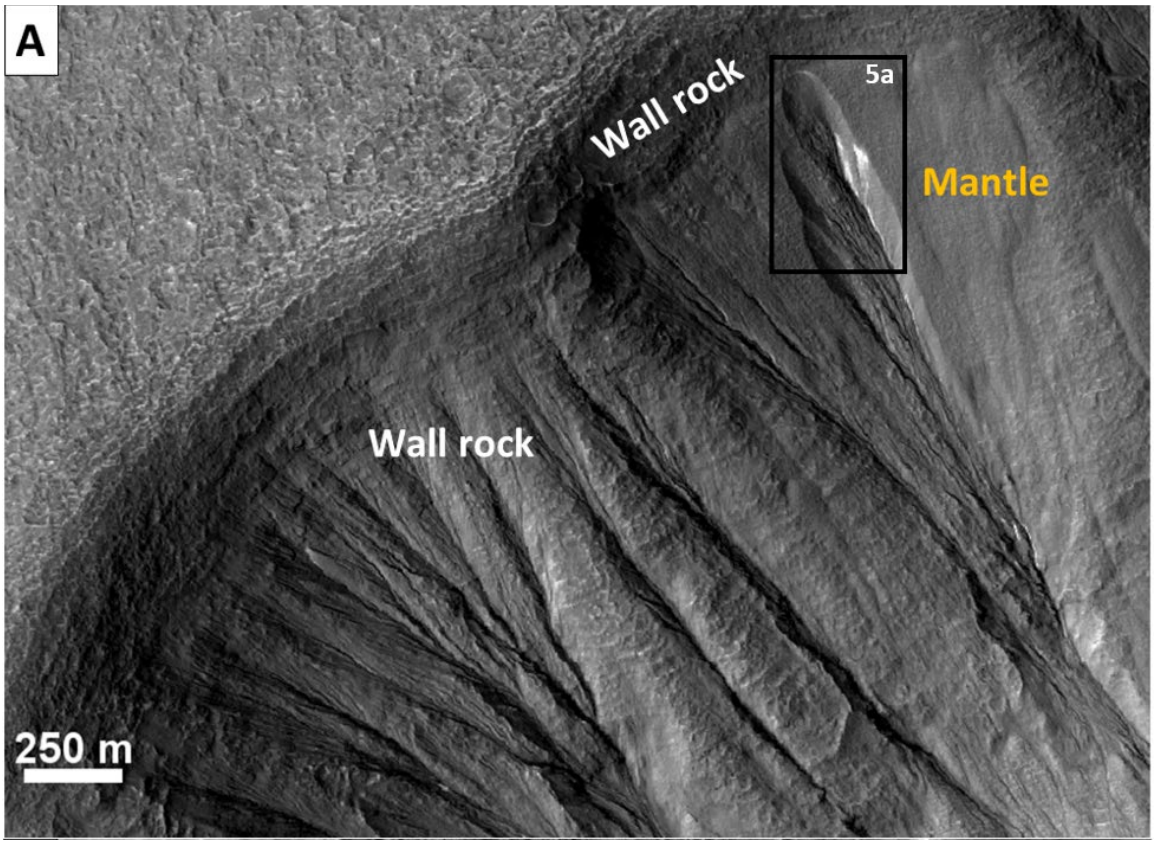
A
Wall rock
5a
Mantle
Wall rock
250 m

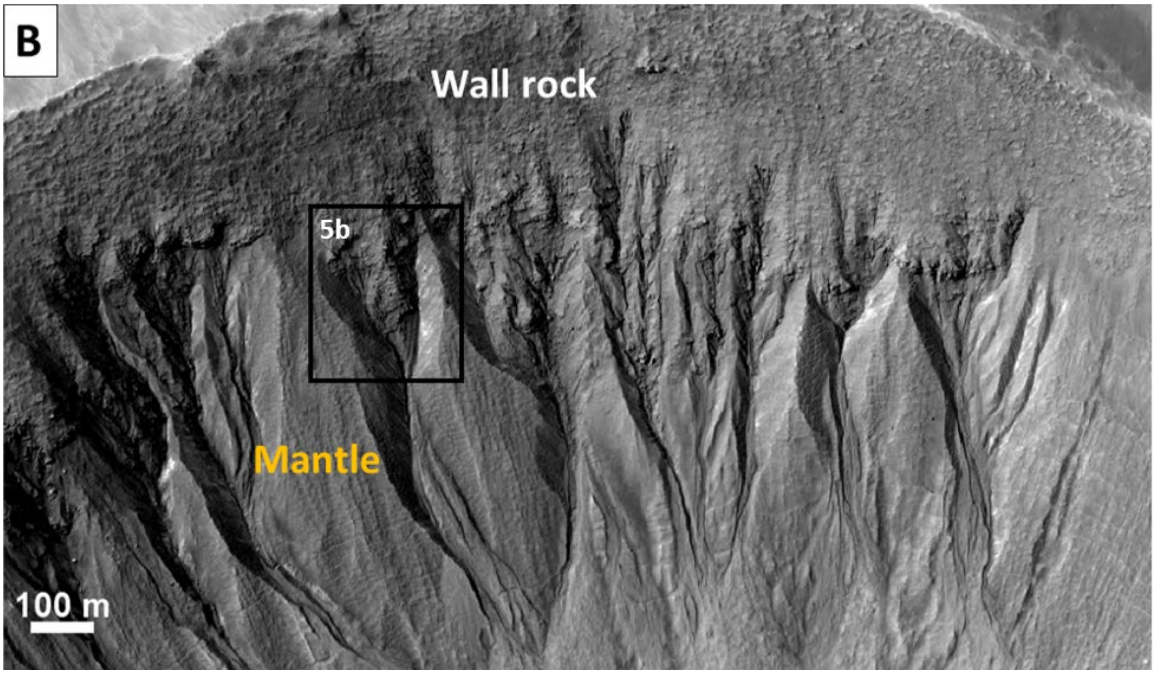
B
Wall rock
5b
Mantle
100 m

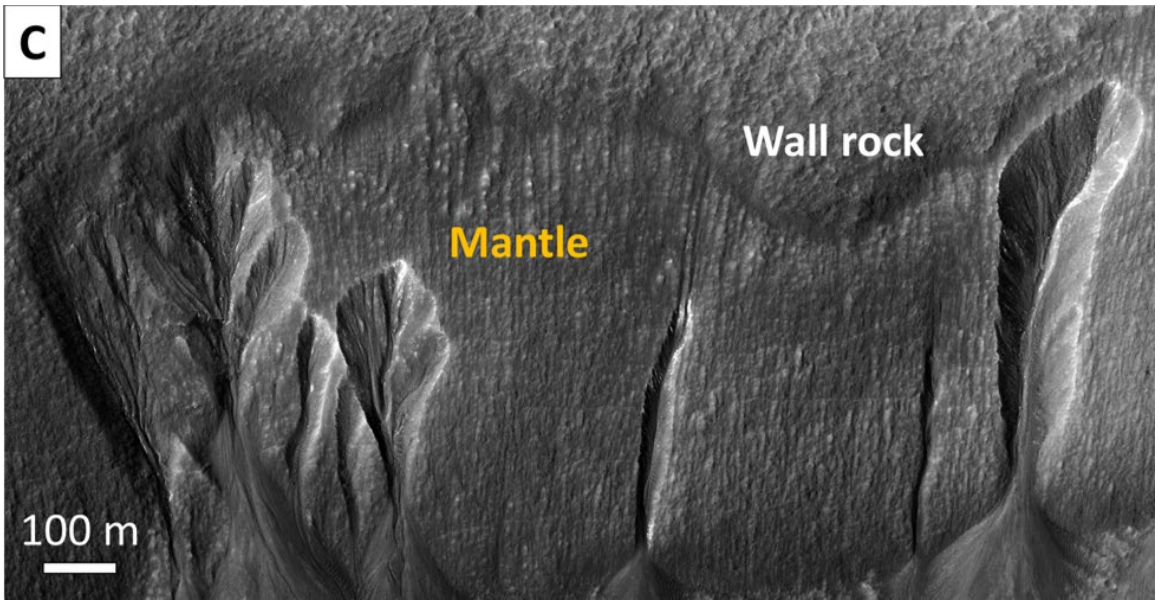

Figure 2.4. Context for light-toned materials within some gullies. Light-toned materials are partially exposed only within the mantle. (A) Gullies are eroded in the mantle adjacent to gullies eroded in the wall rock at 32.9°S, 93.2°E (ESP_013067_1470). (B) Multiple gullies are eroded in the mantle, with some channels continuing into the wall rock at 36°S, 199.4°E (ESP_014329_1435). (C) Gullies eroded to varying depths into the mantle at 37.8°S, 217.9°E (ESP_048824_1420). Black boxes indicate locations shown in Figure 2.5.

Figure 2.4 shows examples of mantle association with wall rock and gullies that host light-toned materials. Gullies in Dao Valles are eroded into two different substrates (Fig. 2.4a). Towards the west, gullies can be seen eroded into wall rock. However, to the east, there is a depression within the smooth mantle with gullies emerging from within the depression. One set of gully channels can even be seen eroded into the wall rock below the mantle, where the mantle is the thinnest, before continuing into the thicker mantle downslope. Multiple channels can also be seen eroded into the mantle in Figure

2.4b, with some channels cross-cutting each other and combining to form larger gullies. In Figure 2.4c, some alcoves to the west appear to be coalescing to form one larger alcove. Gullies generally begin at a relatively uniform height at these locations.

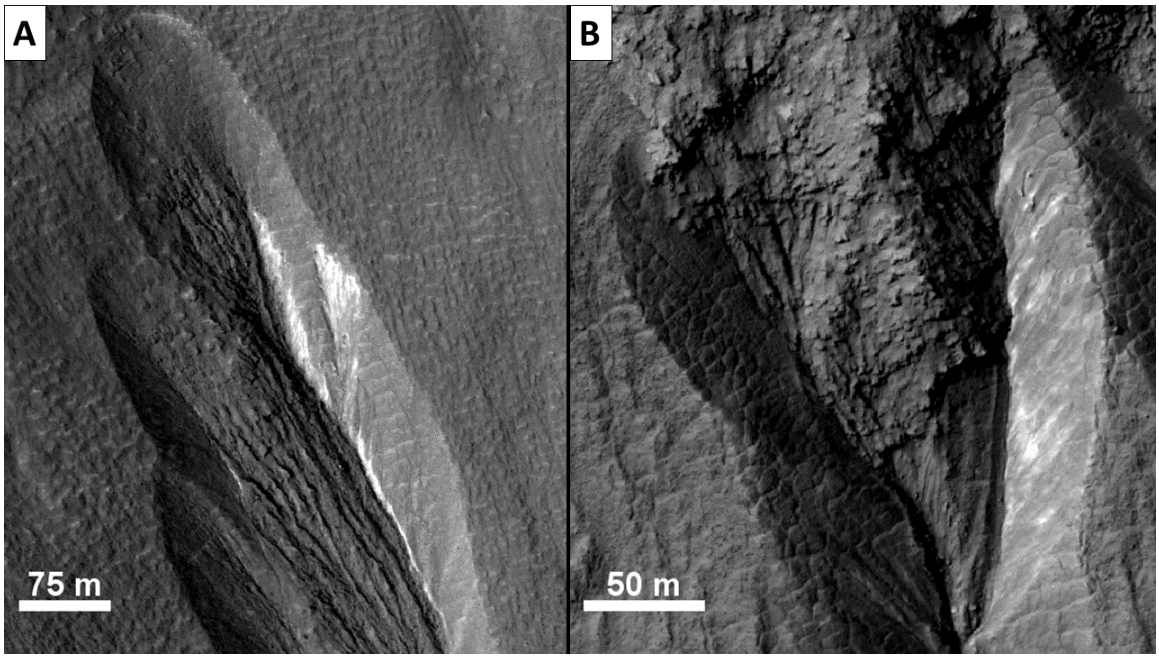

Figure 2.5. Examples of partially exposed lighter-toned materials with evidence of slumping within gully alcoves eroded in the mantle. Numerous channels appear to be visible underlying the alcoves eroded into the mantle at (A) 32.9°S, 93.2°E (ESP_013067_1470) and (B) 36°S, 199.4°E **(**ESP_014329_1435**)**.

Partially exposed, light-toned materials are present within gullies eroded into the mantle in summertime imagery (Figs. 2.4 and 2.5). The light-toned materials are present in patches that range from ~1–40 m in length and generally appear on west-facing alcove walls that show evidence of slumping. Although gullies eroded into wall rock are often nearby (Fig. 2.4a), light-toned materials are not observed within wall rock gullies, or elsewhere in the scene. While there are few polygonal fractures within the alcove walls

where the light-toned materials are exposed (suggesting that the material is relatively fresh), in some cases fracturing is visible in the mantle nearby (Fig. 2.5b).

2.5.3. Light-toned Material Albedo

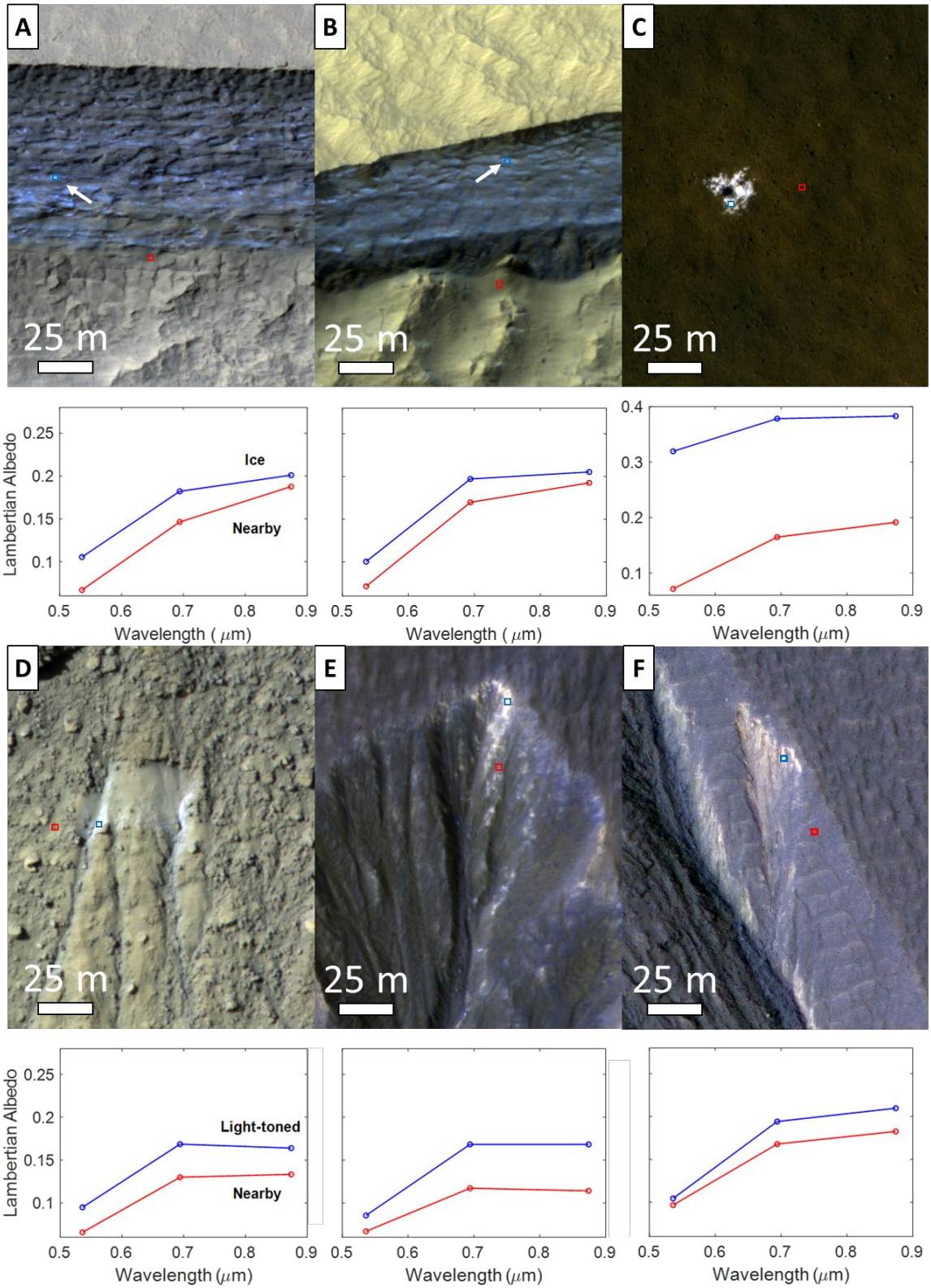
A
B
C
25 m
25 m
25 m
Lambertian Albedo
Ice
Nearby
Wavelength (μm)
Wavelength (μm)
Wavelength (μm)
D
E
F
25 m
25 m
25 m
Light-toned
Nearby
Wavelength (μm)
Wavelength (μm)
Wavelength (μm)

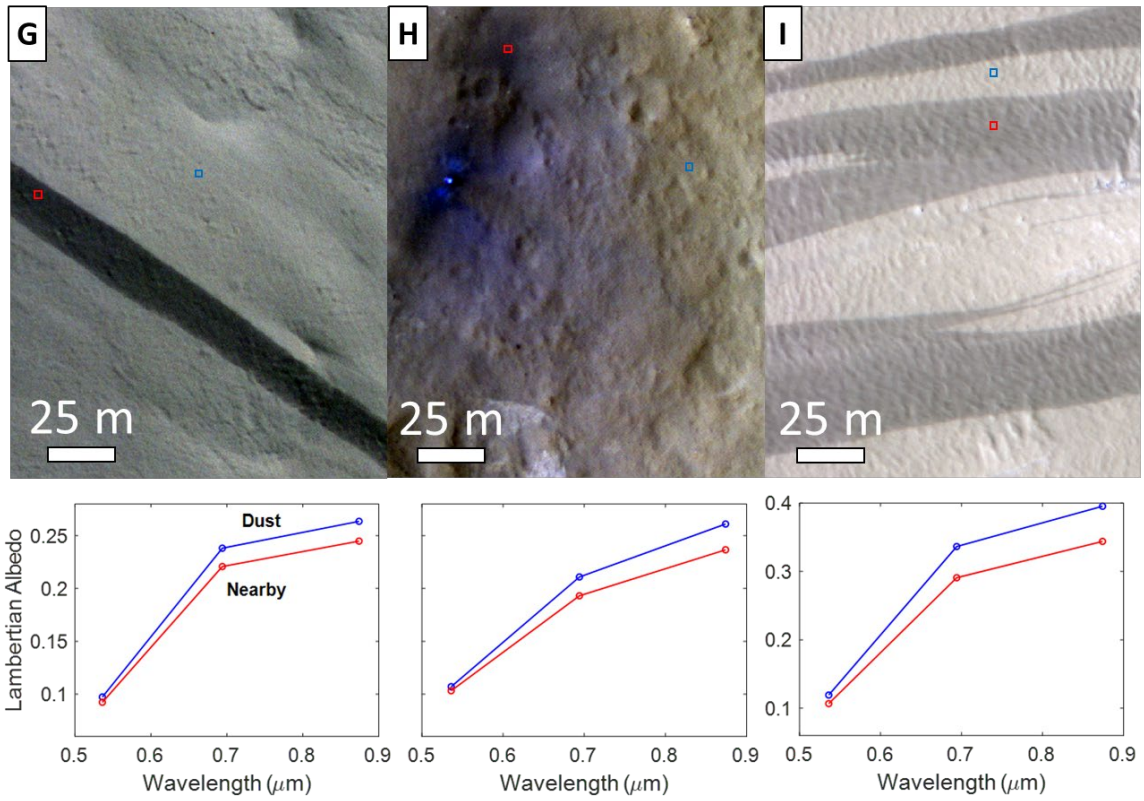

Figure 2.6. HiRISE Lambert albedos of (A–C) known exposures of ice on Mars, (D–F) light-toned materials within gullies and (G–I) dusty materials compared to nearby less dusty regions. (A and B) Icy scarps (Dundas et al., 2018); ESP_040772_1215 and ESP_022389_1230. (C) Ice-exposing impact crater (Byrne et al., 2009); PSP_010625_2360. (D–F) Light-toned materials within Gully 5, Gully 10, and Gully 1; ESP_032012_1415, ESP_048824_1420 and ESP_013067_1470. (G) Slope streak exposing dark substrate, likely from dust avalanching (Sullivan et al., 2001; Dundas, 2020); ESP_058424_2035. (H) Mars Science Laboratory (bright blue dot to the west in the image) landing site a few sols after landing. The landing process blows off dust, exposing a darker substrate around the rover near a relatively dusty area to the east; ESP_028335_1755. (I) Slope streak exposing dark substrate, likely from dust

avalanching (Sullivan et al., 2001; Dundas, 2020); ESP_046740_2175. All images are HiRISE false-color (IRB) and individually contrast-stretched. Note the different y-axis limits in Figures 2.6c and 2.6i. Approximate locations of spectra are shown in boxes (not to scale). White arrows are shown in A and B to help locate blue box locations.

In stretched, false-color IRB images, known exposures of subsurface H_2O ice on Mars (Figs. 2.6a–c and 2.S3) generally appear blue/white in relation to nearby lithic material although there are areas of the icy scarps that resemble the color of nearby lithic material (Figs. 2.6a and b). These icy materials have higher albedo values at each HiRISE filter wavelength relative to their surroundings (corresponding to an increase in brightness in the stretched images), although the magnitude of the difference can vary from relatively low (Fig. 2.6a) to high (Fig. 2.6c). The ice spectra generally show a slight reduction in slope between the 694 and 874 nm filters relative to the nearby material. Apart from this difference in spectral slope, the overall shape of the ice spectra resembles that of the nearby materials, but with greater albedo values. Note that only pixels near with similar slope characteristics were used for spectral comparisons between different groups of materials.

The light-toned materials within gullies (Figs. 2.6d–f and 2.S4) generally also appear blue/white relative to their surroundings. Like the icy scarps, some parts of the light-toned material can resemble their surroundings in color. These light-toned materials also have higher albedos in comparison with adjacent areas, with varying relative magnitudes. The spectral shape of light-toned materials relative to their surroundings

resembles the known ice exposure spectra, although the albedo increase at the 536 nm filter can sometimes be relatively small (e.g., Fig. 2.6f).

In contrast, relatively dusty surfaces (Figs. 2.6g–i and 2.S5) appear more yellow/gray than their darker surroundings. While the presence of dust also increases the albedo at visible wavelengths, the spectral slope is relatively steep. This steep spectral slope caused by dust is consistent with terrestrial-based experiments by Wells et al. (1984) showing increases in surface reflectance at longer visible wavelengths by dust deposition, i.e., the albedo difference at the 536 nm filter is usually negligible, suggesting that the light-toned materials observed within gullies (Figs. 2.6d–f and 2.S4) are not dust. It is interesting to note that in all cases (Figs. 2.6, 2.S3–5), despite the differences in color between the surroundings and the region of interest (ice, light-toned material and dust), the spectral shapes of the surroundings are somewhat similar to the region of interest, but lower in albedo. This result suggests that each region of interest might contain some portion of the surrounding material.

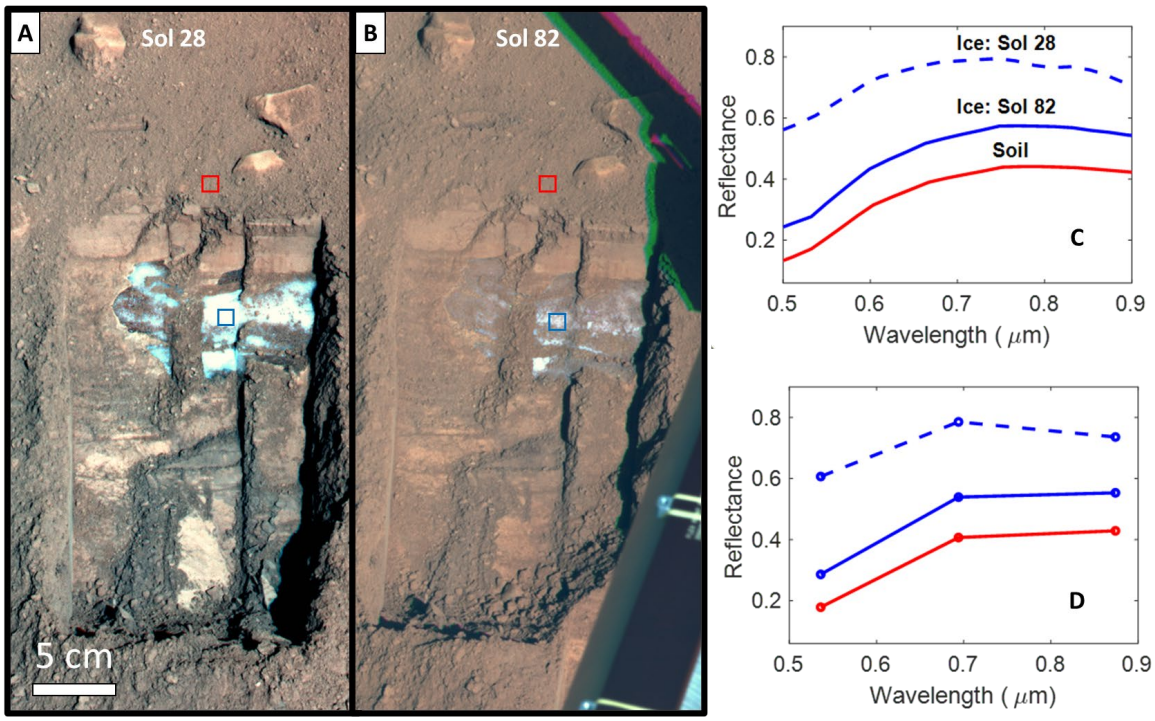

Figure 2.7. Spectral behavior of exposed H_2O ice at the Phoenix landing site compared to nearby soil over time. A) Approximate locations of ice (blue box) and nearby soil (red box) spectra on Sol 28 of the mission. B) Approximate locations of ice (blue box) and nearby soil (red box) spectra on Sol 82 of the mission. C) Spectra of exposed ice on Sol 28 (dashed blue line) and Sol 82 (solid blue line), compared to nearby soil spectra (red line). D) Spectra shown in C, sampled at HiRISE filters. All spectra shown are from Blaney et al. (2009). Surface Stereo Imager (SSI) color images (RGB = 672 nm, 533 nm, 485 nm) derived from ss028rad898689390_132f0r1m1 and ss082rad903481988_196c0r1m1 are shown in A and B, respectively. Observations were collected at the same time of day to minimize viewing geometry, illumination, and calibration differences. The soil spectra did not change (Blaney et al., 2009).

Assessing the behavior of known exposures of ice, light-toned materials within gullies and relatively dusty areas qualitatively using HiRISE data suggests that the light-toned gully materials are more similar to the known exposures of ice than they are to pure dust, and potentially represent a mixture of ice and dust. The evolution of ice exposed at the Phoenix landing site lends support to this ice-dust mixture possibility (Fig. 2.7). After the ice was first exposed on Sol 9, its albedo on Sol 28 (Fig. 2.7a) was significantly higher than that of nearby soil and there was a reduction in spectral slope between 694 and 874 nm (dashed blue line in Figs. 2.7c and d). As noted in Sections 2.2 and 2.3, the ice spectrum is consistent with ~1–1.3 mm ice grains, with < 1 % dust. The observed spectral behavior is similar to the known ice exposures seen in HiRISE data, despite potential differences in instrumentation and viewing conditions. Fifty-four sols later, the ice was not as bright (Fig. 2.7b), and its spectral shape resembled that of soil nearby (solid blue line in Figs. 2.7c and d). Furthermore, the reduction in spectral slope was no longer present, probably because the amount of dust/lithic materials within the ice-dust mixture had increased. Qualitatively similar spectral behavior is observed in the light-toned materials present within Gully 12 (Figure 2.8) over six Mars Years. Initially, the light-toned materials had a significantly higher albedo than nearby materials (Fig. 2.8a). The color of the light-toned materials was white/blue with a slight yellowish tint, and both types of materials showed an increase in spectral slope between 694 and 874 nm. These color and albedo results suggest that dust was present throughout the scene (e.g., Fig. 2.6). After six Mars Years, the light-toned materials were still present, but in a smaller area. The difference in albedo between the light-toned materials relative to the

nearby materials decreased by a factor of ~3, which is comparable to the factor of ~4 decrease in the relative albedo at the Phoenix site. In addition to these similarities in albedo decrease over time, the spectral shape of the light-toned gully materials (e.g., Fig. 2.6d, e, 2.8b and 2.S4a, e, h) is consistent with that of the relatively dusty ice at Phoenix (solid blue line in Fig. 2.7d). Hence the gully materials could represent exposures of H_2O ice that is relatively dustier than previously recognized martian ice exposures.

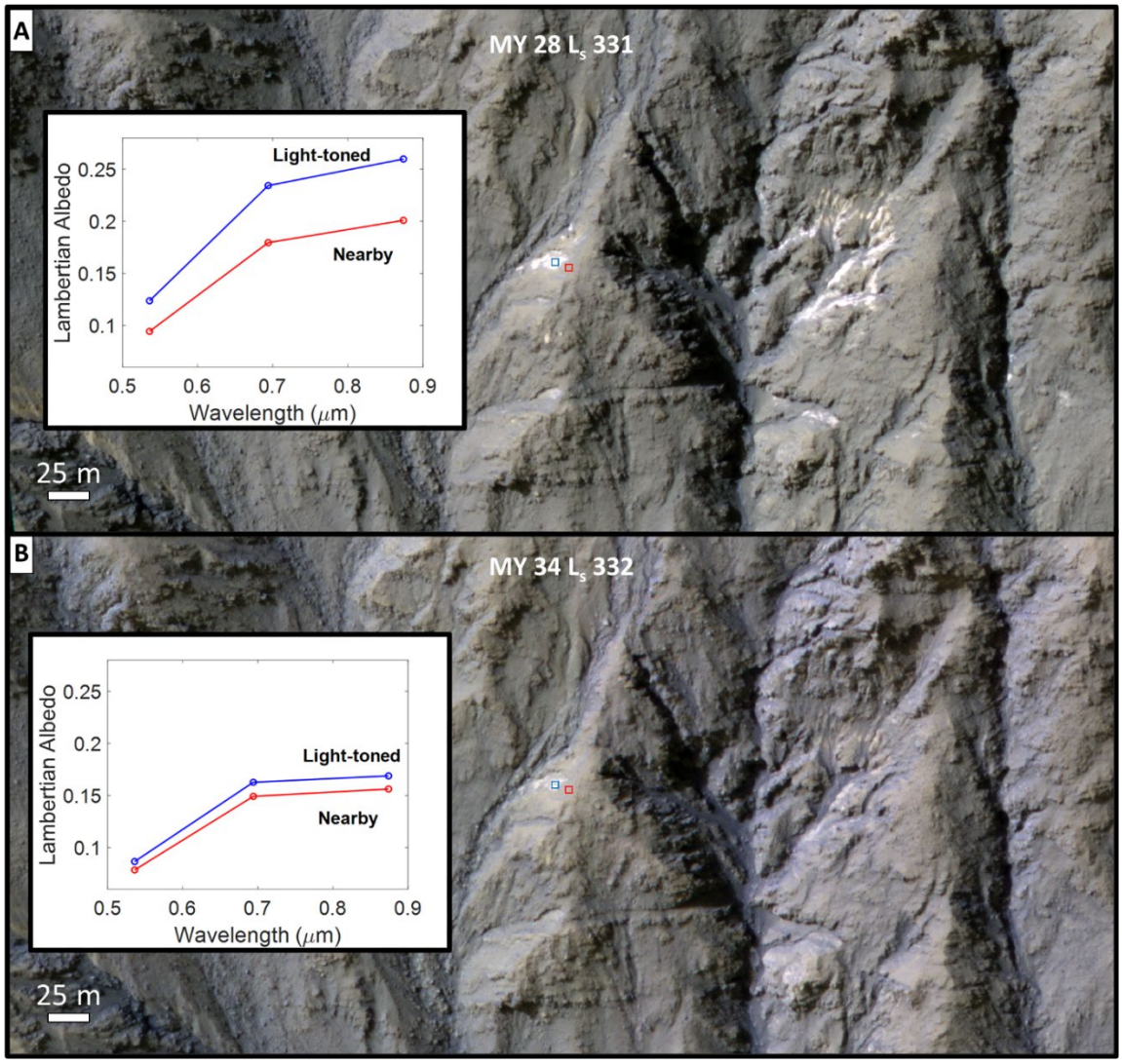

Figure 2.8. Spectral behavior of light-toned materials in Gully 12 over six Mars Years in HiRISE color data. The plots (inset in A and B) show the reduction in albedo of the light-toned materials (blue box) over time, relative to nearby materials (red box). HiRISE images PSP_005706_1425 and ESP_058636_1425 are shown in A and B, respectively.

The exact proportion of ice to dust is difficult to determine because numerous factors can affect the spectral behavior of small areas in HiRISE data (as discussed in Section 2.4) and there are too many unconstrained parameters to accurately model the ice-dust ratios from the observed albedos. However, a qualitative assessment based on spectral shape can be made. For example, the overall shape of the known ice spectra (Fig. 2.6a–c and 2.S3) is similar to the modeled ice spectra containing 0.1% dust (violet curve in Fig. 2.1). This result is consistent with Compact Reconnaissance Imaging Spectrometer for Mars (CRISM; Murchie et al., 2007) data suggesting dust contents of < 1% within scarp ice (Dundas et al., 2018). The overall shape of the light-toned gully material spectra can vary between that of the icy scarps (0.1% dust in modeled spectra) in some cases (e.g., Fig. 2.6d and 2.6e) and modeled spectra containing < 1% dust (Figs. 2.1 and 2.S2) at other locations (e.g., Fig. 2.6f), suggesting that the light-toned gully materials are also consistent with high ice contents.

2.5.4. Changes in Gullies with Light-toned Material

The evolution of light-toned materials within Gully 1 is documented with CTX imagery ~250 sols before they were exposed (Fig. 2.S6a), during the exposure (Fig. 2.S6b), and after they have faded (Fig. 2.S6c) over three Mars Years (Table 2.S4). Ratios of the CTX Lambert albedo of the light-toned material to that of nearby materials for

each image show that the light-toned material was 5% brighter than nearby materials when it was exposed. The change between the three images is localized and discrete, suggesting that the changes are not due to atmospheric effects or instrument noise.

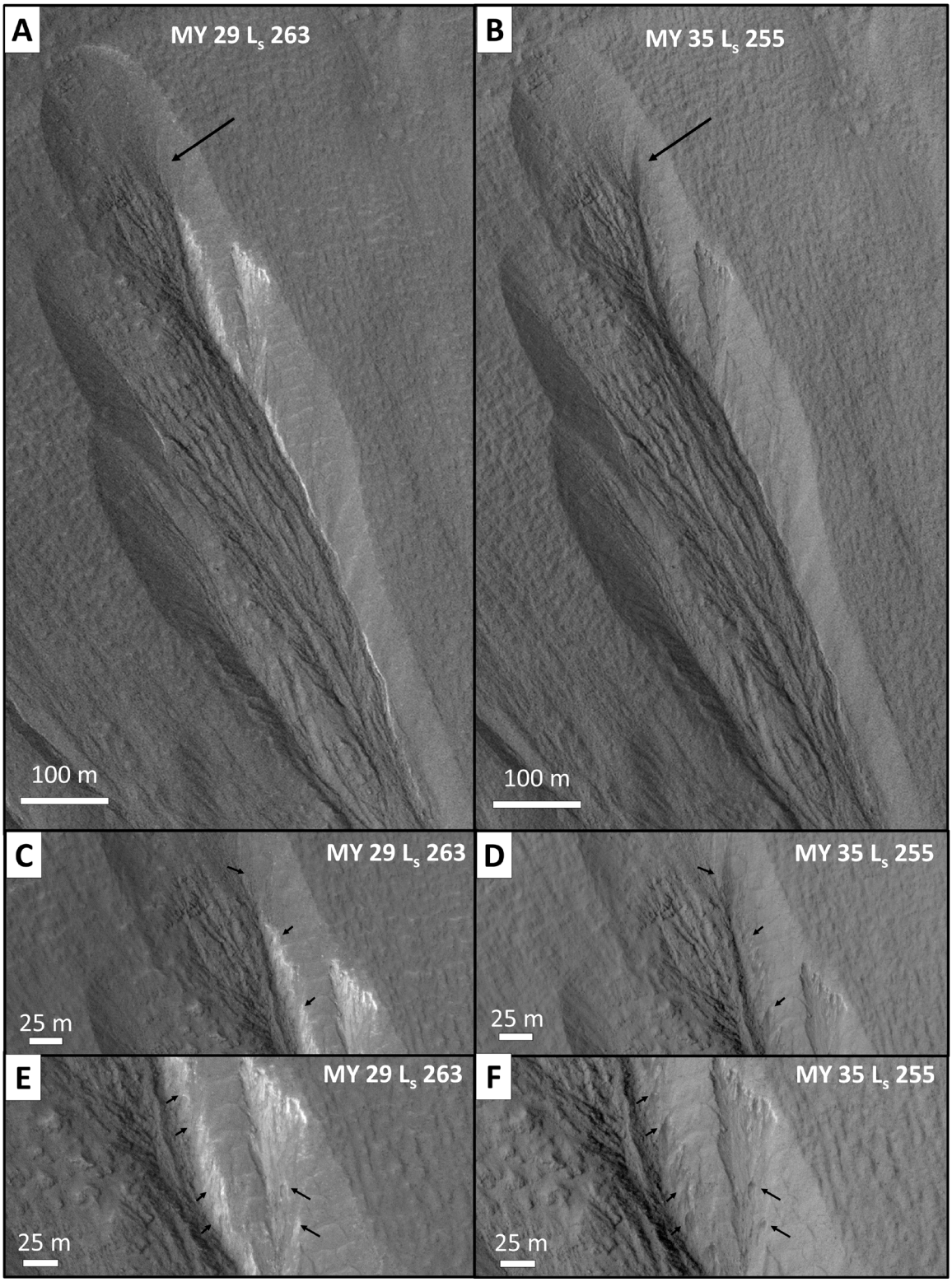
A
MY 29 L_s 263
100 m
B
MY 35 L_s 255
100 m
C
MY 29 L_s 263
25 m
D
MY 35 L_s 255
25 m
E
MY 29 L_s 263
25 m
F
MY 35 L_s 255
25 m

Figure 2.9. Observed changes within Gully 1. The light-toned materials are not present in B, D and F, six MY later. In B (shown in detail in D), a ~50 m slump (black arrow) that appears to show ~10 m topographic retreat is present towards the top of the image, which was not present in A. Other ~10 m slumps and hollows are present in B and D (black arrows) in regions where the light-toned materials were present in A and C. ESP_013067_1470 (A, C and E) and ESP_065800_1470 (B, D and F) were acquired in MY 29, L_s 263 and MY 35, L_s 255, respectively. The two images have incidence angles of 41.8° and 46.1°, with emission angles of 0.3° and 4.4°, respectively. See Supplementary Animations 1–3 (https://doi.org/10.1029/2020JE006539) also.

Figure 2.9 and Supplementary Animations 1–3 show numerous changes observed in Gully 1 over six Mars Years (MYs). First, the light-toned materials present in MY 29 (Figs. 2.9a, c and e) are no longer visible in MY 35 (Figs. 2.9b, d and f). Second, there are multiple locations within the gully alcove where slumping has occurred, with the largest (~50 m in length) slump at the top of the alcove (black arrow in Figs. 2.9a and b). To check whether the appearance of the ~50 m long slump is caused by differences in lighting to first order (see Section 4.1. in Cushing et al., 2015), we measured the width of the slump in Figure 2.9b. We obtained a slump width of ~10 meters. Assuming that the slump is actually a shadow cast by a ridge, we obtain a ridge height of ~10 meters for an incidence angle of 46.1° (Fig. 2.9b), which would cast a ~9 m shadow for an incidence angle of 41.8° (Fig. 2.9a). However, no such ~9 m shadow is apparent in Fig. 2.9a, indicating that this ~50 m slump represents a topographic change of ~10 m; the effect of a ~4° difference in emission angle between the two images is small. Additional, smaller-

scale (~10 m length) slumps might also have occurred at various points within the mantle (black arrows in Figs. 2.9c–f). Alternatively, existing slopes and pit edges may have moved slightly. Third, topographic depressions (Fig. 2.9e) that seem to be present in MY 29 appear to have deepened, although it is possible that slightly different solar illumination angles cause this apparent deepening effect in some cases.

2.6. Discussion

2.6.1. Is the Light-toned Material Dust or Ice?

One hypothesis for the light-toned material having a higher albedo than nearby materials is that it is dust. Dust likely deposits onto all of these surfaces, but it seems unlikely that a highly localized, short-term deposit of dust would form. In addition, this light-toned material occurs only within alcoves eroded into snow-rich mantles, and not nearby rocky walls or surfaces. We suggest that a more plausible explanation is that the light-toned materials are exposed H_2O ice. It may be possible for dust to accumulate within these alcoves as a lag being left behind after the ice disappears (by sublimation and/or melting). However, the appearance, and then subsequent disappearance of these light-toned materials suggests that they are some form of volatile, such as dusty ice, rather than dust alone. Since these light-toned materials are exposed in relatively small (< ~20 m) patches, they cannot be confidently resolved by sparsely available CRISM data. However, the appearance (in HiRISE color data) of these light-toned materials is similar to the > 100 m thick, light-toned ice deposits exposed by steep mid-latitude scarps (Dundas et al., 2018), indicating that these materials are probably also ice, with some amount of dust on, and within the ice.

2.6.2. Is the Ice Frost or Exposed Subsurface H_2O Ice?

Light-toned materials present within and around mid-latitude gully alcoves have been attributed to surficial frosts (H_2O and CO_2) (e.g., Levy et al., 2009b; Dundas et al., 2019), especially during winter and spring imagery. These frost observations have been confirmed by CRISM data at numerous southern mid-latitude active gully sites (Vincendon, 2015). However, the exposed ice seen in Figures 2.4–8, 2.S4 and 2.S6 is unlikely to be persistent frost in equilibrium, due to several observations: (1) The HiRISE data were obtained during late spring/ summer afternoon, when frost is not expected at these latitudes (Schorghofer & Edgett, 2006; Carrozzo et al., 2009; Vincendon et al., 2010a). (2) The morphologies of the exposed ice are reminiscent of exhumation rather than surficial frosts, similar to the recent discovery of much larger-scale, exposed H_2O ice sheets by Dundas et al. (2018). (3) THEMIS infrared data (100 m/pixel) indicate that the gully alcoves containing exposed ice generally have late-afternoon spring/summertime temperatures > ~240 K (Table 2.S4), which are greater than the predicted frost points for CO_2 (150 K; Piqueux et al., 2016) and H_2O (210 K; Schorghofer & Aharonson, 2005). Thus, the ice must be present in the subsurface, and is exposed by slumping of overlying material. Based on the morphology, albedo and setting of the ice, we conclude that dust is likely to be within and overlying the ice. These observations of exposed subsurface H_2O ice therefore represent the lowest latitude (e.g., 32.9°S) detections of H_2O ice to date, and agree with model predictions that near-surface ice is stable on cold, pole-facing slopes poleward of ~30° (Aharonson & Schorghofer, 2006; Vincendon et al., 2010b).

2.6.3. Implications for Gully Formation

The observation of dusty H_2O ice within mid-latitude mantling deposits that often have gullies eroded into them has implications for the processes that can erode the ice, and sometimes the underlying wall rock. In the following sections we review and present some models of gully erosion and discuss the possibility of applying them to gully erosion in the H_2O ice-rich mantle and the wall rock beneath.

2.6.3.1. CO_2 Frost Model

Sand dunes, gully fans and existing gully alcoves/channels (e.g. Figs. 6 and 7 in Dundas et al. (2015b)) are usually sites of the most significant present-day gully activity (Dundas et al., 2019). Aeolian ripples are often observed within such materials, indicative of their unconsolidated nature. Morphological studies (Diniega et al., 2010; Dundas et al., 2010; Dundas et al., 2012; Dundas et al., 2015b; Dundas et al., 2019) and lab experiments (Sylvest et al., 2016; Sylvest et al., 2019) have shown that CO_2 frost processes are excellent candidates for transporting these unconsolidated, granular materials. However, we consider them unlikely to erode gullies into the mantle and the wall rock beneath because of the far greater erosive power needed to erode H_2O ice or rock than transport loose, granular material. In addition, even if CO_2 frost processes can cause boulders to fall and/or be transported on steep slopes in the form of debris flows (Dundas et al., 2019), to date, these sorts of flows have not caused any observable erosion into wall rock, although it is possible that the erosion is too minor to be resolved by HiRISE. Thus, other processes seem likely to explain the erosion of H_2O ice or rock at gully locations.

First, we consider rock erosion. Experimental studies (Viles et al., 2010) and in-situ data (Eppes et al., 2015) have shown that thermal cycling can potentially induce small reductions in strength (~1%) and form cracks in martian rocks. However, the presence of numerous large rocks on ~billion-year old surfaces (Fergason et al., 2006a; Golombek et al., 2006) near the equator, where solar insolation and thermal breakdown processes are most effective (Viles et al., 2010; Eppes et al., 2015) argues against the efficacy of thermal cycling to produce unconsolidated, granular materials for CO_2 frost to transport. Thermal cycling might cause initial weakening (~1%), after which rock surfaces reach equilibrium, with little additional weathering after initial weakening (Viles et al., 2010). At the mid-latitudes, rock breakdown might also occur from CO_2 frost sublimation-freeze cycling and ice wedge formation (Sizemore et al., 2015), but the efficacy of these processes under martian conditions is presently unknown. Another possible rock breakdown mechanism for gullies formed on crater walls is the impact itself, which can create talus for CO_2 frost to transport. Although this mechanism could be applicable in isolation, most mid-latitude slopes are mantled by H_2O ice, which cannot be eroded by CO_2 frost. Additionally, about 35% of all martian gullies have been observed on non-crater wall slopes (on isolated knobs, valley walls, etc.; Harrison et al., 2015) where the effects of impact events will not apply. Thus, although the CO_2 frost model cannot be ruled out, some additional processes might still be required to explain how gullies are eroded into H_2O ice and wall rock. In the sections below, we discuss two models for erosion into H_2O ice and wall rock, that we term the 'H_2O Ice Sublimation Model' and the 'H_2O Ice Melt Model'.

2.6.3.2. H_2O Ice Sublimation Model

To explain erosion into the mantle and the wall rock, some authors (Forget et al., 2016; Dundas et al., 2018; Dundas et al., 2019) have suggested that the removal of overlying dust (e.g., by CO_2 processes) can induce the sublimation of H_2O ice below, eroding gullies into the mantle in an alternating sequence of overlying dust removal and H_2O ice sublimation (which frees up any lithics within the ice for transport, as it ablates). However, ice sublimation typically occurs unevenly due to the nature of vapor diffusion (Luikov & Lebedev, 1973; Wellen, 1979; Law & Van Dijk, 1994). Crystal structure defects act as centers for ice sublimation and are greatly influenced by localized thermal gradients (Law & Van Dijk, 1994). Thus, if the overlying dust is removed and the H_2O ice begins to sublimate, then variations in local solar insolation, surface geometry and ice exposure will dictate the surficial morphology and cause it to erode unevenly. Therefore, sublimation processes in volatile-rich materials form scalloped depressions or pits (Mangold, 2011a; Mangold, 2011b). Evidence for volatile sublimation can be seen in (a) quasi-circular depressions in the south polar cap (Byrne & Ingersoll, 2003), (b) the 'degraded' portions of the mid-latitude mantle (Mustard et al., 2001; Schon et al., 2009; Mangold, 2011a), (c) in ice-rich mid-latitude materials (Zanetti et al., 2010; Dundas et al., 2015a; Harrison et al., 2017; Dundas et al., 2018; Viola & McEwen, 2018) as well as (d) cross-cutting fractures in the form of coalescing pits sometimes associated with gullied terrain (Dickson et al., 2015).

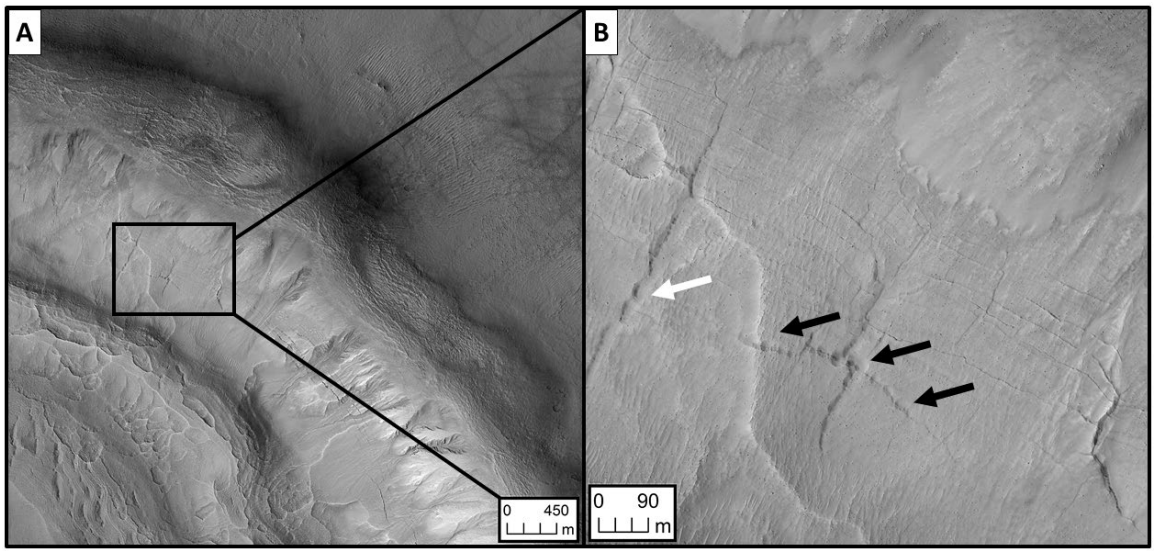

Figure 2.10. Likely sublimation-induced features within mantle units. Crater in Utopia Planitia (ESP_028719_2290 at 48.5°N, 89.4°E) that exhibits (A) large-scale, poorly developed scalloped depressions and (B) cross-slope (black arrows) and downslope (white arrow) coalescing fractures/sublimation pits.

These sublimation processes typically progress downwards through volatile-rich materials, rather than propagating into a channel. Even on slopes, these sublimation features appear to retain their quasi-circular expression (Fig. 2.10), suggesting that sublimation processes play a limited role in the formation of the relatively well-defined V-shaped gully incisions eroded into the mantle.

Additionally, the observation of the same channels eroded into the mantle and wall rock seems unlikely to be explained by the combination of proposed CO_2 frost processes and H_2O ice sublimation. This is because there is probably little to no H_2O ice within the wall rock, and if H_2O sublimates, it will diffuse upwards into the relatively dry and heavy ($m_{CO_2} > m_{H_2O}$) atmosphere (Ingersoll, 1970; Sears & Moore, 2005;

Blackburn et al., 2010) rather than downwards into wall rock. While CO_2 frost processes might be capable of mobilizing loose materials, and potentially trigger boulder-filled flows, we consider CO_2 frost unlikely to erode wall rock unless the wall rock is assumed to be unconsolidated and granular, which is not expected for most martian slopes (see Section 2.6.3.1). Furthermore, we propose that the sublimation of H_2O ice will likely lead to uneven mass loss by vapor diffusion. Thus, neither process seems likely to be able to erode both materials. However, H_2O sublimation could potentially still play a role in the growth of some gully alcoves (Dundas et al., 2018, 2019).

2.6.3.3. H_2O Ice Melt Model

We propose a model for gully formation based on Christensen (2003): (1) Several centimeters of dusty snow are deposited at the mid-latitudes during periods of high obliquity (Jakosky & Carr, 1985; Madeleine et al., 2014). (2) As the snow sublimates and/or melts to form gullies within the snow (often characterized by a V-shaped channel), it builds up a protective lag layer of dust, as is observed on melting snowfields on Earth (e.g., Higuchi & Nagoshi, 1977). The formation of this lag, caused by snow ablation and possible dust storms (Williams et al., 2008; Madeleine et al., 2014) ceases the formation of gullies since the snow is buried and no longer exposed to sunlight. (3) Throughout these processes, the remnant dusty snow is probably metamorphosing into denser, coarse-grained ice. (4) Then, slumping within steep gully alcove walls by aeolian/frost processes leads to partial ice re-exposure. This exposed dusty ice absorbs solar radiation deeper than fresh snow, and continues to melt in the subsurface while eroding channels within the ice. If sufficient meltwater is available at the base of the ice layer, channels can be

eroded into the wall rock beneath. (5) When all the ice disappears from melting and sublimation, the dust within the ice is left behind. Steps (1) through (5) repeat over multiple obliquity cycles, leading to layers of dust and snow building up within the mantle, and gullies forming deeper channels each time ice is exposed, and melts. Evidence for this ice-dust layering within the mantle is supported by modeling results (Madeleine et al., 2014), exposures of mantle stratigraphy within steep scarps (Dundas et al., 2018) and observations of layers within the mantle (Schon et al., 2009).

In this model, small amounts of runoff (~1 mm/day) at the mid-latitudes can be produced during the summer (~50 sols) each year, potentially even under present conditions (Clow, 1987; Williams et al., 2008). Seasonal melting and refreezing can concentrate mechanical weathering at the locations where runoff can remove debris, leading to high rates of erosion despite small amounts of water (termed the Eisrinde effect on Earth; Büdel et al., 1982; Baker, 1985). Additionally, if martian slope materials are already unconsolidated (as discussed in Section 6.3.1; by thermal cycling, impact events, CO_2 frost processes, etc.), then freeze-thaw action can break them down further, leading to debris flows and/or slurries. Gullies can form on thousand year timescales, with ~40 m^3 of liquid water available for each channel, assuming typical gully alcove size and spacing (200 × 200 m^2) and 1 mm of meltwater per day (Christensen, 2003a).

A H_2O ice melt model can explain many gully and mantle characteristics. Melting is favored on pole-facing slopes at lower latitudes, and equator-facing slopes at higher latitudes due to optimal solar insolation for melting shifting to equator-facing slopes poleward of ~45–60° latitude (Costard et al., 2002). This is consistent with gullies losing

their pole-facing preference, and transitioning to being present on equator-facing slopes at higher latitudes (Harrison et al., 2015). In addition, the small amounts of melt formed in near-freezing conditions implies a low rate of chemical weathering and mineralization, which is consistent with the lack of hydrated minerals at gully sites (Núñez et al., 2016).

The observation of gullies eroded into the wall rock that continue into the mantle is also consistent with H_2O ice melt. If the mantle was deposited as dusty snow on slopes, it probably extended further upslope and a single process eroded the mantle and the wall rock. As the mantle was removed, the underlying wall rock gully was exposed. This underlying wall rock gully formed when meltwater percolated downwards and was available for erosion. Where wall rock erosion is not visible today, there may have been insufficient meltwater production and/or the liquid water did not reach the substrate for erosion.

However, H_2O ice melt is not expected to occur at all locations of snow accumulation, such as where the amount of snow accumulation is too low (near the equator) or where conditions are too cold for melting to occur (> 70° latitude). Melting might also cease to occur when the snow becomes too dusty (greater than a few percent) near the surface, because light will not be able to penetrate deeply and cause subsurface heating. Furthermore, H_2O ice melt cannot explain erosion where there are no sources of snow, in addition to present-day gully activity occurring in the winter. Thus, the formation of mid-latitude martian gullies is probably not caused by one single mechanism and is likely dependent on a variety of factors: location, substrate, topography, season, atmospheric conditions and obliquity period. The influence of micro-climates on

individual gully morphology can also play a significant role in gully formation. Gully formation and activity on Mars is therefore likely to be caused by a mixture of many different processes that may not be mutually exclusive.

2.7. Conclusions

Here we present novel evidence consistent with dusty, water ice deposits present within gullies eroded into mid-latitude mantles. Our observations likely represent the lowest latitude (e.g., 32.9°S) detections of H_2O ice to date, in agreement with numerical models that predict stable near-surface ice on pole-facing slopes at latitudes poleward of 30°. These ice deposits are like the materials documented within icy mid-latitude scarps, but with more dust and exposed in smaller patches by slumping. In addition, we observe gullies eroded in wall rock that continue into the mantle, implying that the same process erodes the wall rock and the mantle. We propose a H_2O ice melt model that can explain gullies eroded in the wall rock and the mantle. This H_2O ice melt model is supported by numerical simulations that show that relatively dense H_2O snow on Mars only melts when it contains small amounts of dust. Although the precise physical properties (grain radius, density, etc.) of H_2O ice on Mars are unknown, the observed exposure of dusty H_2O ice provides a mechanism for it to melt under some conditions and form some gullies. Subsurface H_2O ice melt could potentially be even occurring today, and access to liquid water within the ice could provide potential abodes for any extant life. However, H_2O ice melt is not expected to occur at all locations of H_2O ice on Mars, and martian gullies are likely to form by a combination of many different processes (e.g., CO_2 frost, H_2O ice sublimation, H_2O ice melt, etc.). Future work to model the formation and

evolution of H_2O ice in the martian mid-latitudes and refine the conditions under which martian H_2O ice melt is possible is currently ongoing.

2.8. Acknowledgments

The authors would like to thank Deanne Rogers, Colin Dundas and Kaj Williams for formal reviews that significantly improved the manuscript. We are immensely grateful to Steve Ruff, Gary Clow, Serina Diniega, Sarah Rogers, Steve Warren and Alejandro Martinez for providing informal reviews of the manuscript. Tanya Harrison, Sophia Casanova, Jeff Plaut, Jay Serla, Anna Grau, Anmol Lal, Tristan Kimball, Sean Peters, Heather Lethcoe, Jay Dickson and Abby Fraeman also gave very helpful feedback and advice. Additionally, we would like to thank the HiRISE, CTX and THEMIS teams for their excellent work.

The authors declare that they have no competing financial interests.

2.9. Data Availability Statements

HiRISE imagery is available at https://hirise.lpl.arizona.edu/. CTX imagery can be accessed at http://ode.rsl.wustl.edu/mars/. THEMIS data can be accessed using JMARS, available at https://jmars.asu.edu/. Phoenix Surface Stereo Imager (SSI) data is available at https://pds-imaging.jpl.nasa.gov/data/phoenix/phxssi_1xxx/. H_2O ice refractive index data (Warren and Brandt, 2008) is available at https://atmos.uw.edu/ice_optical_constants/. Results and data from the snow-dust spectral model and the martian snow/ice thermal conductivity modeling in the supporting information are available in (Khuller & Christensen, 2020) (repository: https://doi.org/10.5281/zenodo.4356920).

2.10. Supplementary Material

Text 2.S1. Thermal Conductivity of Snow and Ice on Mars

The effective thermal conductivity of snow K_s is a combination of heat conduction within the ice lattice, pore gas conduction K_g, thermal radiative transfer K_r and water vapor diffusion across pores K_v. Hence, snow thermal conductivity is dependent on the density ρ and the grain size of the snow. Additionally, on Mars, the snow conductivity is strongly dependent on the temperature T, and rises rapidly as temperatures approach the melting point (Figure 2.S1) due to latent heat transfer by vapor diffusion within snow pores in a low atmospheric pressure CO_2 environment (Clow, 1987). These latent heat effects can even cause the thermal conductivity of martian snow to exceed that of solid ice (using eqns. 3-4 in Chapter 10, p. 205 of Paterson (1994), for example) for temperatures greater than ~255 K. The thermal conductivity of solid ice does not show this strong dependence on temperature because vapor diffusion within the ice in its solid state is negligible. Based on Clow (1987) and the model of Brailsford and Major (1964), the snow thermal conductivity is given by

$$K_s = \frac{K_i}{4}\left[\frac{(3\phi - 1)K_p}{K_i} + 2 - 3\phi + \left\{\left[\frac{(3\phi - 1)K_p}{K_i} + 2 - 3\phi\right]^2 + \frac{8K_p}{K_i}\right\}^{\frac{1}{2}}\right] \quad (1)$$

where ϕ is the snow porosity, K_i is the thermal conductivity of solid ice (Yen, 1981; Paterson, 1994),

$$K_i = 9.828\exp(-0.0057T)\ W\ m^{-1}K^{-1} \quad (2)$$

and K_p is the effective conductivity of the pores, given by the sum of

$$K_p = K_g + K_v + K_r \tag{3}$$

The gas thermal conductivity K_g is

$$K_g = \rho^* C_p D_h^* \left(\frac{T}{273}\right)^{n-1} \tag{4}$$

where ρ^* is the density of CO_2 under standard Earth conditions (1013 mbar and 273 K), $C_p = 770 + 0.62(T - 198)$ is the specific heat of the gas, $D_h^* = 8.54 \times 10^{-6}\ m^2\ s^{-1}$ is the diffusivity constant of CO_2 and $n = 2$.

The vapor diffusion conductivity due to latent heat transfer K_v is

$$K_v = 4D_v^* \left(\frac{\mu_v L_s}{273R}\right)^2 \left(\frac{1013 e_s}{PT}\right) \tag{5}$$

where $D_v^* = 1.37 \times 10^{-5}\ m^2\ s^{-1}$ is the diffusivity of water vapor in CO_2, μ_v is the molecular weight of water, L_s is the latent heat of H_2O sublimation, R is the gas constant, e_s is the saturation vapor pressure over water ice and P is the local atmospheric pressure.

Finally, the radiative conductivity across a pore cavity is given by

$$K_r = 4\sigma\varepsilon d T^3 \tag{6}$$

where σ is the Stefan-Boltzmann constant, ε is the thermal infrared snow emissivity and d is the pore diameter. For additional details on the derivation of the equation above, refer to Clow (1987).

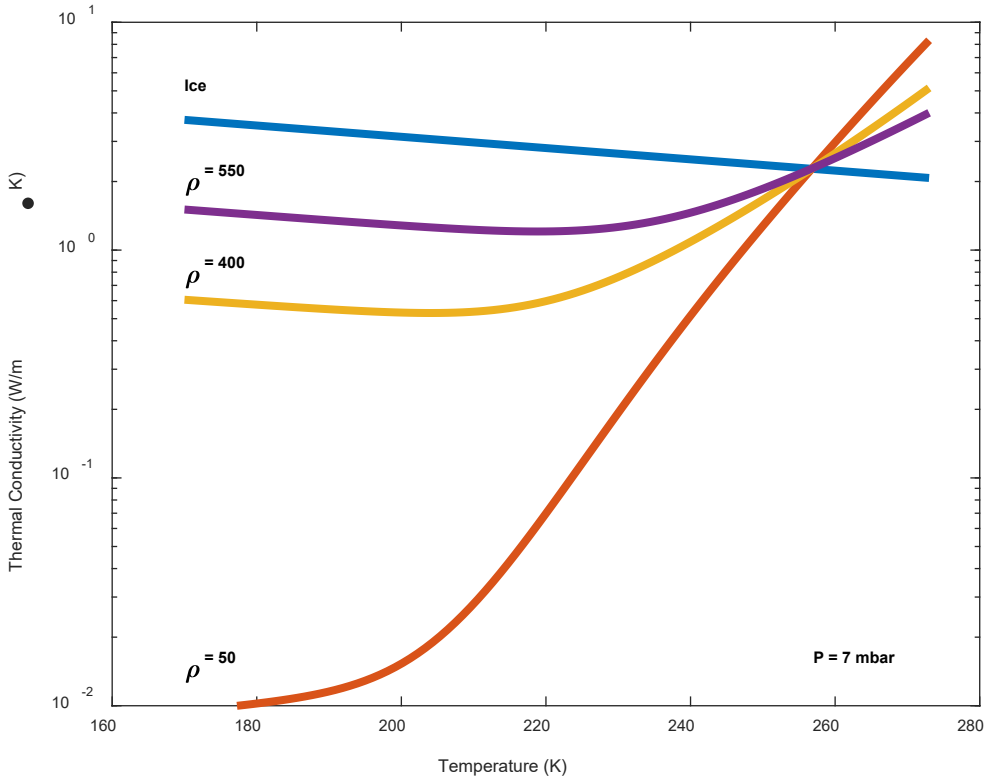

Figure 2.S1. Thermal conductivity of snow and ice on Mars for a range of temperatures and densities for an atmospheric pressure of 7 mbar. The assumed grain radius for each snow density shown is given in parentheses: 50 kg/m^3 (50 µm), 400 kg/m^3 (800 µm) and 550 kg/m^3 (4 mm).

Knowing the thermal conductivity of martian snow and ice is important because it affects the heat balance within snow and ice, and whether the snow/ice will change its phase (from solid to liquid or gas). Figure 2.S1 shows the thermal conductivity of martian snow and ice for average present-day conditions on Mars (atmospheric pressure of 7 mbar). As snow density increases, the thermal conductivity of the snow approaches that of glacier ice, but exceeds the thermal conductivity of glacier ice above ~250 K due to vapor diffusion/latent heat effects. Models of dusty martian snow find that despite the

elevated thermal conductivity of snow (at 550 kg/m^3, for example) above ~250 K, melting temperatures of 273 K can be attained within the snow under present-day conditions (Clow, 1987; Williams et al., 2008). The precise density and grain radius of martian snow are currently unknown, but analysis of in-situ data (Gyalay et al., 2019) and radar measurements (Bramson et al., 2017) suggest grain radii of ~1–1.3 mm and ~640 kg/m^3, which imply that the snow has not metamorphosed into glacier ice yet and could potentially melt under favorable conditions.

Text 2.S2. Modeling the Spectral Albedo of Ice-Dust Mixtures

The ice-dust mixture spectral albedo model is derived from terrestrial models for snow-dust mixtures (Warren & Wiscombe, 1980; Wiscombe & Warren, 1980; Dang et al., 2015), using Mie theory (Matzler, 2002). A delta-Eddington radiative transfer model is used to calculate the spectral albedo of dust-snow mixtures using refractive index data for H_2O ice (Warren & Brandt, 2008) and martian dust (Wolff et al., 2009).

Because the albedo of a mixture of ice and dust are sought, the scattering properties of each component are combined as an external mixture (it is assumed that dust particles are not located inside the ice grains) using the model of Dang et al. (2015). Scattering by all grains is assumed to be similar to spheres in their far fields. In this model, the size distribution of each component is given by $n_{ice}(r_{ice})$ and $n_{dust}(r_{dust})$, for ice and dust, respectively, where the units of n are particles per m^3 and r_{ice}, r_{dust} represent the radii of ice and dust grains, respectively, in meters. Each particle has volume $V = \frac{4}{3}\pi r^3$ and cross-sectional area $A = \pi r^2$. For n values scaled by scale factors f_{ice} and f_{dust}, the total density of the ice-dust mixture is given by:

$$\rho_{total} = f_{ice}\rho_{ice}\sum_{ice} V_{ice}n_{ice} + f_{dust}\rho_{dust}\sum_{dust} V_{dust}n_{dust} \quad (7)$$

where $\rho_{ice} = 917\ kg/m^3$ and $\rho_{dust} = 870\ kg/m^3$ (Allen et al., 1998; Dang et al., 2015). Based on the formulas for scattering by spheres, the complex refractive index $m(\lambda)$ and the dimensionless size parameter x are required as inputs to the Mie scattering code (Matzler, 2002):

$$x = \frac{2\pi r}{\lambda} \quad (8)$$

where λ is the wavelength, and r is the average grain radius of the material. We then calculate the following quantities for ice and dust, separately:

$$\sigma_{ext} = \pi r^2 Q_{ext} \quad (9)$$

$$\bar{\omega} = \sigma_{scat}/\sigma_{ext} \quad (10)$$

$$g = mean(\cos(\theta)) \quad (11)$$

where σ_{ext} is the extinction cross section, Q_{ext} is the dimensionless extinction efficiency, $\bar{\omega}$ is the single-scattering albedo, σ_{scat} is the scattering cross section, g is the

asymmetry factor and θ is the scattering angle (see van de Hulst (1957) for a review of these terms).

Defining the mass fractions of ice and dust to be C_{ice} and C_{dust}, we obtain (ignoring the negligible mass of air):

$$C_{ice} + C_{dust} = 1 \tag{12}$$

The scaling factors f_{ice} and f_{dust} are then given by:

$$f_{ice} = \frac{C_{ice}\rho_{snow}}{\rho_{ice}\sum V_{ice}n_{ice}} \tag{13}$$

$$f_{dust} = \frac{C_{dust}\rho_{snow}}{\rho_{dust}\sum V_{dust}n_{dust}} \tag{14}$$

where ρ_{snow} is the density of the snow. The total extinction cross-section σ_{ext}^{total}, scattering cross section σ_{scat}^{total}, single-scattering albedo ϖ^{total} and asymmetry parameter g^{total} of the mixture are given by:

$$\sigma_{ext}^{total} = f_{dust}\sigma_{ext}^{dust} + f_{ice}\sigma_{ext}^{ice} \tag{15}$$

$$\sigma_{scat}^{total} = f_{dust}\sigma_{scat}^{dust} + f_{ice}\sigma_{scat}^{ice} \tag{16}$$

$$\bar{\omega}^{total} = \sigma_{scat}^{total}/\sigma_{ext}^{total} \tag{17}$$

$$g^{total} = [g_{ice}f_{ice}\sigma_{scat}^{ice} + g_{dust}f_{dust}\sigma_{scat}^{dust}]/\sigma_{scat}^{total} \tag{18}$$

Using the delta-Eddington approximation for a semi-infinite material, we obtain the following transformations for g^{total} and $\bar{\omega}^{total}$:

$$\bar{\omega}_*{}^{total} = \frac{(1-g^{total})^2\bar{\omega}^{total}}{1-(g^{total})^2\bar{\omega}^{total}} \tag{19}$$

$$g_*^{total} = \frac{g^{total}}{1+g^{total}} \tag{20}$$

The albedo, A of the mixture is given by:

$$A\,(\mu_0) = \frac{\bar{\omega}_*{}^{total}}{1+P}\,\frac{1-b_*\xi\mu_o}{1+\xi\mu_0} \tag{21}$$

where μ_0 is the zenith cosine ($\mu_0 = \cos(\theta_{zenith})$ for a given zenith/solar incidence angle θ_{zenith}, $b_* = g_*^{total}/(1 - \bar{\omega}_*{}^{total} g_*^{total})$, $\xi = \left[3\left(1 - \bar{\omega}_*{}^{total} g_*^{total}\right)\left(1 - \bar{\omega}_*{}^{total}\right)\right]^{1/2}$ and $P = 2\xi/(3(1 - \bar{\omega}_*{}^{total} g_*^{total}))$.

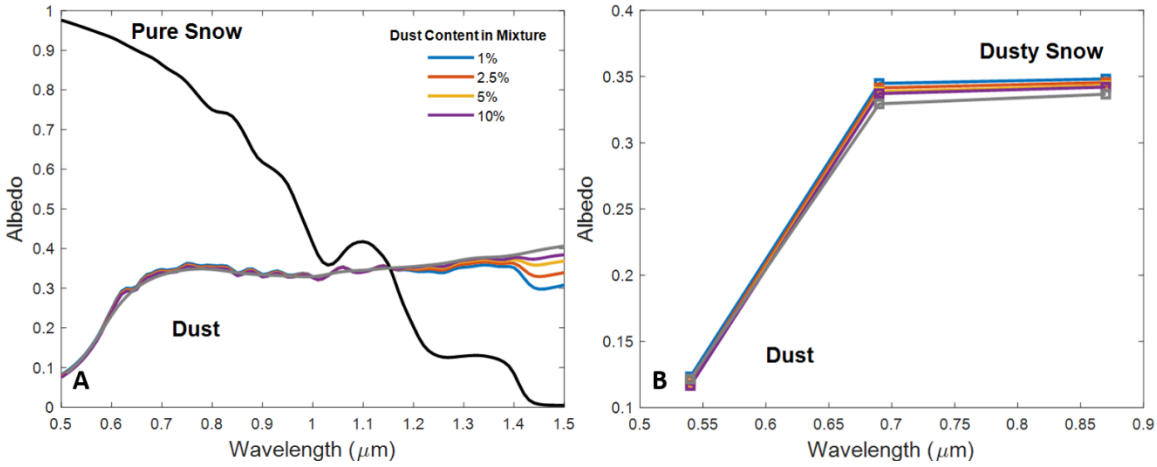

Figure 2.S2. The effect of dust (gray) on the spectral albedo of pure snow (black) for dust contents > 1% between a) 0.5–1.5 µm wavelengths and b) sampled at HiRISE color filter center wavelengths, showing albedos of only dusty snow and pure dust. These computations are for a semi-infinite, 550 kg/m^3 (40% porosity) snowpack with snow and dust grain radii of 1000 and 1.8 µm, respectively, and a solar zenith angle of 49.5°. Note the different y-axis limits.

Note that all modeled albedos shown in this work are for $\mu_o = 0.65$, i.e., a solar incidence angle of 49.5°, which is generally close to the average incidence angle of the HiRISE observations used here. ρ_{snow} was assumed to be 550 kg/m^3 (40% porosity). At visible wavelengths, the modeled albedos are primarily sensitive to (in order of

decreasing sensitivity): dust properties (amount, grain radius and density), the snow grain radius and the snow density, with a negligible effect of the solar incidence angle for wavelengths < 1 μm (Warren & Wiscombe, 1980; Wiscombe & Warren, 1980; Dang et al., 2015). Results were smoothed by a Gaussian filter with a standard deviation of 1, to smooth the minute oscillations of Mie scattering theory which are not applicable to natural deposits (Kieffer, 1990).


A
250 m

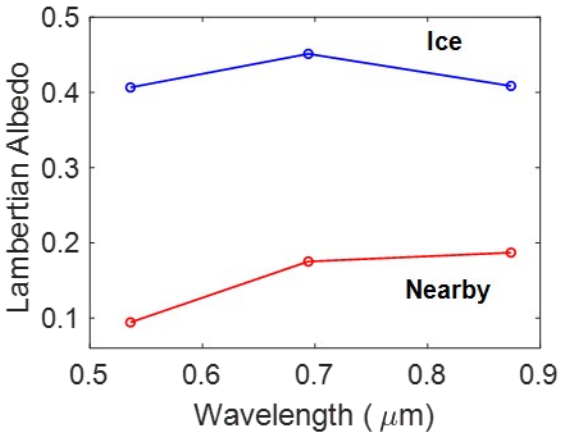
Lambertian Albedo
0.5
0.4
0.3
0.2
0.1
Ice
Nearby
0.5
0.6
0.7
0.8
0.9
Wavelength (μm)

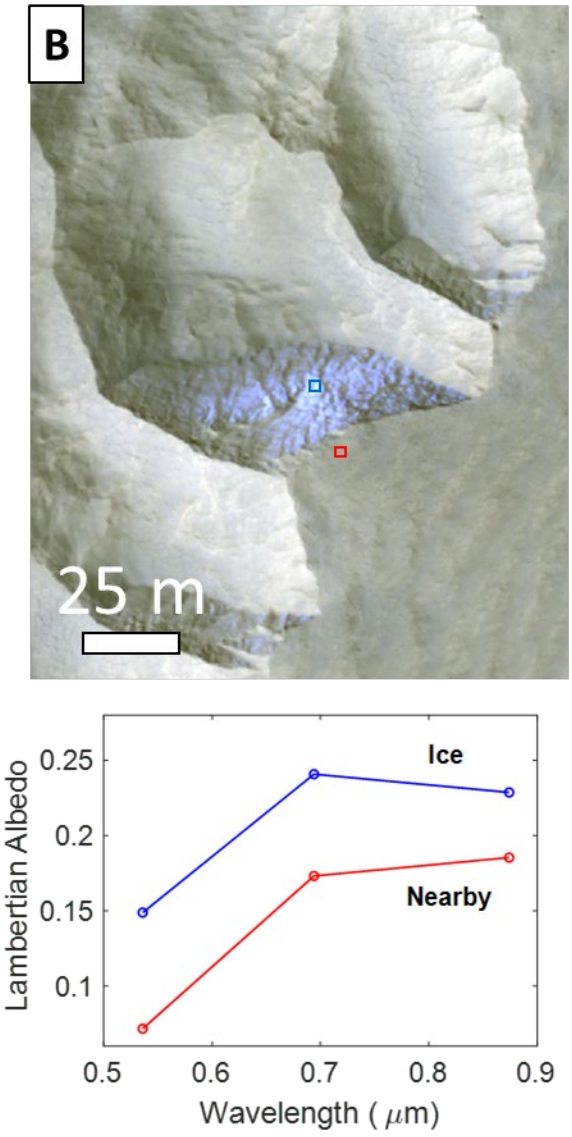

Figure 2.S3. HiRISE Lambert albedos of known H_2O ice compared to surrounding terrain. A) Surface ice deposit at Louth Crater; ESP_045439_2505 and B) Icy scarp; ESP_045290_2350. Images are HiRISE false-color (IRB) and individually contrast-stretched. Approximate locations of spectra (averaged from 5 × 5 pixel boxes) are shown in boxes (not to scale).

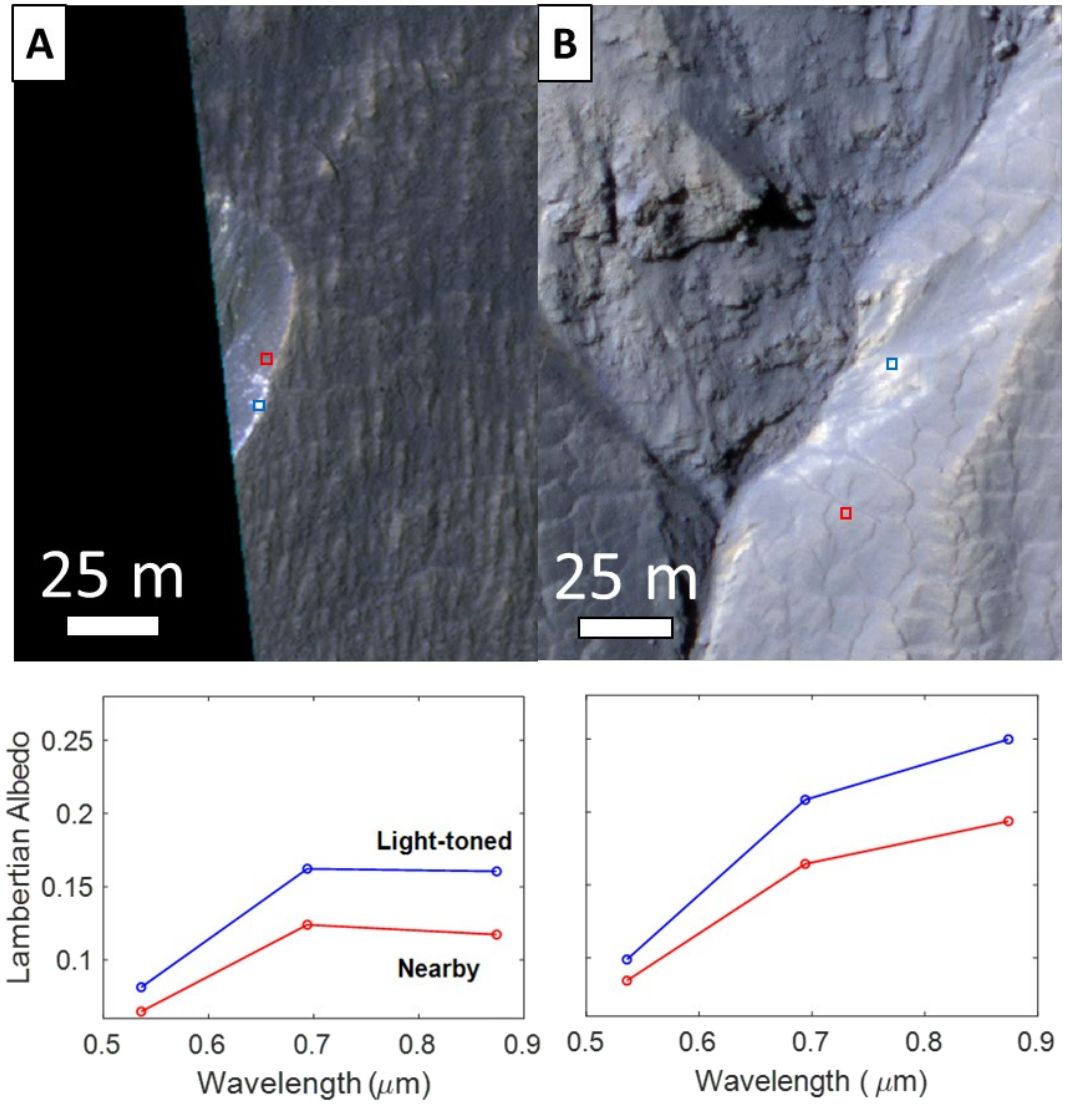
A
B
25 m
25 m
Lambertian Albedo
0.25
0.2
0.15
0.1
Light-toned
Nearby
0.5
0.6
0.7
0.8
0.9
Wavelength (μm)
Wavelength (μm)

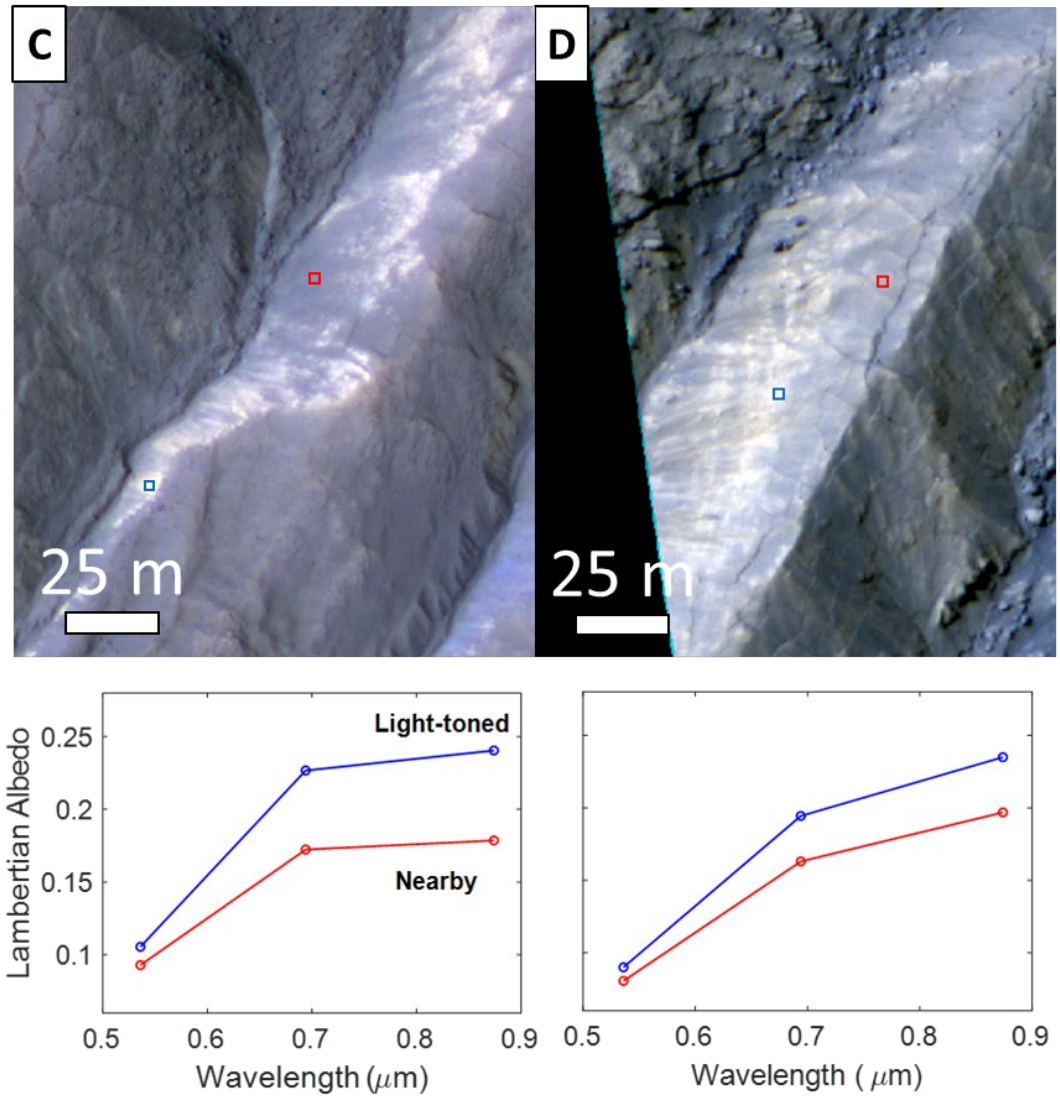
C
D
25 m
25 m
Light-toned
Nearby
Lambertian Albedo
0.25
0.2
0.15
0.1
0.5
0.6
0.7
0.8
0.9
Wavelength (μm)
Wavelength (μm)

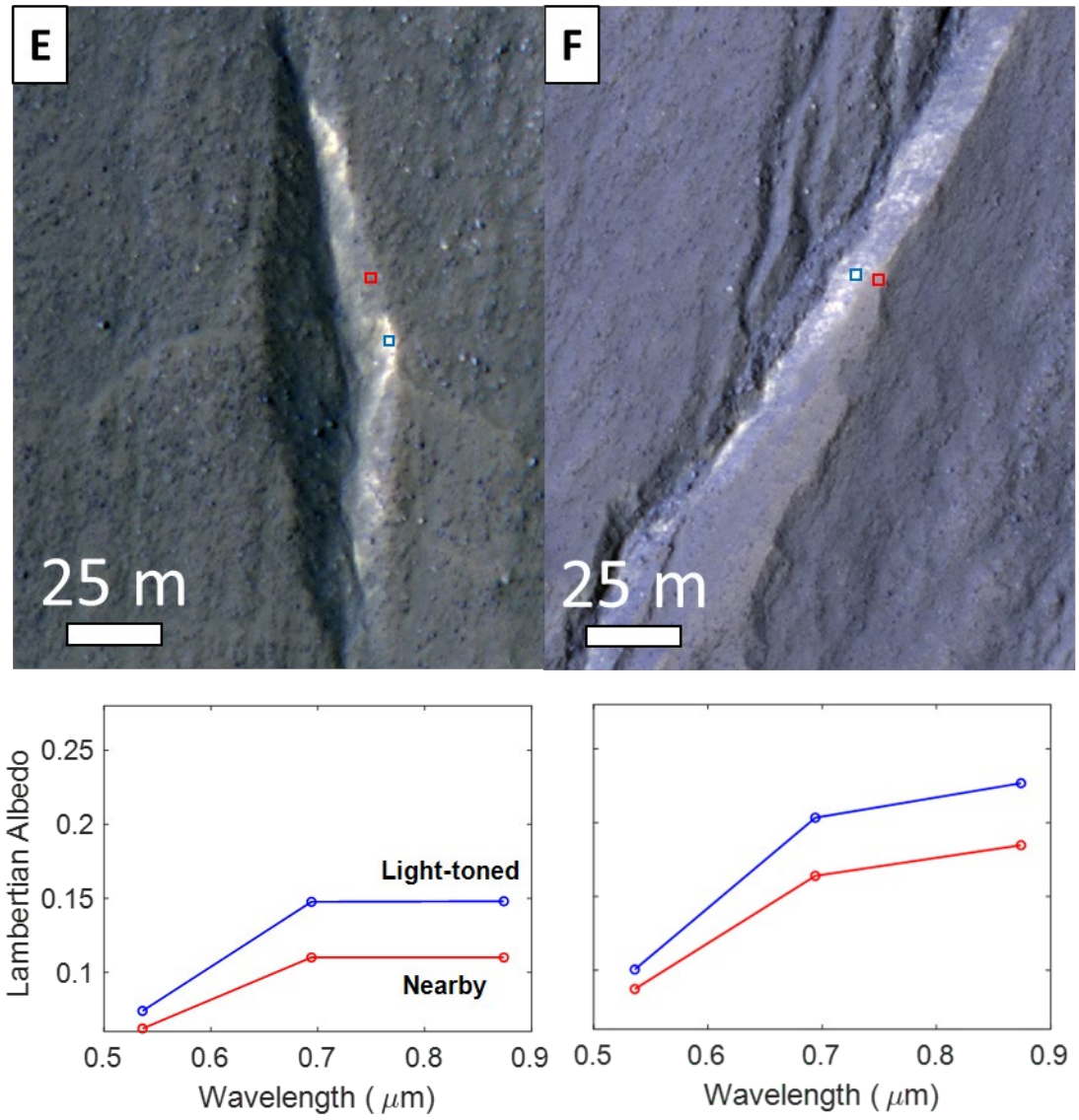
E
F
25 m
25 m
Lambertian Albedo
0.25
0.2
0.15
0.1
Light-toned
Nearby
0.5
0.6
0.7
0.8
0.9
Wavelength (μm)
0.5
0.6
0.7
0.8
0.9
Wavelength (μm)

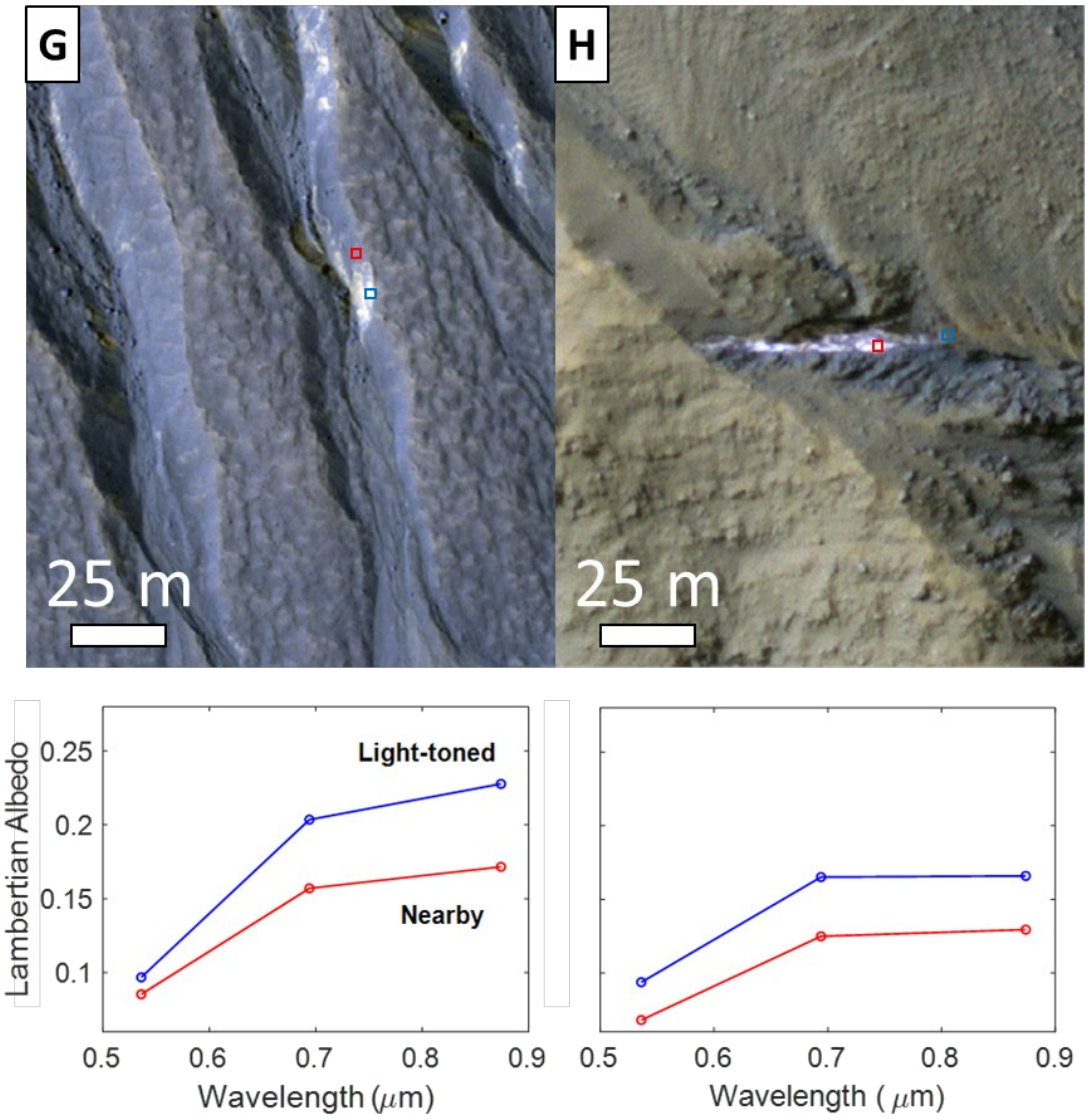

Figure 2.S4. HiRISE Lambert albedos of light-toned materials within gullies compared to surrounding terrain. A) Gully 9; ESP_031220_1420, B) Gully 2; ESP_014329_1435, C) Gully 3; PSP_004145_1455, D) Gully 4; ESP_023137_1400, E) Gully 7; ESP_049168_1425, F) Gully 8; ESP_013235_1445, G) Gully 6; ESP_013314_1450 and H) Gully 11; ESP_058636_1425. Images are HiRISE false-color (IRB) and individually contrast-stretched. Approximate locations of spectra (averaged from 5 × 5 pixel boxes) are shown in boxes (not to scale).

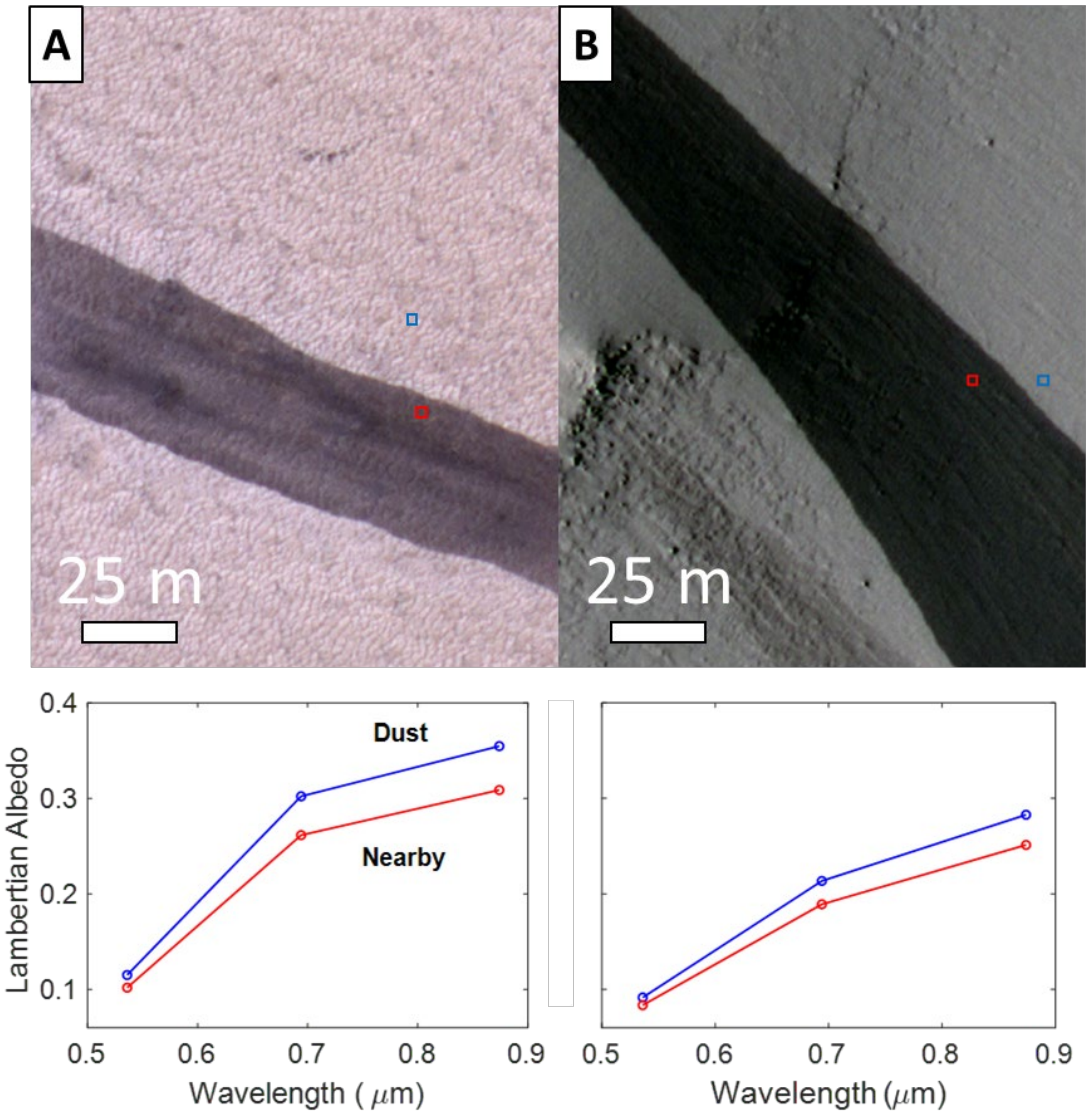

Figure 2.S5. HiRISE Lambert albedos of dusty materials compared to surrounding terrain (less dusty regions). A and B) Slope streaks exposing dark substrates, likely from dust avalanching; ESP_055613_1745 and ESP_029420_1800. Images are HiRISE false-color (IRB) and individually contrast-stretched. Approximate locations of spectra are shown in boxes (not to scale).

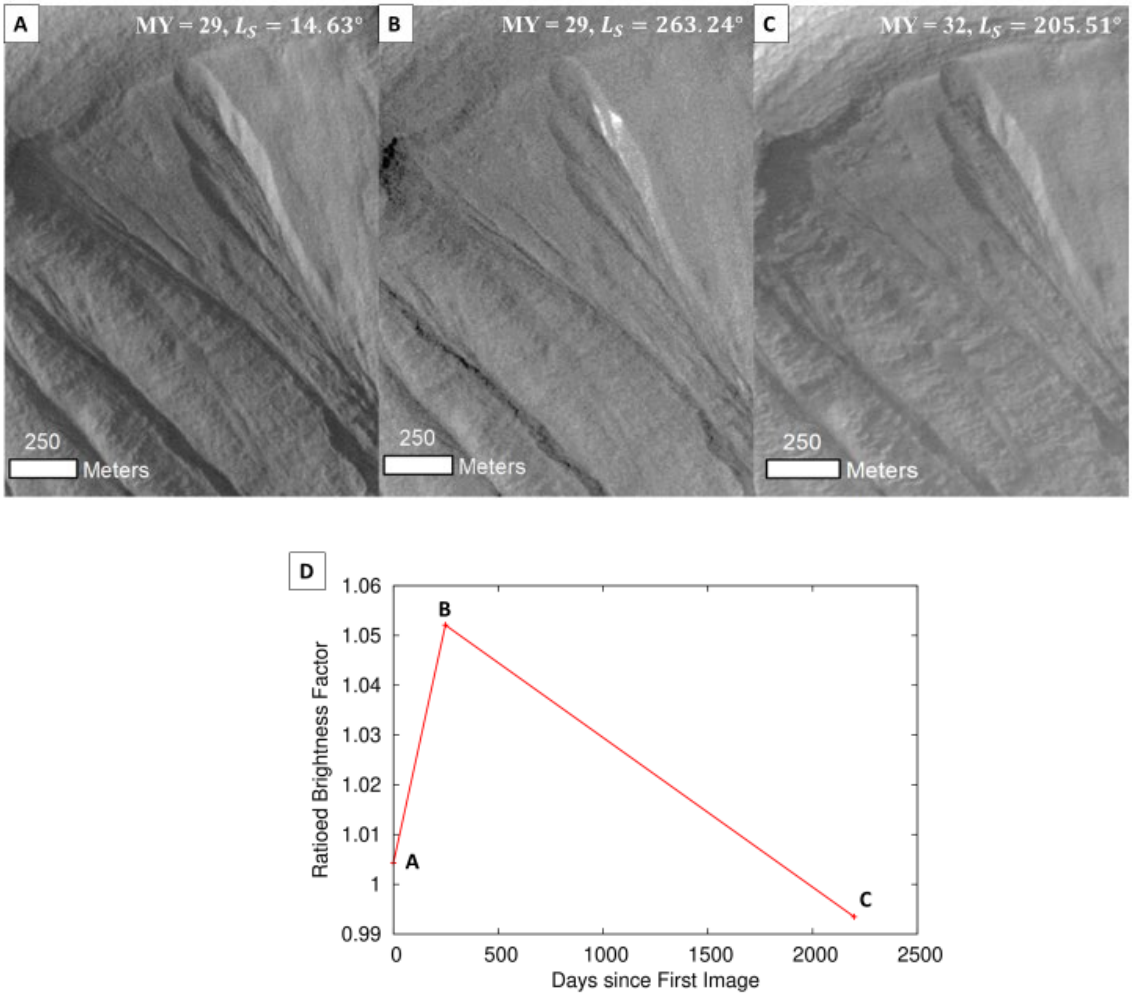

Figure 2.S6. Evolution of light-toned materials in Gully 1 over three Mars Years. (Top) No evidence of light-toned material is seen in A, which is exposed in B, but appears to have faded in C. Portions of CTX images (~5 m/pixel) A (P15_006804_1484), B (B09_013067_1468) and C (F06_038332_1466) are shown here. (Bottom) Ratios of light-toned material and adjacent pixel Lambert albedo from A, B and C show a 5% increase in relative brightness over the light-toned materials in image B.

Table 2.S1. Selected HiRISE Observations of Light-toned Materials within Gullies (G).

Site	Observation ID	Latitude	Longitude	Date	L_s
G1	ESP_013067_1470	-32.926	93.193	5/10/09	263.2
G2	ESP_014329_1435	-36.033	199.473	8/17/09	322.6
G3	PSP_004145_1455	-34.305	329.123	6/15/07	258.0
G4	ESP_023137_1400	-39.453	210.769	7/4/11	322.2
G5	ESP_032012_1415	-38.362	195.329	6/5/13	324.8
G6	ESP_013314_1450	-34.791	189.035	5/29/09	275.3
G7	ESP_049168_1425	-37.088	183.808	1/21/17	303.4
G8	ESP_013235_1445	-35.252	186.351	5/23/09	271.5
G9	ESP_031220_1420	-37.830	217.977	3/25/13	288.5
G10	ESP_048824_1420	-37.856	217.947	12/25/16	287.1
G11	ESP_058636_1425	- 37.086	191.984	1/29/19	332
G12	PSP_005706_1425	- 37.095	191.992	10/15/07	331

Table 2.S2. Selected HiRISE Observations of Ice-rich Materials (I).

Site	Observation ID	Latitude	Longitude	Date	L_s	Reference
I1	ESP_022389_1230	-56.645	114.054	5/7/11	287.8	Dundas et al. (2018)
I2	ESP_040772_1215	-58.091	93.697	4/8/15	322.3	
I3	ESP_045290_2350	54.781	212.025	3/25/16	127.6	

I4	ESP_045439_2505	70.230	103.239	4/6/16	133.2	Brown et al. (2008)
I5	PSP_010625_2360	55.564	150.607	11/1/18	150.8	Byrne et al. (2009)

Table 2.S3. Selected HiRISE Observations of Dusty Materials (D).

Site	**Observation ID**	**Latitude**	**Longitude**	**Date**	**L_s**	**Reference**
D1	ESP_028335_1755	-4.603	137.447	8/12/12	153.9	
D2	ESP_029420_1800	0.086	37.928	11/4/12	201.0	Dundas (2020)
D3	ESP_046740_2175	37.312	229.126	6/16/16	186.7	
D4	ESP_055613_1745	-5.469	263.886	6/7/18	189.3	
D5	ESP_058424_2035	23.498	213.540	1/12/19	323.1	

Table 2.S4. Selected THEMIS Observations (Temperatures (T)) of light-toned materials.

Gully	**Observation ID**	**L_s**	**Local Time**	**T (K)**
1	I08099005	278	16.5	260.03
2	I42200002	315	15	271
3	I24951004	286	16.5	251
4	I17018004	307	16	273

5	I25018005	289	16.4	254
6	I24856003	282	16.6	249
7	I76456002	354	17.8	212
8	I07921004	269	16.6	279
9	I75544002	313	17.8	247
10	I75544002	313	17.8	247

Table 2.S5. Selected CTX Observations for Gully 1.

Observation ID	**Latitude**	**Longitude**	**Date**	**L_s**
P15_006804_1484_XN_31S267W	-33	93	1/8/08	14.63
B09_013067_1468_XN_33S266W			5/10/09	263.24
F06_038332_1466_XN_33S266W			9/30/14	205.51

REFERENCES

Aharonson, O., & Schorghofer, N. (2006). Subsurface ice on Mars with rough topography. *Journal of Geophysical Research: Planets, 111*(E11).

Arfstrom, J., & Hartmann, W. K. (2005). Martian flow features, moraine-like ridges, and gullies: Terrestrial analogs and interrelationships. *Icarus, 174*(2), 321-335.

Baker, V. (1985). *Problems in the paleohydrologic and hydroclimatologic interpretation of valley networks.* Paper presented at the Water on Mars Conference, Moffett Field, California.

Balme, M., Mangold, N., Baratoux, D., Costard, F., Gosselin, M., Masson, P., et al. (2006). Orientation and distribution of recent gullies in the southern hemisphere of Mars: observations from High Resolution Stereo Camera/Mars Express (HRSC/MEX) and Mars Orbiter Camera/Mars Global Surveyor (MOC/MGS) data. *Journal of Geophysical Research: Planets, 111*(E5).

Bell III, J., Malin, M., Caplinger, M., Fahle, J., Wolff, M., Cantor, B., et al. (2013). Calibration and performance of the mars reconnaissance orbiter context camera (CTX). *International Journal of Mars Science and Exploration, 8*, 1-14.

Bell III, J., Rice, M., Johnson, J., & Hare, T. (2008). Surface albedo observations at Gusev crater and Meridiani Planum, Mars. *Journal of Geophysical Research: Planets, 113*(E6).

Berman, D. C., Hartmann, W. K., Crown, D. A., & Baker, V. R. (2005). The role of arcuate ridges and gullies in the degradation of craters in the Newton Basin region of Mars. *Icarus, 178*(2), 465-486.

Bibring, J.-P., Langevin, Y., Poulet, F., Gendrin, A., Gondet, B., Berthé, M., et al. (2004). Perennial water ice identified in the south polar cap of Mars. *Nature, 428*(6983), 627-630.

Blackburn, D. G., Bryson, K. L., Chevrier, V. F., Roe, L. A., & White, K. F. (2010). Sublimation kinetics of CO2 ice on Mars. *Planetary and Space Science, 58*(5), 780-791.

Blaney, D., Archer, D., Arvidson, R., Cull, S., Ellehøj, M., Fisher, D., et al. (2009). Multi-spectral imaging of the Phoenix landing site: Characteristics of surface and subsurface ice, rocks, and soils. *LPI*, 2047.

Bleamaster III, L. F., & Crown, D. A. (2005). Mantle and gully associations along the walls of Dao and Harmakhis Valles, Mars. *Geophysical Research Letters, 32*(20).

Boynton, W. V., Feldman, W. C., Mitrofanov, I. G., Evans, L. G., Reedy, R. C., Squyres, S. W., et al. (2004). The Mars Odyssey Gamma-Ray Spectrometer instrument suite. *Space Science Reviews, 110*, 37-83.

Bramson, A., Byrne, S., & Bapst, J. (2017). Preservation of midlatitude ice sheets on Mars. *Journal of Geophysical Research: Planets, 122*(11), 2250-2266.

Bramson, A. M., Byrne, S., Putzig, N. E., Sutton, S., Plaut, J. J., Brothers, T. C., & Holt, J. W. (2015). Widespread excess ice in Arcadia Planitia, Mars. *Geophysical Research Letters, 42*(16), 6566-6574.

Brandt, R. E., & Warren, S. G. (1993). Solar-heating rates and temperature profiles in Antarctic snow and ice. *J. Glaciol., 39*(131), 99-110.

Brown, A. J., Byrne, S., Tornabene, L. L., & Roush, T. (2008). Louth crater: Evolution of a layered water ice mound. *Icarus, 196*(2), 433-445.

Büdel, J., Fischer, L., & Busche, D. (1982). *Climatic geomorphology* (Vol. 443): Princeton University Press Princeton.

Byrne, S. (2009). The polar deposits of Mars. *Annual Review of Earth and Planetary Sciences, 37*, 535-560.

Byrne, S., Dundas, C. M., Kennedy, M. R., Mellon, M. T., McEwen, A. S., Cull, S. C., et al. (2009). Distribution of mid-latitude ground ice on Mars from new impact craters. *Science, 325*(5948), 1674-1676.

Byrne, S., & Ingersoll, A. P. (2003). A sublimation model for Martian south polar ice features. *Science, 299*(5609), 1051-1053.

Carr, M. H. (2001). Mars Global Surveyor observations of Martian fretted terrain. *Journal of Geophysical Research: Planets, 106*(E10), 23571-23593.

Carrozzo, F., Bellucci, G., Altieri, F., D'aversa, E., & Bibring, J.-P. (2009). Mapping of water frost and ice at low latitudes on Mars. *Icarus, 203*(2), 406-420.

Chinnery, H. E., Hagermann, A., Kaufmann, E., & Lewis, S. R. (2020). The penetration of solar radiation into granular carbon dioxide and water ices of varying grain sizes on Mars. *Journal of Geophysical Research: Planets, 125*(4), e2019JE006097.

Christensen, P. (2003). Formation of recent martian gullies through melting of extensive water-rich snow deposits. *Nature, 422*(6927), 45-48. 10.1038/nature01436

Christensen, P., Engle, E., Anwar, S., Dickenshied, S., Noss, D., Gorelick, N., & Weiss-Malik, M. (2009). *JMARS-a planetary GIS.* Paper presented at the AGU Fall Meeting Abstracts.

Christensen, P. R., Jakosky, B. M., Kieffer, H. H., Malin, M. C., McSween, H. Y., Nealson, K., et al. (2004). The Thermal Emission Imaging System (THEMIS) for the Mars 2001 Odyssey Mission. *Space Science Reviews, 110*(1-2), 85-130.

Clow, G., & Haberle, R. (1990). Characteristics of the martian atmospheric surface layer. *Scientific Results of the NASA-Sponsored Study Project on Mars: Evolution of Volcanism, Techtonics, and Volatiles.*, 111.

Clow, G., & Haberle, R. (1991). Free convection in the Martian atmosphere. *Reports of Planetary Geology and Geophysics Program*.

Clow, G. D. (1987). Generation of liquid water on Mars through the melting of a dusty snowpack. *Icarus, 72*(1), 95-127.

Conway, S. J., & Balme, M. R. (2014). Decameter thick remnant glacial ice deposits on Mars. *Geophysical Research Letters, 41*(15), 5402-5409. 10.1002/2014GL060314

Conway, S. J., Butcher, F. E., de Haas, T., Deijns, A. A., Grindrod, P. M., & Davis, J. M. (2018). Glacial and gully erosion on Mars: A terrestrial perspective. *Geomorphology, 318*, 26-57.

Costard, F., Forget, F., Mangold, N., & Peulvast, J. P. (2002). Formation of recent martian debris flows by melting of near-surface ground ice at high obliquity. (Reports).(geophysical research on Mars). *Science, 295*(5552), 110. 10.1126/science.1066698

Cuffey, K. M., & Paterson, W. S. B. (2010). *The physics of glaciers*: Academic Press.

Cull, S., Arvidson, R. E., Mellon, M. T., Skemer, P., Shaw, A., & Morris, R. V. (2010). Compositions of subsurface ices at the Mars Phoenix landing site. *Geophysical Research Letters, 37*(24).

Cushing, G. E., Okubo, C. H., & Titus, T. N. (2015). Atypical pit craters on Mars: New insights from THEMIS, CTX, and HiRISE observations. *Journal of Geophysical Research: Planets, 120*(6), 1023-1043.

Dang, C., Brandt, R. E., & Warren, S. G. (2015). Parameterizations for narrowband and broadband albedo of pure snow and snow containing mineral dust and black carbon. *Journal of Geophysical Research: Atmospheres, 120*(11), 5446-5468.

Daubar, I. J., Dundas, C. M., Byrne, S., Geissler, P., Bart, G., McEwen, A. S., et al. (2016). Changes in blast zone albedo patterns around new martian impact craters. *Icarus, 267*, 86-105.

Delamere, W. A., Tornabene, L. L., McEwen, A. S., Becker, K., Bergstrom, J. W., Bridges, N. T., et al. (2010). Color imaging of Mars by the high resolution imaging science experiment (HiRISE). *Icarus, 205*(1), 38-52.

Dickson, J. L., Head, J. W., & Fassett, C. I. (2012). Patterns of accumulation and flow of ice in the mid-latitudes of Mars during the Amazonian. *Icarus, 219*(2), 723-732.

Dickson, J. L., Head, J. W., Goudge, T. A., & Barbieri, L. (2015). Recent climate cycles on Mars: Stratigraphic relationships between multiple generations of gullies and the latitude dependent mantle. *Icarus, 252*, 83-94.

Dickson, J. L., Head, J. W., & Kreslavsky, M. (2007). Martian gullies in the southern mid-latitudes of Mars: Evidence for climate-controlled formation of young fluvial features based upon local and global topography. *Icarus, 188*(2), 315-323.

Dickson, J. L., Head, J. W., & Marchant, D. R. (2010). Kilometer-thick ice accumulation and glaciation in the northern mid-latitudes of Mars: Evidence for crater-filling events in the Late Amazonian at the Phlegra Montes. *Earth and Planetary Science Letters, 294*(3-4), 332-342.

Diniega, S., Byrne, S., Bridges, N. T., Dundas, C. M., & McEwen, A. S. (2010). Seasonality of present-day Martian dune-gully activity. *Geology, 38*(11), 1047-1050.

Dozier, J., Green, R. O., Nolin, A. W., & Painter, T. H. (2009). Interpretation of snow properties from imaging spectrometry. *Remote Sensing of Environment, 113*, S25-S37.

Dundas, C. M. (2020). Geomorphological evidence for a dry dust avalanche origin of slope streaks on Mars. *Nature Geoscience, 13*(7), 473-476.

Dundas, C. M., Bramson, A. M., Ojha, L., Wray, J. J., Mellon, M. T., Byrne, S., et al. (2018). Exposed subsurface ice sheets in the Martian mid-latitudes. *Science (New York, N.Y.), 359*(6372), 199. 10.1126/science.aao1619

Dundas, C. M., & Byrne, S. (2010). Modeling sublimation of ice exposed by new impacts in the martian mid-latitudes. *Icarus, 206*(2), 716-728.

Dundas, C. M., Byrne, S., & McEwen, A. S. (2015a). Modeling the development of Martian sublimation thermokarst landforms. *Icarus, 262*, 154-169.

Dundas, C. M., Diniega, S., Hansen, C. J., Byrne, S., & McEwen, A. S. (2012). Seasonal activity and morphological changes in Martian gullies. *Icarus, 220*(1), 124-143.

Dundas, C. M., Diniega, S., & McEwen, A. S. (2015b). Long-term monitoring of martian gully formation and evolution with MRO/HiRISE. *Icarus, 251*, 244-263.

Dundas, C. M., McEwen, A. S., Diniega, S., Byrne, S., & Martinez-Alonso, S. (2010). New and recent gully activity on Mars as seen by HiRISE. *Geophysical Research Letters, 37*(7).

Dundas, C. M., McEwen, A. S., Diniega, S., Hansen, C. J., Byrne, S., & McElwaine, J. N. (2019). The formation of gullies on Mars today. *Geological Society, London, Special Publications, 467*(1), 67-94.

Eppes, M.-C., Willis, A., Molaro, J., Abernathy, S., & Zhou, B. (2015). Cracks in Martian boulders exhibit preferred orientations that point to solar-induced thermal stress. *Nature Communications, 6*(1), 1-11.

Farmer, C. B. (1976). Liquid water on Mars. *Icarus, 28*(2), 279-289.

Farmer, C. B., Davies, D. W., & LaPorte, D. D. (1976). Mars: Northern summer ice cap—Water vapor observations from Viking 2. *Science, 194*(4271), 1339-1341.

Feldman, W. C., Boynton, W. V., Tokar, R. L., Prettyman, T. H., Gasnault, O., Squyres, S. W., et al. (2002). Global distribution of neutrons from Mars: Results from Mars Odyssey. *Science, 297*, 75-78.

Fergason, R. L., Christensen, P. R., Bell, J. F., III, Golombek, M. P., Herkenhoff, K. E., & Kieffer, H. H. (2006). Physical properties of the Mars Exploration Rover landing sites as inferred from Mini-TES–derived thermal inertia. *Journal of Geophysical Research, 111*(E02S21), doi:10.1029/2005JE002583.

Fisher, D. A. (2005). A process to make massive ice in the martian regolith using long-term diffusion and thermal cracking. *Icarus, 179*(2), 387-397.

Forget, F., Pilorget, C., Pottier, A., & Meslin, P. (2016). *Deep incision of the Latitude Dependent Mantle in Martian gullies formed by CO 2 sublimation processes.* Paper presented at the Unnumbered abstract presented at the Workshop on Martian Gullies and their Earth Analogs.

Gaddis, L., Anderson, J., Becker, K., Becker, T., Cook, D., Edwards, K., et al. (1997). *An overview of the integrated software for imaging spectrometers (ISIS).* Paper presented at the Lunar and Planetary Science Conference.

Golombek, M. P., Crumpler, L. S., Grant, J. A., Greeley, R., Cabrol, N. A., Parker, T., et al. (2006). Geology of the Gusev cratered plains from the Spirit rover transverse. *Journal of Geophysical Research: Planets, 111*(E2).

Gulick, V. C., Glines, N., Hart, S., & Freeman, P. (2019). Geomorphological analysis of gullies on the central peak of Lyot Crater, Mars. *Geological Society, London, Special Publications, 467*(1), 233-265.

Gyalay, S., Dobrea, E. Z. N., Chu, K., & Pitman, K. M. (2019). Nonlinear spectral mixture modeling to estimate water-ice abundance of martian regolith. *Icarus, 329*, 79-87.

Hapke, B. (2012). *Theory of reflectance and emittance spectroscopy*: Cambridge university press.

Harrison, T., Stuurman, C., Osinski, G., & Tornabene, L. (2017). *Deposition and erosion of the scalloped depression bearing terrain in western Utopia Planitia, Mars.* Paper presented at the Lunar and Planetary Science Conference.

Harrison, T. N., Malin, M., & Edgett, K. (2009). *Present-day gully activity observed by the Mars Reconnaissance Orbiter (MRO) Context Camera (CTX).* Paper presented at the AAS/Division for Planetary Sciences Meeting Abstracts# 41.

Harrison, T. N., Osinski, G. R., Tornabene, L. L., & Jones, E. (2015). Global documentation of gullies with the Mars Reconnaissance Orbiter Context Camera and implications for their formation. *Icarus, 252*, 236-254.

Head, J., Neukum, G., Jaumann, R., Hiesinger, H., Hauber, E., Carr, M., et al. (2005). Tropical to mid-latitude snow and ice accumulation, flow and glaciation on Mars. *Nature, 434*(7031), 346-351.

Head, J. W., Mustard, J. F., Kreslavsky, M. A., Milliken, R. E., & Marchant, D. R. (2003). Recent ice ages on Mars. *Nature, 426*(6968), 797-802.

Hecht, M. H. (2002). Metastability of liquid water on Mars. *Icarus, 156*, 373-386. 10.1006/icar.2001.6794

Heldmann, J. L., Carlsson, E., Johansson, H., Mellon, M. T., & Toon, O. B. (2007). Observations of Martian gullies and constraints on potential formation mechanisms: II. The northern hemisphere. *Icarus, 188*(2), 324-344.

Heldmann, J. L., & Mellon, M. T. (2004). Observations of martian gullies and constraints on potential formation mechanisms. *Icarus, 168*(2), 285-304. 10.1016/j.icarus.2003.11.024

Higuchi, K., & Nagoshi, A. (1977). Effect of particulate matter in surface snow layers on the albedo of perennial snow patches. *IAHS AISH Publication, 118*, 95-97.

Hoffman, N. (2002). Active Polar Gullies on Mars and the Role of Carbon Dioxide. *Astrobiology, 2*(3), 313-323. 10.1089/153110702762027899

Holt, J. W., Safaeinili, A., Plaut, J. J., Head, J. W., Phillips, R. J., Seu, R., et al. (2008). Radar sounding evidence for buried glaciers in the southern mid-latitudes of Mars. *Science, 322*(5905), 1235-1238.

Hudson, T. L., Aharonson, O., Schorghofer, N., Farmer, C. B., Hecht, M. H., & Bridges, N. T. (2007). Water vapor diffusion in Mars subsurface environments. *Journal of Geophysical Research: Planets, 112*(E5).

Ingersoll, A. P. (1970). Mars: Occurrence of liquid water. *Science, 168*(3934), 972-973.

Jakosky, B. M., & Carr, M. A. (1985). Possible precipitation of ice at low latitudes of Mars during periods of high obliquity. *Nature, 315*, 559-561.

Jakosky, B. M., Henderson, B. G., & Mellon, M. T. (1995). Chaotic obliquity and the nature of the Martian climate. *Journal of Geophysical Research: Planets, 100*(E1), 1579-1584.

Kaempfer, T. U., & Schneebeli, M. J. J. o. G. R. A. (2007). Observation of isothermal metamorphism of new snow and interpretation as a sintering process. *112*(D24).

Kayetha, V. K., Prasad, A. K., Cervone, G., & Singh, R. P. (2007). Effect of dust storm on ocean color and snow parameters. *Journal of the Indian Society of Remote Sensing, 35*(1), 1.

Kieffer, H. H. (1979). Mars south polar spring and summer temperatures: A residual CO2 frost. *J. Geophys. Res., 84*, 8263-8289.

Kieffer, H. H. (1990). H2O grain size and the amount of dust in Mars' residual north polar cap. *Journal of Geophysical Research: Solid Earth, 95*(B2), 1481-1493.

Kieffer, H. H., S.C. Chase, J., Martin, T. Z., Miner, E. D., & Palluconi, F. D. (1976). Martian North Pole summer temperatures: Dirty water ice. *Science, 194*, 1341-1344.

Kieffer, H. H., Titus, T. N., Mullins, K. F., & Christensen, P. R. (2000). Mars south polar spring and summer behavior observed by TES: Seasonal cap evolution controlled by frost grain size. *Journal of Geophysical Research: Planets, 105*(E4), 9653-9699.

Kite, E. S., Michaels, T. I., Rafkin, S., Manga, M., & Dietrich, W. E. (2011). Localized precipitation and runoff on Mars. *Journal of Geophysical Research: Planets, 116*(E7).

Kossacki, K. J., & Markiewicz, W. J. (2004). Seasonal melting of surface water ice condensing in martian gullies. *Icarus, 171*(2), 272-283. 10.1016/j.icarus.2004.05.018

Kreslavsky, M. A., & Head, J. W. (2002). Mars: Nature and evolution of young latitude-dependent water-ice-rich mantle. *Geophysical Research Letters, 29*(15), 14-11-14-14. 10.1029/2002GL015392

Law, J., & Van Dijk, D. (1994). Sublimation as a geomorphic process: a review. *Permafrost and Periglacial Processes, 5*(4), 237-249.

Leighton, R. B., & Murray, B. C. (1966). Behavior of carbon dioxide and other volatiles on Mars. *Science, 153*, 136-144.

Levy, J., Head, J. W., & Marchant, D. R. (2010). Concentric crater fill in the northern mid-latitudes of Mars: Formation processes and relationships to similar landforms of glacial origin. *Icarus, 209*(2), 390-404.

Levy, J. S., Head, J. W., & Marchant, D. R. (2007). Lineated valley fill and lobate debris apron stratigraphy in Nilosyrtis Mensae, Mars: Evidence for phases of glacial modification of the dichotomy boundary. *Journal of Geophysical Research: Planets, 112*(E8).

Levy, J. S., Head, J. W., & Marchant, D. R. (2009a). Thermal contraction crack polygons on Earth and Mars; classification, distribution, and implications for recent cold desert processes. In (Vol. 90). Washington, DC: Washington, DC, United States: American Geophysical Union.

Levy, J. S., Head, J. W., Marchant, D. R., Dickson, J. L., & Morgan, G. A. (2009b). Geologically recent gully–polygon relationships on Mars: Insights from the Antarctic Dry Valleys on the roles of permafrost, microclimates, and water sources for surface flow. *Icarus, 201*(1), 113-126. 10.1016/j.icarus.2008.12.043

Liston, G. E., & Winther, J.-G. (2005). Antarctic surface and subsurface snow and ice melt fluxes. *Journal of Climate, 18*(10), 1469-1481.

Liston, G. E., Winther, J.-G., Bruland, O., Elvehøy, H., & Sand, K. (1999). Below-surface ice melt on the coastal Antarctic ice sheet. *J. Glaciol., 45*(150), 273-285.

Luikov, A., & Lebedev, D. (1973). Study of the ice sublimation process. *International Journal of Heat and Mass Transfer, 16*(6), 1087-1096.

Madeleine, J. B., Head, J. W., Forget, F., Navarro, T., Millour, E., Spiga, A., et al. (2014). Recent ice ages on Mars: the role of radiatively active clouds and cloud microphysics. *Geophysical Research Letters, 41*(14), 4873-4879.

Malin, M. C., Bell III, J. F., Cantor, B. A., Caplinger, M. A., Calvin, W. M., Clancy, R. T., et al. (2007). Context Camera Investigation on board the Mars Reconnaissance Orbiter. *Journal of Geophysical Research: Planets, 112*(E5). https://agupubs.onlinelibrary.wiley.com/doi/abs/10.1029/2006JE002808doi:doi:10.1029/2006JE002808

Malin, M. C., & Edgett, K. S. (2000). Evidence for recent groundwater seepage and surface runoff on Mars. *Science, 288*, 2330-2335.

Mangold, N. (2003). Geomorphic analysis of lobate debris aprons on Mars at Mars Orbiter Camera scale: Evidence for ice sublimation initiated by fractures. *Journal of Geophysical Research: Planets, 108*(E4).

Mangold, N. (2011a). Ice sublimation as a geomorphic process: A planetary perspective. *Geomorphology, 126*(1-2), 1-17.

Mangold, N. (2011b). Water ice sublimation-related landforms on Mars. *Geological Society, London, Special Publications, 356*(1), 133-149.

Matzler, C. (2002). Matzler's Matlab Code For Mie Theory.

McEwen, A. S., Eliason, E. M., Bergstrom, J. W., Bridges, N. T., Hansen, C. J., Delamere, W. A., et al. (2007a). Mars Reconnaissance Orbiter's High Resolution Imaging Science Experiment (HiRISE). *Journal of Geophysical Research: Planets, 112*(E5). https://agupubs.onlinelibrary.wiley.com/doi/abs/10.1029/2005JE002605doi:doi:10.1029/2005JE002605

McEwen, A. S., Hansen, C., Delamere, W. A., Eliason, E., Herkenhoff, K. E., Keszthelyi, L., et al. (2007b). A closer look at water-related geologic activity on Mars. *Science, 317*(5845), 1706-1709.

Mellon, M. T., Arvidson, R. E., Sizemore, H. G., Searls, M. L., Blaney, D. L., Cull, S., et al. (2009). Ground ice at the Phoenix landing site: Stability state and origin. *Journal of Geophysical Research: Planets, 114*(E1). https://doi.org/10.1029/2009JE003417

Mellon, M. T., Feldman, W. C., & Prettyman, T. H. (2004). The presence and stability of ground ice in the southern hemisphere of Mars. *Icarus, 169*(2), 324-340.

Mellon, M. T., & Jakosky, B. M. (1995). The distribution and behavior of Martian ground ice during past and present epochs. *Journal of Geophysical Research: Planets, 100*(E6), 11781-11799.

Mellon, M. T., & Phillips, R. J. (2001). Recent gullies on Mars and the source of liquid water. *Journal of Geophysical Research: Planets, 106*(E10), 23165-23179.

Milazzo, M., Herkenhoff, K., Becker, K., Russell, P., Delamere, A., & McEwen, A. (2015). MRO/HiRISE Radiometric Calibration Update. *LPI*(1832), 1498.

Milliken, R., Mustard, J., & Goldsby, D. (2003). Viscous flow features on the surface of Mars: Observations from high-resolution Mars Orbiter Camera (MOC) images. *Journal of Geophysical Research: Planets, 108*(E6).

Mitrofanov, I., Anfimov, D., Kozyrev, A., Litvak, M., Sanin, A., Tret'yakov, V., et al. (2002). Maps of subsurface hydrogen from the high energy neutron detector, Mars Odyssey. *Science, 297*(5578), 78-81.

Murchie, S., Arvidson, R., Bedini, P., Beisser, K., Bibring, J.-P., Bishop, J. L., et al. (2007). Compact Reconnaissance Imaging Spectrometer for Mars (CRISM) on Mars Reconnaissance Orbiter (MRO). *Journal of Geophysical Research, 112*(E05S03). 10.1029/2006JE002682

Musselwhite, D. S., Swindle, T. D., & Lunine, J. I. (2001). Liquid CO2 breakout and the formation of recent small gullies on Mars. *Geophysical Research Letters, 28*(7), 1283-1285. 10.1029/2000GL012496

Mustard, J. F., Christopher, D. C., & Moses, K. R. (2001). Evidence for recent climate change on Mars from the identification of youthful near-surface ground ice. *Nature, 412*(6845), 411. 10.1038/35086515

Neumann, T. A., Albert, M. R., Engel, C., Courville, Z., & Perron, F. (2009). Sublimation rate and the mass-transfer coefficient for snow sublimation. *International Journal of Heat and Mass Transfer, 52*(1-2), 309-315.

Núñez, J., Barnouin, O., Murchie, S., Seelos, F., McGovern, J., Seelos, K., & Buczkowski, D. (2016). New insights into gully formation on Mars: Constraints from composition as seen by MRO/CRISM. *Geophysical Research Letters, 43*(17), 8893-8902.

Pierce, T. L., & Crown, D. A. (2003). Morphologic and topographic analyses of debris aprons in the eastern Hellas region, Mars. *Icarus, 163*(1), 46-65.

Piqueux, S., Kleinböhl, A., Hayne, P. O., Heavens, N. G., Kass, D. M., McCleese, D. J., et al. (2016). Discovery of a widespread low-latitude diurnal CO2 frost cycle on Mars. *Journal of Geophysical Research: Planets, 121*(7), 1174-1189.

Plaut, J. J., Safaeinili, A., Holt, J. W., Phillips, R. J., Head, J. W., Seu, R., et al. (2009). Radar evidence for ice in lobate debris aprons in the mid-northern latitudes of Mars. *Geophysical Research Letters, 36*(2).

Rice, M. S., Reynolds, M., Studer-Ellis, G., Bell III, J. F., Johnson, J. R., Herkenhoff, K. E., et al. (2018). The albedo of Mars: Six Mars years of observations from Pancam on the Mars Exploration Rovers and comparisons to MOC, CTX and HiRISE. *Icarus, 314*, 159-174.

Richardson, M. I., & Mischna, M. A. (2005). Long-term evolution of transient liquid water on Mars. *Journal of Geophysical Research: Planets, 110*(E3).

Schon, S. C., Head, J. W., & Milliken, R. E. (2009). A recent ice age on Mars: Evidence for climate oscillations from regional layering in mid-latitude mantling deposits. *Geophysical Research Letters, 36*(15).

Schorghofer, N. (2010). Fast numerical method for growth and retreat of subsurface ice on Mars. *Icarus, 208*(2), 598-607.

Schorghofer, N., & Aharonson, O. (2005). Stability and exchange of subsurface ice on Mars. *Journal of Geophysical Research: Planets, 110*(E5).

Schorghofer, N., & Edgett, K. S. (2006). Seasonal surface frost at low latitudes on Mars. *Icarus, 180*(2), 321-334.

Schorghofer, N., & Forget, F. (2012). History and anatomy of subsurface ice on Mars. *Icarus, 220*(2), 1112-1120.

Schwerdtfeger, P. (1969). Absorption, scattering and extinction of light in ice and snow. *Nature, 222*(5191), 378-379.

Schwerdtfeger, P., & Weller, G. (1967). The measurement of radiative and conductive heat transfer in ice and snow. *Archiv für Meteorologie, Geophysik und Bioklimatologie, Serie B, 15*(1-2), 24-38.

Sears, D. W., & Moore, S. R. (2005). On laboratory simulation and the evaporation rate of water on Mars. *Geophysical Research Letters, 32*(16).

Sizemore, H. G., Zent, A. P., & Rempel, A. W. (2015). Initiation and growth of Martian ice lenses. *Icarus, 251*, 191-210.

Smith, D. E., Zuber, M. T., Frey, H. V., Garvin, J. B., Head, J. W., Muhleman, D. O., et al. (2001). Mars Orbiter Laser Altimeter: Experiment summary after the first year of global mapping of Mars. *Journal of Geophysical Research: Planets, 106*(E10), 23689-23722.

Smith, M. D. (2004). Interannual variability in TES atmospheric observations of Mars during 1999–2003. *Icarus, 167*(1), 148-165.

Smith, P. H., Tamppari, L., Arvidson, R., Bass, D., Blaney, D., Boynton, W. V., et al. (2009). H2O at the Phoenix landing site. *Science, 325*(5936), 58-61.

Soderblom, J. M., Bell III, J. F., Hubbard, M. Y., & Wolff, M. J. (2006). Martian phase function: Modeling the visible to near-infrared surface photometric function using HST-WFPC2 data. *Icarus, 184*(2), 401-423.

Squyres, S. W. (1979). The distribution of lobate debris aprons and similar flows on Mars. *J. Geophys. Res., 84*(No. B14), 8087-8096.

Squyres, S. W., & Carr, M. H. (1986). Geomorphic evidence for the distribution of ground ice on Mars. *Science, 231*, 249-252.

Stuurman, C., Osinski, G., Holt, J., Levy, J., Brothers, T., Kerrigan, M., & Campbell, B. (2016). SHARAD detection and characterization of subsurface water ice deposits in Utopia Planitia, Mars. *Geophysical Research Letters, 43*(18), 9484-9491.

Sullivan, R., Thomas, P., Veverka, J., Malin, M., & Edgett, K. S. (2001). Mass movement slope streaks imaged by the Mars Orbiter Camera. *Journal of Geophysical Research, 106*, 23,607-623,633.

Sylvest, M. E., Conway, S. J., Patel, M. R., Dixon, J. C., & Barnes, A. (2016). Mass wasting triggered by seasonal CO2 sublimation under Martian atmospheric conditions: Laboratory experiments. *Geophysical Research Letters, 43*(24), 12,363-312,370.

Sylvest, M. E., Dixon, J. C., Conway, S. J., Patel, M. R., McElwaine, J. N., Hagermann, A., & Barnes, A. (2019). CO2 sublimation in Martian gullies: laboratory experiments at varied slope angle and regolith grain sizes. *Geological Society, London, Special Publications, 467*(1), 343-371.

Titus, T. N., Kieffer, H. H., & Christensen, P. R. (2003). Exposed water ice discovered near the south pole of Mars. *Science, 299*(5609), 1048-1051.

Viles, H., Ehlmann, B., Wilson, C. F., Cebula, T., Page, M., & Bourke, M. (2010). Simulating weathering of basalt on Mars and Earth by thermal cycling. *Geophysical Research Letters, 37*(18).

Vincendon, M. (2015). Identification of Mars gully activity types associated with ice composition. *Journal of Geophysical Research: Planets, 120*(11), 1859-1879.

Vincendon, M., Forget, F., & Mustard, J. (2010a). Water ice at low to midlatitudes on Mars. *Journal of Geophysical Research: Planets, 115*(E10).

Vincendon, M., Mustard, J., Forget, F., Kreslavsky, M., Spiga, A., Murchie, S., & Bibring, J. P. (2010b). Near-tropical subsurface ice on Mars. *Geophysical Research Letters, 37*(1).

Viola, D., & McEwen, A. S. (2018). Geomorphological Evidence for Shallow Ice in the Southern Hemisphere of Mars. *Journal of Geophysical Research: Planets, 123*(1), 262-277. 10.1002/2017JE005366

Warren, S. G. (1984). Impurities in snow: Effects on albedo and snowmelt. *Annals of Glaciology, 5*, 177-179.

Warren, S. G. (2019). Optical properties of ice and snow. *Philosophical Transactions of the Royal Society A, 377*(2146), 20180161.

Warren, S. G., & Brandt, R. E. (2008). Optical constants of ice from the ultraviolet to the microwave: A revised compilation. *Journal of Geophysical Research: Atmospheres, 113*(D14).

Warren, S. G., & Wiscombe, W. J. (1980). A model for the spectral albedo of snow.2. Snow containing atmospheric aerosols. *J. Atmos. Sci., 37*(No. 12), 2734-2745.

Weidelt, H.-J. (1976). Manual of reforestation and erosion control for the Philippines.

Wellen, E. W. (1979). *Sublimation of ice from permafrost silt at the CRREL tunnel.* University of Alaska, Fairbanks,

Weller, G. E. (1969). Radiation diffusion in Antarctic ice media. *Nature, 221*(5178), 355-356.

Wells, E. N., Veverka, J., & Thomas, P. (1984). Experimental study of albedo changes caused by dust fallout. *Icarus, 58*, 331-338.

Williams, K. E., Toon, O. B., Heldmann, J. L., McKay, C., & Mellon, M. T. (2008). Stability of mid-latitude snowpacks on Mars. *Icarus, 196*(2), 565-577. 10.1016/j.icarus.2008.03.017

Wiscombe, W. J., & Warren, S. G. (1980). A model for the spectral albedo of snow.1. Pure snow. *J. Atmos. Sci., 37*(No. 12), 2712-2733.

Wolff, M., Smith, M., Clancy, R., Arvidson, R., Kahre, M., Seelos, F., et al. (2009). Wavelength dependence of dust aerosol single scattering albedo as observed by the Compact Reconnaissance Imaging Spectrometer. *Journal of Geophysical Research: Planets, 114*(E2). https://doi.org/10.1029/2009JE003350

Zanetti, M., Hiesinger, H., Reiss, D., Hauber, E., & Neukum, G. (2010). Distribution and evolution of scalloped terrain in the southern hemisphere, Mars. *Icarus, 206*(2), 691-706.

Chapter 3

SPECTRAL ALBEDO OF DUSTY MARTIAN H_2O SNOW AND ICE

Aditya R. Khuller[1], Philip R. Christensen[1], Stephen G. Warren[2]

[1]School of Earth and Space Exploration, Arizona State University, Tempe, AZ 85281.

[2]Department of Atmospheric Sciences, University of Washington, Seattle, WA 98195.

Citation: Khuller, A.R., Christensen, P.R., S.G. Warren, (2021). Spectral Albedo of Dusty Martian H2O Snow and Ice. *Journal of Geophysical Research: Planets.*

Key Points:

- Small amounts (< 1%) of martian dust can lower the albedo of H_2O ice at visible wavelengths from ~1.0 to as low as ~0.1.
- Dusty (> 0.01% dust) firn and glacier ice have a lower albedo than pure dust, making them difficult to distinguish using HiRISE images.
- Observations of excess ice at the Phoenix landing site are matched by modeled 350-µm snow grains with 0.015% dust.

Abstract

Recent evidence of exposed H_2O ice on Mars suggests that this ice was deposited as dusty (~1% dust) snow. This dusty snow is thought to have been deposited and subsequently buried over the last few million years. On Earth, freshly fallen snow metamorphoses with time into firn and, if deep enough, into glacier ice. While spectral measurements of martian ice have been made, no model of the spectral albedo of dusty martian firn or glacier ice exists at present. Accounting for dust and snow metamorphism is important because both factors reduce the albedo of snow and ice by large amounts. However, the dust content and physical properties of martian H_2O ice are poorly constrained. Here we present a model of the spectral albedo of H_2O snow and ice on Mars, which is based on validated terrestrial models. We find that small amounts (< 1%) of martian dust can lower the albedo of H_2O ice at visible wavelengths from ~1.0 to as low as ~0.1. Additionally, our model indicates that dusty (> 0.01% dust) firn and glacier ice have a lower albedo than pure dust, making them difficult to distinguish in visible/near-infrared images commonly used to detect H_2O ice on Mars. Observations of excess ice at the Phoenix landing site are matched by 350-μm snow grains with 0.015% dust, indicating that the snow has not yet metamorphosed into glacier ice. Our model results can be used to characterize orbital observations of martian H_2O ice and refine climate-model predictions of ice stability.

3.1. Introduction

The presence, stability, and physical nature of H_2O ice on Mars has major implications for understanding martian history, evolution, and future robotic and manned exploration. However, the pervasive presence of dust on Mars causes the ice to contain typically ~1% dust (Dundas et al., 2018; Khuller & Christensen, 2021). The ice is thought to have been deposited as snow during periods of high obliquity that occurred numerous times over the last few million years (Jakosky & Carr, 1985; Christensen, 2003a; Madeleine et al., 2014). At visible wavelengths, dust is far more absorbing than H_2O ice (Fig. 1; Warren & Wiscombe, 1980; Wolff et al., 2009), so small amounts of dust can lower the albedo at these wavelengths (e.g., Dozier et al., 2009; Painter et al., 2013). Lower albedos lead to enhanced radiative heating, which affects the ice's energy balance and its stability and evolution over time.

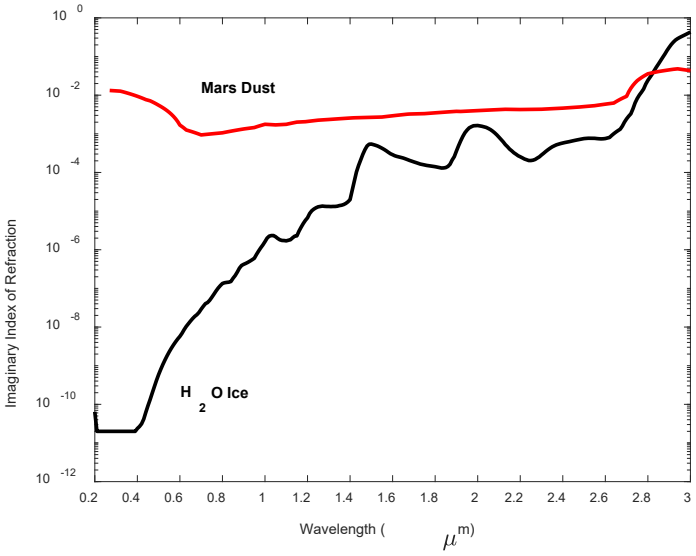

Figure 3.1. Imaginary index of refraction for Mars dust (Wolff et al., 2009) and H_2O ice (Warren & Brandt, 2008).

Radiative heating is also enhanced by snow metamorphism. On Earth, fresh snow (with density 50 – 100 kg/m^3) quickly metamorphoses due to vapor diffusion, overburden pressure, and the potential formation of liquid water. These effects cause snow grains to grow, increasing the bulk density of the snow to form firn (550 – 830 kg/m^3), and subsequently glacier ice (830 kg/m^3) (Cuffey & Paterson, 2010). Coarser snow grains reduce the number of scattering events per unit pathlength, thereby increasing the likelihood of photon absorption, and reducing the albedo. Snow that has metamorphosed into glacier ice absorbs up to five times more solar radiation than snow, which can lead to subsurface melting within the ice, as is seen on Earth (Brandt & Warren, 1993; Liston & Winther, 2005).

Recent observations have indicated that dusty H_2O ice is currently being exposed at martian mid-latitudes (e.g., Byrne et al., 2009; Dundas et al., 2018; Khuller & Christensen, 2021). The precise nature (grain size and dust content) of this exposed ice is currently uncertain, and estimates of the time scale of martian snow metamorphism range from decades/centuries (Clow, 1987; Kieffer, 1990) to millions of years (Bramson et al., 2017). While the spectral albedo of dusty martian H_2O snow has been calculated for some cases (Clow, 1987; Kieffer, 1990; Cull et al., 2010b; Singh et al., 2018; Gyalay et al., 2019), no model of dusty martian firn/glacier ice (i.e., H_2O ice with small air content) exists at present. Modeling the spectral albedo of dusty snow, firn, and glacier ice will allow for detailed characterization of the observed exposures of dusty martian ice, and help improve global climate models (GCMs) that are currently unable to completely

replicate the spatial distribution of ice deposits on Mars (Madeleine et al., 2014; Haberle et al., 2017; Naar et al., 2020).

In this paper, we model the spectral albedo of dusty martian H_2O snow and ice across the solar spectrum (0.3 – 3 μm), and compare our results with in-situ measurements of martian ice at the Phoenix landing site (Blaney et al., 2009; Smith et al., 2009).

3.2. Methods

We incorporate the spectral absorption properties of martian dust (Wolff et al., 2009) into models that have been used for mixtures of dust with terrestrial snow and glacier ice. Refractive index data for water-ice are taken from Warren and Brandt (2008). The densities of pure H_2O ice and martian dust are assumed to be 917 kg/m^3 and 1300 kg/m^3, respectively (Moore & Jakosky, 1989; Moore et al., 1999; Arvidson et al., 2004). To calculate the albedos of dusty martian snow, we use Mie theory and the Delta-Eddington method (Joseph et al., 1976; Warren & Wiscombe, 1980; Dang et al., 2015). For dusty martian firn/glacier ice, we use a "specular Delta-Eddington" model that was initially developed by Mullen and Warren (1988) for modeling the albedo of terrestrial lake ice. Subsequently, it was modified for firn/glacier ice, and validated against spectral measurements of terrestrial firn and glacier ice, some of which contained volcanic ash (Dadic et al., 2013). This model incorporates an optional specular flat surface overlying a scattering layer whose properties are calculated using the Delta-Eddington method. The overlying specular surface occurs in glacier ice, and to some extent in firn, but not in snow, leading to the authors using a 'specularity parameter' *s*, which varies from 0 for an

optically rough, scattering medium such as snow, to 1 for a flat, smooth surface such as ice (Dadic et al., 2013). Details are provided in Appendix 3.A.

Type	**Density (kg/m^3)**	**Grain Radius r_{ice}**	**Specific surface area SSA (m^2/kg)**	**Specularity Parameter s**
Snow	50 - 550	50 μm – 500 μm	6.5 - 65	0
Firn	550 - 830	500 μm – 3 mm	1.1– 6.5	1
Glacier Ice	830 - 917	3 – 16 mm	0.2 – 1.1	1

Table 3.1. Model parameters used for different types of snow and ice, classified based on their density and approximate grain size. The specific surface area is the area of air-ice interfaces per unit mass of ice. It is reciprocally related to grain size, as $SSA = 3 / (r_{ice} \times 917\ kg/m^3)$. The values of SSA for glacier ice are those measured by Dadic et al. (2013). We model a variety of snow and ice grain sizes (Table 3.1) because martian ice has been observed in-situ only at the Phoenix landing site, where no direct measurements of grain size, dust content or density were made (Smith et al., 2009). In order to distinguish between snow and ice, all snow densities greater than 550 kg/m^3 were modeled as firn/glacier ice rather than snow because the primary scattering mechanism within dense ice is caused by the bubbles present within the ice rather than the snow grains (Warren, 2019). The "grain sizes" listed in Table 3.1 for glacier ice are derived from the Specific

Surface Area (SSA; the area of air-ice interfaces per unit mass of ice), following Bohren (1983), who showed that bubbly ice can be modeled as very-coarse-grained snow. Unless specified, all calculations are performed assuming a solar zenith angle of 49.5° (the effective zenith angle for diffuse incidence), and assuming that the snow/ice is thick enough to obscure any underlying material (> ~1 m; termed semi-infinite). The grain radius for dust is set to 1.8 μm for all calculations shown in Section 3.3, based on orbital and in-situ observations of martian dust that indicate this approximate size range (Wolff et al., 2009; Goetz et al., 2010). Model results are compared with measured albedo of observed in-situ excess ice (ice exceeding the soil pore space) at the Phoenix landing site (68.22°N, 234.25°E; Blaney et al., 2009; Smith et al., 2009).

3.3. Results

3.3.1. Grain Size Effects

Figure 3.2 illustrates how larger snow grains increase the likelihood of photon absorption (Dang et al., 2015), which leads to a reduction in albedo. There is a noticeable transition between snow albedos and firn/glacier ice albedos. In particular, the absorption features at 1.5 μm and 2 μm caused by overtones and combinations of fundamental vibrational modes become damped. At these two wavelengths the albedo is very small; the glacier ice has higher albedo than coarse-grained snow because of specular reflection.

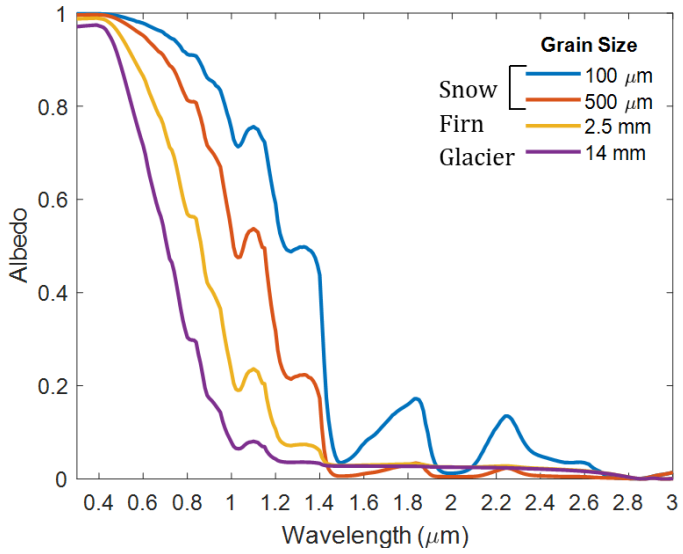

Figure 3.2. Albedo variation of clean snow, firn and glacier ice albedo with grain size.

3.3.2. Martian Dust Effects

Martian dust is 3 to 9 orders of magnitude more strongly absorbing than H_2O ice at wavelengths 0.2-1.0 µm (Fig. 3.1). Thus, small amounts of dust significantly reduce the single-scattering albedo $\bar{\omega}$ of H_2O snow and ice. $\bar{\omega}$ is a dimensionless parameter that ranges from 0 to 1: $\bar{\omega} = 0$ for pure absorption and $\bar{\omega} = 1$ for pure scattering.

Figure 3 illustrates how the addition of small amounts of dust (10^{-4}% – 0.1%, i.e., 1-1000 ppm by weight) drastically alters the single-scattering coalbedo $(1 - \bar{\omega})$. Dust increases $(1 - \bar{\omega})$ dramatically for $\lambda < 1.2$ µm, where the imaginary index of refraction for martian dust is several orders of magnitude larger than that of H_2O ice, causing greater absorption. Also note the general increase in $(1 - \bar{\omega})$ with grain size for the pure cases (black curves in Figure 3.3), because larger grains are more absorptive.

At longer wavelengths, the imaginary index of ice is more similar to that of dust, and the greater volume fraction of ice in the mixture causes the effect of even 0.1% dust to be

almost negligible for snow (Figs. 3.2a and b). For firn and glacier ice, the addition of dust > 0.01% causes the coalbedo ($1 - \bar{\omega}$) to *decrease* at longer wavelengths, indicating an increase in scattering within the ice-dust mixture. The coalbedo is approximately proportional to rn_i; i.e. the product of grain radius r and imaginary index n_i (Eq. 10 of Bohren & Barkstrom, 1974). Although the imaginary index of dust is 1-2 orders of magnitude larger than that of ice at these wavelengths, the size of dust particles is 3-4 orders of magnitude smaller than the ice grains, allowing the addition of dust to reduce the coalbedo.

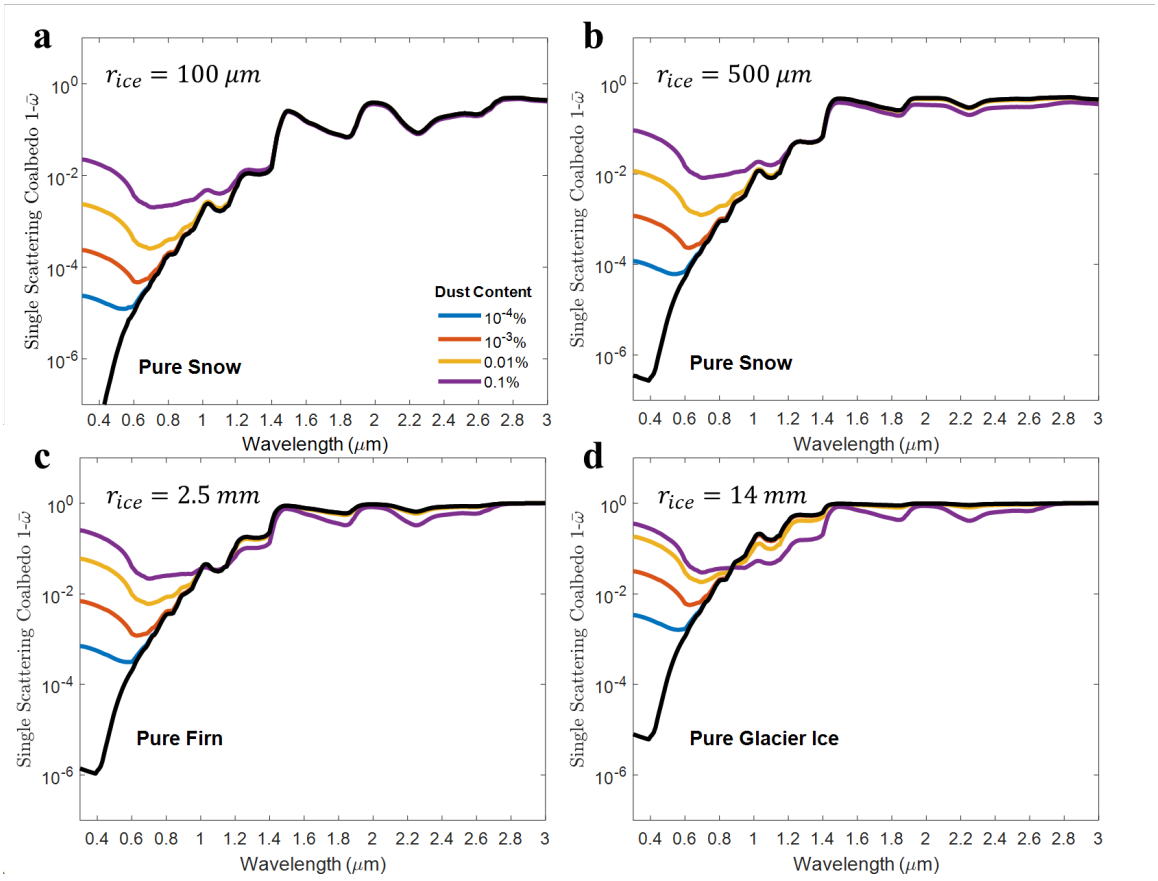

Figure 3.3. Effect of dust amounts on the single-scattering coalbedo for 100 µm, 500 µm, 2.5 mm, and 14 mm snow/ice grain sizes.

Figure 3.4 shows the effects of small amounts of martian dust on snow and glacier ice albedo. In fine-grained snow, dust reduces the albedo for $\boldsymbol{\lambda}$ < ~1.4 µm (Fig. 3.4a). As the ice grain radius increases, dust causes greater reductions of albedo (Figs. 3.4b, c and d), because radiation penetrates more deeply in coarser grained snow and ice, where it encounters more absorbing material before reemerging at the surface. However, adding dust to coarser grained snow and ice causes an increase in albedo for wavelengths larger than 1.2 µm, 1.0 µm and 0.9 µm in Figures 3.4b, c and d, respectively.

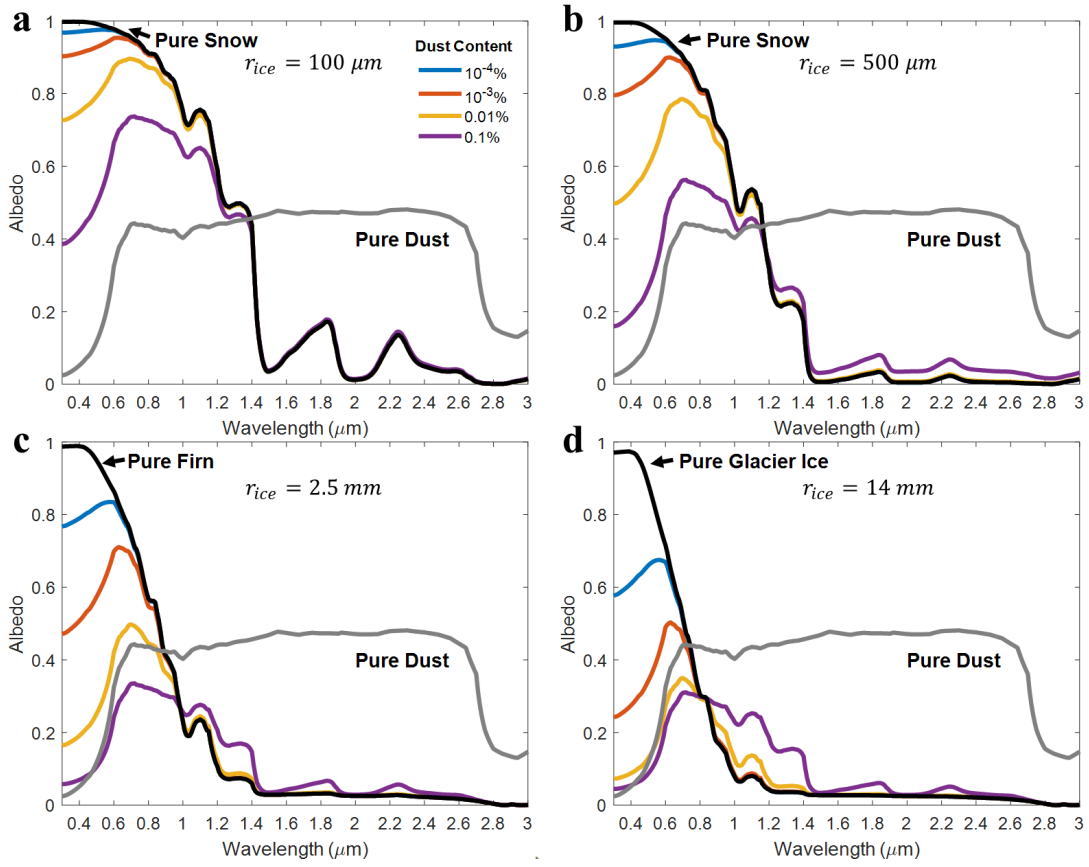

Figure 3.4. Albedo for various dust amounts in snow/ice of grain sizes 100 $\boldsymbol{\mu}$m, 500 µm, 2.5 mm and 14 mm. The albedo of pure snow/ice (black) and pure dust (gray) are also shown.

3.4. Comparison with Phoenix Ice Data

At present, the only available in-situ observations of excess martian ice are from the Phoenix landing site. Orbital measurements of ice over the entire solar spectrum are available, but atmospheric effects make quantitative analysis of dust content and ice grain size challenging. Thus, while the Phoenix measurements cover only part of the solar spectrum (~0.45 – 1 μm), they can be compared with our model results for dusty snow and ice.

What was measured at the Phoenix landing site was the radiance reflected by the target (ice or soil), ratioed to the radiance reflected by a calibration surface (a "perfectly diffusive reflective white surface"), and corrected for the incidence angle of the sunlight (Zamani et al., 2009; Drube et al., 2010). The Phoenix team's conversion from measured radiance to the albedo plotted in Figure 3.5 thus implicitly makes the default assumption that the soil or ice target is an isotropic reflector, since its actual bidirectional reflectance distribution function (BRDF) is unknown.

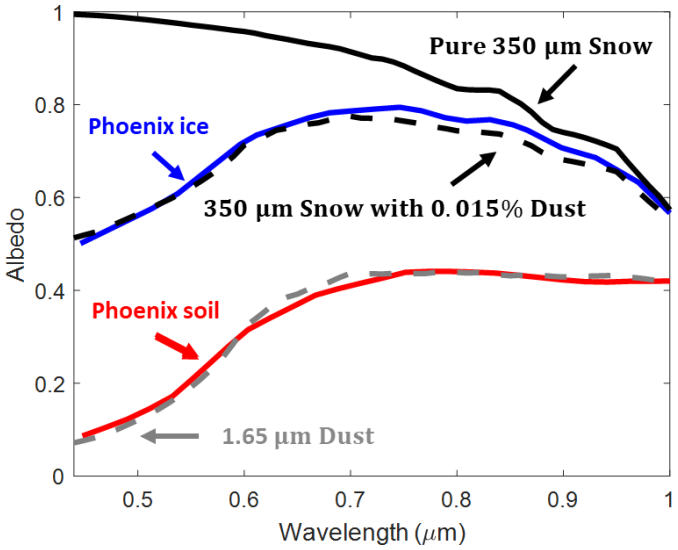

Figure 3.5. Comparison of calculated albedo with observations from the Phoenix landing site (Blaney et al., 2009).

The soil albedo observed at the Phoenix landing site is well matched by the model result for 1.65 µm martian dust, suggesting that small amounts of dust may be present on the surfaces near the ice (Fig. 5). From Figure 3.4, it is apparent that the grain size of the Phoenix ice must be less than 2.5 mm, because the addition of small amounts of dust does not increase firn or glacier ice albedo at wavelengths near 1 µm enough to match the Phoenix ice albedo of ~0.6 (Fig. 3.5). Although the solar incidence angle for the Phoenix observations (~45°) is slightly smaller than the angle used in Figure 3.4 (49.5°), this difference in angle causes a negligible effect at these wavelengths (Wiscombe & Warren, 1980).

We varied the snow grain size to produce an agreement between modeled and observed albedo near wavelengths of 1 µm, where dust amounts up to 0.1% have minimal effect. This procedure led to us obtaining a 350 µm snow grain size. However,

all clean snow grain sizes produce results that exceed the Phoenix observations at shorter wavelengths. To match the Phoenix observations, the inclusion of 0.015% dust (1.3 μm grain size) was required (Fig. 3.5). This result constrains the output from previous modeling work by Cull et al. (2010b), who reported that this relatively friable ice contained up to 1% dust. Unfortunately, Cull et al. (2010) were unable to derive grain-size estimates because the bidirectional reflectance model they used would have required observationally determining the scattering properties (asymmetry parameter) of the ice to model the ice-dust mixture, which was not done at the Phoenix site. More recently, Gyalay et al. (2019) used a third, separate technique to estimate that the ice content was up to 93% by volume, or 87% by weight, based on their assumed densities for soil and ice. That result was obtained for a modeled grain size of ~1 mm, with 60 μm soil grains (Gyalay et al., 2019). However, their estimated ice content is likely to be too low, because dust contents greater than 1% make dusty snow and ice indistinguishable from pure dust at visible wavelengths (see Fig. S2 in Khuller & Christensen, 2021).

3.5. Discussion

3.5.1. Detecting H_2O Ice using HiRISE Images

Data with high spectral resolution but relatively coarse spatial resolution (~18 m/pixel) are available from the Compact Reconnaissance Imaging Spectrometer for Mars (CRISM; Murchie et al., 2007). For finer spatial resolution, recent attempts to identify H_2O ice on Mars (e.g., Byrne et al., 2009; Dundas et al., 2018; Dundas et al., 2021) have used relative color variations within images formed from three bands in the visible and near-infrared (VNIR), with pixel size ~25 cm, from the High Resolution Imaging Science

Experiment (HiRISE; McEwen et al., 2007a). In stretched false-color images of likely ice-hosting features on Mars, materials considered to be ice are those that appear relatively blue (i.e., having relatively higher values in HiRISE's blue-green filter, centered at 0.536 μm).

However, our modeling results indicate that snow metamorphism and the addition of small amounts of dust drastically alter the albedo of H_2O ice at the HiRISE filter wavelengths. Thus, it is possible for ice to appear relatively yellow/white in stretched, false-color HiRISE images even though it contains less than 1% dust (Khuller & Christensen, 2021). Dusty ice can also resemble nearby lithic material at visible wavelengths, when present as firn or glacier ice with 0.01 – 0.1% dust (Figs. 4c and d), potentially like some of the recently discovered scarps thought to be ice-rich (e.g., Fig. 2 of Dundas et al., 2021). Greater amounts of dust (> 1%) will cause snow and ice to be indistinguishable at these wavelengths.

3.5.2. Origin of Ice at the Phoenix Landing Site

A dusty-snow origin for the excess ice at the Phoenix landing site is questioned primarily because of the presence of a few pebbles overlying the ice (Mellon et al., 2009; Sizemore et al., 2015). While a few models have been proposed to explain the presence of excess ice in the near-surface (Fisher, 2005; Sizemore et al., 2015), those models are difficult to reconcile with decameter-thick ice deposits being discovered throughout the mid-latitudes of Mars (Byrne et al., 2009; Dundas et al., 2018; Khuller & Christensen, 2021). These recent discoveries indicate that it is more likely that the majority of shallow ice on Mars was deposited as dusty snow, which was subsequently buried through lag

buildup and aeolian activity. Snow burial likely caused dust, pebbles and boulders to be incorporated within and on top of the ice, as is seen on Earth (Boulton, 1978). Alternatively, lithics within and on top of the ice might also have been emplaced by impact ejecta and/or meteorites.

A 350 μm grain size for the ice exposed at the Phoenix landing site is smaller than the 700 – 800 μm grain size derived for H_2O ice at the northern residual polar cap (Langevin et al., 2005). However, the H_2O ice at the cap experiences seasonal deposition and sublimation of H_2O and CO_2 frost, which can mobilize dust and alter local thermal and atmospheric conditions (Kieffer, 1990; Langevin et al., 2005). These frost processes make it difficult to constrain the age and rate of metamorphism of the cap H_2O ice. In contrast, the Phoenix ice was buried under a few centimeters of soil and dust. Radar detections suggest that the Phoenix ice might extend to depths of 9 – 66 m (Putzig et al., 2014). Assuming an average depth (or equivalently, subsurface ice thickness) of 40 m, this amount of ice could have been deposited as dusty snow over the last 1 Myr (Madeleine et al., 2014).

The cross-sectional area of snow grains (or equivalently, the snow grain size squared) grows linearly with time (Stephenson, 1967; Gow, 1969; Linow et al., 2012). Thus, if the initial snow grain size was 50 μm, the rate of snow metamorphism for the Phoenix ice is 0.12 $\mu m^2/yr$, which is an order of magnitude greater than the rate of snow metamorphism we derive using estimates from Bramson et al. (2017). Bramson et al. (2017) obtained a value of 86 Myr for 550 kg/m^3 firn to metamorphose into 917 kg/m^3 density glacier ice. Based on Table 3.1, these density values correspond to grain sizes of

500 μm and 16 mm. Assuming these grain sizes implies that the rate of snow metamorphism is $((16\ \mathrm{mm})^2 - (0.5\ \mathrm{mm})^2)/(86\ \times 10^6\ \mathrm{years}) = 3\ \mu\mathrm{m}^2/\mathrm{yr}$. Note that these predicted rates of snow metamorphism can vary greatly with local atmospheric and thermal conditions. For example, ice that might have experienced melting (Khuller & Christensen, 2021) is likely to have experienced far greater rates of metamorphism, because even slight melting results in a rapid increase in grain size (Warren, 2019). Based on the optical properties of the Phoenix ice it seems most likely that it formed by deposition from the atmosphere as snow with small amounts of incorporated dust.

3.6. Summary

We have modeled the effects of dust and snow metamorphism on the albedo of martian H_2O ice. Both effects generally cause a reduction in albedo, thereby increasing the energy absorbed by the ice. For example, dust can reduce the albedo of fine-grained snow (100 μm) from its pure-snow value of 0.9 – 1.0, down to 0.4 – 0.7, for wavelengths short of 1 μm. Similarly, the addition of small amounts of dust (10^{-4}% – 0.1%) reduces the visible albedo of pure H_2O ice to as low as ~0.1, depending on the wavelength and the grain size of the ice. In some cases, the albedo of dusty firn and glacier ice can be lower than that of pure dust alone. At long wavelengths, 0.1% dust can increase the albedo of coarse-grained snow, firn and glacier ice (Fig. 3.4). Accounting for these radiative effects is crucial to our understanding and detection of exposed H_2O ice on Mars. 0.01 – 0.1% dust can render firn and glacier ice indistinguishable from pure dust at HiRISE filter wavelengths. Thus, dusty snow and ice might not necessarily appear

relatively blue in stretched, false-color images (as is commonly assumed for martian H_2O ice).

Our model matches measurements of the excess ice observed at the Phoenix landing site, using 350 μm snow with 0.015% dust. This result suggests that the snow has not yet metamorphosed into glacier ice. If the results of our modeling are incorporated into GCMs, simulations of the distribution of martian H_2O ice may be improved. In addition, results can be compared with currently ongoing studies of atmospherically-corrected orbital measurements of H_2O ice using hyperspectral CRISM data (e.g., Pascuzzo et al., 2019a).

3.7. Acknowledgments

We would like to thank Peter Mullen for very kindly sharing his code to model the spectral albedo of terrestrial glacier ice. In addition, we are very thankful to Mike Wolff for sharing the martian dust refractive index data. Sarah Rogers and Steve Ruff provided very helpful feedback.

3.8. Data Availability

Phoenix Surface Stereo Imager (SSI) data is available at https://pds-imaging.jpl.nasa.gov/data/phoenix/phxssi_1xxx/. Results and data from the snow/ice-dust spectral model are available in (Khuller et al., 2021a) (repository: https://doi.org/10.5281/zenodo.4653768).

3.9. Appendix 3. A: Calculating Albedos for Dusty Martian Snow and Ice

3.A.1. Albedo of Pure Snow and Dust

For snow and dust, we use a Mie scattering code (Matzler, 2002) to calculate single-scattering quantities separately, based on terrestrial models for snow (Wiscombe & Warren, 1980; Dang et al., 2015). Scattering by snow and dust grains is assumed to be similar to spheres in their far fields, with radii r_{ice} and r_{dust}, respectively, in meters. Each particle has volume $V = \frac{4}{3}\pi r^3$ and cross-sectional area $A = \pi r^2$ (i.e., $V_{ice}, V_{dust}, A_{ice}$ and A_{dust}). Based on the formulas for scattering by spheres, the complex refractive index $m(\lambda)$ and the dimensionless size parameter x are required as inputs to the Mie scattering code:

$$x = \frac{2\pi r}{\lambda} \tag{A1}$$

where λ is the wavelength, and r is the average grain radius of the material. We then calculate the following quantities for ice and dust, separately:

$$\sigma_{ext} = \pi r^2 Q_{ext} \tag{A2}$$

$$\bar{\omega} = \sigma_{scat}/\sigma_{ext} \tag{A3}$$

$$g = mean(\cos(\theta)) \tag{A4}$$

where σ_{ext} is the extinction cross section, Q_{ext} is the dimensionless extinction efficiency, $\bar{\omega}$ is the single-scattering albedo, σ_{scat} is the scattering cross section, g is the asymmetry factor and θ is the scattering angle (see van de Hulst (1957) for a review of these terms). The absorption and scattering efficiencies Q_{abs} and Q_{sca} are also calculated for each material. Note that we average over a small range of grain radii ($r \pm \frac{r}{10}$) to eliminate the unrealistic ripple generated by Mie theory (Wiscombe & Warren, 1980).

Using the delta-Eddington approximation for a semi-infinite material, we obtain the following transformations for g and $\bar{\omega}$:

$$\bar{\omega}_* = \frac{(1-g)^2\bar{\omega}}{1-g^2\bar{\omega}} \tag{A5}$$

$$g_* = \frac{g}{1+g} \tag{A6}$$

The albedo, A of pure snow and dust is given by (for the semi-infinite case):

$$A\,(\mu_0) = \frac{\bar{\omega}_*}{1+P}\,\frac{1-b_*\xi\mu_0}{1+\xi\mu_0} \tag{A7}$$

where μ_0 is the zenith cosine ($\mu_0 = \cos(\theta_{zenith})$ for a given zenith/solar incidence angle θ_{zenith}, $b_* = g_*/(1 - \bar{\omega}_* g_*)$, $\xi = [3(1 - \bar{\omega}_* g_*)(1 - \bar{\omega}_*)]^{1/2}$ and $P = 2\xi/(3(1 - \bar{\omega}_* g_*))$.

3.A.2. Albedo of Pure Firn and Glacier Ice

The albedo of firn and glacier ice accounts for specular reflection at the surface. Based on terrestrial models for firn and glacier ice, the albedo A is given by:

$$A = sR_1 + \frac{(1 - sR_1)(sA_{trans} + (1 - s)A_{inc})(1 - sR_2)}{1 - sR_2A_d} \tag{A8}$$

where s is the "specularity parameter", which specifies the degree to which the upper surface behaves specularly; s ranges from 0 to 1. R_1 is the external reflection coefficient (air to ice), whereas R_2 is the internal reflection coefficient (ice to air). A_{inc} and A_{trans} are the delta-Eddington albedos calculated for incident and transmitted light at angles $\theta_i = \theta_{zenith}$ and θ_t, respectively. Scattering is assumed to take place only due to air bubbles within the ice. Snell's law gives:

$$\frac{n_2}{n_1} = \frac{sin(\theta_i)}{sin(\theta_t)} = m_{rat} \tag{A9}$$

where m_{rat} is the ratio of the real components of the refractive indices of the transmitted media to the incident media (i.e., air: 1 and ice: n_{ice}).

Squaring the cosine of the transmitted angle $(\cos(\theta_t))^2 = \mu_{trans}^2$ gives

$$\mu_{trans}^2 = 1 - \frac{1 - \mu_0^2}{m_{rat}^2} \tag{A10}$$

If $\mu_{trans}^2 \leq 0$, the light undergoes total internal reflection and the net transmittance $T = 0$. In all other cases, from Fresnel laws, the polarized reflectances R_s and R_p are given by:

$$R_s = \left(\frac{\mu_0 - m_{rat}\mu_{trans}}{\mu_0 + m_{rat}\mu_{trans}}\right)^2 \tag{A11}$$

$$R_P = \left(\frac{\mu_{trans} - m_{rat}\mu_0}{\mu_{trans} + m_{rat}\mu_0}\right)^2 \tag{A12}$$

These reflectances are used to calculate the transmittance T:

$$T = 1 - (R_s + R_P)/2 \tag{A13}$$

T is then used to calculate R_2:

$$R_2 = 2\int_0^1 f(R_2)d\mu \tag{A14}$$

where $f(R_2) = 1 - T_x\mu$. T_x can be calculated using the transmittance equations above, using the refractive index for air-to-ice ($m_{rat} = 1/n_{ice}$), and μ (which is integrated from 0 to 1 for the entire hemisphere).

To calculate A_d,

$$A_d = 2\int_0^1 \frac{f(A_d)}{R_2}\,d\mu \tag{A15}$$

where $f(A_d) = A(\mu)(1 - T_x)\mu$. $A(\mu)$ is the delta-Eddington albedo for a direct beam at incidence angle $\cos^{-1}\mu$.

To compute the delta-Eddington albedos ($A_{inc}, A_{trans}, A(\mu)$ and A_d), the specific surface area (SSA) is used as an input, along with firn/glacier ice density ρ_{ice}. The porosity ϕ is then related to the density by $\rho_{ice} = (1-\phi)917$.

For absorption by firn/glacier ice, the absorption coefficient β_{abs} can be calculated from the imaginary part of the ice refractive index k_{ice} and the ice porosity,

$$\beta_{abs} = \frac{(1-\phi)4\pi k_{ice}}{\lambda} \tag{A16}$$

The scattering coefficient β_{sca} can be calculated using the SSA and the porosity,

$$\beta_{sca} = \frac{SSA(1-\phi)917}{2} = \frac{(SSA)\rho}{2} \tag{A17}$$

This is the same as Eq. 5 of Dadic et al. (2013). Adding β_{sca} and β_{abs} gives the extinction coefficient $\beta_{ext} = \beta_{abs} + \beta_{sca}$. The asymmetry parameter g is taken from Mullen & Warren (1988). The single-scattering albedo $\bar{\omega}$ and the optical depth τ are then given by $\bar{\omega} = \beta_{sca}/\beta_{ext}$ and $\tau = z/\beta_{ext}$, where z is the thickness of the ice. $z \geq 20$ m is assumed to be optically semi-infinite, so z = 20 m is assumed for all cases.

3.A.3. Albedo of Dusty Snow, Firn and Glacier Ice

For snow and dust, using the absorption and scattering efficiencies Q_{abs} and Q_{sca} and the areas of the particles, the absorption and scattering cross-sections can be calculated:

$$\sigma_{abs} = Q_{abs}A \tag{A18}$$

$$\sigma_{sca} = Q_{sca}A \tag{A19}$$

The mass absorption and scattering coefficients can then be derived for snow and dust:

$$k_{abs} = \frac{\sigma_{abs}}{m} = \frac{\sigma_{abs}}{\rho V} \tag{A20}$$

$$k_{sca} = \frac{\sigma_{sca}}{m} = \frac{\sigma_{sca}}{\rho V} \tag{A21}$$

For firn and glacier ice, mass absorption and scattering coefficients can be derived using β_{abs} and β_{sca}:

$$k_{abs} = \frac{\beta_{abs}}{\rho_{ice}} \tag{A22}$$

$$k_{sca} = \frac{\beta_{sca}}{\rho_{ice}} \tag{A23}$$

Let the mass fractions of ice and dust be given by:

$$C_{ice} + C_{dust} = 1 \tag{A24}$$

The absorption, scattering and extinction coefficients of the mixture ($\beta_{abs,net}$, $\beta_{sca,net}$ and $\beta_{ext,net}$) can be calculated by weighting the previously derived properties of ice and dust by their respective mass fractions,

$$\beta_{abs,net} = C_{ice}\rho_{ice}k_{abs,ice} + C_{dust}\rho_{dust}k_{abs,dust} \tag{A25}$$

$$\beta_{sca,net} = C_{ice}\rho_{ice}k_{sca,ice} + C_{dust}\rho_{dust}k_{sca,dust} \tag{A26}$$

$$\beta_{ext,net} = \beta_{abs,net} + \beta_{sca,net} \tag{A27}$$

Note that ρ_{ice} is the density of the pure snowpack, firn or glacier ice being modeled. Using these coefficients, the single-scattering albedo, optical depth, and the asymmetry parameter of the mixture ($\bar{\omega}_{net}$, τ_{net} and g_{net}) can be found:

$$\bar{\omega}_{net} = \beta_{sca,net}/\beta_{ext,net} \tag{A28}$$

$$\tau_{net} = z\beta_{ext,net} \tag{A29}$$

$$g_{net} = \frac{C_{ice}g_{ice}k_{sca,ice} + C_{dust}g_{dust}k_{sca,dust}}{C_{ice}k_{sca,ice} + C_{dust}k_{sca,dust}} \tag{A30}$$

The albedo of dusty snow and glacier ice can then be found using Equations (A7) and (A8), respectively, with the mixture optical properties derived in Equations (A28–A30).

REFERENCES

Arvidson, R. E., Anderson, R. C., Bartlett, P., Bell, J. F., III, Blaney, D., Christensen, P. R., et al. (2004). Localization and physical properties experiments conducted by Spirit at Gusev Crater. *Science, 305*, 821-824.

Blaney, D., Archer, D., Arvidson, R., Cull, S., Ellehøj, M., Fisher, D., et al. (2009). Multi-spectral imaging of the Phoenix landing site: Characteristics of surface and subsurface ice, rocks, and soils. *LPI*, 2047.

Bohren, C. F. (1983). Colors of snow, frozen waterfalls, and icebergs. *JOSA, 73*(12), 1646-1652.

Bohren, C. F., & Barkstrom, B. R. (1974). Theory of the optical properties of snow. *Journal of Geophysical Research, 79*(30), 4527-4535. https://doi.org/10.1029/JC079i030p04527

Boulton, G. (1978). Boulder shapes and grain-size distributions of debris as indicators of transport paths through a glacier and till genesis. *Sedimentology, 25*(6), 773-799.

Bramson, A., Byrne, S., & Bapst, J. (2017). Preservation of midlatitude ice sheets on Mars. *Journal of Geophysical Research: Planets, 122*(11), 2250-2266. https://doi.org/10.1002/2017JE005357

Brandt, R. E., & Warren, S. G. (1993). Solar-heating rates and temperature profiles in Antarctic snow and ice. *J. Glaciol., 39*(131), 99-110.

Byrne, S., Dundas, C. M., Kennedy, M. R., Mellon, M. T., McEwen, A. S., Cull, S. C., et al. (2009). Distribution of mid-latitude ground ice on Mars from new impact craters. *Science, 325*(5948), 1674-1676.

Christensen, P. (2003). Formation of recent martian gullies through melting of extensive water-rich snow deposits. *Nature, 422*(6927), 45-48. 10.1038/nature01436

Clow, G. D. (1987). Generation of liquid water on Mars through the melting of a dusty snowpack. *Icarus, 72*(1), 95-127.

Cuffey, K. M., & Paterson, W. S. B. (2010). *The physics of glaciers*: Academic Press.

Cull, S., Arvidson, R. E., Mellon, M. T., Skemer, P., Shaw, A., & Morris, R. V. (2010). Compositions of subsurface ices at the Mars Phoenix landing site. *Geophysical Research Letters, 37*(24). https://doi.org/10.1029/2010GL045372

Dadic, R., Mullen, P. C., Schneebeli, M., Brandt, R. E., & Warren, S. G. (2013). Effects of bubbles, cracks, and volcanic tephra on the spectral albedo of bare ice near the Transantarctic Mountains: Implications for sea glaciers on Snowball Earth.

Journal of Geophysical Research: Earth Surface, 118(3), 1658-1676. https://doi.org/10.1002/jgrf.20098

Dang, C., Brandt, R. E., & Warren, S. G. (2015). Parameterizations for narrowband and broadband albedo of pure snow and snow containing mineral dust and black carbon. *Journal of Geophysical Research: Atmospheres, 120*(11), 5446-5468. https://doi.org/10.1002/2014JD022646

Dozier, J., Green, R. O., Nolin, A. W., & Painter, T. H. (2009). Interpretation of snow properties from imaging spectrometry. *Remote Sensing of Environment, 113*, S25-S37.

Drube, L., Leer, K., Goetz, W., Gunnlaugsson, H., Haspang, M., Lauritsen, N., et al. (2010). Magnetic and optical properties of airborne dust and settling rates of dust at the Phoenix landing site. *Journal of Geophysical Research: Planets, 115*(E5). https://doi.org/10.1029/2009JE003419

Dundas, C. M., Bramson, A. M., Ojha, L., Wray, J. J., Mellon, M. T., Byrne, S., et al. (2018). Exposed subsurface ice sheets in the Martian mid-latitudes. *Science (New York, N.Y.), 359*(6372), 199. 10.1126/science.aao1619

Dundas, C. M., Mellon, M. T., Conway, S. J., Daubar, I. J., Williams, K. E., Ojha, L., et al. (2021). Widespread Exposures of Extensive Clean Shallow Ice in the Mid-Latitudes of Mars. *Journal of Geophysical Research: Planets*, e2020JE006617. https://doi.org/10.1029/2020JE006617

Fisher, D. A. (2005). A process to make massive ice in the martian regolith using long-term diffusion and thermal cracking. *Icarus, 179*(2), 387-397.

Goetz, W., Pike, W., Hviid, S., Madsen, M. B., Morris, R., Hecht, M., et al. (2010). Microscopy analysis of soils at the Phoenix landing site, Mars: Classification of soil particles and description of their optical and magnetic properties. *Journal of Geophysical Research: Planets, 115*(E8). https://doi.org/10.1029/2009JE003437

Gow, A. J. (1969). On the rates of growth of grains and crystals in South Polar firn. *J. Glaciol., 8*(53), 241-252.

Gyalay, S., Dobrea, E. Z. N., Chu, K., & Pitman, K. M. (2019). Nonlinear spectral mixture modeling to estimate water-ice abundance of martian regolith. *Icarus, 329*, 79-87.

Haberle, R. M., Clancy, R. T., Forget, F., Smith, M. D., & Zurek, R. W. (2017). *The atmosphere and climate of Mars*: Cambridge University Press.

Jakosky, B. M., & Carr, M. A. (1985). Possible precipitation of ice at low latitudes of Mars during periods of high obliquity. *Nature, 315*, 559-561.

Joseph, J. H., Wiscombe, W., & Weinman, J. (1976). The delta-Eddington approximation for radiative flux transfer. *J. Atmos. Sci., 33*(12), 2452-2459.

Khuller, A. R., & Christensen, P. R. (2021). Evidence of Exposed Dusty Water Ice within Martian Gullies. *Journal of Geophysical Reasearch: Planets*. https://doi.org/10.1029/2020JE006539

Khuller, A. R., Christensen, P. R., & Warren, S. G. (2021). *Repository: Spectral Albedo of Dusty Martian H2O Snow and Ice*. Retrieved from: https://doi.org/10.5281/zenodo.4653768

Kieffer, H. H. (1990). H2O grain size and the amount of dust in Mars' residual north polar cap. *Journal of Geophysical Research: Solid Earth, 95*(B2), 1481-1493. https://doi.org/10.1029/JB095iB02p01481

Langevin, Y., Poulet, F., Bibring, J.-P., Schmitt, B., Douté, S., & Gondet, B. (2005). Summer evolution of the north polar cap of Mars as observed by OMEGA/Mars express. *Science, 307*(5715), 1581-1584.

Linow, S., Hörhold, M. W., & Freitag, J. (2012). Grain-size evolution of polar firn: a new empirical grain growth parameterization based on X-ray microcomputer tomography measurements. *J. Glaciol., 58*(212), 1245-1252.

Liston, G. E., & Winther, J.-G. (2005). Antarctic surface and subsurface snow and ice melt fluxes. *Journal of Climate, 18*(10), 1469-1481.

Madeleine, J. B., Head, J. W., Forget, F., Navarro, T., Millour, E., Spiga, A., et al. (2014). Recent ice ages on Mars: the role of radiatively active clouds and cloud microphysics. *Geophysical Research Letters, 41*(14), 4873-4879. https://doi.org/10.1002/2014GL059861

Matzler, C. (2002). Matzler's Matlab Code For Mie Theory. Bern, Switzerland: Institute of Applied Physics, University of Bern.

McEwen, A. S., Eliason, E. M., Bergstrom, J. W., Bridges, N. T., Hansen, C. J., Delamere, W. A., et al. (2007). Mars Reconnaissance Orbiter's High Resolution Imaging Science Experiment (HiRISE). *Journal of Geophysical Research: Planets, 112*(E5). https://agupubs.onlinelibrary.wiley.com/doi/abs/10.1029/2005JE002605doi:doi:10.1029/2005JE002605

Mellon, M. T., Arvidson, R. E., Sizemore, H. G., Searls, M. L., Blaney, D. L., Cull, S., et al. (2009). Ground ice at the Phoenix landing site: Stability state and origin. *Journal of Geophysical Research: Planets, 114*(E1). https://doi.org/10.1029/2009JE003417

Moore, H. J., Bickler, D. B., Crisp, J. A., Eisen, H. J., Gensler, J. A., Haldemann, A. F. C., et al. (1999). Soil-like deposits observed by Sojourner, and Pathfinder Rover. *Journal of Geophysical Research, 104*(E4), 8729-8746. https://doi.org/10.1029/1998JE900005

Moore, H. J., & Jakosky, B. M. (1989). Viking landing sites, remote-sensing observations, and physical properties of Martian surface materials. *Icarus, 81*(1), 164-184.

Mullen, P. C., & Warren, S. G. (1988). Theory of the optical properties of lake ice. *Journal of Geophysical Research: Atmospheres, 93*(D7), 8403-8414. https://doi.org/10.1029/JD093iD07p08403

Murchie, S., Arvidson, R., Bedini, P., Beisser, K., Bibring, J.-P., Bishop, J. L., et al. (2007). Compact Reconnaissance Imaging Spectrometer for Mars (CRISM) on Mars Reconnaissance Orbiter (MRO). *Journal of Geophysical Research, 112*(E05S03). https://doi.org/10.1029/2006JE002682

Naar, J., Forget, F., Madeleine, J.-B., Millour, E., Spiga, A., Vals, M., et al. (2020). Recent Formation of Ice-Rich Latitude-Dependent Mantle from Polar Ice Reservoirs. *LPI Contributions, 2099*, 6041.

Painter, T. H., Seidel, F. C., Bryant, A. C., McKenzie Skiles, S., & Rittger, K. (2013). Imaging spectroscopy of albedo and radiative forcing by light-absorbing impurities in mountain snow. *Journal of Geophysical Research: Atmospheres, 118*(17), 9511-9523. https://doi.org/10.1002/jgrd.50520

Pascuzzo, A., Condus, T., Mustard, J., & Arvidson, R. (2019). The Effects of Ice and Dust Aerosols, and Surface Scattering on the Interpretation of the Martian North Polar Ice Cap Surface Characteristics Using CRISM VNIR-SWIR Data. *LPI Contributions, 2089*, 6380.

Putzig, N. E., Phillips, R. J., Campbell, B. A., Mellon, M. T., Holt, J. W., & Brothers, T. C. (2014). SHARAD soundings and surface roughness at past, present, and proposed landing sites on Mars: Reflections at Phoenix may be attributable to deep ground ice. *Journal of Geophysical Research: Planets, 119*(8), 1936-1949. https://doi.org/10.1002/2014JE004646

Singh, D., Flanner, M., & Millour, E. (2018). Improvement of Mars surface snow albedo modeling in LMD Mars GCM with SNICAR. *Journal of Geophysical Research: Planets, 123*(3), 780-791. https://doi.org/10.1002/2017JE005368

Sizemore, H. G., Zent, A. P., & Rempel, A. W. (2015). Initiation and growth of Martian ice lenses. *Icarus, 251*, 191-210.

Smith, P. H., Tamppari, L., Arvidson, R., Bass, D., Blaney, D., Boynton, W. V., et al. (2009). H2O at the Phoenix landing site. *Science, 325*(5936), 58-61.

Stephenson, P. (1967). Some considerations of snow metamorphism in the Antarctic ice sheet in the light of ice crystal studies. *Physics of Snow and Ice: proceedings, 1*(2), 725-740.

van de Hulst, H. (1957). Light Scattering by Small Particles. In: New York: John Wiley & Sons.

Warren, S. G. (2019). Optical properties of ice and snow. *Philosophical Transactions of the Royal Society A, 377*(2146), 20180161.

Warren, S. G., & Brandt, R. E. (2008). Optical constants of ice from the ultraviolet to the microwave: A revised compilation. *Journal of Geophysical Research: Atmospheres, 113*(D14). https://doi.org/10.1029/2007JD009744

Warren, S. G., & Wiscombe, W. J. (1980). A model for the spectral albedo of snow.2. Snow containing atmospheric aerosols. *J. Atmos. Sci., 37*(No. 12), 2734-2745.

Wiscombe, W. J., & Warren, S. G. (1980). A model for the spectral albedo of snow.1. Pure snow. *J. Atmos. Sci., 37*(No. 12), 2712-2733.

Wolff, M., Smith, M., Clancy, R., Arvidson, R., Kahre, M., Seelos, F., et al. (2009). Wavelength dependence of dust aerosol single scattering albedo as observed by the Compact Reconnaissance Imaging Spectrometer. *Journal of Geophysical Research: Planets, 114*(E2). https://doi.org/10.1029/2009JE003350

Zamani, P., Tamppari, L., Lemmon, M., Keller, U., Hecht, M., Cooper, B., et al. (2009). *Phoenix Software Interface Specification*. Retrieved from https://pds-imaging.jpl.nasa.gov/data/phoenix/phxsci_0xxx/document/cam_edr_rdr_sis.pdf

Chapter 4

THE DISTRIBUTION OF FROSTS ON MARS: LINKS TO PRESENT-DAY GULLY ACTIVITY

A. R. Khuller[1], P. R. Christensen[1], T. N. Harrison[1†] and S. Diniega[2]

[1]School of Earth and Space Exploration, Arizona State University, Tempe, AZ, USA.

[2]Jet Propulsion Laboratory, California Institute of Technology, Pasadena, CA, USA.

†Current affiliation: Planet Labs, Washington DC, USA.

Citation: Khuller, A.R., Christensen, P.R., Harrison, T.N., Diniega S., (2021). The Distribution of Frosts on Mars: Links to Present-Day Gully Activity. *Journal of Geophysical Research: Planets.*

Key Points:

- CO_2 frost is detected at all latitudes, and near the equator it is largely restricted to low thermal inertia regions
- Small amounts of H_2O frost can form at most latitudes during the night, but are difficult to detect with current instrumentation at Mars
- 47% of all gullies overlap with CO_2 frost detections but present-day activity appears to occur in loose, unconsolidated materials

Abstract

Numerous types of activity in mid-latitude martian gullies have been observed over the last decade. Some activity has been constrained to occur in the coldest times of year, suggesting that surficial frosts that form seasonally and diurnally might play a key role in this activity. Here we use thermal infrared data to explore the global, spatial and temporal variation of temperatures conducive to CO_2 and H_2O frost formation on Mars, and assess their distribution relative to gully landforms. CO_2 frost detections are observed at all latitudes and are strongly correlated with dusty, low thermal inertia regions near the equator. While it is difficult to accurately detect the formation of H_2O frost, the global H_2O frost point distribution generally follows water vapor column abundance, and is weakly correlated with surface pressure. Most global CO_2 frost detections do not contain gullies, but 47% of all gullies, and 73% of active gullies (76% in the south, and 25% in the north) do overlap with CO_2 frost detections. We predict that the conditions necessary for significant present-day gully activity include a few centimeters of CO_2 frost within loose, unconsolidated sediments (I ~300 $J\ m^{-2}\ K^{-1}\ s^{-0.5}$) on relatively steep (< 20º) slopes. Additionally, it could be possible for small amounts of H_2O frosts to play a role in present-day equatorial mass wasting events. However, whether present-day gully activity is representative of gully formation is still open to debate, because it seems unlikely that frosts can erode channels into rocky substrates – even considering geologic timescales.

4.1. Introduction

4.1.1. Gullies on Mars

Gullies are predominantly found within latitudes of ~30º–50º in either martian hemisphere (Malin & Edgett, 2001), with most gullies in this latitude range occurring on pole-facing slopes (e.g., Harrison et al., 2015). These gullies typically consist of a broad upslope alcove that feeds into a channel, leading to a depositional apron of debris downslope. Numerous mechanisms for gully formation have been suggested: release of liquid water/brine from shallow (Malin & Edgett, 2000; Mellon & Phillips, 2001) or deep aquifers (Gaidos, 2001); liquid CO_2 aquifers (Musselwhite et al., 2001); melting of pore ice (Costard et al., 2002; Gilmore & Phillips, 2002); melting snowpacks (Christensen, 2003b); melting of seasonal H_2O frost (Kossacki & Markiewicz, 2004); frosted granular flow (Hugenholtz, 2008); CO_2 gas-fluidized flows (Hoffman, 2002; Cedillo-Flores et al., 2011; Dundas et al., 2019), and dry granular flow (Treiman, 2003; Shinbrot et al., 2004; Pelletier et al., 2008; Kolb et al., 2010).

A wide variety of gully activity has been observed over the last two decades, with a diverse range of morphologies and erosional characteristics (Malin et al., 2006; Harrison et al., 2009; Dundas et al., 2010; Dundas et al., 2012; Dundas et al., 2015b; Harrison et al., 2015; Dundas et al., 2019). Observed activity has included channel lengthening, erosion within gully channels, channel abandonment, sinuous curve migration and the formation of lobate deposits (e.g., Dundas et al., 2012; Dundas et al., 2019). Some of this activity has been constrained by repeat imagery to occur in the coldest times of the year (during winter and spring; Harrison et al., 2009; Diniega et al.,

2010; Dundas et al., 2010; Dundas et al., 2012; Dundas et al., 2015b; Diniega et al., 2018; Dundas et al., 2019). The often-contemporaneous presence of seasonal/diurnal frosts has led some authors (Diniega et al., 2010; Dundas et al., 2010; Dundas et al., 2012; Dundas et al., 2015b; Dundas et al., 2019) to suggest that the formation and disappearance of these frosts might play a key role in this present-day activity.

4.1.2. Frosts on Mars

Frost formation is highly dependent on two key factors: (1) surface temperature and (2) the atmospheric partial pressure of the condensable gas (Kieffer, 1968). The two primary condensable gases on Mars are CO_2 and H_2O. Because the martian atmosphere is primarily composed of CO_2, CO_2 frost formation is not diffusion-limited, i.e., frost formation can continue to take place as long as CO_2 ice latent heat energy requirements are met when the surface is at the local frost point (~148 K at a surface pressure of 610 Pa) (Piqueux et al., 2016). The local CO_2 frost point oscillates within ± 2 K during each martian year (Fig. S1) due to the seasonal variation in surface pressure caused by net condensation/transport of CO_2 to and from the poles every year. Local surface pressure also varies with elevation, giving a total range in CO_2 frost point of ~130 K to 154 K across the planet.

H_2O condensation can occur in the form of clouds (on condensation nuclei provided by airborne dust; Whiteway et al., 2009), precipitation as snow (Jakosky & Carr, 1985; Spiga et al., 2017), radiation fogs (Ryan & Sharman, 1981) or at the surface (Ryan et al., 1982; Hart & Jakosky, 1986; Svitek & Murray, 1990; Cull et al., 2010a; Spiga et al., 2017), depending on the vertical distribution of water vapor in the column

and the local temperature. Typically, water vapor is concentrated below a certain condensation height and is assumed to be well-mixed near the surface (Smith, 2002). Since H_2O is a minor component of the martian atmosphere (with a global, annual average of ~13 pr - μm; Smith, 2002), surficial H_2O frost formation is limited by diffusion and the partial pressure of H_2O when the surface is at the H_2O frost point (~193 K at a partial pressure of 7 pr - μm) (Schorghofer & Edgett, 2006). Thus, the contents of martian surficial frosts are dominated volumetrically by CO_2, although small amounts of H_2O frosts are also present and typically precede CO_2 frost deposition due to the higher condensation temperature of H_2O.

The latitudinal distribution of martian frosts has been studied by numerous authors using a combination of visible, thermal and spectral measurements in addition to theoretical modeling. In the polar regions, layers of seasonal, predominantly CO_2 frost (with minor amounts of H_2O) cover Mars' residual polar caps which are primarily composed of H_2O ice (Farmer et al., 1976; Kieffer et al., 1976; Kieffer, 1979). This 'seasonal cap' extends to ~50° latitude in both hemispheres (Piqueux et al., 2015). Additionally, frosts can also form at the mid-to-high latitudes. H_2O frosts were first documented in-situ at the Viking Lander 2 site (47.96ºN) during the winter (Svitek & Murray, 1990). Schorghofer and Edgett (2006) showed that seasonal frosts extend to latitudes as low as 24ºS on cold, pole-facing slopes based on Mars Global Surveyor (MGS) Mars Orbiter Camera (MOC; Malin & Edgett, 2001) imagery, modeling and thermal infrared data from the MGS Thermal Emission Spectrometer (TES; Christensen et al., 2001) and the Mars Odyssey Thermal Emission Imaging System (THEMIS;

Christensen et al., 2004). Using hyperspectral data from the Mars Express Observatoire pour la Minéralogie, l'Eau, les Glaces, et l'Activité (OMEGA; Bibring et al., 2005) and the Mars Reconnaissance Orbiter (MRO) Compact Reconnaissance Imaging Spectrometer for Mars (CRISM; Murchie et al., 2007), Carrozzo et al. (2009) and Vincendon et al. (2010a, 2010b) detected seasonal frosts in both hemispheres. Using these methods, H_2O frost was detected at latitudes down to 13ºS and 32ºN, whereas the lowest latitude CO_2 frost detection was made at 34ºS (Carrozzo et al., 2009; Vincendon et al., 2010a; Vincendon et al., 2010b). TES daytime albedo and temperature data have also been used to infer the presence and distribution of daytime H_2O frosts, placing equatorward limits of ~40ºN and ~50ºS (Bapst et al., 2015). While early albedo and thermal measurements (Kieffer et al., 1977) suggested the presence of equatorial, predawn frosts in a few regions, the first direct detection of equatorial H_2O frosts was made by the Opportunity rover at 2ºS (Landis, 2007). These discoveries were followed by localized CO_2 frost detections at 9ºS (Cushing & Titus, 2008) and 18ºN (Titus & Cushing, 2014) using TES and THEMIS data. Widespread CO_2 frosts were subsequently detected at equatorial latitudes by Piqueux et al. (2016) from MRO Mars Climate Sounder (MCS; McCleese et al., 2007) data, showing the presence of a diurnal CO_2 frost cycle within dusty, equatorial regions.

In order to assess the potential connection between frosts and recent gully activity, Vincendon (2015) conducted a detailed survey using CRISM and OMEGA observations over active southern mid-latitude gullies (as reported by Malin et al., 2006; Harrison et al., 2009; Dundas et al., 2010; Dundas et al., 2012; Dundas et al., 2015b) and

found seasonal spectral signatures of H_2O and CO_2 frosts to coincide with numerous locations of recent activity. However, work done using VNIR spectroscopy usually relies on daytime measurements, which precludes nighttime frost detection. Thermal infrared data does not have this limitation.

4.1.3. This Study

In this paper, we use THEMIS data (binned at 500 m/pixel) and TES (~3 km/pixel) thermal infrared data to explore the global, spatial and temporal variation of CO_2 and H_2O frosts on Mars. We then investigate the correlation of frost locations with gully landforms and assess present-day gully activity conditions. In the following section, we describe the methods used to map and validate the global distribution of frosts, along with potential limitations. In the third section, we present the frost mapping results in relation to surface properties and discuss seasonal variations. In the fourth section, we examine the relationship of frosts with the distribution of gullies and equatorial mass-wasting events. We model the amounts of CO_2 frost at different latitudes and slope geometries in the fifth section. In the sixth section, we characterize the thermophysical properties of active gully materials. Finally, we discuss the implications of the observed distribution of frosts with gullies, and the effects of frosts on gully activity and formation.

4.2. Data and Methods

4.2.1. The 2001 Mars Odyssey Thermal Emission Imaging System (THEMIS)

The THEMIS instrument is comprised of an infrared imager (100 m/pixel)with nine ~1 μm bands, centered from 6.78 to 14.88 μm. Emitted spectral radiance measured

by THEMIS is converted to brightness temperature assuming an emissivity of unity; no atmospheric correction to the data is applied (Christensen et al., 2003).

4.2.1.1. Instrument Calibration

THEMIS has a single-pixel noise equivalent spectral radiance (NESR) of 2.72×10^{-2} W m^{-2} sr^{-1} μm^{-1} in band 9, corresponding to a 1-σ noise equivalent delta temperature (NEDT) of ~0.4 K at 245 K; and 1.1 K at 180 K (Christensen et al., 2003). However, averaging pixels together improves the signal to noise. In this study, we averaged five 100 m THEMIS pixels, thereby reducing the NESR by a factor of five. NEDT can be calculated from the NESR,

$$NEDT(T, \lambda, NESR) = \frac{NESR}{5dL(\lambda, T)/dT} \quad (1)$$

where L is the Planck function, and is a function of wavelength, λ and temperature, T.

$$L(\lambda, T) = \frac{c_1}{\lambda^5 \left(e^{\frac{c_2}{\lambda T}} - 1\right)} \quad (2)$$

and its derivative, with respect to T,

$$\frac{dL}{dT} = Lc_2 \frac{exp\left(e^{\frac{c_2}{\lambda T}}\right)}{T^2 \lambda \left(e^{\frac{c_2}{\lambda T}} - 1\right)} \quad (3)$$

where $c_1 = 1.191042 \times 10^8\ W\ m^{-2}\ sr^{-1}\ \mu m^{-4}$, $c_2 = 1.4387752 \times 10^4\ K\ \mu m$ (Cao & Shao, 2013) and $\lambda = 12.57\ \mu m$ (THEMIS band 9 center wavelength). At the lower limit of the global CO_2 frost point range (130 K), the NEDT is 1.4 K, whereas at 154 K, the upper limit, the NEDT is ~0.5 K. This means that a measured temperature of 130 K has an uncertainty of 1.4 K and could imply warmer or cooler surface temperatures.

4.2.1.2. Data Processing and Atmospheric Correction

We used JMARS (Christensen et al., 2009b) to search for THEMIS images with temperatures $T_{THEMIS} \leq 156.5$ K, to account for the NEDT and additional uncertainties in calculating the local CO_2 frost point (due to small-scale variations in surface pressure, scale height, etc.). Systematic noise was removed by excluding images with calibration errors and dropouts. The remaining THEMIS images were then spatially averaged to a resolution of 500 m/pixel.

Ideally, all standard Planetary Data System (PDS) processed THEMIS images (Christensen et al., 2003) with pixels at or below the local CO_2 frost point would be counted as frost detections, after accounting for the instrument NEDT (discussed above). However, standard THEMIS processing does not account for atmospheric effects due to water ice clouds, increased dust opacity, etc., that can result in warmer apparent surface temperatures. For example, Piqueux et al. (2016), looking at MCS data, found that the atmosphere was typically ~6 K warmer than the surface when surface temperatures approached the local CO_2 frost point at night. Thus, to ensure that CO_2 frost detections were not missed in their study, a suitable value between 0–9 K was often subtracted from the original surface brightness temperatures, based on radiative transfer modeling using collocated limb MCS measurements (Piqueux et al., 2016). THEMIS images rarely have collocated limb measurements to perform a similar atmospheric correction. To help mitigate this issue, we subtracted a value of 5 K from all standard THEMIS images that have minimum surface brightness temperatures ≤ 156.5 K to account for these atmospheric effects.

4.2.1.3. CO_2 frost Detections

Only 'atmospherically corrected' pixels (5 K subtraction) with NEDT-buffered temperatures at, or below the local CO_2 frost point $T_{CO_2,local}$ were counted as CO_2 frost detections:

$$T_{THEMIS} - 5\ K - NEDT(T) \leq T_{CO_2,local}(P) \quad (4)$$

in which $T_{CO_2,local}$ was computed using Clapeyron's law and the local surface pressure P at the relevant season derived from the online version of the Mars Climate Database (http://www-mars.lmd.jussieu.fr/mcd_python/; Forget et al., 2016; Millour et al., 2018). Note that small (< 1 mm) CO_2 frost grains can have thermal infrared emissivities of less than 1 (Piqueux et al., 2016), resulting in standard THEMIS images with CO_2 frost often having temperatures lower than 130 K, the global average minimum frost point. This apparent temperature lowering is caused by the assumption that the surface has an emissivity of 1 during standard THEMIS processing. However, this temperature lowering does not affect whether CO_2 frost is detected.

Two sets of CO_2 frost detections were compiled. First, CO_2 frost detections were searched for globally to assess their overall distribution. For this set of detections, we used Mars Year (MY) 26 data, when the local solar time of observations was around 3 a.m./p.m. and no global dust storm occurred (Smith, 2009). The overall coverage between MYs for THEMIS does not vary significantly (see global coverage maps at http://global-data.mars.asu.edu/bin/themis.pl), so data from MY 26 is representative of typical observational conditions, although the local solar time of THEMIS observations has changed from MY 26 to MY 35. Second, CO_2 frost detections over gully locations

(Harrison et al., 2015; Vincendon, 2015; Dundas et al., 2019) were searched for using THEMIS images from MYs 26–35 that overlapped with gully locations to quantify the correlation between gullies and CO_2 frost.

4.2.1.4. Validation and Limitations

4.2.1.4.1. CTX and CRISM

To investigate the accuracy of these THEMIS CO_2 frost detections at a location where CO_2 frost was expected (based on the season and latitude), we inspected available visible (MRO Context Camera (CTX; Malin et al., 2007)), thermal (THEMIS) and spectral (CRISM) data for evidence of frosts within a THEMIS detection (Fig. 4.1A). On the pole-facing wall of an unnamed crater (38.8ºS, 195.9ºE) at L_s = 140.64, the CTX image (Fig. 4.1B) shows bright white deposits on the pole-facing wall, especially within sheltered facets and gully alcoves. THEMIS (Fig. 4.1C; L_s = 143) temperatures at 7:43 a.m. local solar time range from 150–186 K, with the bright white regions in the CTX image highlighted by 150 K temperatures (CO_2 frost point). By inspecting band-depth parameter maps from CRISM, the bright white regions are strongly highlighted in both the BD1435 (Fig. 4.1D) and the BD1500 (Fig. 4.1E) parameter maps that are indicative of diagnostic absorptions due to CO_2 and H_2O respectively (Viviano-Beck et al., 2014). CO_2 frosts are less spatially extensive than H_2O frosts in the visible/spectral observations made during the warmer afternoon. Although only one such location was inspected, this shows that CO_2 frost can be detected using these 500 m/pixel THEMIS datasets. Additionally, a few equatorial detections (not shown) where CO_2 frosts may not be expected were also inspected using available CRISM/HiRISE/CTX data. These locations

were found to contain dusty, low thermal inertia materials ideal for the formation of small amounts of CO_2 frost (Piqueux et al., 2016).

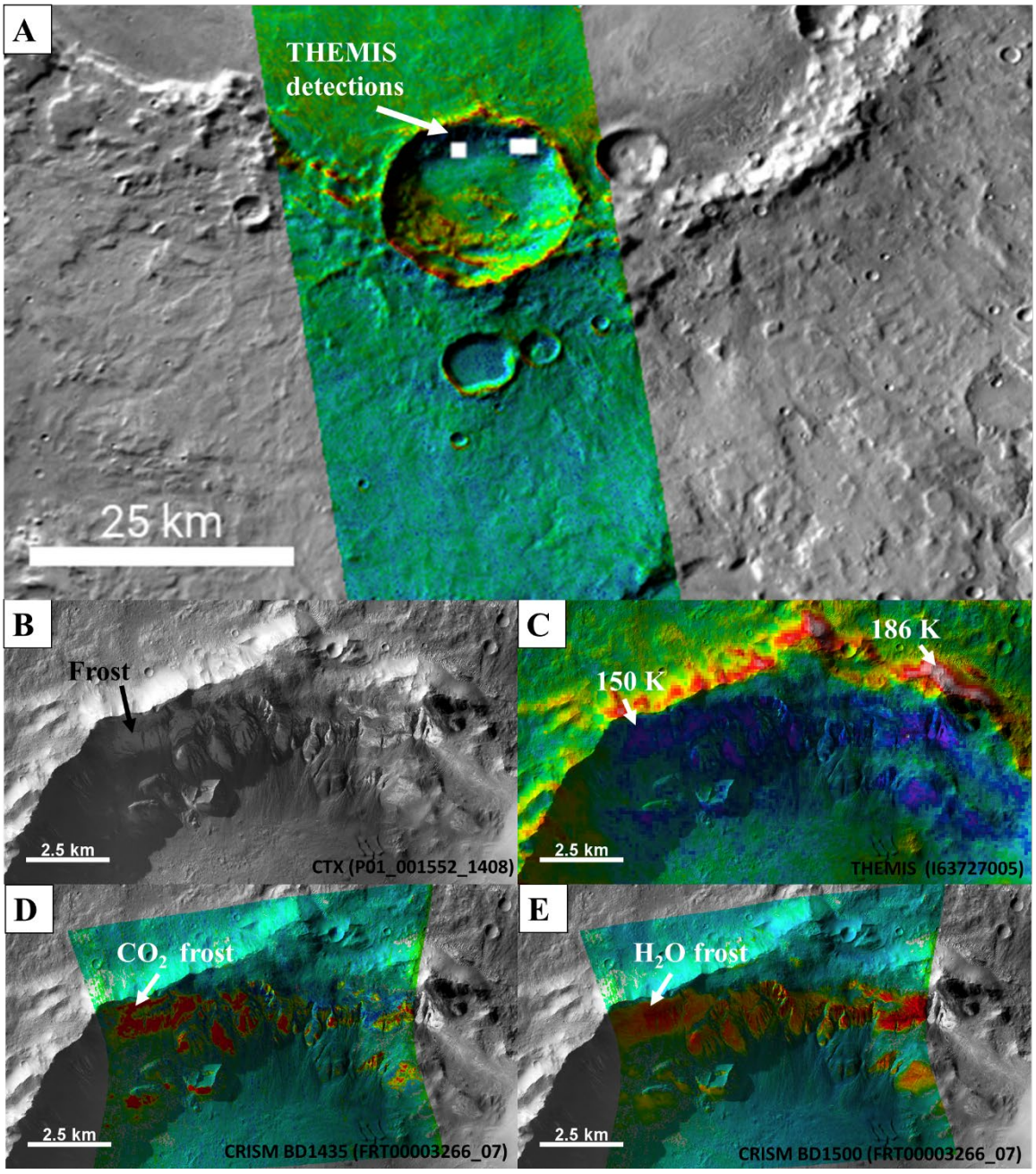

Figure 4.1. Inspecting for frosts at the surface (38.8ºS, 195.9ºE) during southern winter within (A) THEMIS (500 m/pixel) detections (white boxes indicate locations of

detections, but are not to scale) using (B) CTX, where frosts are seen as bright white patches, (C) THEMIS, in which temperatures range from 186 K (reddish hues) to 150 K (purplish hues), (D) CRISM BD1435 parameter map, where reddish tones represent a high 1.435 μm band depth indicative of CO_2 ice and (E) CRISM BD1500 parameter map, where reddish tones represent a high 1.5 μm band depth, indicative of H_2O ice. CTX image P01_001552_1408, THEMIS image I63727005 and CRISM image FRT00003266_07 are shown here.

Despite using this approach, the presence of CO_2 frosts can be difficult to confirm at all locations. For example, it is possible that frosts formed within shadowed topographical facets are unaccounted for, especially at the sub-pixel scale. Additionally, the THEMIS NEDT present at CO_2 frost temperatures and our method of accounting for atmospheric effects can also lead to non-detections as well as false positives. However, our CO_2 frost detections show an excellent correlation with previous atmospherically corrected, coarse-resolution MCS detections of CO_2 frost (Fig. 4.S2).

4.2.2. MGS Thermal Emission Spectrometer (TES)

The TES instrument is a Fourier transform Michelson interferometer with a spectral range of 6 to 50 μm, at ~3 km spatial resolution. A detailed description of the TES instrument and associated calibration methods can be found in Christensen et al. (2001).

4.2.2.1. Water Vapor Column Abundance

Nadir, daytime (2 p.m. local solar time) TES spectra can be used to monitor the seasonal dependence and annual distribution of water vapor column abundance in the

atmosphere of Mars (Smith, 2002). A detailed description on the retrieval of water vapor column abundance from TES spectra is given in Smith (2002). Seasonal TES data are derived from nadir-geometry spectra that are binned by 2 degrees in solar longitude (L_s) and 2 degrees in latitude, with all longitudes averaged together. Annually averaged TES data are derived from nadir-geometry spectra that are binned by 5 degrees in L_s, latitude and 7.5 degrees in longitude.

Water vapor column abundance can be used to derive the local partial pressure to get an estimate of the local H_2O frost point, t_{H_2O} (Stull, 2000):

$$t_{H_2O} = \left[\frac{1}{T_o} - \frac{R}{L} ln\left(\frac{PP}{e_o}\right)\right]^{-1} \quad (5)$$

Where T_o is the temperature (273 K) at the triple point vapor pressure e_o (611 Pa), R is the universal gas constant (8.314 J K^{-1} mol^{-1}), L is the latent heat of sublimation (51,058 J mol^{-1}) and PP is the partial pressure of water vapor (in Pa). Assuming a well-mixed, hydrostatic and isothermal atmosphere, the partial pressure PP is given by

$$PP = \frac{gQ_{H_2O}\rho m_{CO_2}}{m_{H_2O}} \frac{1}{1 - exp(-H_C/H_{SC})} \quad (6)$$

Where g is the gravitational acceleration (3.7 m/s^2), Q_{H_2O} is the amount of water vapor (in $pr - \mu m$), m_{CO_2} and m_{H_2O} are the molecular weights of CO_2 (44 g/mol) and H_2O (18 g/mol), with H_c representing the water vapor condensation height (above which it is assumed that there is negligible water vapor; Smith, 2002) derived from TES data and H_{SC} (assumed to be 11 km) is the atmospheric scale height (Schorghofer & Aharonson, 2005). For assessing the seasonal, latitudinal variation of the H_2O frost point, H_c values were used from Smith (2002), whereas for the global, seasonally averaged

data, H_c was set to 25 km, the mean global condensation height (Smith, 2002). Since the vertical distribution of water vapor on Mars is not well known near the surface (Tamppari & Lemmon, 2020), it is difficult to use observations of temperatures at or below the H_2O frost temperature as confirmation for the formation of H_2O frost. Thus, in this work we only present maps of the predicted H_2O frost point.

4.3. Frost Distribution

4.3.1. CO_2 Frost

4.3.1.1. Relation with Topography and Thermal Inertia

CO_2 frost detections are observed at all latitudes (Fig. 2). Outside of the seasonal CO_2 caps (poleward of ~50º in both hemispheres), detections are scattered in the southern hemisphere and more widespread in the north. Near the equator, CO_2 frost detections are present at high elevations in the Tharsis (150–300°E, 50°N–20°S) and Elysium (135–153°E, 14–32°N) regions despite lower predicted CO_2 frost points, likely due to lower downwelling radiance from the reduced amount of atmosphere and atmospheric dust at high elevations (Piqueux et al., 2016).

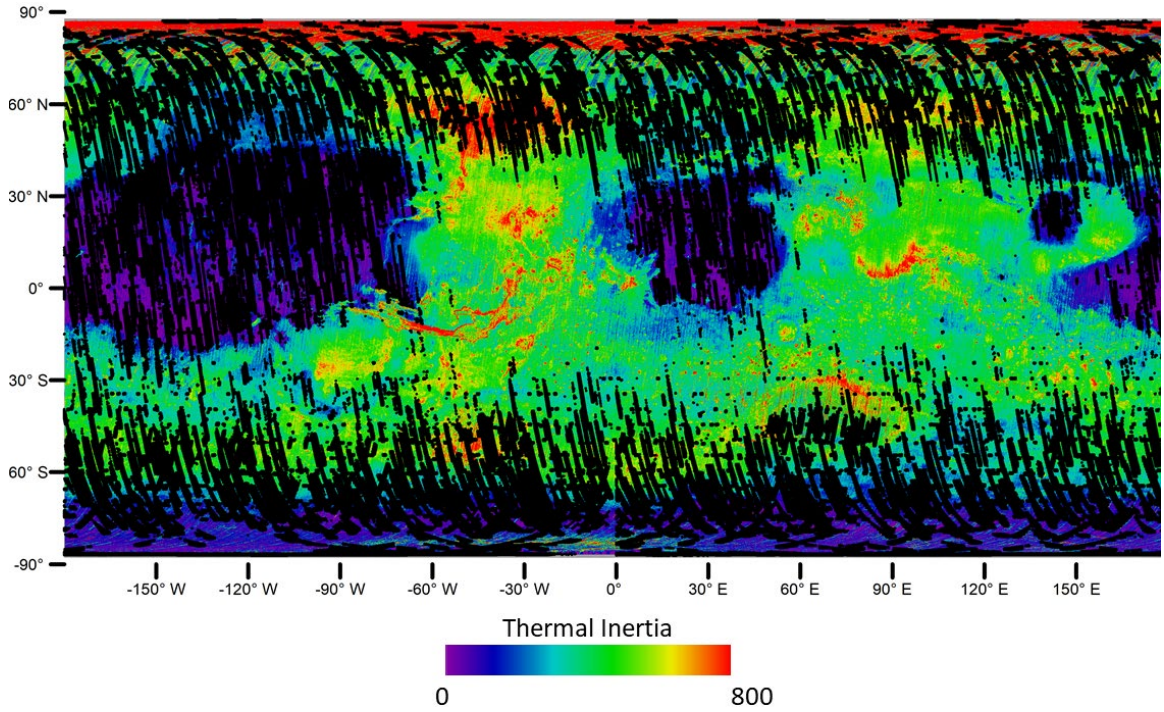

Figure 4.2. CO_2 frost detections from THEMIS in MY 26 (black) overlaid on TES nighttime thermal inertia (Putzig and Mellon, 2007).

Near the equator, consistent with results from previous, coarse resolution thermal data (Piqueux et al., 2016), CO_2 frost detections show an excellent correlation with the dusty, low thermal inertia deposits of Tharsis, Elysium and Arabia Terra (0–60°E, 40°N–10°S). These frosts are likely diurnal, and form during nighttime radiative cooling (Piqueux et al., 2016). At higher latitudes, this trend of frosted low thermal inertia regions disappears, with frost detections increasing in number near the poles, due to the presence of the seasonal CO_2 caps.

4.3.1.2. Seasonal Variation

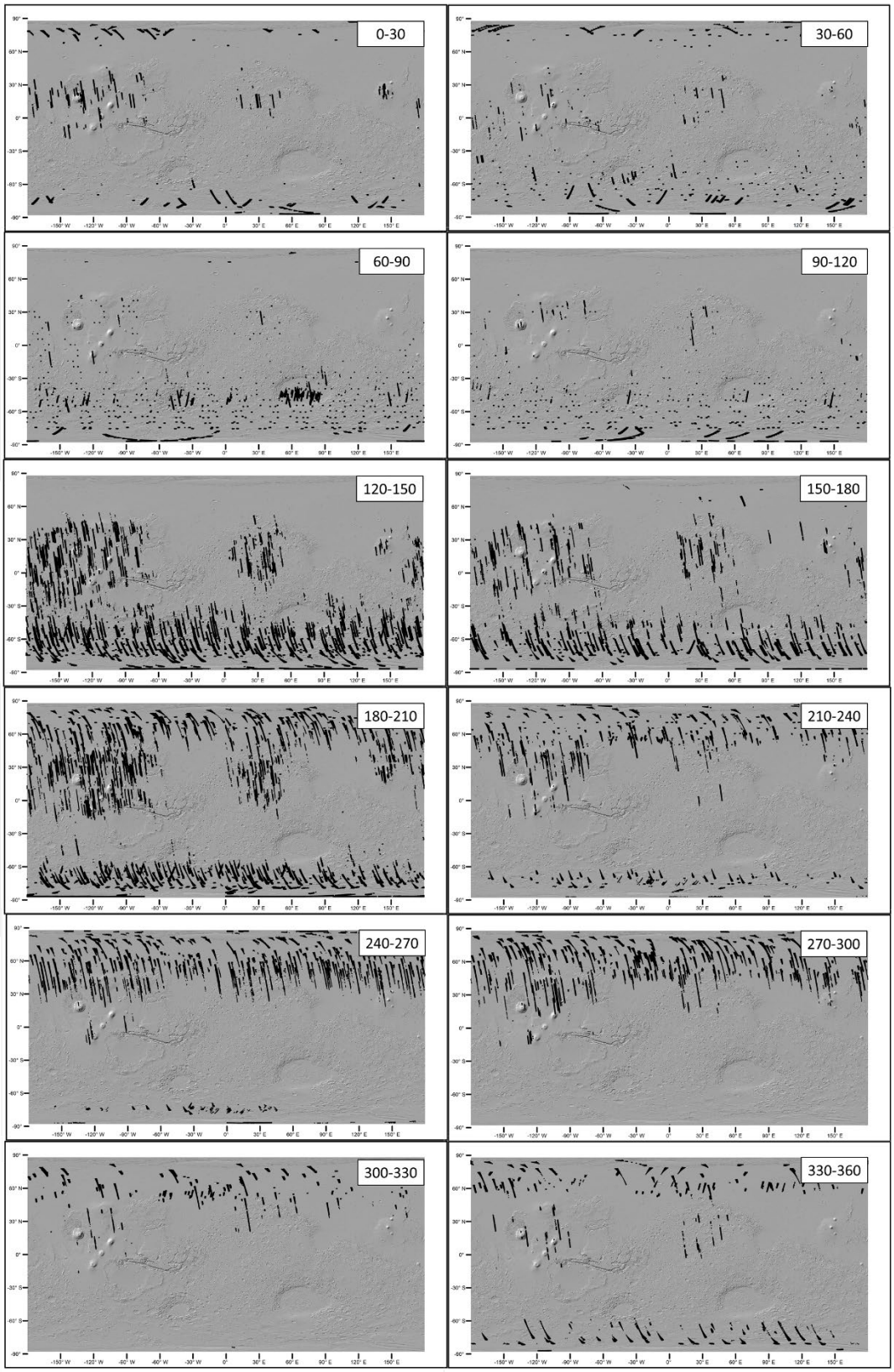
0-30
30-60
60-90
90-120
120-150
150-180
180-210
210-240
240-270
270-300
300-330
330-360

Figure 4.3. The seasonal variation of CO_2 frost detections (black) made by THEMIS in MY 26.

During southern autumn (L_s 0–90), there are scattered CO_2 frost detections likely representing the seasonal cap extending to ~70ºN (Fig. 4.3). The number of detections present in the equatorial dust deposits between L_s 0–30 reduces after L_s 30. In addition, there are scattered detections between ~45ºS and the south pole. During southern winter (L_s 90–180), there are fewer detections in the northern high latitudes. The equatorial dust deposits show the greatest number of detections during this time, and detections poleward of 30ºS are observed after L_s 120. In southern spring (L_s 180–270), similar to the distribution in the northern hemisphere during southern autumn, the seasonal cap is seen extending to ~70ºS, with almost no detections between 70ºS to 15ºS. This seasonal cap begins retreating after L_s 210. Detections are present in the Tharsis deposits but are largely absent in Elysium and Arabia, especially after L_s 210. In southern summer (L_s 270–360), there are a few scattered detections poleward of 70ºS, and within Tharsis in the southern hemisphere. Almost no detections are present between 70ºS and 20ºS. Scattered detections are present in the northern hemisphere, although detections over Elysium and Arabia are absent until L_s 330.

4.3.2. H_2O Frost Point

4.3.2.1. Relation with Topography and Thermal Inertia

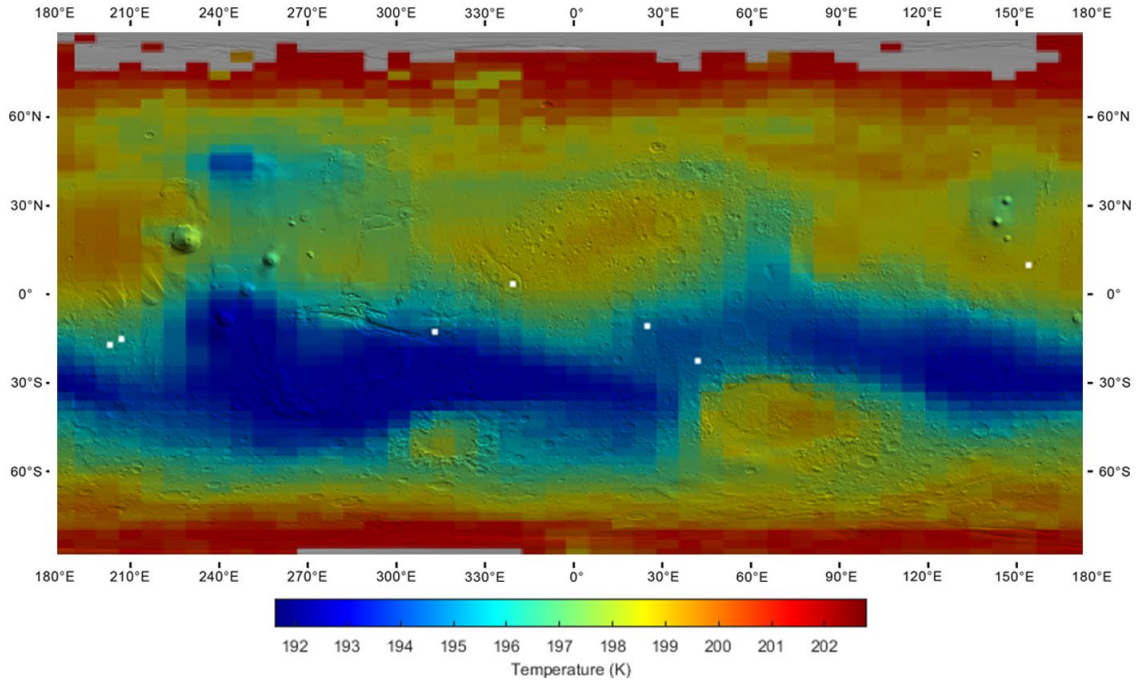

Figure 4.4. Global map of H_2O frost temperature (color) calculated using seasonally averaged TES water vapor column abundance for MY = 26 overlaid on MOLA hillshade topography. Sites of equatorial mass wasting (McEwen et al., 2018) are shown as white squares.

In general, the distribution of the H_2O frost point (Fig. 4.4) follows the distribution of water vapor column abundance, with a relatively weaker dependence on average local surface pressure (Fig. 4.S3). Much of the southern mid-latitudes show a relatively low frost point (~192 K), whereas the Hellas region has a relatively high frost point (~201 K). The frost point temperature shows a strong hemispherical dependence, with the northern hemisphere having a higher derived frost point (in general) than the southern hemisphere. This hemispherical difference is most likely due to differences in average elevation between the two hemispheres that cause variations in water vapor abundance and transport (Jakosky & Farmer, 1982; Bapst et al., 2015).

Surface thermophysics (thermal inertia and albedo) dictate the surface, subsurface and atmospheric temperatures significantly, thereby affecting where water vapor can condense onto the surface. However, unlike the distribution of CO_2 frost detections, there is little to no correlation with surface thermophysical properties. Annually averaged, nighttime TES data (Fig. 4.S3) indicate that temperatures fall below the predicted H_2O frost point almost globally (in accordance with Davies (1979)), but whether condensation occurs in the form of clouds/fogs/snow or surficial frosts cannot be inferred from the data.

4.3.2.2. Seasonal Variation

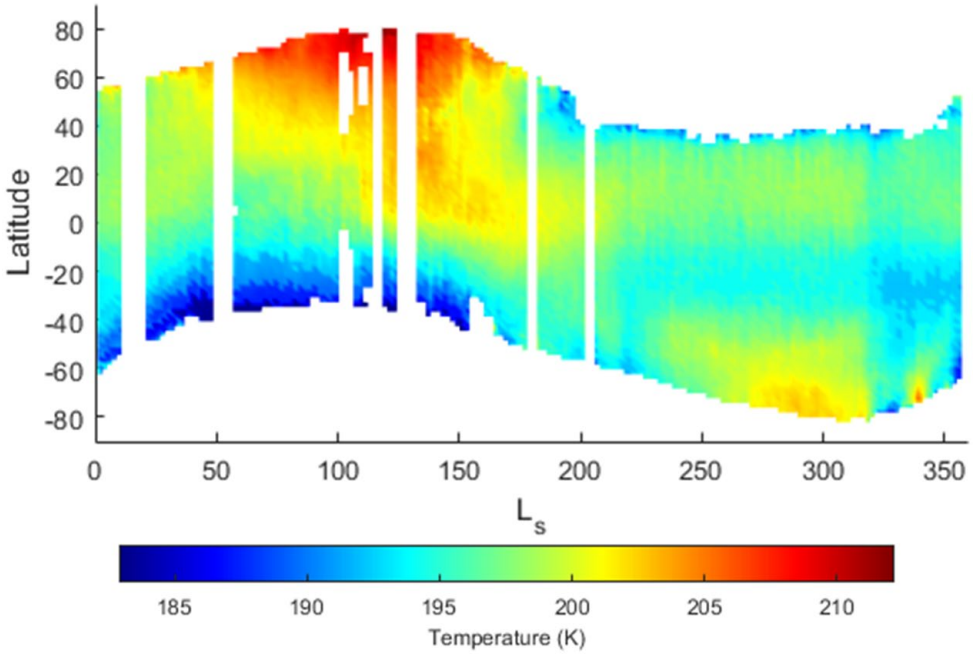

Figure 4.5. Seasonal and latitudinal variation of H_2O frost temperature calculated using TES water vapor column abundance and condensation level data for MY = 26.

The northern latitudes record the highest H_2O frost temperatures on the planet every year, from mid-spring until mid-summer, between $L_S \cong 75$ and $L_S \cong 135$ (Fig. 5).

A corresponding minimum is observed in the southern hemisphere during this time. This pattern is caused by the sublimation of the northern polar cap at ~70ºN and frost formed within the regolith at the mid-latitudes (~50–70ºN) turning into vapor, thereby creating an increase in local water vapor abundance during the northern summer (Jakosky & Farmer, 1982). A similar maximum is observed in the southern hemisphere between $L_S \cong 240$ and $L_S \cong 310$, caused by an increase in vapor abundance from H_2O frost sublimation and hemispherical circulation from north to south (Smith, 2002). These seasonal variations correspond well to the recession of the seasonal CO_2 polar caps (as illustrated in Fig. 4.4), with local maxima in both hemispheres occurring after the removal of overlying CO_2 frost due to increasing surface temperatures. This warming causes H_2O frost to sublime and increase the local H_2O frost temperature (due to higher local vapor abundance). Frost point predictions match well with in-situ measurements made at the Phoenix and Opportunity landing sites. The local H_2O frost point measurement made at the surface (194–209 K) made by the Phoenix lander at 68.2ºN from $L_S = 78$ to $L_S = 148$ match well with temperatures derived from zonally-averaged TES data (Fig. 4.5) despite Phoenix measurements potentially being affected by local water vapor contributions from exposed sublimating ice (Zent et al., 2016). Similarly, H_2O frost observed in-situ at the Opportunity rover from visible data (Landis, 2007) is also matched well with frost point predictions (Fig. 4.S4) made using regional TES data and modeled surface temperatures from KRC, a one-dimensional planetary thermal model (Kieffer, 2013). Frost was detected at 6:15 a.m. local solar time, when modeled temperatures fall below the expected frost point (~195 K, derived from TES data), and disappeared at 9:21 a.m.,

when modeled surface temperatures (~232 K) exceed the frost point. This behavior is expected to occur throughout the year, with temperatures at 6:15 a.m. always falling below the expected frost point.

4.4. Relationship of Frost Observations with Gullies and Equatorial Mass-Wasting

Gully and equatorial mass-wasting sites were compared with frost locations (see Section 4.S3 in the supporting information for more details). While sites of active equatorial mass-wasting (McEwen et al., 2018) lie within regions where H_2O frost temperatures can be attained (Fig. 4.4, 4.S3), it is difficult to quantify their correlation due to the reasons discussed earlier. Thus, we only quantify the distribution of CO_2 frost with gullies, shown in Table 4.1.

Table 4.1. THEMIS CO_2 Frost Detections relative to Gullies

Gully dataset	**Total**	**North**	**South**
All Gullies[a]	47% (2337 of 4978)	17% (88 of 505)	50% (2249 of 4473)
Active Gullies[b]	73% (119 of 162)	25% (2 of 8)	76% (117 of 154)
Active Gullies with VNIR CO_2 Detections[c]	79% (19 of 24)	N/A	79% (19 of 24)

[a]Harrison et al. (2015). [b]Dundas et al. (2019). [c]Vincendon (2015).

Table 4.1 indicates that about half of all gullies (Harrison et al., 2015) overlap with CO_2 frost detections. Active gullies (Dundas et al., 2019) show much a better correlation, with 73% of all active gullies overlapping with CO_2 frost detections, although

only two out of eight active gullies in the northern hemisphere overlap with CO_2 frost detections. Similarly, most active gullies (79%) that were judged to contain CO_2 frost based on VNIR data (Vincendon, 2015) overlap with THEMIS CO_2 frost detections. Thus, 21% of active gullies with VNIR CO_2 frost detections (five out of twenty-four gullies) do not have THEMIS detections, suggesting that THEMIS CO_2 frost detections might miss around 21% of all locations that actually have CO_2 frost, although the sample size is relatively small. Thus, the results in Table 4.1 for all, and active gullies might be underestimates.

There is a notable hemispherical difference between gully frost correlations. For example, regions such as Acidalia Planitia (10–50ºN, 0–60ºW) and portions of Utopia Planitia (30–50ºN, 90–130ºE) host multiple gullies where CO_2 frost is not detected in this study. This difference is likely due to the timing of perihelion, resulting in shorter winters in the northern hemisphere relative to the south, despite the northern and southern mid-latitudes having relatively similar thermophysical properties. The lack of CO_2 frost within these northern gullies is consistent with the hypothesis that northern gullies generally appear more degraded than those in the south (e.g., Heldmann et al., 2007) due to less modification by frost processes under present-day conditions (Dundas et al., 2012).

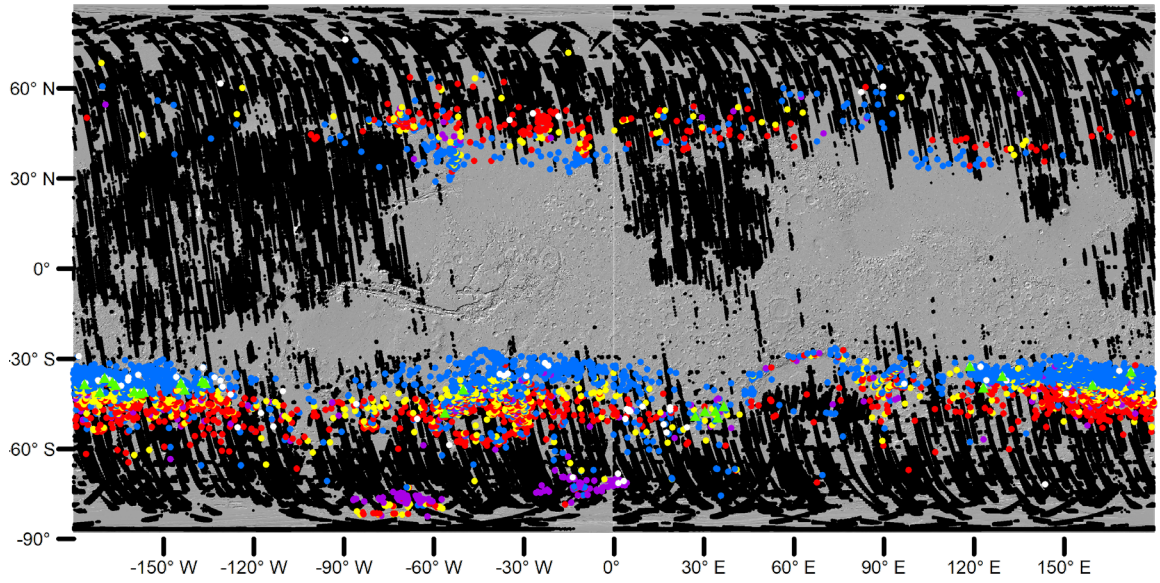

Figure 4.6. CO_2 frost detections from THEMIS in MY 26 (black) with global gully distribution (blue = poleward-facing preference, yellow = east/west, red = equatorward, purple = no preference; Harrison et al., 2015), active gullies (white; Dundas et al., 2019) and active gullies likely to contain CO_2 frost based on VNIR data (green triangles; Vincendon, 2015).

Comparing the global distribution of CO_2 frost detections with gully distribution (Fig. 4.6), it is apparent that although CO_2 frost is likely to form at all latitudes on Mars, gullies are largely restricted to the mid-latitudes. For example, there are no gullies present in the frosted, dusty equatorial regions of Tharsis, Arabia and Elysium. Similarly, the number of gullies poleward of 60º latitude in either hemisphere is relatively small in comparison with the mid-latitudes.

CO_2 frost has been detected at gully locations during various times of day (3–9 a.m./p.m.), primarily due to THEMIS' changing orbit over time, and various frost targeting campaigns (Fig. 4.S5). It is difficult to ascertain whether frosts forming at

night/early morning survive at all gully locations throughout the day, but the good correlation with late afternoon VNIR detections made by Vincendon (2015) suggests that frosts do survive throughout the day at some sites of present-day gully activity.

4.5. Variation of CO_2 Frost Amounts with Latitude and Slope Properties

We used KRC to model the thickness of condensed CO_2 on mid-latitude, pole-facing slopes where most gullies are found through the year (Fig. 4.7). For each latitude, predicted upper and lower limits of CO_2 thicknesses were calculated assuming the density of solid CO_2 to be 1600 kg/m^3. For the upper limit cases, we modeled 15 cm of 350 $J\ m^{-2}\ K^{-1}\ s^{-0.5}$ material over 800 $J\ m^{-2}\ K^{-1}\ s^{-0.5}$ wall rock. For the lower limit cases we modeled 10 cm of 350 $J\ m^{-2}\ K^{-1}\ s^{-0.5}$ material over 1900 $J\ m^{-2}\ K^{-1}\ s^{-0.5}$ H_2O ice ($\sqrt{k\rho c_p} = \sqrt{2.4 \times 917 \times 1650}$ = 1900 $J\ m^{-2}\ K^{-1}\ s^{-0.5}$, assuming pure H_2O ice at 210 K; Williams et al., 2008). The surface albedo was assumed to be 0.2 in all cases. Modeled frost thicknesses range from $<$ 1 mm at 30º S to ~50 cm at 60ºS. At lower latitudes, appreciable frost thicknesses are only attained on steep slopes with slope angles > 20º. Poleward of 50º, frost is predicted to accumulate on equator-facing slopes, even on 10º slopes. These results are consistent with modeled CO_2 thicknesses of ~30 cm found to occur at ~54.5ºS (Pilorget & Forget, 2016) and ~1 m thick CO_2 ice slabs found near the southern pole at ~89ºS (Smith et al., 2001b; Kieffer et al., 2006; Portyankina et al., 2017). Using the 40ºS pole-facing slope with 15 cm of 350 $J\ m^{-2}\ K^{-1}\ s^{-0.5}$ material over 800 $J\ m^{-2}\ K^{-1}\ s^{-0.5}$ wall rock as the base case, we tested the sensitivity of these predictions (Fig. 4.S6). Apart from the slope angles, the two most important parameters are the slope azimuth and the lower material thermal inertia. For example, increasing the lower

material thermal inertia from 450 to 1650 reduces the modeled frost thickness from ~17 cm to almost zero (Fig. 4.S6a). This effect is particularly important for cases where there are gullies eroded into loose regolith that overlies more consolidated material, such as wall rock or H_2O ice. Similarly, appreciable amounts of CO_2 frost only form on pole-facing slopes (180º azimuth) at 40º latitude for the modeled base case (Fig. 4.S6b).

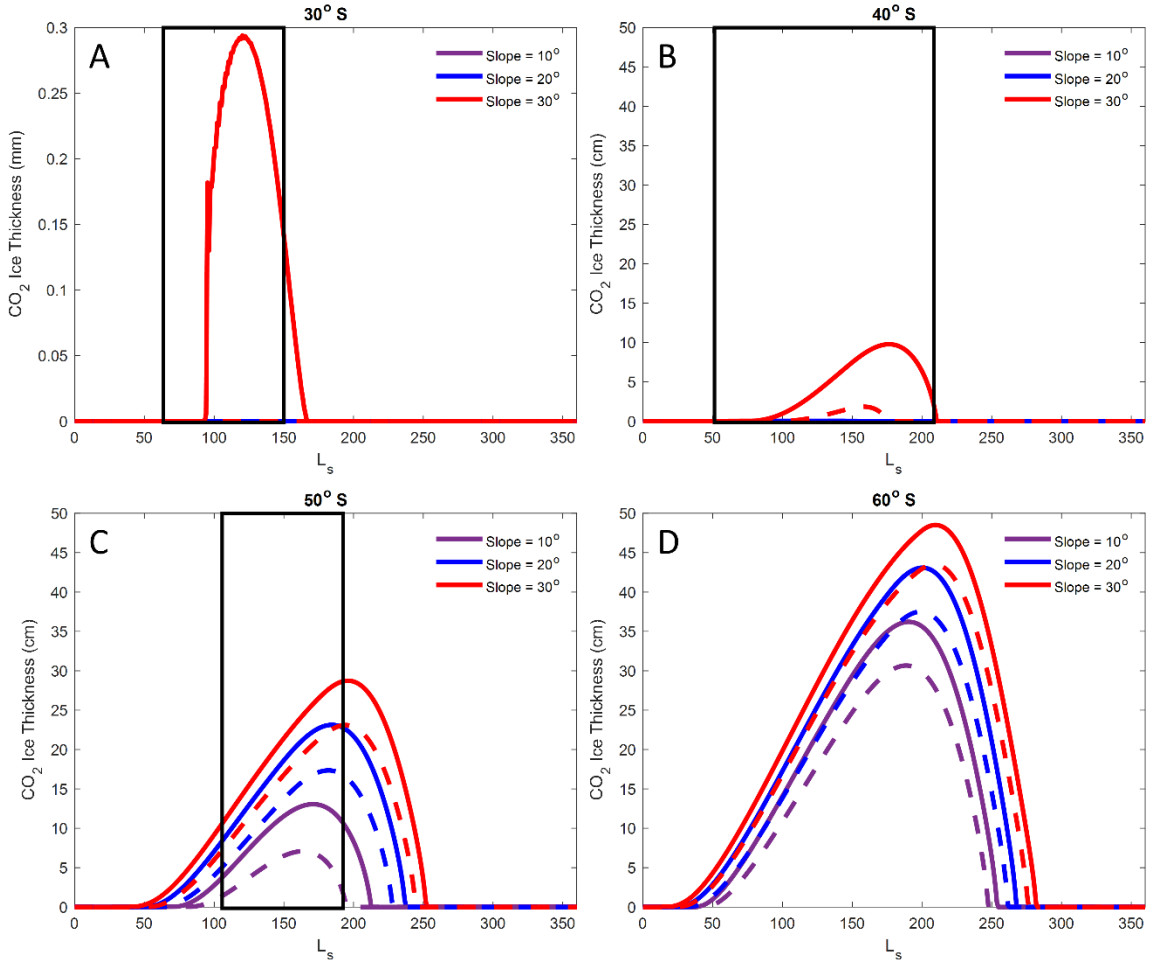

Figure 4.7. Variation of CO_2 frost thickness with latitude and slope angle for pole-facing slopes. calculated using KRC. For each case, predicted upper (solid lines) and lower (dashed lines) limits are shown. Black boxes span approximate ranges of constrained

present-day activity (Dundas et al., 2019). Note the difference in y-axis scale between A and B–D.

Comparisons between the evolution of CO_2 mass and present-day gully activity can also be made. At 30ºS, the seasonal time span of constrained present-day activity (Dundas et al., 2019) almost completely encompasses the time of frost accumulation and ends near late winter as frost amounts drop. Although the seasonal time span of present-day activity increases at 40ºS, activity also ends when frost amounts drop, in the spring. At 50ºS, the seasonal span of present-day activity narrows, but ends close to when peak frost amounts form on pole-facing slopes although frost amounts drop on equator-facing slopes during early spring. These observations suggest that there is a link between frost amounts, the timing of frost disappearance and present-day gully activity.

4.6. Thermophysical Properties of Present-Day Gully Activity Materials

While a variety of 'fluvial' morphological characteristics have been observed and proposed to be linked to frosts (Dundas et al., 2019), most of this current activity seems to have occurred within loose, unconsolidated materials in sandy dunes, or sediments present within existing gully alcoves and fans (Dundas et al., 2010, 2012, 2015). Ripples are present within these present-day gully activity materials, indicative of their unconsolidated nature (e.g., Fig. 4.8).

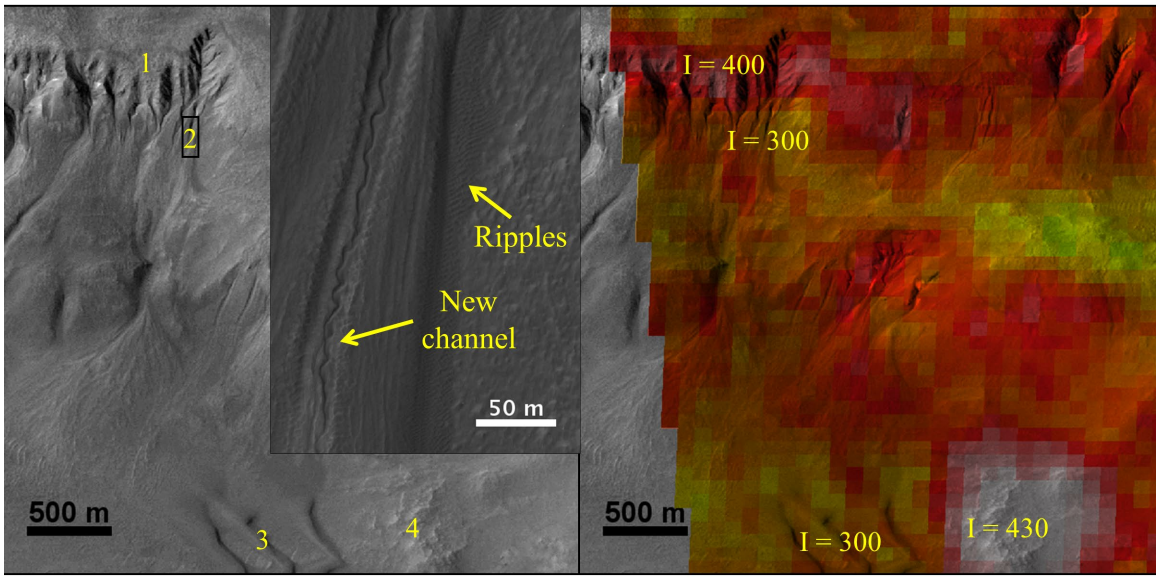

Figure 4.8. Estimated thermal inertia (I) from KRC at location of present-day gully activity at 38.9ºS, 196ºE (Dundas et al., 2019) inferred from THEMIS nighttime image I08114006 overlaid on CTX image J05_046702_1412. Slope geometry at each site (1-4) was obtained from the KRC layer in JMARS. HiRISE image ESP_046702_1410 is inset, showing ripples within new channel materials at site 2.

Figure 4.8 shows that these materials have a derived thermal inertia (I) of ~300 $J\ m^{-2}\ K^{-1}\ s^{-0.5}$ (obtained by fitting nighttime THEMIS data for an albedo of 0.14, dust opacity of 0.3, and derived geometry to KRC output curves run for varying thermal inertias). Assuming that these slope materials are unconsolidated to several diurnal thermal skin depths, then their average particle size is ~1 mm (Presley & Christensen, 1997b; Christensen et al., 2003), corresponding to medium/coarse sand.

4.7. Discussion

4.7.1. CO_2 Frost Distribution and Relation to Gullies

We observe that temperatures conducive to CO_2 frost formation are present at all latitudes (Fig. 4.3), with several factors governing their presence: (1) local surface pressure and its variation with season, (2) surface thermal inertia, (3) solar insolation, and downwelling IR flux variations with latitude and season, (4) atmospheric dust, and ice opacity conditions. Modeling results indicate that the amount of frost increases with latitude (Fig. 4.7), and pole-facing slopes with low-thermal inertia materials are favorable locations for frost formation. Frost formative conditions can be enhanced and persist longer within existing gully topography (i.e., topographically shadowed gully alcoves, channels, etc.), resulting in a positive feedback system between gully activity and frosts (e.g., Harrison et al., 2015). The observation of frosts near and within active gully alcoves (e.g., Dundas et al., 2019) is consistent with these frosts playing a key role in this activity.

Granular, unconsolidated materials (I ~300 $J\ m^{-2}\ K^{-1}\ s^{-0.5}$) found near and within gully alcoves are ideal for a condensation-sublimation process that can destabilize grains and induce downslope movements. This process is illustrated in Figure 9. Interstitial CO_2 gas present in the porous regolith condenses as the grains cool to the local frost point (Fig. 4.9a), typically at night in the upper few microns of regolith (Piqueux et al., 2016). Frost mass builds up while latent heat requirements are satisfied (Fig. 4.9b). During the day, solar heating and downwelling radiation may cause surface temperatures to rise above the frost point; when this occurs, condensed frost sublimates and turns into gas, diffusing back into the atmosphere (Fig. 4.9c). The sublimating gas can dislodge grains and induce sediment transport, especially on slopes (Fig. 4.9d). If diurnal temperatures remain at the frost point over multiple days, the frost will build up, leading

to greater gas flux and increased rates of sediment transport when sublimation occurs. At high latitudes (> ~50º), frosts can anneal to form translucent slabs that can lead to even higher gas flux buildup and debris transport (e.g., Piqueux et al., 2003; Kieffer et al., 2006; Pilorget & Forget, 2016) although most active, non-dune gullies are located at lower latitudes (~30º–40º), where evidence for this basal sublimation process is rare (Dundas et al., 2019).

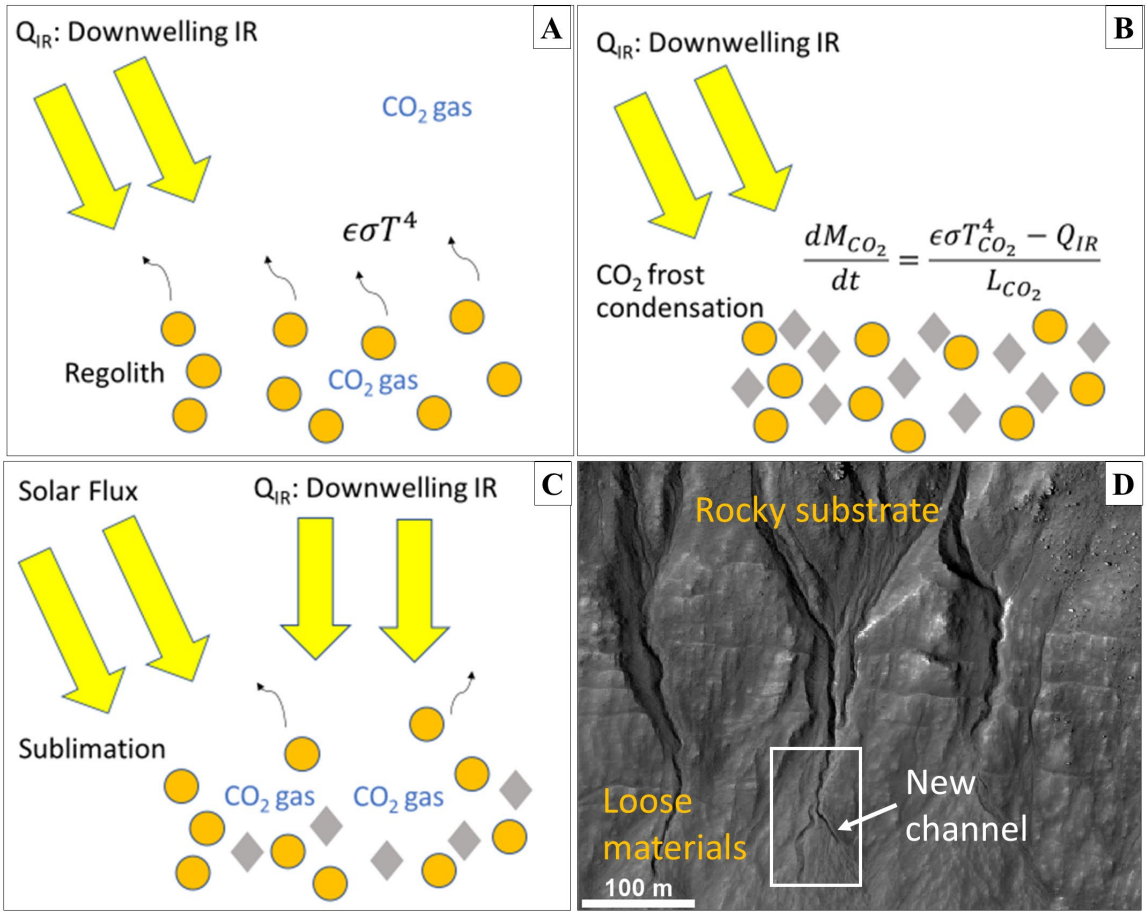

Figure 4.9. The formation and effects of CO_2 frost on gully activity. (A) Nighttime radiative cooling causes the regolith temperature to fall to the CO_2 condensation temperature. (B) Frosts form on, and within the regolith, with frost mass buildup

continuing as long as there is energy input to satisfy latent heat requirements. (C) Solar fluxes can cause rapid heating that leads to frost sublimation, and grains being dislodged and moved. (D) This can lead to downslope movement and present-day channel formation in loose regolith/sediments such as at 37.49ºS, 222.95ºE, adapted from Dundas et al. (2015b). Present-day activity seems to be constrained to loose, unconsolidated materials within, or downslope of gully alcoves eroded into rocky substrates.

Due to the rates and effects of observed present-day gully activity, some authors (e.g., Dundas et al., 2019) argue that CO_2 frost processes could form gullies. If gullies are formed due to frosts, this suggests that areas and latitudes where no gullies are present are caused by a lack of (1) sufficiently steep slopes (e.g., Conway et al., 2019), and/or (2) temperatures and time required to form the necessary amounts of frosts for gully formation. Global crater distribution studies indicate that 1–3 km diameter craters are pervasive across all latitudes (see Fig. 1 in Robbins & Hynek, 2012), so slopes for CO_2 frost processes to erode are likely available without a strong mid-latitudinal preference. Additionally, CO_2 frost detections are observed at all latitudes and do not show the strong mid-latitudinal preference that gullies show. Additionally, while ~50% of gullies in the southern hemisphere overlap with CO_2 frost detections, the same is not true for northern gullies (~20% overlap). Unless CO_2 frost is being missed by THEMIS in the north, the lack of correlation with northern gullies can perhaps be explained if most gullies in the north formed during longer winter seasons (under different obliquity and eccentricity conditions (Dundas et al., 2012; Pilorget & Forget, 2016; Dundas et al., 2019), although this does not fully explain the lack of correlation at other latitudes. Alternatively, this

discrepancy could be caused by the amount of CO_2 frost necessary to produce gully activity, which increases with latitude (Fig. 4.7). Because most constrained present-day gully activity has occurred between 30–40ºS (Dundas et al., 2019), it seems that the optimal amount of frost needed is on the order of a few centimeters per year (Fig. 4.7a and 4.7b), assuming pole-facing slopes with 350 $J\ m^{-2}\ K^{-1}\ s^{-0.5}$ material overlying higher thermal inertia wall rock or H_2O ice.

While CO_2 frost is an excellent candidate for transporting loose materials, it is likely much more difficult for frost to erode the rocky substrates where gullies are located. Eroding these rocky substrates would require sublimating CO_2 gas to diffuse downward into rock. However, the diffusion of sublimating frosts will largely occur upwards into the atmosphere (Blackburn et al., 2010; unless there is a vapor diffusion barrier present, such as an overlying slab of ice/dust; Pilorget & Forget, 2016). Thus, it seems difficult for frost sublimation processes to erode rocky substrates (e.g., Fig. 4.9d). It seems more likely for present-day frosts to only mobilize loose materials within pre-existing gullies cut into rocky substrates, or to form channels within loose, unconsolidated materials such as dunes.

4.7.2. H_2O Frost Distribution and Relation to Gullies and Mass-Wasting

H_2O frost is probably widespread, but is difficult to observe or model due to its relatively small amounts and the lack of knowledge on the vertical distribution of water vapor. However, H_2O frosts have been observed in-situ by the Opportunity rover at 1.95ºS during late winter at L_s = 100 (Landis, 2007), can readily form on cold, pole-facing slopes in the mid-latitudes (Carrozzo et al., 2009; Vincendon et al., 2010a) and

diurnally at equatorial latitudes during the winter (especially in shadowed, sloping facets; Schorghofer et al., 2019).

Spectral detections by Vincendon (2015) of H_2O frosts present at locations of present-day gully activity where CO_2 frosts were absent suggests that H_2O frosts could play a role in this activity. However, it is difficult to ascertain the exact amount and role of H_2O frosts in present-day gully activity.

Nevertheless, numerous examples of recent, dynamic activity have also been documented near the equator, where little to no CO_2 frosts are likely to form. This activity can be in the form of Recurring Slope Lineae (RSL) (e.g., McEwen et al., 2014), slope streaks (e.g., Aharonson et al., 2003) and poorly developed gully-like landforms (e.g., McEwen et al., 2018). While the exact cause for these mass wasting activities remains unclear, it is possible for H_2O frost-triggered activity to play a role in their formation. Although it is difficult for small pockets of exposed H_2O frost on Mars to melt due to the high evaporative rate of H_2O ice (Ingersoll, 1970), the presence of dust can potentially allow for small (~ μm) amounts of melting to occur seasonally at equatorial latitudes (Fig. 4.S7; Farmer, 1976; Kossacki & Markiewicz, 2004) and perhaps trigger mass-wasting events. If H_2O frosts contribute to mass-wasting, they are likely to do so during the warmest times of day/year, and repeat imagery will be needed to constrain this activity.

4.8. Conclusions and Implications for Martian Gullies

Using thermal infrared data, we find that frosts (CO_2 and H_2O) form at all latitudes on Mars, in varying amounts. CO_2 frost is also observed near the equator within

the low thermal inertia dust deposits present at Tharsis, Elysium and Arabia, consistent with previous coarser resolution studies (Piqueux et al., 2016). TES water vapor abundance data indicate that relatively small amounts of H_2O frosts can form at most latitudes during the night, although the lack of knowledge on the near-surface distribution of water vapor means that their presence is difficult to confirm based on observations from orbit.

About half (47%) of all gullies overlap with CO_2 frost detections, although CO_2 frost was not detected over ~80% of all northern gullies. However, validation against VNIR CO_2 frost detections over active gullies (Vincendon, 2015) suggests that THEMIS might miss about 21% of all locations that have CO_2 frost. Thus, it is possible for more gullies to have CO_2 frost than our estimates, although the sample size for this validation is relatively small (twenty-four gullies). Seasonal constraints on gully activity timing, frost presence from visible imagery (e.g., Dundas et al., 2019), spectral data (e.g., Vincendon, 2015) and thermal data (73% of all active gullies overlap with CO_2 frost detections) therefore indicate that it is likely for most present-day activity to be caused by frosts (CO_2, and possibly H_2O). Most of this present-day activity is occurring in the southern hemisphere (e.g., Dundas et al., 2019), and only two out of eight northern hemisphere active gullies overlap with CO_2 frost detections. Small amounts of H_2O/CO_2 frosts might also play a role in equatorial mass-wasting. Based on our modeling results, we predict that the formation of a few centimeters of frost within loose, unconsolidated sediments (I ~300 $J\ m^{-2}\ K^{-1}\ s^{-0.5}$) on relatively steep (< 20º) slopes is necessary for significant present-day gully activity.

However, whether present-day gully activity is representative of gully formation is still open to debate, with details on CO_2 frost-induced gully formation mechanisms remaining unresolved. Despite CO_2 frosts forming at all latitudes, the majority of global CO_2 frost detections do not correlate with gullies. In particular, most gullies are restricted to the mid-latitudes but CO_2 frost detections are found near-globally. This discrepancy between frost locations and gullies could be due to the lack of sufficient amounts of CO_2 frost to mobilize slope material at low latitudes, and/or that CO_2 frost sublimation is not the only factor involved in gully formation. Regardless, it seems difficult for frosts to be able to erode rocky substrates – even considering geologic timescales. Thus, it seems likely that mid-latitude gullies on Mars are probably not formed by one single mechanism, and instead probably depend on a variety of factors: location, topography, season, atmospheric conditions and obliquity period.

4.9. Acknowledgments

The authors would like to thank Deanne Rogers, Mathieu Vincendon and an anonymous reviewer for formal reviews. Mike Smith kindly provided the binned TES data. Kimm Murray, Sylvain Piqueux, Hugh Kieffer, Anmol Lal, Sarah Rogers, Scott Dickenshied, Jon Hill, Jeff Plaut, Jay Serla and Meg Burris provided very helpful feedback and support. ARK acknowledges the support of the Barrett Bidstrup, R. Greeley Scholarships and the NASA Mars Odyssey Project for this work. SD's work was carried out at the Jet Propulsion Laboratory, California Institute of Technology, under a contract with the National Aeronautics and Space Administration.

4.10. Data Availability

The THEMIS, HiRISE, CRISM and CTX data used in this work is accessible through JMARS (https://jmars.asu.edu/). The 1-D numerical model KRC is available at: http://krc.mars.asu.edu. Binned TES data is available from Smith (2019). MOLA elevation and MCS data are available through the Planetary Data System at: http://pds-geosciences.wustl.edu/missions/mgs/megdr.htm and https://pds-atmospheres.nmsu.edu/data_and_services/atmospheres_data/MARS/data_archive.html, respectively. ArcGIS is accessible at: http://desktop.arcgis.com/en/arcmap/. Normalized gully maps can be obtained from Harrison et al. (2015), Vincendon (2015) and Dundas et al. (2019). Results and data are available in Khuller et al. (2020) (repository: https://doi.org/10.5281/zenodo.4446319).

4.11. Supporting Material

Figure 4.S1 illustrates the calculated variation of the local CO_2 frost point derived from surface pressure data at the Viking Lander sites (Hess et al., 1980). Figure 4.S2 shows a comparison of CO_2 frost detections as observed by MCS (Piqueux et al., 2016) and THEMIS. Figure 4.S3 shows annually averaged global maps of surface pressure derived from MOLA elevation data, water vapor column abundance for MY = 26 and nighttime (LST ~2 am) temperatures from Smith (2002). Figure 4.S4 illustrates modelled surface temperatures at the approximate location of Opportunity rover frost image site (Landis, 2007) using KRC. Figure 4.S5 describes the variation of gully THEMIS CO_2 frost detections with latitude and local solar time. Figure 4.S6 shows results of our sensitivity analysis for predicted CO_2 frost thicknesses at 40ºS. Figure 4.S7 shows minimum possible lifetimes of H_2O frosts buried under layers of dust.

4.11.1. Text S1.

Figure 4.S1 that the local CO_2 frost point, calculated by using Clapeyron's law and the local surface pressure oscillates within $\pm$ 2 K per Martian year, consistent with the variation in surface pressure caused by net transport of CO_2 to and from the poles every year. Maxima is attained during southern summer, when the southern cap is retreating, with minima occurring at L_s 150, during which time CO_2 is locked within the southern polar cap. There are variations in local surface pressure (and therefore CO_2 frost point) caused due to local topography, circulation and latitude, but the overall trend remains similar (Hourdin et al., 1993).

4.11.2. Text S2.

Based on the work of Farmer (1976), the survival of a thin layer of H_2O frost buried under dust was analyzed for minimum lifetime conditions (when vapor molecules are immediately and completely convected away). This minimum lifetime τ is given by

$$\tau = W \times \frac{10^{23}}{3}\left(\frac{k_B T_{sat} d}{D_{eff} p_{sat}}\right)$$

where W is the thickness of the H_2O frost, k_B is the Boltzmann constant, d is the thickness of the dust layer, D_{eff} is the effective diffusion coefficient.

For H_2O ice buried under thin layers of dust, diffusion is limited by the overlying dust and is proportional to the porosity of the dust material. Minimum lifetimes for small amounts of H_2O are frost are shown in Fig. 4.S7. For 10 μm of ice under 1 cm of dust, the ice does not melt but can survive for numerous days (with average porosity dust). For a thicker dust layer of 10 cm, the ice can reach melting temperatures for all values of the effective diffusion coefficient, although survival times vary between ~6 minutes to ~417

days. For larger survival times this indicates that the ice can melt and refreeze diurnally depending on the dust temperature for multiple days. A key assumption made for this analysis is that the mass of ice is substantially smaller than the mass of the overlying layer/mixture of dust in order for sufficient energy input to be provided to satisfy latent heat losses and maintain required evaporation rates (Farmer, 1976).

4.11.3. Text S3.

The Harrison et al. (2015) global gully database contains location data for gully clusters. Gully clusters that fall within a crater are represented by the crater center coordinates, along with a crater radius. However, the Dundas et al. (2019) active gully database contains location data for individual gullies, and so does the gully data from Vincendon (2015).

In order to facilitate a uniform comparison with frost temperature data (using the 'intersect' functions of the 'Select by Location' tool in ArcGIS), the following changes were made to the above gully database data:

1. The Harrison et al. (2015) database was used as is, but where gullies were not present in craters (i.e., no radius data was present), a radius of 0.1 km was assumed to cover the gully extent, since that is the standard spatial resolution of THEMIS.
2. The individual gullies from Dundas et al. (2019) and Vincendon (2015) were matched and grouped into gully clusters from the Harrison et al. (2015) database. Thus, the updated databases of Dundas et al. (2019) and Vincendon (2015) also represent clusters of gullies (i.e., multiple gullies present in the same cluster are

eliminated) and each cluster has a radius taken from the updated Harrison et al. (2015) database.

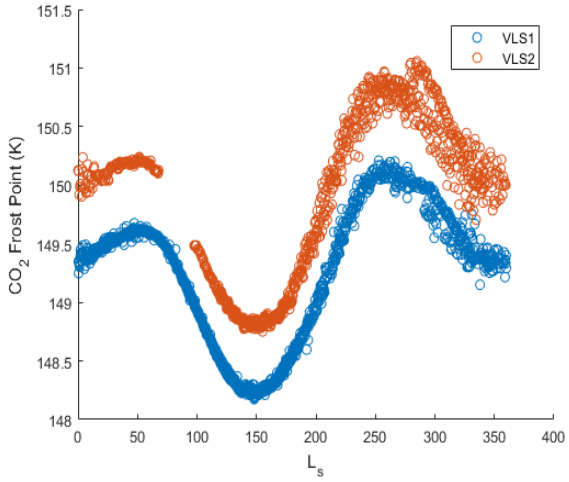

Figure 4.S1. Seasonal Variation of CO_2 frost point at Viking Lander Sites 1 (VLS1) and 2 (VLS2) from Viking Lander pressure data (Hess et al., 1980).

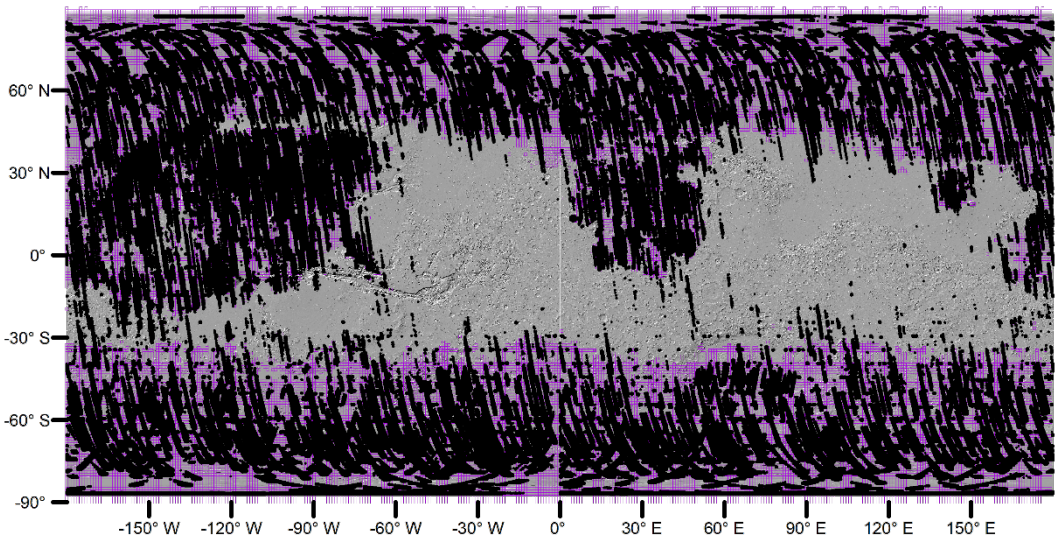

Figure 4.S2. Comparison of CO_2 frost detections as observed by MCS (purple; Piqueux et al., 2016) and THEMIS (black).

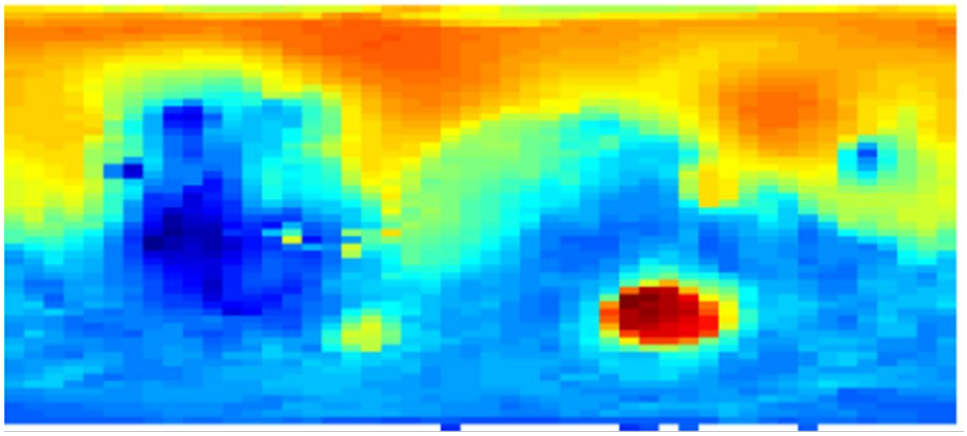

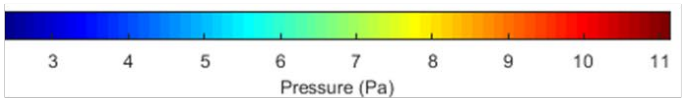
3
4
5
6
7
8
9
10
11
Pressure (Pa)

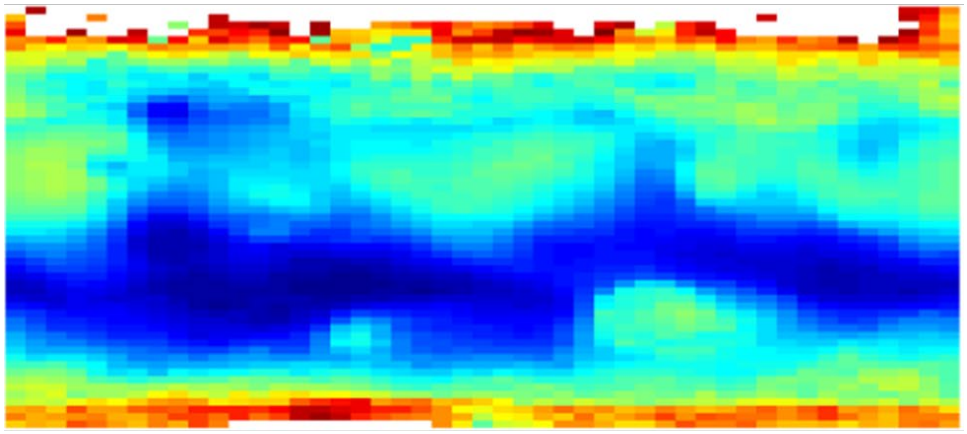

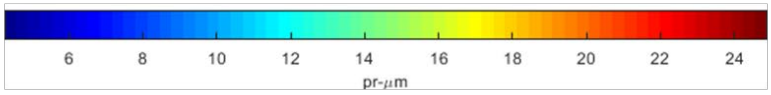
6
8
10
12
14
16
18
20
22
24
pr-μm

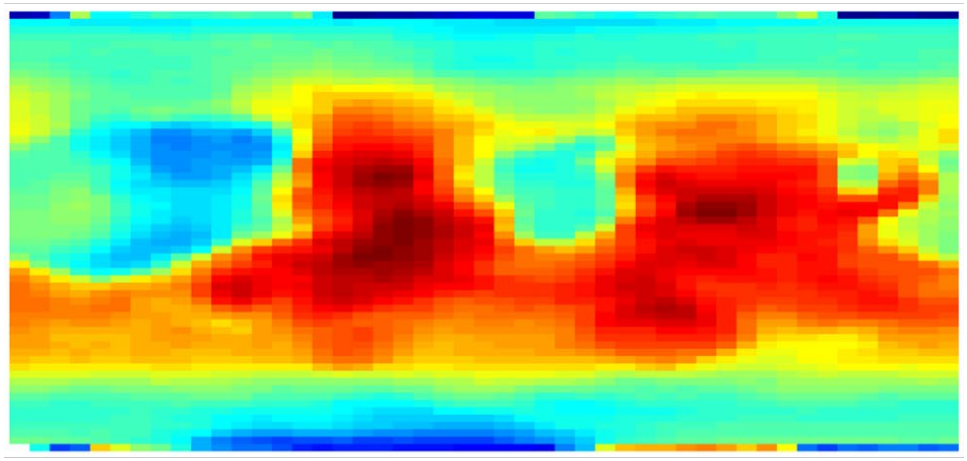

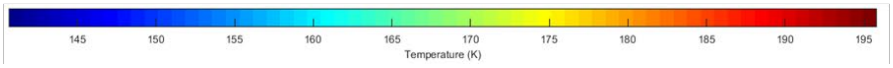
145
150
155
160
165
170
175
180
185
190
195
Temperature (K)

Figure 4.S3. Maps of (top) annually averaged surface pressure derived from MOLA elevation data, (middle) annually averaged water vapor column abundance for MY = 26 and (bottom) annually averaged nighttime (LST ~2 am) temperatures from Smith (2002).

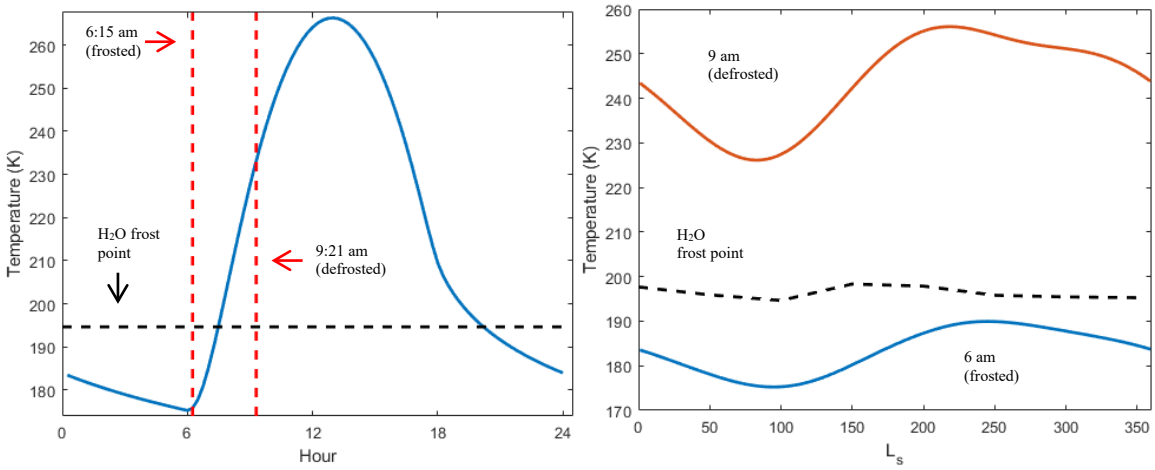

Figure 4.S4. Modelled surface temperatures at approximate location of Opportunity rover frost image site at -1.95ºN, 354.48ºE (Landis, 2007) using KRC. (Left) Diurnal temperature (blue) shown with predicted regional water frost point (black) derived from TES data (Smith, 2002) and visual, in-situ frost observation times (red). (Right) Seasonal variation of temperatures at LST 6 a.m. (blue), 9 a.m. (red) along with smoothed predicted regional water frost point (black) derived from TES data (Smith, 2002). Temperatures are for a surface albedo of 0.15, thermal inertia of 219 $J\ m^{-2}\ K^{-1}\ s^{-0.5}$, with a visible dust opacity of 0.3, slope of 0.04º and an azimuth of 341.56º.

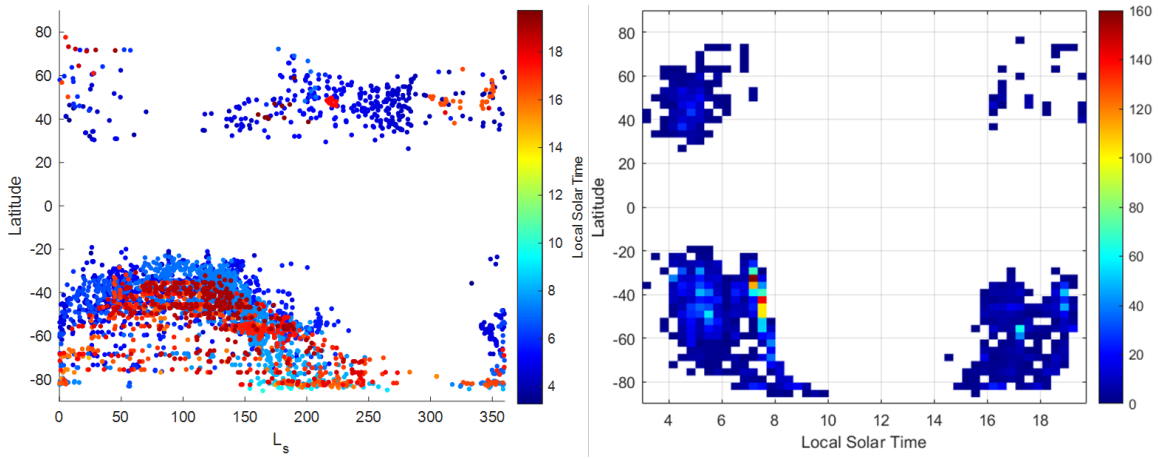

Figure 4.S5. (Left) Local solar time variation of THEMIS CO_2 frost detections over all gullies with respect to solar longitude. (Right) 2D histogram of local solar time variation versus latitude of THEMIS CO_2 frost detections over all gullies. Local solar time and latitude data was binned into bins of 50 values. The dense concentration around 7 a.m. local solar time is because of a recent THEMIS early morning frost monitoring campaign.

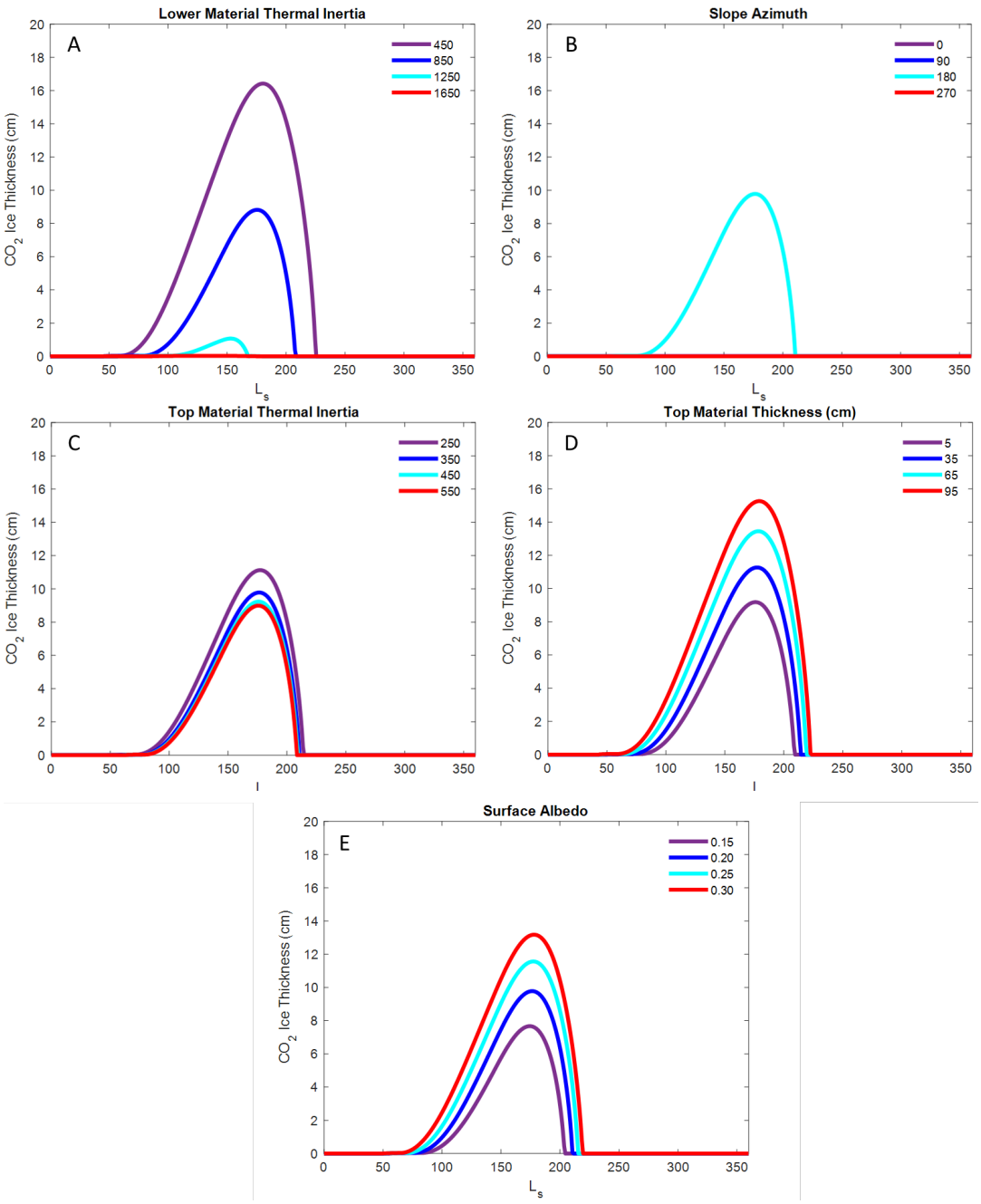

Figure 4.S6. Sensitivity analysis of modeled CO_2 frost thicknesses at 40ºS latitude for variations in A) lower material thermal inertia, B) slope azimuth, C) top material thermal inertia, D) top material thickness and E) surface albedo. A pole-facing slope with 15 cm

of 350 $J\ m^{-2}\ K^{-1}\ s^{-0.5}$ material over 800 $J\ m^{-2}\ K^{-1}\ s^{-0.5}$ wall rock was used as the base case for this analysis.

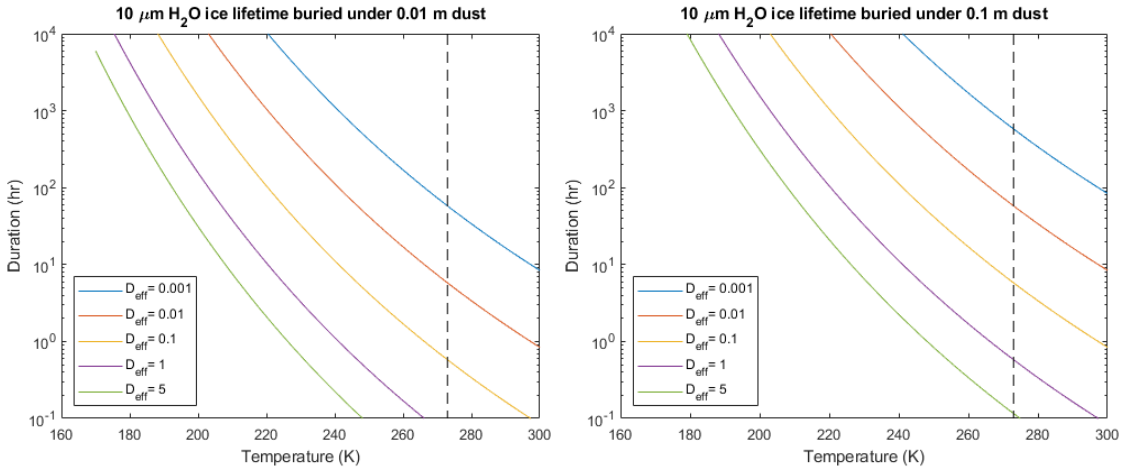

Figure 4.S7. H_2O frost lifetime buried under (left) 0.01 m, and (right) 0.1 m dust for different values of the effective diffusion coefficient, based on Farmer (1976). Values smaller than 1 represent diffusion through low porosity dust, values near ~5 are expected to be more common (Hudson et al., 2007). The vertical dashed line represents the triple point temperature of H_2O, above which melting can be possible (depending on the local partial pressure).

REFERENCES

Aharonson, O., Schorghofer, N., & Gerstell, M. F. (2003). Slope streak formation and dust deposition rates on Mars. *Journal of Geophysical Research: Planets, 108*(E12). https://doi.org/10.1029/2003JE002123

Bapst, J., Bandfield, J. L., & Wood, S. E. (2015). Hemispheric asymmetry in martian seasonal surface water ice from MGS TES. *Icarus, 260*, 396-408. https://doi.org/10.1016/j.icarus.2015.07.025

Bibring, J.-P., Langevin, Y., Gendrin, A., Gondet, B., Poulet, F., Berthe, M., et al. (2005). Mars Surface Diversity as Revealed by the OMEGA/Mars Express Observations. *Science, 307*, 1576-1581.

Blackburn, D. G., Bryson, K. L., Chevrier, V. F., Roe, L. A., & White, K. F. (2010). Sublimation kinetics of CO2 ice on Mars. *Planetary and Space Science, 58*(5), 780-791.

Cao, C., & Shao, X. (2013). Planck Calculator for Infrared Remote Sensing. Retrieved from https://ncc.nesdis.noaa.gov/data/planck.html

Carrozzo, F., Bellucci, G., Altieri, F., D'aversa, E., & Bibring, J.-P. (2009). Mapping of water frost and ice at low latitudes on Mars. *Icarus, 203*(2), 406-420.

Cedillo-Flores, Y., Treiman, A. H., Lasue, J., & Clifford, S. M. (2011). CO2 gas fluidization in the initiation and formation of Martian polar gullies. *Geophysical Research Letters, 38*(21). https://doi.org/10.1029/2011GL049403

Christensen, P. R. (2003). Formation of recent Martian gullies through melting of extensive water-rich snow deposits. *Nature, 422*(6927), 45.

Christensen, P. R., Bandfield, J. L., Bell III, J. F., Gorelick, N., Hamilton, V. E., Ivanov, A., et al. (2003). Morphology and composition of the surface of Mars: Mars Odyssey THEMIS results. *Science, 300*(5628), 2056-2061.

Christensen, P. R., Bandfield, J. L., Hamilton, V. E., Ruff, S. W., Kieffer, H. H., Titus, T. N., et al. (2001). Mars Global Surveyor Thermal Emission Spectrometer experiment: Investigation description and surface science results. *J. Geophys. Res., 106*, 23,823-823,871. https://doi.org/10.1029/2000JE001370

Christensen, P. R., Engle, E., Anwar, S., Dickenshied, S., Noss, D., Gorelick, N., & Weiss-Malik, M. (2009). JMARS - A Planetary GIS. *AGU 2009 Fall Meeting, abstract id.IN22A-06*.

Christensen, P. R., Jakosky, B. M., Kieffer, H. H., Malin, M. C., McSween, H. Y., Nealson, K., et al. (2004). The Thermal Emission Imaging System (THEMIS) for the Mars 2001 Odyssey Mission. *Space Science Reviews, 110*(1-2), 85-130.

Conway, S., Harrison, T., Soare, R., Britton, A., & Steele, L. (2019). New slope-normalized global gully density and orientation maps for Mars. *Geological Society, London, Special Publications, 467*(1), 187-197.

Costard, F., Forget, F., Mangold, N., & Peulvast, J. P. (2002). Formation of recent martian debris flows by melting of near-surface ground ice at high obliquity. *Science, 295*(5552), 110. 10.1126/science.1066698

Cull, S., Arvidson, R., Morris, R., Wolff, M., Mellon, M., & Lemmon, M. (2010). Seasonal ice cycle at the Mars Phoenix landing site: 2. Postlanding CRISM and ground observations. *Journal of Geophysical Research: Planets, 115*(E5). https://doi.org/10.1029/2009JE003410

Cushing, G. E., & Titus, T. N. (2008). MGS-TES thermal inertia study of the Arsia Mons Caldera. *Journal of Geophysical Research: Planets, 113*(E6). https://doi.org/10.1029/2007JE002910

Davies, D. W. (1979). The relative humidity of Mars' atmosphere. *J. Geophys. Res., 84*, 8335-8340. https://doi.org/10.1029/JB084iB14p08335

Diniega, S., Byrne, S., Bridges, N. T., Dundas, C. M., & McEwen, A. S. (2010). Seasonality of present-day Martian dune-gully activity. *Geology, 38*(11), 1047-1050.

Diniega, S., Widmer, J., Hansen, C., & Portyankina, G. (2018). Present-Day (and Amazonian) Frost-Driven Geomorphic Changes on Martian Sandy Slopes. *LPI Contributions, 2086*.

Dundas, C. M., Diniega, S., Hansen, C. J., Byrne, S., & McEwen, A. S. (2012). Seasonal activity and morphological changes in Martian gullies. *Icarus, 220*(1), 124-143.

Dundas, C. M., Diniega, S., & McEwen, A. S. (2015). Long-term monitoring of martian gully formation and evolution with MRO/HiRISE. *Icarus, 251*, 244-263.

Dundas, C. M., McEwen, A. S., Diniega, S., Byrne, S., & Martinez-Alonso, S. (2010). New and recent gully activity on Mars as seen by HiRISE. *Geophysical Research Letters, 37*(7). https://doi.org/10.1029/2009GL041351

Dundas, C. M., McEwen, A. S., Diniega, S., Hansen, C. J., Byrne, S., & McElwaine, J. N. (2019). The formation of gullies on Mars today. *Geological Society, London, Special Publications, 467*(1), 67-94.

Farmer, C. B. (1976). Liquid water on Mars. *Icarus, 28*(2), 279-289.

Farmer, C. B., Davies, D. W., & LaPorte, D. D. (1976). Mars: Northern summer ice cap—Water vapor observations from Viking 2. *Science, 194*(4271), 1339-1341.

Forget, F., Pilorget, C., Pottier, A., & Meslin, P. (2016). *Deep incision of the Latitude Dependent Mantle in Martian gullies formed by CO2 sublimation processes.* Paper presented at the Workshop on Martian Gullies and their Earth Analogs, London, U.K.

Gaidos, E. J. (2001). Cryovolcanism and the recent flow of liquid water on Mars. *Icarus, 153*(1), 218-223.

Gilmore, M. S., & Phillips, E. L. (2002). Role of aquicludes in formation of Martian gullies. *Geology, 30*(12), 1107-1110.

Harrison, T. N., Malin, M., & Edgett, K. (2009). *Present-day gully activity observed by the Mars Reconnaissance Orbiter (MRO) Context Camera (CTX).* Paper presented at the AAS/Division for Planetary Sciences Meeting Abstracts# 41.

Harrison, T. N., Osinski, G. R., Tornabene, L. L., & Jones, E. (2015). Global documentation of gullies with the Mars Reconnaissance Orbiter Context Camera and implications for their formation. *Icarus, 252*, 236-254.

Hart, H. M., & Jakosky, B. M. (1986). Composition and stability of the condensate observed at the Viking Lander 2 site on Mars. *Icarus, 66*(1), 134-142.

Heldmann, J. L., Carlsson, E., Johansson, H., Mellon, M. T., & Toon, O. B. (2007). Observations of Martian gullies and constraints on potential formation mechanisms: II. The northern hemisphere. *Icarus, 188*(2), 324-344.

Hess, S., Ryan, J., Tillman, J., Henry, R., & Leovy, C. (1980). The annual cycle of pressure on Mars measured by Viking Landers 1 and 2. *Geophysical Research Letters, 7*(3), 197-200. https://doi.org/10.1029/GL007i003p00197

Hoffman, N. (2002). Active Polar Gullies on Mars and the Role of Carbon Dioxide. *Astrobiology, 2*(3), 313-323. 10.1089/153110702762027899

Hourdin, F., Le Van, P., Forget, F., & Talagrand, O. (1993). Meteorological variability and the annual surface pressure cycle on Mars. *J. Atmos. Sci., 50*(21), 3625-3640.

Hudson, T. L., Aharonson, O., Schorghofer, N., Farmer, C. B., Hecht, M. H., & Bridges, N. T. (2007). Water vapor diffusion in Mars subsurface environments. *Journal of Geophysical Research: Planets, 112*(E5). https://doi.org/10.1029/2006JE002815

Hugenholtz, C. H. (2008). Frosted granular flow: A new hypothesis for mass wasting in martian gullies. *Icarus, 197*(1), 65-72.

Ingersoll, A. P. (1970). Mars: Occurrence of liquid water. *Science, 168*(3934), 972-973.

Jakosky, B. M., & Carr, M. A. (1985). Possible precipitation of ice at low latitudes of Mars during periods of high obliquity. *Nature, 315*, 559-561.

Jakosky, B. M., & Farmer, C. B. (1982). The seasonal and global behavior of water vapor in the Mars atmosphere: Complete global results of the Viking atmospheric water detector experiment. *Journal of Geophysical Research: Solid Earth, 87*(B4), 2999-3019. https://doi.org/10.1029/JB087iB04p02999

Khuller, A. R., Christensen, P. R., Harrison, T. N., & Diniega, S. (2020). *Repository: The Distribution of Frosts on Mars: Links to Present-Day Gully Activity*. Retrieved from: https://doi.org/10.5281/zenodo.4446319

Kieffer, H. H. (1968). *Near infrared spectral reflectance of simulated Martian frosts.* (Doctoral dissertation), California Institute of Technology, Pasadena, CA. Retrieved from https://thesis.library.caltech.edu/2906/

Kieffer, H. H. (1979). Mars south polar spring and summer temperatures: A residual CO2 frost. *J. Geophys. Res., 84*, 8263-8289. https://doi.org/10.1029/JB084iB14p08263

Kieffer, H. H. (2013). Thermal model for analysis of Mars infrared mapping. *Journal of Geophysical Research: Planets, 118*(3), 451-470. https://doi.org/10.1029/2012JE004164

Kieffer, H. H., Christensen, P. R., & Titus, T. N. (2006). CO2 jets formed by sublimation beneath translucent slab ice in Mars' seasonal south polar ice cap. *Nature, 442*(7104), 793.

Kieffer, H. H., Martin, T. Z., Peterfreund, A. R., Jakosky, B. M., Miner, E. D., & Palluconi, F. D. (1977). Thermal and albedo mapping of Mars during the Viking primary mission. *J. Geophys. Res., 82*, 4249-4292. https://doi.org/10.1029/JS082i028p04249

Kieffer, H. H., S.C. Chase, J., Martin, T. Z., Miner, E. D., & Palluconi, F. D. (1976). Martian North Pole summer temperatures: Dirty water ice. *Science, 194*, 1341-1344.

Kolb, K. J., Pelletier, J. D., & McEwen, A. S. (2010). Modeling the formation of bright slope deposits associated with gullies in Hale Crater, Mars: Implications for recent liquid water. *Icarus, 205*(1), 113-137.

Kossacki, K. J., & Markiewicz, W. J. (2004). Seasonal melting of surface water ice condensing in martian gullies. *Icarus, 171*(2), 272-283. 10.1016/j.icarus.2004.05.018

Landis, G. (2007). *Observation of frost at the equator of Mars by the Opportunity rover.* Paper presented at the Lunar and Planetary Science Conference, League City, Texas.

Lemmon, M. T., Wolff, M. J., Smith, M. D., Clancy, R. T., Banfield, D., Landis, G. A., et al. (2004). Atmospheric imaging results from the Mars Exploration Rovers: Spirit and Opportunity. *Science, 306*, 1753-1756.

Malin, M., & Edgett, K. S. (2001). Mars global surveyor Mars orbiter camera: interplanetary cruise through primary mission. *Journal of Geophysical Research: Planets, 106*(E10), 23429-23570. https://doi.org/10.1029/2000JE001455

Malin, M. C., Bell III, J. F., Cantor, B. A., Caplinger, M. A., Calvin, W. M., Clancy, R. T., et al. (2007). Context Camera Investigation on board the Mars Reconnaissance Orbiter. *Journal of Geophysical Research: Planets, 112*(E5). https://doi.org/10.1029/2006JE002808

Malin, M. C., & Edgett, K. S. (2000). Evidence for recent groundwater seepage and surface runoff on Mars. *Science, 288*, 2330-2335.

Malin, M. C., Edgett, K. S., Posiolova, L. V., McColley, S. M., & Dobrea, E. Z. N. (2006). Present-day impact cratering rate and contemporary gully activity on Mars. *Science, 314*(5805), 1573-1577.

McCleese, D., Schofield, J., Taylor, F., Calcutt, S., Foote, M., Kass, D., et al. (2007). Mars Climate Sounder: An investigation of thermal and water vapor structure, dust and condensate distributions in the atmosphere, and energy balance of the polar regions. *Journal of Geophysical Research: Planets, 112*(E5). https://doi.org/10.1029/2006JE002790

McEwen, A. S., Dundas, C. M., Mattson, S. S., Toigo, A. D., Ojha, L., Wray, J. J., et al. (2014). Recurring slope lineae in equatorial regions of Mars. *Nature Geoscience, 7*(1), 53.

McEwen, A. S., Thomas, M., & Dundas, C. M. (2018). *Active gullies and mass wasting on equatorial Mars.* Paper presented at the European Planetary Science Congress.

Mellon, M. T., & Phillips, R. J. (2001). Recent gullies on Mars and the source of liquid water. *Journal of Geophysical Research: Planets, 106*(E10), 23165-23179. https://doi.org/10.1029/2000JE001424

Millour, E., Forget, F., Spiga, A., Vals, M., Zakharov, V., Montabone, L., et al. (2018). The Mars Climate Database (version 5.3). *From Mars Express to ExoMars*.

Murchie, S., Arvidson, R., Bedini, P., Beisser, K., Bibring, J.-P., Bishop, J. L., et al. (2007). Compact Reconnaissance Imaging Spectrometer for Mars (CRISM) on Mars Reconnaissance Orbiter (MRO). *Journal of Geophysical Research, 112*(E05S03). https://doi.org/10.1029/2006JE002682

Musselwhite, D. S., Swindle, T. D., & Lunine, J. I. (2001). Liquid CO2 breakout and the formation of recent small gullies on Mars. *Geophysical Research Letters, 28*(7), 1283-1285. 10.1029/2000GL012496

Pelletier, J. D., Kolb, K. J., McEwen, A. S., & Kirk, R. L. (2008). Recent bright gully deposits on Mars: Wet or dry flow? *Geology, 36*(3), 211-214.

Pilorget, C., & Forget, F. (2016). Formation of gullies on Mars by debris flows triggered by CO 2 sublimation. *Nature Geoscience, 9*(1), 65.

Piqueux, S., Byrne, S., & Richardson, M. I. (2003). Sublimation of Mars's southern seasonal CO2 ice cap and the formation of spiders. *Journal of Geophysical Research: Planets, 108*(E8). https://doi.org/10.1029/2002JE002007

Piqueux, S., Kleinböhl, A., Hayne, P. O., Heavens, N. G., Kass, D. M., McCleese, D. J., et al. (2016). Discovery of a widespread low-latitude diurnal CO2 frost cycle on Mars. *Journal of Geophysical Research: Planets, 121*(7), 1174-1189. https://doi.org/10.1002/2016JE005034

Piqueux, S., Kleinböhl, A., Hayne, P. O., Kass, D. M., Schofield, J. T., & McCleese, D. J. (2015). Variability of the Martian seasonal CO2 cap extent over eight Mars Years. *Icarus, 251*, 164-180.

Portyankina, G., Hansen, C. J., & Aye, K.-M. (2017). Present-day erosion of Martian polar terrain by the seasonal CO2 jets. *Icarus, 282*, 93-103.

Presley, M. A., & Christensen, P. R. (1997). Thermal conductivity measurements of particulate materials, Part II: Results. *J. Geophys. Res., 102*, 6651-6566. https://doi.org/10.1029/96JE03303

Robbins, S. J., & Hynek, B. M. (2012). A new global database of Mars impact craters≥ 1 km: 2. Global crater properties and regional variations of the simple-to-complex transition diameter. *Journal of Geophysical Research: Planets, 117*(E6). https://doi.org/10.1029/2011JE003967

Ryan, J., & Sharman, R. (1981). H2O frost point detection on Mars? *Journal of Geophysical Research: Oceans, 86*(C1), 503-511. https://doi.org/10.1029/JC086iC01p00503

Ryan, J., Sharman, R., & Lucich, R. (1982). Mars water vapor, near-surface. *Journal of Geophysical Research: Oceans, 87*(C9), 7279-7284. https://doi.org/10.1029/JC087iC09p07279

Schorghofer, N., & Aharonson, O. (2005). Stability and exchange of subsurface ice on Mars. *Journal of Geophysical Research: Planets, 110*(E5). https://doi.org/10.1029/2004JE002350

Schorghofer, N., & Edgett, K. S. (2006). Seasonal surface frost at low latitudes on Mars. *Icarus, 180*(2), 321-334.

Schorghofer, N., Levy, J., & Goudge, T. (2019). High-Resolution Thermal Environment of Recurring Slope Lineae in Palikir Crater, Mars, and Its Implications for Volatiles. *Journal of Geophysical Research: Planets*. https://doi.org/10.1029/2019JE006083

Shinbrot, T., Duong, N.-H., Kwan, L., & Alvarez, M. M. (2004). Dry granular flows can generate surface features resembling those seen in Martian gullies. *Proceedings of the National Academy of Sciences, 101*(23), 8542-8546.

Smith, D. E., Zuber, M. T., & Neumann, G. A. (2001). Seasonal variations of snow depth on Mars. *Science, 294*(5549), 2141-2146.

Smith, D. E., Zuber, M. T., Solomon, S. C., Phillips, R. J., Head, J. W., Garvin, J. B., et al. (1999). The global topography of Mars and implications for surface evolution. *Science, 284*(5419), 1495-1503.

Smith, M. D. (2002). The annual cycle of water vapor on Mars as observed by the Thermal Emission Spectrometer. *Journal of Geophysical Research: Planets, 107*(E11), 25-21-25-19. https://doi.org/10.1029/2001JE001522

Smith, M. D. (2009). THEMIS observations of Mars aerosol optical depth from 2002–2008. *Icarus, 202*(2), 444-452.

Smith, M. D. (2019). *THEMIS observations during MY 33 and 34*. Retrieved from: https://data.mendeley.com/datasets/8sv44gs4k5/2

Spiga, A., Hinson, D. P., Madeleine, J.-B., Navarro, T., Millour, E., Forget, F., & Montmessin, F. (2017). Snow precipitation on Mars driven by cloud-induced night-time convection. *Nature Geoscience, 10*(9), 652-657.

Stull, R. (2000). *Meteorology for scientists and engineers*: Brooks/Cole.

Svitek, T., & Murray, B. (1990). Winter frost at Viking Lander 2 site. *Journal of Geophysical Research: Solid Earth, 95*(B2), 1495-1510. https://doi.org/10.1029/JB095iB02p01495

Tamppari, L. K., & Lemmon, M. T. (2020). Near-surface atmospheric water vapor enhancement at the Mars Phoenix lander site. *Icarus*, 113624.

Titus, T. N., & Cushing, G. E. (2014). The Mars Diurnal CO2 Cycle as Observed in the Tharsis Region. *AGUFM, 2014*, P51C-3957.

Treiman, A. H. (2003). Geologic settings of Martian gullies: Implications for their origins. *Journal of Geophysical Research: Planets, 108*(E4). https://doi.org/10.1029/2002JE001900

Vincendon, M. (2015). Identification of Mars gully activity types associated with ice composition. *Journal of Geophysical Research: Planets, 120*(11), 1859-1879. https://doi.org/10.1002/2015JE004909

Vincendon, M., Forget, F., & Mustard, J. (2010a). Water ice at low to midlatitudes on Mars. *Journal of Geophysical Research: Planets, 115*(E10). https://doi.org/10.1029/2010JE003584

Vincendon, M., Mustard, J., Forget, F., Kreslavsky, M., Spiga, A., Murchie, S., & Bibring, J. P. (2010b). Near-tropical subsurface ice on Mars. *Geophysical Research Letters, 37*(1). https://doi.org/10.1029/2009GL041426

Viviano-Beck, C. E., Seelos, F. P., Murchie, S. L., Kahn, E. G., Seelos, K. D., Taylor, H. W., et al. (2014). Revised CRISM spectral parameters and summary products based on the currently detected mineral diversity on Mars. *Journal of Geophysical Research: Planets, 119*(6), 1403-1431. https://doi.org/10.1002/2014JE004627

Whiteway, J., Komguem, L., Dickinson, C., Cook, C., Illnicki, M., Seabrook, J., et al. (2009). Mars water-ice clouds and precipitation. *Science, 325*(5936), 68-70.

Williams, K. E., Toon, O. B., Heldmann, J. L., McKay, C., & Mellon, M. T. (2008). Stability of mid-latitude snowpacks on Mars. *Icarus, 196*(2), 565-577. 10.1016/j.icarus.2008.03.017

Zent, A., Hecht, M., Hudson, T., Wood, S., & Chevrier, V. (2016). A revised calibration function and results for the Phoenix mission TECP relative humidity sensor. *Journal of Geophysical Research: Planets, 121*(4), 626-651. https://doi.org/10.1002/2015JE004933

Chapter 5

CHARACTERISTICS OF THE BASAL INTERFACE OF THE MARTIAN SOUTH POLAR LAYERED DEPOSITS

Aditya R. Khuller[1,2] and Jeffrey J. Plaut[2]

[1]School of Earth and Space Exploration, Arizona State University, Tempe, AZ, USA.

[2]Jet Propulsion Laboratory, California Institute of Technology, Pasadena, CA, USA.

Key Points:

- We present new, detailed (~44,000 points) maps of SPLD basal elevation and topography using MARSIS data
- We report the reflected basal echo power from 3 MARSIS frequencies, showing large spatial variability but minimal dependence on frequency
- Areas with high basal echo power are widespread, and not limited to the location of potential subglacial water bodies in Ultimi Scopuli

Abstract

We expand on previous studies of the South Polar Layered Deposits' (SPLD) basal interface using data acquired by the Mars Advanced Radar for Subsurface and Ionospheric Sounding (MARSIS) to obtain detailed maps of elevation, topography, and reflected radar power. Using these maps, we derive the thickness (ranging from 0 to 3.7 km) and volume of the SPLD (~1.60×10^6 km^3). While most basal interfaces reflect less power than the average SPLD surface, areas with basal echo power exceeding that of the surface are widespread throughout the SPLD, including at the location of potential subglacial water bodies in Ultimi Scopuli. The occurrence of these high basal echo power signatures appears to be largely frequency independent in MARSIS data. While the cause of the relatively high basal echo power values is uncertain, our observations suggest that this behavior is widespread, and not unique to Ultimi Scopuli.

5.1. Introduction

The South Polar Layered Deposits (SPLD) are several kilometer-thick stacks of layered H_2O ice-rich deposits extending outward from the martian south pole. These deposits are thought to have been emplaced over the last 10 – 100s of million years in the form of atmospherically deposited H_2O ice, dust, and minor amounts of CO_2 ice (Cutts, 1973; Herkenhoff & Plaut, 2000; Koutnik et al., 2002; Plaut, 2005; Becerra et al., 2019). The layers within the SPLD are potentially linked to changes in Mars' obliquity and orbital eccentricity over time, and therefore might hold millions of years of Mars' recent climatic history.

Initial radar sounding of the SPLD revealed the presence of the basal interface, where the H_2O ice-rich SPLD lie in contact with the substrate (Plaut et al., 2007). The locations of this basal interface were mapped to obtain subsurface topography, and provide estimates of the thickness and the volume of the SPLD (Plaut et al., 2007). In some cases, this basal interface showed anomalously bright reflections that were brighter than the surface return. The presence of subsurface liquid water was initially ruled out due to the cold temperatures expected at the base of the SPLD (Plaut et al., 2007). However, recent analyses at a few locations of bright basal reflectors suggests there may be a liquid water component at the interface (Orosei et al., 2018; Lauro et al., 2021), although the presence and stability of liquid water is under debate (Arnold et al., 2019; Sori & Bramson, 2019). Thus, key questions about the properties of the basal interface below the SPLD remain unanswered. In this work we build on previous studies by making use of the wealth of data acquired by the Mars Advanced Radar for Subsurface

and Ionospheric Sounding (MARSIS) since 2005 over the south polar region to further assess the characteristics of the SPLD basal interface.

5.2. Methods

5.2.1. Mars Advanced Radar for Subsurface and Ionospheric Sounding (MARSIS)

MARSIS is a multi-frequency synthetic aperture orbital sounding radar onboard the European Space Agency's Mars Express spacecraft (Picardi et al., 2004; Jordan et al., 2009). MARSIS operates simultaneously at 2 of 4 frequency bands (1.8, 3.0, 4.0 and 5.0 MHz) with a 1 MHz bandwidth. After on-board processing, MARSIS' along-track resolution is 5 – 10 km, with a cross-track footprint of 10 – 30 km. MARSIS data have a vertical resolution of ~150 m in free space, and about 50 – 100 m in typical geological materials.

5.2.2. 3D Imaging Volume

In this work, we use a compiled south polar data set from MARSIS data collected since 2005, consisting of over 2000 orbits taken in the 3 higher frequency bands (3, 4 and 5 MHz) to generate a 3D radar imaging volume (Text 5.S1 in the supporting information; Gim et al., 2018; Plaut et al., 2018; Plaut, 2020). Note that MARSIS data cannot be acquired poleward of 87°S. Key features of this 3D radar imaging volume are: (1) voxel (volume pixel) dimensions of 1.5 km x 1.5 km (horizontal) x 50 m (depth), (2) depth correction is applied in the subsurface using a wave speed in pure water ice (real dielectric constant $\varepsilon = 3.1$), (3) overlapping echo frames from different orbits are averaged, (4) empty voxels are filled with horizontally applied nearest neighbor interpolation in the volumes used for interface detection, and (5) slices are extracted for

all vertical and horizontal planes in each volume for individual study and animations. By assuming that the wave speed is equal to that in pure water ice, reflectors are repositioned in an approximately correct geometry to facilitate identification of interfaces. In areas known to contain lenses of CO_2 ice (Phillips et al., 2011), some distortions in reflector position can occur. However, this effect is evident in only a small fraction of the 3D volume (described in Section 5.4.3.).

5.2.3. Basal Interface Mapping and Power Characteristics

We identified and marked the basal interface reflector for all slices where it was discernible in the volume in RGB color composite images (red, 3 MHz; green, 4 MHz; blue, 5 MHz). The basal reflector was identified as the deepest linear feature below the surface return that was distinct in one or more frequency bands and contiguous with the internal SPLD structure above it. Figure 5.1 shows an example of this basal interface detection. The thickness of the reflector can vary slightly, and is typically 2 - 3 voxels thick (equivalent to 50 – 100 m uncertainty in depth). In some cases, multiple candidate basal interfaces were present, in which case a selection was made based on the elevation, context and relative brightness in the subject slice and in its neighbors. We also extracted the reflected radar power of the basal interface at each frequency for all mapped basal interface points, and report it relative to the surface reflected power (Text 5.S2 in the supporting information). This relative basal reflected power allows for a quantitative assessment of basal dielectric properties and compensates for any ionospheric attenuation or other observation-specific radiometric variations (Lauro et al., 2010; Orosei et al., 2018).

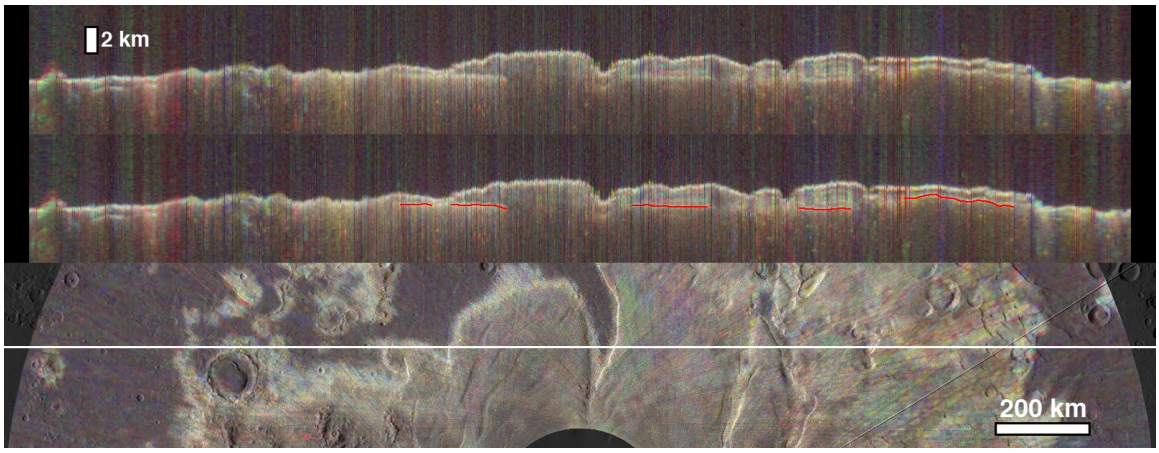

Figure 5.1. Top: Vertical slice through the MARSIS 3D volume, equivalent to a radargram. The vertical dimension is converted to distance, assuming a wave speed in water ice for all points in the subsurface. Color assignments are: red, 3 MHz; green, 4 MHz; blue, 5 MHz. Middle: Same as top image, with basal interface detections marked in red. Bottom: Horizontal slice taken at an elevation between the typical positions of the basal interface and the SPLD surface, with MOLA hillshade added for context. White line indicates the position of the slice in the top panels. This image is rotated 90 degrees counterclockwise from the orientation of later map figures. Image center is 84.1°S, 90.0°E.

We determined the elevation of each detection of the basal interface relative to the International Astronomical Union (IAU; Seidelmann et al., 2002) reference ellipsoid, using the water ice depth correction (e.g., Phillips et al., 2008). Then, the elevation of the Mars Orbiter Laser Altimeter (MOLA; Smith et al., 2001a; 256 pixels per degree gridded radius data in polar stereographic projection) surface overlying each subsurface interface was extracted to find the thickness of the SPLD at each point. We interpolated the basal elevation points and the elevations at the unit boundary to obtain a map of basal interface

topography using the Natural Neighbor algorithm in ArcGIS (Childs, 2004). This interpolated basal interface topography map was then subtracted from the MOLA surface topography to obtain a thickness map of the SPLD. Points along the SPLD unit boundary were constrained to have zero thickness.

5.3. Results

5.3.1. Basal Interface Topography

We mapped about 44,000 points on the SPLD basal interface (Fig. 5.2a), representing a 25x improvement over previous work (Plaut et al., 2007). Most of the basal interface detections lie at elevations 3 – 4 km above the reference ellipsoid. However, unusually low elevation detections are present in Ultima Lingula (which also contains high elevation detections), and within some craters. The highest elevation of the basal interface is about ~4.7 km above the ellipsoid. Note that we have omitted the unusually deep depressions in the near-polar region previously mapped by Plaut et al. (2007) because their regional context suggests that they represent a distinct unit that lies below the base of the SPLD (Fig. 5.S1).

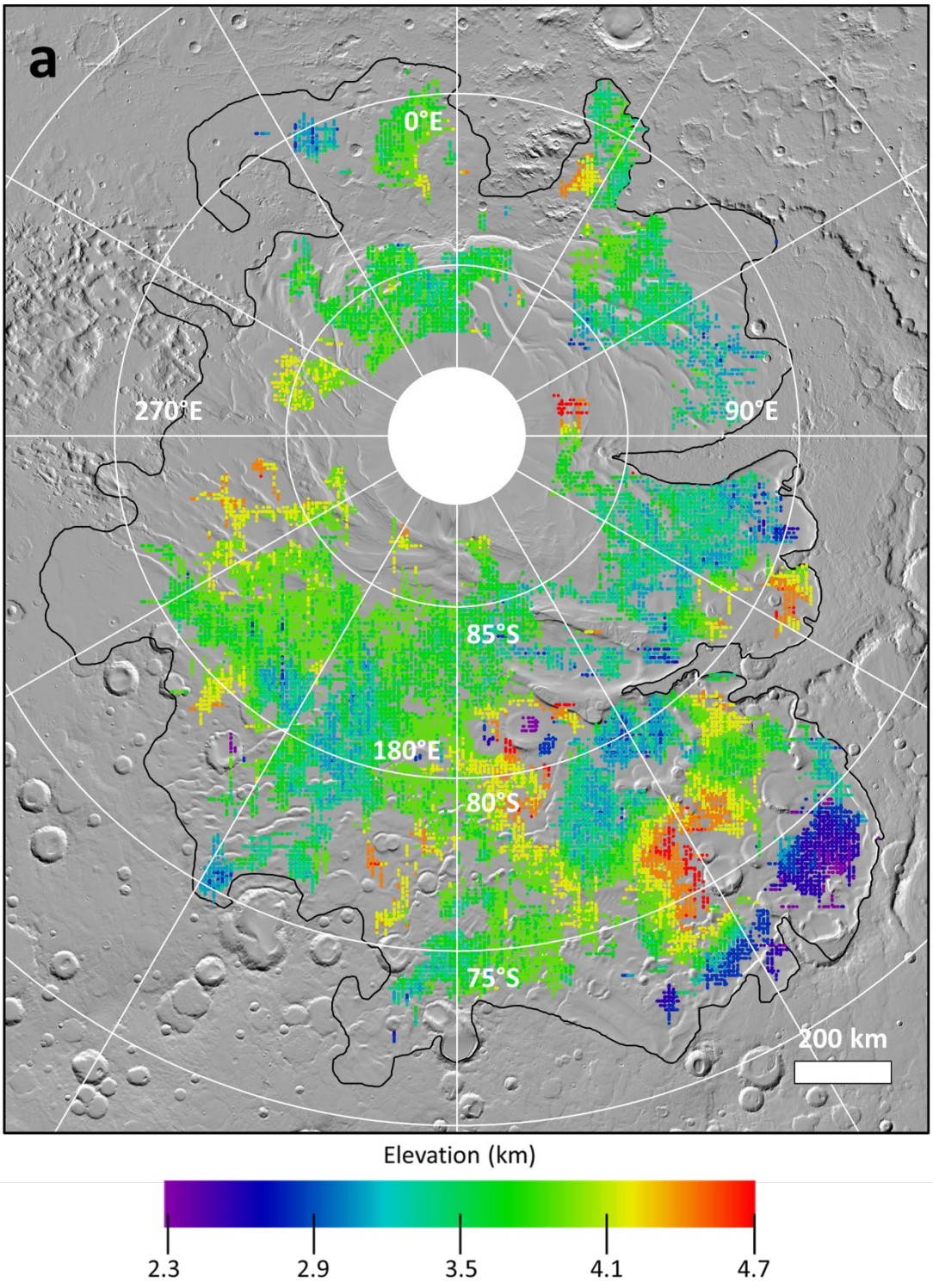
a
0°E
270°E
90°E
85°S
180°E
80°S
75°S
200 km
Elevation (km)
2.3
2.9
3.5
4.1
4.7

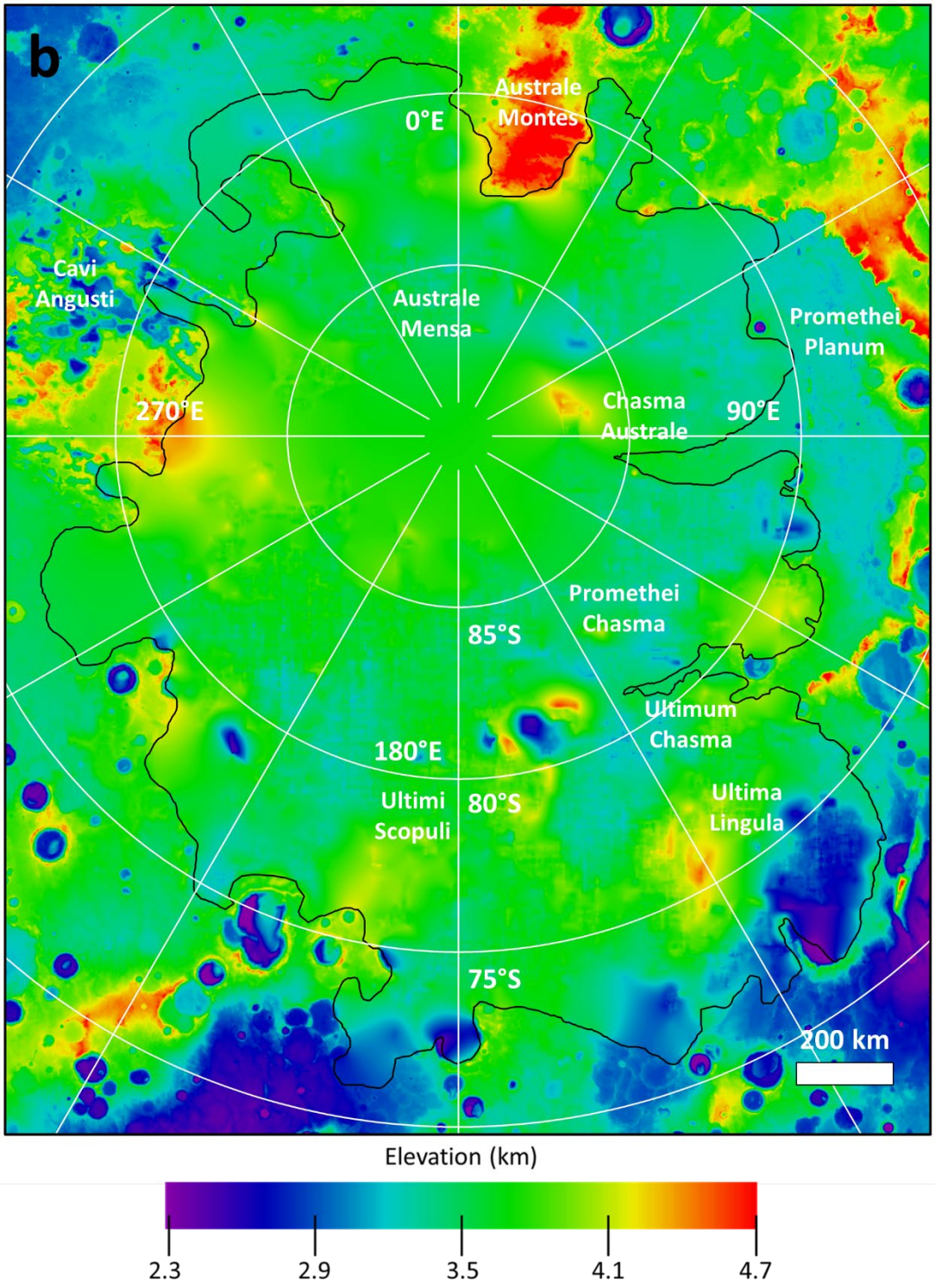

Figure 5.2. a) Elevations of the SPLD basal interface, relative to the Mars IAU reference ellipsoid, based on MARSIS measurements. b) Interpolated topography of the SPLD

basal interface based on MARSIS measurements, with MOLA data shown outside the SPLD. The SPLD unit boundary is outlined in black on both maps.

Most basal interfaces appear relatively flat in the 3D volume. However, in some cases, likely subsurface depressions (corresponding to impact craters or other basins) are observed. Near 87°S, 90°E, we observe an unusually high elevation region near the polar cap. This feature is just south of a previously identified subsurface dome near 87°S, 49°E, thought to represent a local region of enhanced H_2O ice accumulation (Whitten et al., 2017). Basal interface topography near the SPLD boundary often appears to extend off the PLD, indicating that the deposits were emplaced on complex, pre-existing topography.

5.3.2. Basal Interface Time Delay and SPLD Thickness and Volume

Figure 5.3a shows one-way time delay measurements of the SPLD basal interface, and Figure 5.3b shows the resultant interpolated thickness map of the SPLD. The thickest portions of the SPLD (~3.7 km) lie below the residual polar cap near 0°E, whereas regions of moderate thickness 1.5 – 2 km) are distributed throughout the interior of the SPLD. Outside of the residual cap area, the SPLD material is concentrated asymmetrically towards the eastern hemisphere, with numerous clusters of moderate thickness present near the three chasmata (Chasma Australe, Promethei Chasma, and Ultimum Chasma) and Ultima Lingula. These regions of moderate thickness are approximately concentric around the south pole, although there are a few exceptions. For instance, while the distal areas of the SPLD are generally low in thickness (< ~1 km), the anomalous low elevation region in Ultima Lingula (near 73°S, 140°E) coincides with a

region of moderate thickness. An unusually high thickness region near 81°S, 166°E is a partially buried crater filled with SPLD materials. Around 75°S, 150°E, a regional trend of alternating structures of high and low elevation appears to be present under the SPLD (Fig. 5.3a). These high-low elevation sequences are oriented parallel to thrust fault-related landforms including Thyles Rupes, which is centered at 69.3°S, 132.3°E (Klimczak et al., 2018).

While our study utilized an areally more extensive SPLD unit outline (based on Tanaka et al., 2014) that might increase the derived volume over previous studies, we also excluded the anomalously deep areas in the near-polar region that were mapped previously (Plaut et al., 2007). Thus, we derive a SPLD volume of ~1.60×10^6 km^3, corresponding to a global equivalent water layer thickness of ~11.1 m, which is consistent with previous mapping (Plaut et al., 2007).

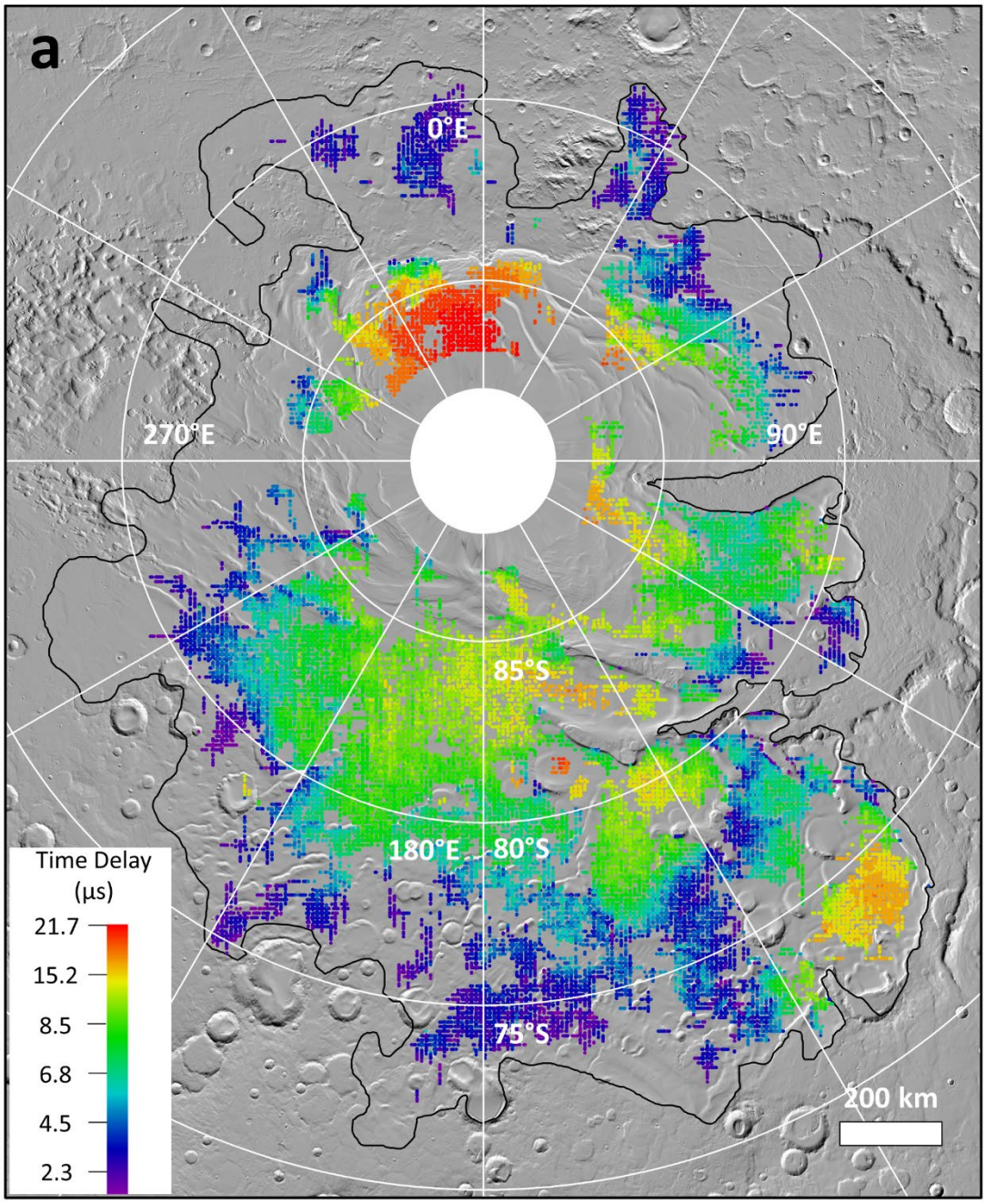
a
0°E
270°E
90°E
85°S
180°E
80°S
75°S
Time Delay
(µs)
21.7
15.2
8.5
6.8
4.5
2.3
200 km

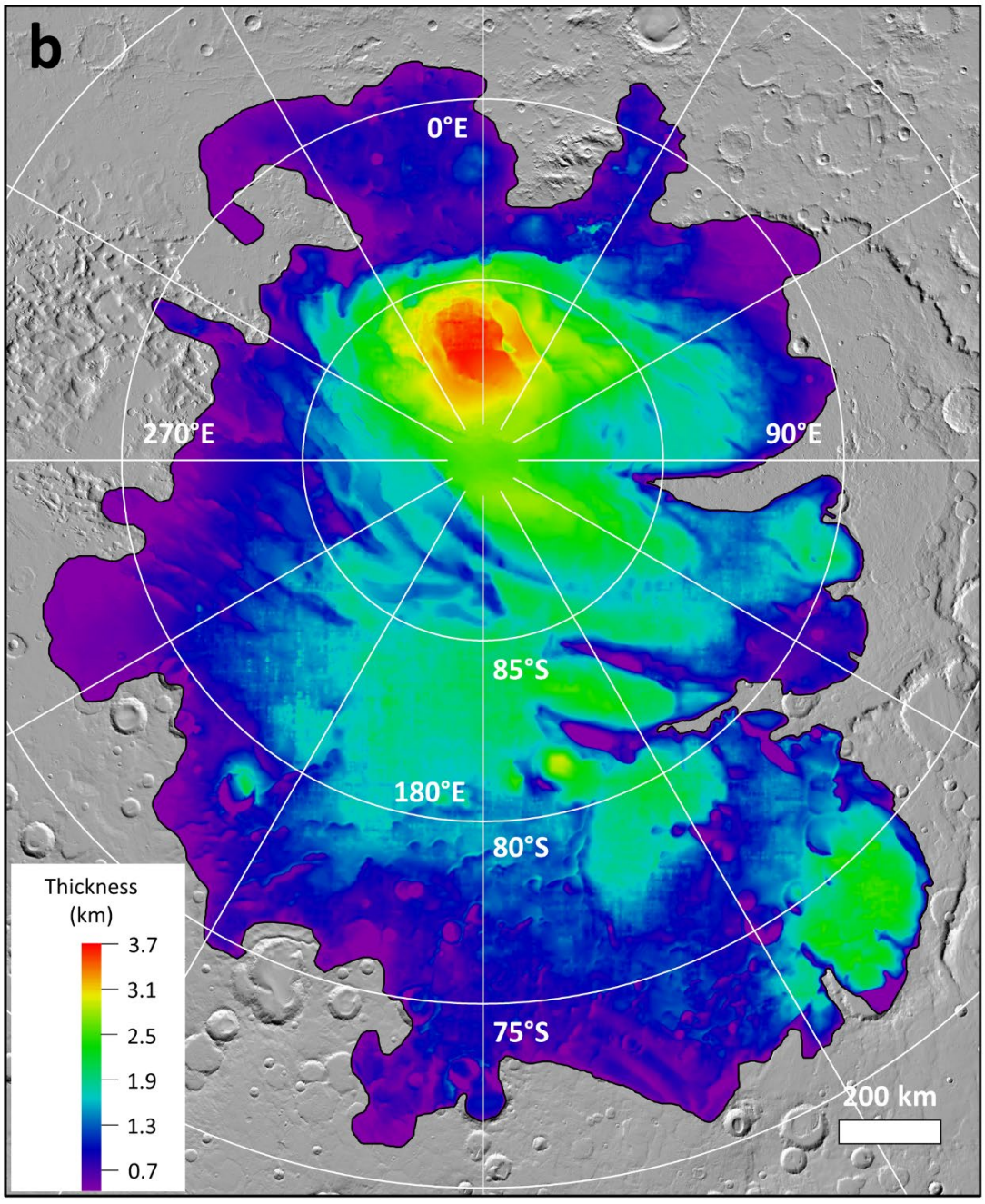

Figure 5.3. a) One-way time delay measurements between the surface and the SPLD basal interface. b) Thickness of the SPLD, based on interpolated MARSIS measurements

and MOLA surface topography. Points along the margin of the SPLD (black outline) were constrained to have zero thickness.

5.3.3. Basal Interface Reflected Power

A map of the basal interface reflected power relative to that of the average SPLD surface using 4 MHz data (Text 5.S2) is shown in Figure 5.4a. Areas with high values (warm colors) indicate regions where the basal interface power exceeds that of the surface. Although most basal interface values are lower than that of the surface, as expected, there are numerous regions where the reflected power of the basal interface exceeds that of the surface. The most prominent example of this behavior is below the south polar residual cap, i.e., the thickest portion of the SPLD, between 340°E and 0°E. Other bright basal reflectors appear to be scattered throughout the SPLD, suggesting that the process(es) causing this behavior may be widespread. Figure 5.4b illustrates the distribution of bright basal reflectors, showing regions where basal interface power relative to the surface is greater than 4 dB and the interface is deeper than 1 km (to exclude shallow basal reflectors). While the regions where there is potential evidence for liquid water (near 81°S, 193°E; Orosei et al., 2018; Lauro et al., 2021) do indeed have bright basal reflectors in our data, the signature is not unique to this area.

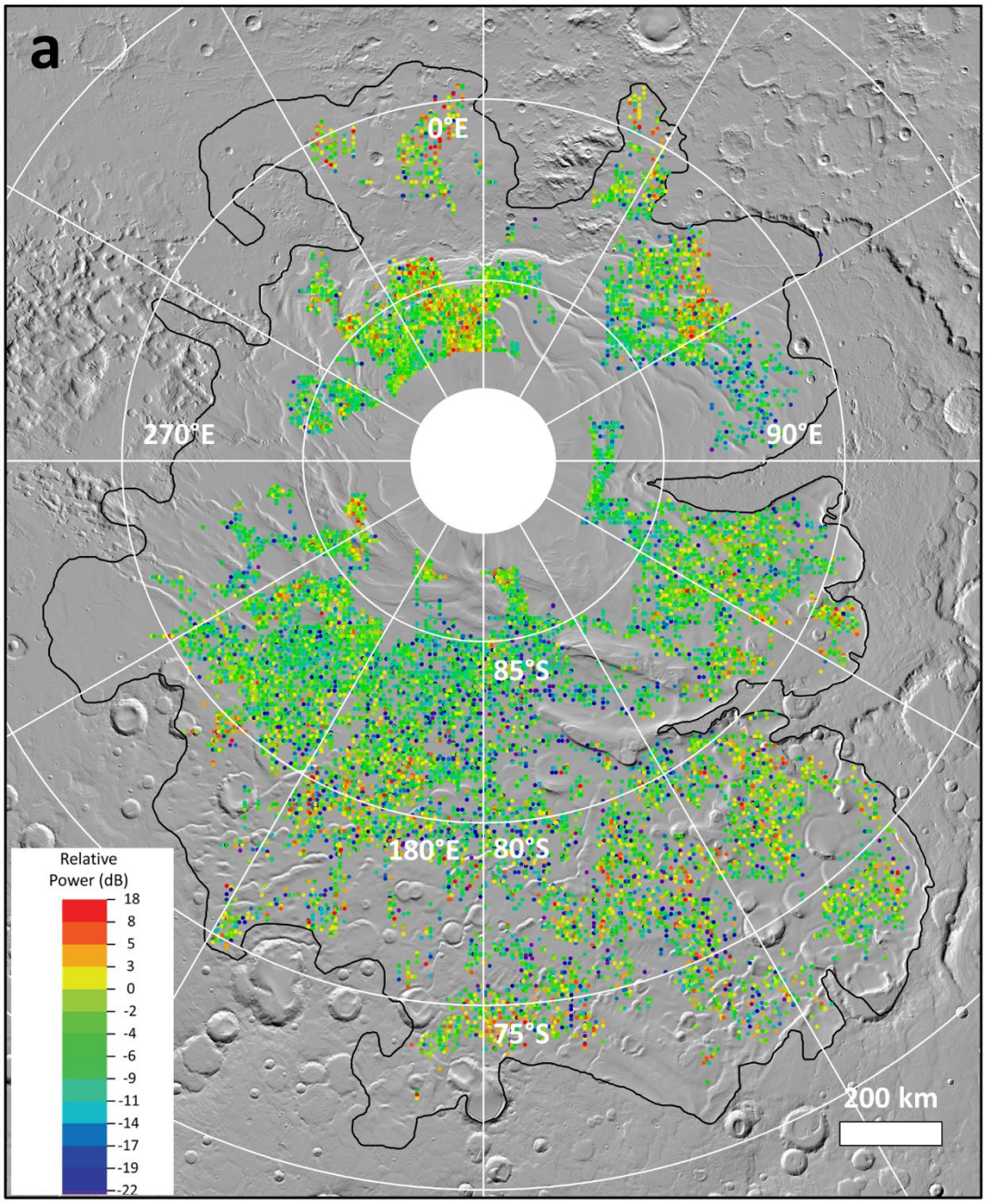
a
0°E
270°E
90°E
85°S
180°E
80°S
75°S
Relative
Power (dB)
18
8
5
3
0
-2
-4
-6
-9
-11
-14
-17
-19
-22
200 km

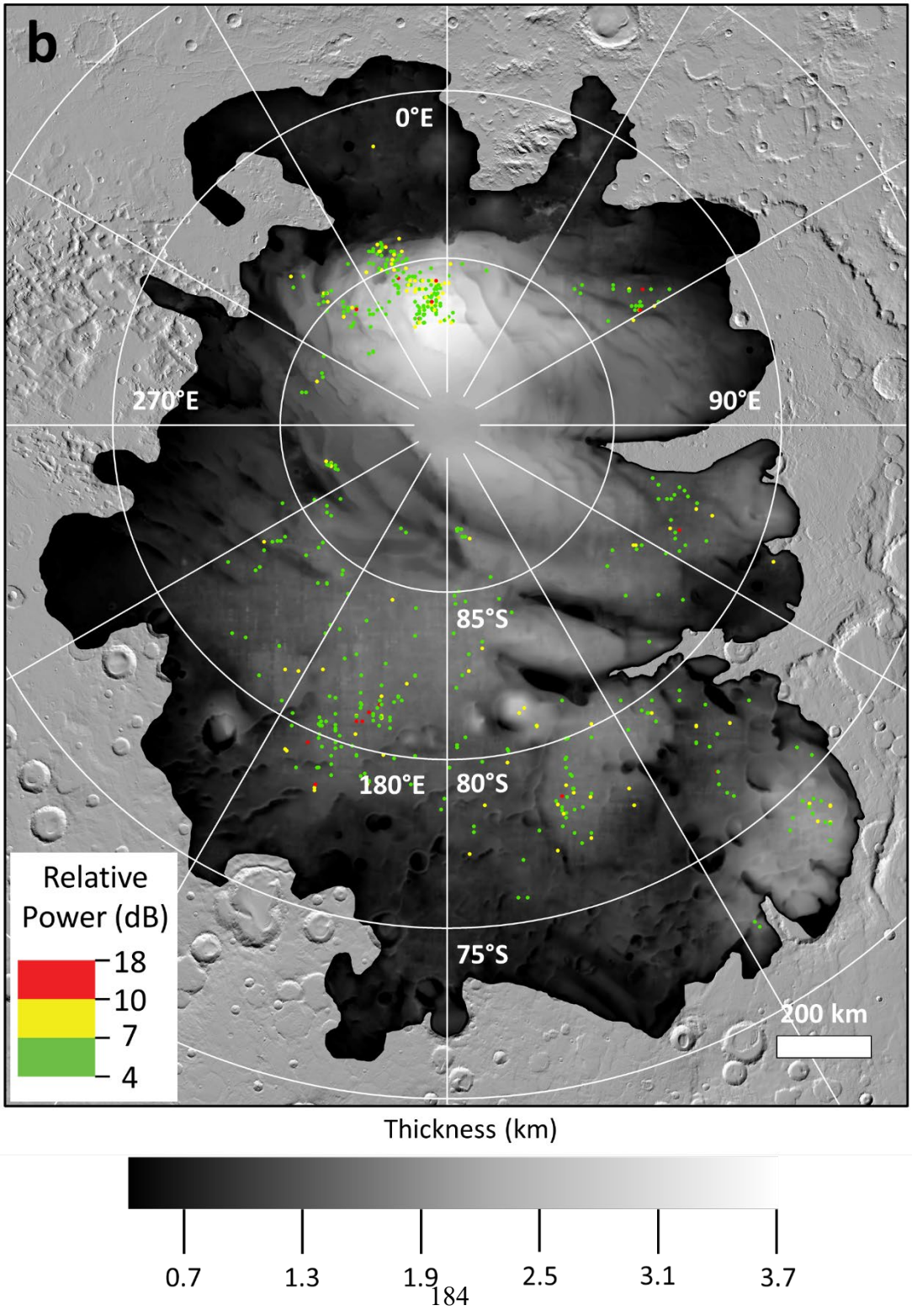
b
0°E
270°E
90°E
85°S
180°E
80°S
75°S
Relative Power (dB)
18
10
7
4
200 km
Thickness (km)
0.7
1.3
1.9
2.5
3.1
3.7

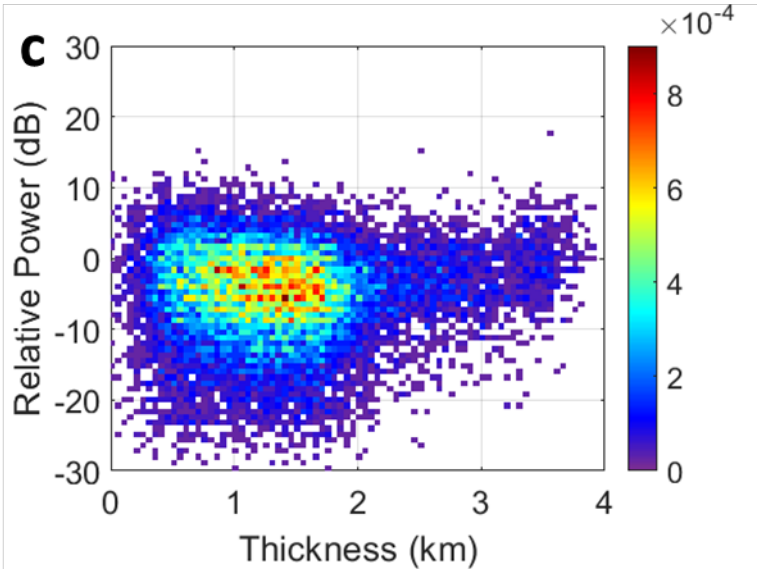

Figure 5.4. a) Basal interface reflected power relative to that of the average SPLD surface for 4 MHz MARSIS data. b) Regions where the basal interface reflected power exceeds that of the average SPLD surface by values greater than 4 dB (in 4 MHz MARSIS data) and the interface is deeper than 1 km. Grayscale map shows SPLD thickness (same as Figure 5.3b). c) Two-dimensional histogram of basal interface reflected power at 4 MHz, relative to that of the average SPLD surface, versus SPLD thickness. Colors indicate the fraction of observations per bin relative to the total.

Figure 5.4c shows a 2D histogram of basal interface reflected power relative to that of the average SPLD surface, versus SPLD thickness (Text 5.S2). The scatter of points does not follow what might be an expected pattern of decreasing basal reflected power with increasing thickness. This suggests that absorption in the bulk SPLD medium is not a major control on the basal reflector power at these frequencies. Instead, there is a mostly symmetrical, main concentration of values centered near ~1.5 km and -5 dB (warmer colors in Fig. 5.4a and green regions in Fig. 5.3). A secondary cloud of points

displays high relative power at large thicknesses (> 2 km), including the thickest near-polar regions. Other regions of high relative power are typically in areas where the SPLD is thin, possibly resulting from lower attenuation. 2D histograms using 3, 4 and 5 MHz data show virtually identical relationships between relative basal interface power and SPLD thickness (Figs. 5.S2 and 5.S3).

5.4. Discussion

5.4.1. Areas Lacking Basal Reflectors

There are several large regions of the PLD where MARSIS does not detect basal reflectors (e.g., 85°S, 30°E; 85°S, 75°E; 85°S, 135°E; 80 – 85°S, 270°E; see Fig. 5.2a). The absence of apparent basal reflectors could be due to the following reasons: (1) loss of the MARSIS signal between the surface and the basal interface, due to scattering and/or absorption, (2) a lack of contrast in dielectric constant at the basal interface, or (3) unfavorable geometry of the interface, such as roughness or slopes leading to scattering away from the nadir look direction. For example, the gap in reflectors around 30°E corresponds to the expected position of the Prometheus impact basin rim, which may produce rough buried topography that inhibits a strong reflection at the basal contact (Byrne & Ivanov, 2004; Whitten et al., 2017). The gap around 75°E is not so easily explained, as it presumably corresponds to the flat interior of the impact basin, Promethei Planum. Scattered gaps in the distal lobes toward 180°E may be related to rough heavily cratered highlands terrain. Several gap regions poleward of 85°S do not bear any clear relationship with exposed topography, but are found in regions previously noted to have

unusually deep reflectors (Plaut et al., 2007), which we now interpret to lie at the base of an earlier, pre-SPLD deposit (see below).

5.4.2. Possible Evidence for sub-SPLD Dorsa Argentea Formation Reflectors

Plaut et al. (2007) reported a series of buried depressions that appeared to be present in the basal topography from MARSIS measurements between 84° and 87°S, from 95° to 295°E. As mentioned above, we interpret these depressions to be a separate, distinct interface from the rest of the SPLD basal interface (Fig. 5.S1). This depression-hosting interface likely represents a second, deeper unit. In some cases, this deeper unit appears to merge with subsurface detections of the Hesperian-aged Dorsa Argentea Formation (DAF; Plaut et al., 1988; Kress & Head, 2015). Radar evidence for the DAF extending under the Amazonian-aged SPLD has been reported previously (e.g., near the Prometheus basin; Whitten et al., 2020), suggesting that the DAF forms a continuous unit beneath the SPLD. Our observations are consistent with this suggestion, and seem to indicate that the unit that hosts the buried depressions is a portion of the DAF. However, this sub-SPLD DAF unit is not visible throughout the SPLD, perhaps for similar reasons discussed above for the lack of basal interface detections at some SPLD locations. The presence of a sub-PLD paleo-polar deposit in Planum Australe is analogous in some ways to the "basal unit" of Planum Boreum in the north (Malin & Edgett, 2001; Fishbaugh & Head, 2005). Like the north polar basal unit, the sub-SPLD unit identified here is penetrated by MARSIS frequencies, but typically not by the higher frequency SHARAD (Shallow Radar; Seu et al., 2007) (Selvans et al., 2010; Nerozzi & Holt, 2019). Where

exposed, the north polar basal unit differs morphologically from the DAF, but the stratigraphic position and radar properties of the two units are similar.

5.4.3. Buried CO_2 Ice

Subsurface CO_2 ice deposits have been detected in some parts of the SPLD using SHARAD data, with an estimated total volume of 16,500 km^3 (Phillips et al., 2011; Bierson et al., 2016; Putzig et al., 2018). While the known volume of buried CO_2 is large relative to Mars' total atmospheric mass, it only represents ~1% of the total SPLD volume. Because the dielectric constant for CO_2 ice (~2.1) is lower than that used for the depth correction in our MARSIS 3D volume (3.1), some distortion (e.g., internal layers not parallel) due to deposits of CO_2 ice can occur (Fig. 5.S4). However, the thickest portion (~1 km) of these deposits is present in a part of Australe Mensa that is outside the available MARSIS data limit of 87°S (Fig. 5.S4). Other scattered areas with CO_2 ice are present around Australe Mensa, but the thickness of these deposits is relatively small (< 500 m), which causes a small distortion of underlying layers and interfaces. For example, the presence of a 500 m thick CO_2 ice slab would lead to a ~90 m vertical misplacement of underlying features under our assumption of a pure H_2O ice column. This value is comparable to our uncertainty in marking the position of the basal reflector. Assuming this distortion is present in all the regions where CO_2 ice has been detected previously, we estimate the errors in the reported SPLD elevations and total volume due to CO_2 ice as ~100 m and < 0.5%, respectively.

We find no evidence for significant "hidden" CO_2 deposits elsewhere in the SPLD (e.g., postulated in the NPLD in Broquet et al. (2020), and "reflection-free zones" in

Phillips et al. (2011)), although the sensitivity to such deposits in our method would make their detection difficult. Our assumption of a water ice wave speed results in a plausible geometry of the basal interface both regionally and locally. This observation, using the improved resolution and coverage over previous mapping, reinforces earlier conclusions that the load of the SPLD has resulted in little to no deflection of the lithosphere (Plaut et al., 2007; Ojha et al., 2020).

5.4.4. Potential Presence of Subglacial Water Bodies

Recent analyses of MARSIS data at Ultimi Scopuli suggest that bright subsurface basal relative power returns (up to ~ 5 dB at 4 MHz) from a few ~20 km regions at this location indicate the presence of multiple subglacial water bodies (Orosei et al., 2018; Lauro et al., 2021). These bright regions are visible in Figure 5.4a, with a value of 6.3 ± 1.7 dB at 4 MHz for their relative power (Text 5.S2), similar to the values obtained by Orosei et al. (2018) and Lauro et al. (2021). Note that those studies present basal power relative to the median of the surface power along each orbit, whereas we normalize basal power relative to the overall average SPLD surface power. The presence of stable, subsurface liquid water may require an anomalously high geothermal heat flux at these locations (e.g., Hecht et al., 2018; Sori & Bramson, 2019). However, it has been proposed that liquid water solutions with magnesium/calcium perchlorates might be stable at these locations in a super-cooled state (Lauro et al., 2021). We deem it unlikely that the bright reflectors under the thickest SPLD areas are due to liquid water, as they commonly extend close to the surface where the mean annual surface temperature is too low to permit even super-cooled perchlorate brines to remain liquid.

Our observations suggest that the process(es) causing these anomalously bright subsurface echoes may be widespread across the SPLD. If the presence of liquid water in the form of subglacial water bodies is widespread under the PLD, then our improved map of basal topography can be used in hydrogeological models (Arnold et al., 2019) to assess the hydraulic potential of the basal interface at these locations of bright subsurface basal power return.

5.5. Conclusions

(1) We have expanded on previous work to characterize the basal interface of the SPLD using a large compilation of MARSIS radar data. By mapping ~44,000 points, we generated new, detailed maps of elevation, topography, and reflected radar power of the basal interface.

(2) We found that the thickness of the PLD ranges from 0 to 3.7 km, and the total volume is about 1.60×10^6 km^3. While most basal interfaces appear relatively flat, numerous regions have subsurface depressions, likely caused by impact craters or other basins. We observe a group of unusually deep radar interfaces that we interpret to be part of a distinct, separate unit from the rest of the basal interface. These deeper interfaces appear to merge with previous subsurface radar detections of the Hesperian-aged DAF, suggesting that the DAF forms a continuous unit under the SPLD.

(3) Areas with relatively high basal echo power are widespread throughout the SPLD. The process(es) that are causing these anomalous bright basal reflections may not be limited to regions with potential subglacial water bodies in Ultimi Scopuli. The signatures of these bright basal echo power regions are independent of frequency in

MARSIS data. Although the presence and stability of liquid water at these locations is debated, our improved maps of basal topography can help assess the hydraulic potential of these bright basal reflector locations.

5.6. Acknowledgments

We would like to thank Andrew Dombard, Jennifer Whitten and an anonymous reviewer for formal reviews that significantly improved the manuscript. Additionally, we thank Daniele Bellutta and Yonggyu Gim for assistance in constructing the 3D volumes of MARSIS data, and Than Putzig, Isaac Smith and Aaron Russell for providing the locations of the CO_2 ice deposits detected by SHARAD. We are also grateful to Sarah Rogers and Alex Huff for very useful feedback and advice. Some of this work was carried out at the Jet Propulsion Laboratory, California Institute of Technology, under a contract with the National Aeronautics and Space Administration.

5.7. Data Availability Statements

MARSIS data are available at the ESA Planetary Science Archive (https://archives.esac.esa.int/psa/#!Table%20View/MARSIS=instrument) and at NASA's Planetary Data System (https://pds-geosciences.wustl.edu/missions/mars_express/marsis.htm). Data from the figures in the main text and the supporting information are available in Khuller and Plaut (2021) (repository: https://doi.org/10.5281/zenodo.4653741).

5.8. Supporting Material

5.8.1. Text S1. Details on construction of the MARSIS 3D volumes

Compilation of the MARSIS 3D volumes (Gim et al., 2018; Plaut et al., 2018; Plaut, 2020) can be summarized as follows: The entire MARSIS data set was processed with optimized ionospheric correction (McMichael et al., 2017) with radargrams referenced to the Mars ellipsoid datum. A time-to-depth conversion was applied to all echoes later than the surface return using a real dielectric constant of 3.1 (water ice). All candidate MARSIS polar observations were evaluated for quality, with those lacking subsurface echoes discarded. Data were sorted by frequency band. All MARSIS echo profiles ("frames") poleward of 80 degrees (N and S) were sorted into lateral spatial bins 1.5 km x 1.5 km in size, in polar stereographic projection. For each frequency band, spatial bins containing more than one frame were averaged in power, converted to dB units and assigned to DN values in 8-bit (256 DN) images. This conversion can be reversed to extract power values in dB. For visualization, nearest neighbor interpolation was applied in the horizontal direction only. Non-interpolated volumes were also retained for point measurements.

The horizontal interpolation could in some cases result in spurious horizontal features that may be misinterpreted as continuous linear reflectors. However, we believe that such artifacts are rare, due to the high density of coverage (few empty voxels, especially closer to the pole), and by visual analysis of non-interpolated volume slices, where most basal reflectors are prominent even without interpolation.

Off-nadir surface topography can produce radar returns that arrive at times later than the nadir surface and can be misinterpreted as subsurface interfaces; this is the classic "clutter" problem in radar sounding. While the original MARSIS polar observations

frequently contain such clutter, the 3D volumes are relatively free of these features. This is because the position of a given clutter-producing surface feature in time delay depends on its cross-track distance from the nadir point. When 3D volume spatial bins are populated with multiple MARSIS tracks at a variety of ground track azimuths, clutter echoes tend to get distributed into many nearby bins, and are "absorbed" into the voxel column averages. The result is that clutter echoes are spread into background noise, rather than adding as discrete features. This effect was confirmed by comparing original clutter-containing radargrams with slices from the 3D volumes along the same azimuth. With a few exceptions, the clutter was suppressed in the 3D data. In addition, our identification of basal interface echoes required a continuity of the feature in adjacent slices, which would not be expected for spurious features arising from surface clutter.

5.8.2. Text S2. Calculating basal and surface reflected power from the MARSIS 3D volume

To derive the reflected power from interfaces noted in the MARSIS 3D volume, we used the non-interpolated version of the 3D volume for each frequency (3, 4 and 5 MHz). For each identified basal interface segment, the brightest pixel within ± 3 pixels vertically was assumed to represent the basal interface, from which the power was derived. Reflected power values for the surface were obtained by deriving the power from the brightest pixel within ± 3 vertical pixels of the MOLA surface position. For Figure 4a in the main text and Figure S2, the basal power is shown relative to the average power of the SPLD surface overlying the basal detections. We obtained average values of SPLD surface power equal to 107.8 ± 6.0 dB, 104.6 ± 7.5 dB, and 93.6 ± 6.6 dB at 3, 4

and 5 MHz, respectively. Note that these values are relative to an arbitrary reference point, because MARSIS data are not absolutely calibrated. For the location of the potential subglacial water body area, the four points within our dataset closest to the detections made by Orosei et al. (2018) were at 81.02°S, 192.6°E (7.8 dB), 81.04°S, 192.79°E (4.7 dB), 81.07°S, 192.67°E (7.8 dB), 81.09°S, 192.7°E (5.0 dB), giving a mean value of 6.3 dB at 4 MHz for their relative power, with a standard deviation of 1.7 dB. Figure S3 shows the basal power relative to the local surface power, i.e., the power at the surface directly above the reported basal interface.

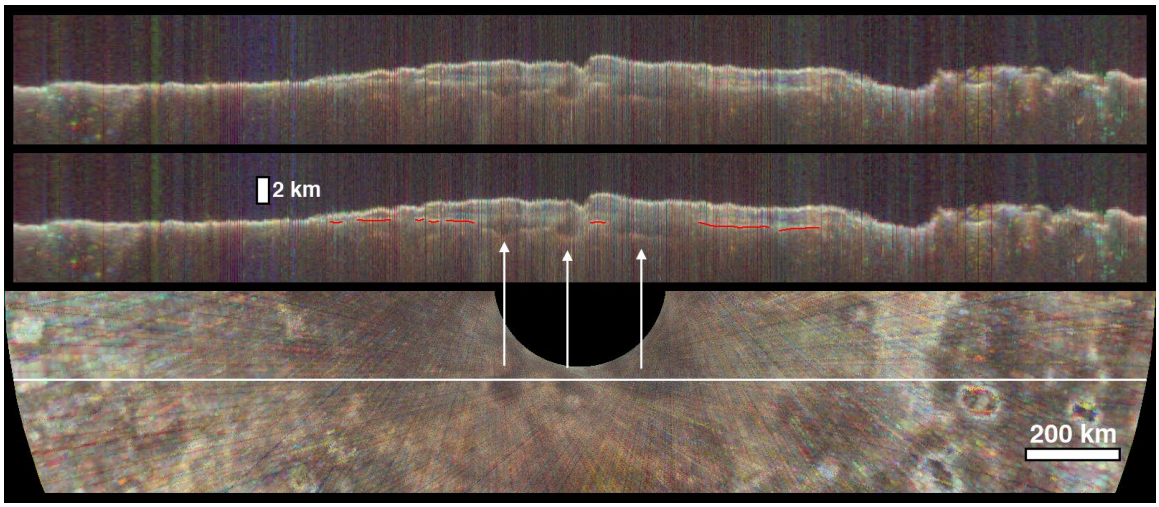

Figure 5.S1. Top: Vertical slice showing returns from apparent depressions with floors >1 km below the normal SPLD basal interface. Middle: Same vertical slice with SPLD basal reflector marked in red. The deeper interfaces (white arrows) appear disconnected from the main SPLD structure and thus were not mapped as the basal interface. Bottom: Horizontal slice taken at an elevation between the depression floors and the base of the SPLD shows the map pattern of the features. Similar echoes extend from this area toward the exposed, pitted terrain of Cavi Angusti and the surrounding Dorsa Argentea

Formation, suggesting a genetic relationship between the exposed terrain and the buried depressions. Image center is 86.5°S, 180.0°E.

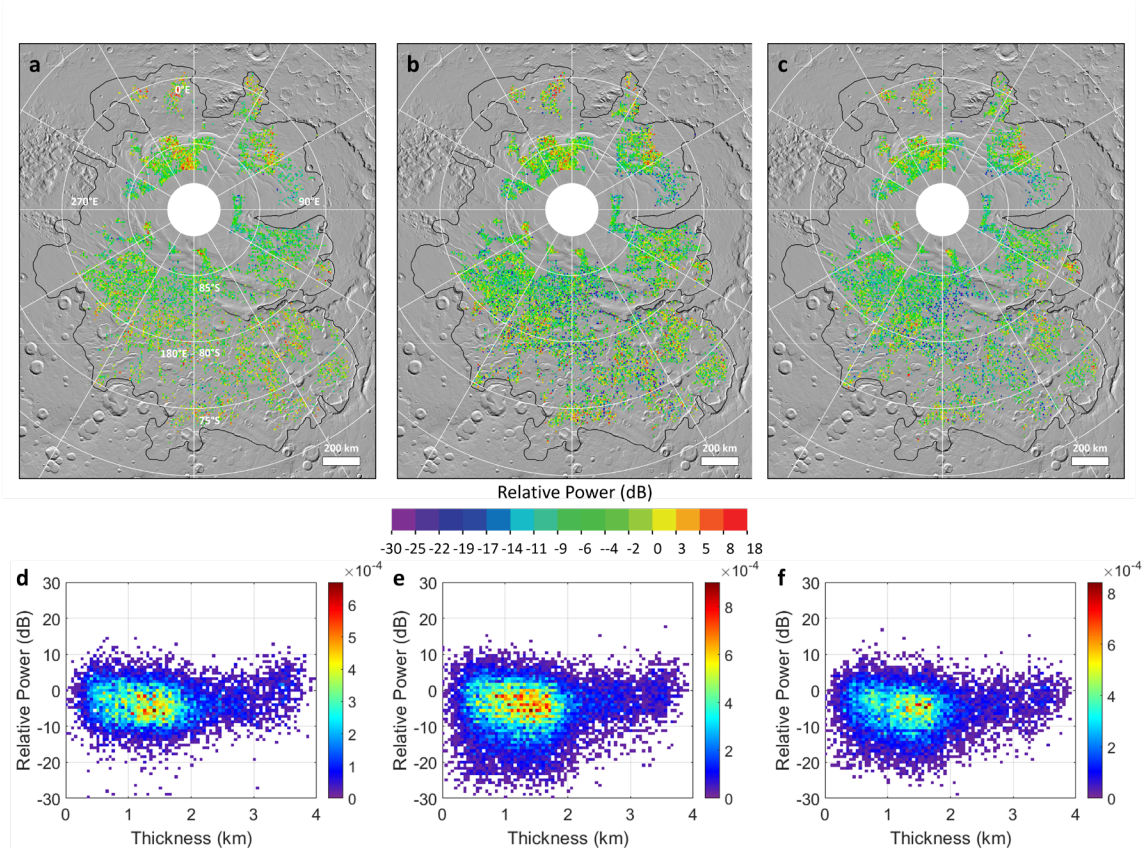

Figure 5.S2. a–c) Basal interface reflected power relative to that of the average SPLD surface for 3, 4 and 5 MHz MARSIS data, respectively. d–f) Two-dimensional histogram of basal interface reflected power at 3, 4 and 5 MHz, respectively, relative to that of the average SPLD surface, versus SPLD thickness. Colors indicate the fraction of

observations per bin relative to the total.

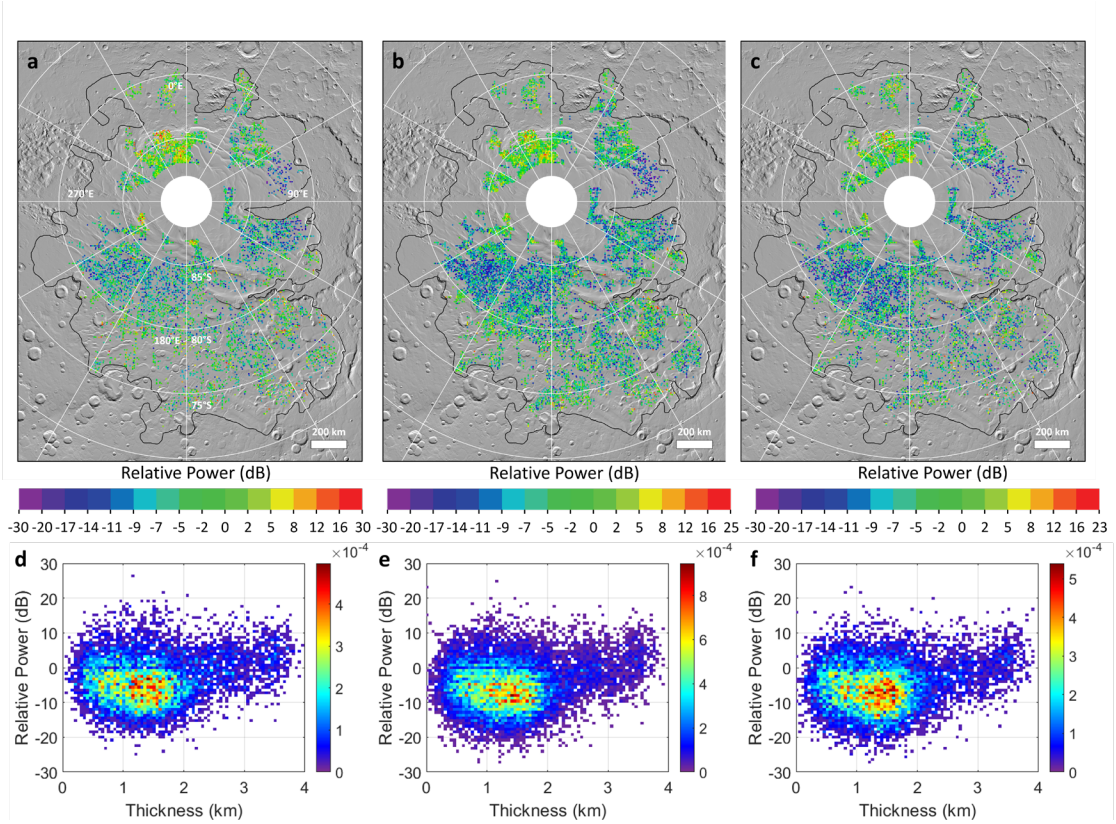

Figure 5.S3. a–c) Basal interface reflected power relative to that of the local SPLD surface for 3, 4 and 5 MHz MARSIS data, respectively. d–f) Two-dimensional histogram of basal interface reflected power at 3, 4 and 5 MHz, respectively, relative to that of the local SPLD surface, versus SPLD thickness. Colors indicate the fraction of observations per bin relative to the total.

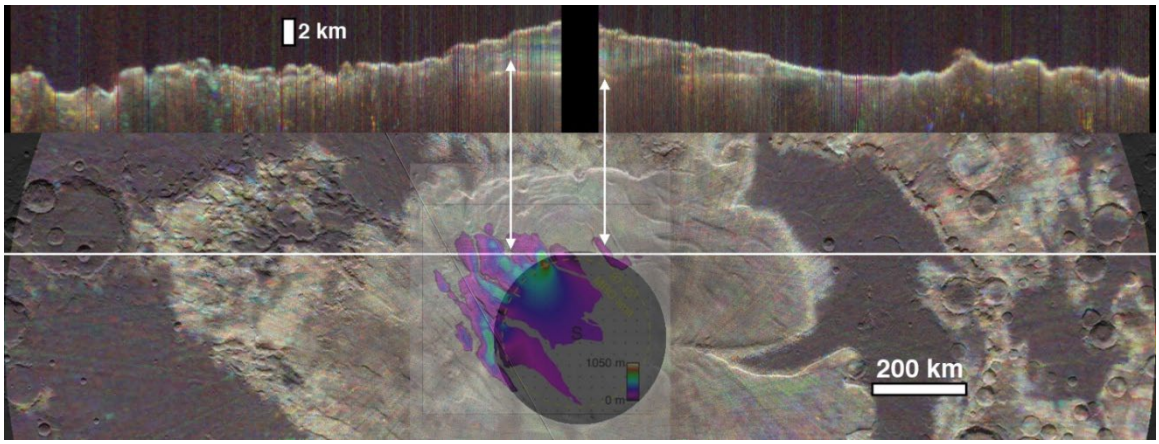

Figure 5.S4. Top: Vertical slice over the high elevation regions of Australe Mensa, which include the south polar residual cap. Bottom: Horizontal slice taken at an elevation between the typical positions of the basal interface and the SPLD surface, with MOLA hillshade added for context, and the map of buried CO_2 deposit thickness from SHARAD observations superimposed, adapted from Putzig et al. (2018). Arrows indicate parts of the MARSIS volume slice that may show residual depth correction errors (e.g., internal layers not parallel) due to passage through lower dielectric CO_2 ice. Note that SHARAD data can be acquired up to 87.45°S, versus 87.0°S for MARSIS. Center of radargram image is 87.2°S, 0.0°E.

REFERENCES

Arnold, N. S., Conway, S. J., Butcher, F. E., & Balme, M. R. (2019). Modeled subglacial water flow routing supports localized intrusive heating as a possible cause of basal melting of Mars' south polar ice cap. *Journal of Geophysical Research: Planets, 124*(8), 2101-2116. https://doi.org/10.1029/2019JE006061

Becerra, P., Sori, M. M., Thomas, N., Pommerol, A., Simioni, E., Sutton, S. S., et al. (2019). Timescales of the climate record in the south polar ice cap of Mars. *Geophysical Research Letters, 46*(13), 7268-7277. https://doi.org/10.1029/2019GL083588

Bierson, C., Phillips, R., Smith, I., Wood, S., Putzig, N., Nunes, D., & Byrne, S. (2016). Stratigraphy and evolution of the buried CO2 deposit in the Martian south polar cap. *Geophysical Research Letters, 43*(9), 4172-4179. https://doi.org/10.1002/2016GL068457

Broquet, A., Wieczorek, M. A., & Fa, W. (2020). Flexure of the Lithosphere Beneath the North Polar Cap of Mars: Implications for Ice Composition and Heat Flow. *Geophysical Research Letters, 47*(5), e2019GL086746. https://doi.org/10.1029/2019GL086746

Byrne, S., & Ivanov, A. (2004). Internal structure of the Martian south polar layered deposits. *Journal of Geophysical Research: Planets, 109*(E11). https://doi.org/10.1029/2004JE002267

Childs, C. (2004). Interpolating surfaces in ArcGIS spatial analyst. *ArcUser, July-September, 3235*(569), 32-35.

Cutts, J. A. (1973). Nature and origin of layered dust deposits of the martian polar regions. *J. Geophys. Res., 78*(No. 20), 4231-4249. https://doi.org/10.1029/JB078i020p04231

Fishbaugh, K. E., & Head, J. W. (2005). Origin and characteristics of the Mars north polar basal unit and implications for polar geologic history. *Icarus, 174*(2), 444-474.

Gim, Y., Bellutta, D., & Plaut, J. (2018). Construction of MARSIS 3D Radar Maps of the Martian Polar Regions. *Lunar and Planetary Science Conference, 49*(2083), 1793.

Head III, J. W., & Pratt, S. (2001). Extensive Hesperian-aged south polar ice sheet on Mars: Evidence for massive melting and retreat, and lateral flow and ponding of meltwater. *Journal of Geophysical Research: Planets, 106*(E6), 12275-12299. https://doi.org/10.1029/2000JE001359

Hecht, M., Fisher, D., Catling, D. C., & Kounaves, S. P. (2018). RE: Radar evidence of subglacial liquid water on Mars (Orosei et al.).

Herkenhoff, K. E., & Plaut, J. J. (2000). Surface ages and resurfacing rates of the polar layered deposits on Mars. *Icarus, 144*(2), 243-253.

Jordan, R., Picardi, G., Plaut, J., Wheeler, K., Kirchner, D., Safaeinili, A., et al. (2009). The Mars express MARSIS sounder instrument. *Planetary and Space Science, 57*(14-15), 1975-1986.

Khuller, A. R., & Plaut, J. J. (2021). *Repository: Characteristics of the Basal Interface of the Martian South Polar Layered Deposits*. Retrieved from: https://doi.org/10.5281/zenodo.4653741

Klimczak, C., Kling, C. L., & Byrne, P. K. (2018). Topographic expressions of large thrust faults on Mars. *Journal of Geophysical Research: Planets, 123*(8), 1973-1995. https://doi.org/10.1029/2017JE005448

Koutnik, M., Byrne, S., & Murray, B. (2002). South polar layered deposits of Mars: The cratering record. *Journal of Geophysical Research: Planets, 107*(E11), 10-11-10-10. https://doi.org/10.1029/2001JE001805

Kress, A. M., & Head, J. W. (2015). Late Noachian and early Hesperian ridge systems in the south circumpolar Dorsa Argentea Formation, Mars: Evidence for two stages of melting of an extensive late Noachian ice sheet. *Planetary and Space Science, 109*, 1-20.

Lauro, S. E., Mattei, E., Pettinelli, E., Soldovieri, F., Orosei, R., Cartacci, M., et al. (2010). Permittivity estimation of layers beneath the northern polar layered deposits, Mars. *Geophysical Research Letters, 37*(14). https://doi.org/10.1029/2010GL043015

Lauro, S. E., Pettinelli, E., Caprarelli, G., Guallini, L., Rossi, A. P., Mattei, E., et al. (2021). Multiple subglacial water bodies below the south pole of Mars unveiled by new MARSIS data. *Nature Astronomy*, 1-8.

Malin, M., & Edgett, K. S. (2001). Mars global surveyor Mars orbiter camera: interplanetary cruise through primary mission. *Journal of Geophysical Research: Planets, 106*(E10), 23429-23570. https://doi.org/10.1029/2000JE001455

McMichael, J. G., Gim, Y., Arumugam, D. D., & Plaut, J. J. (2017). *Radar autofocus algorithm incorporating terrain knowledge for correction of Mars' ionospheric distortion in MARSIS observations.* Paper presented at the 2017 IEEE Radar Conference (RadarConf).

Nerozzi, S., & Holt, J. (2019). Buried ice and sand caps at the North Pole of Mars: revealing a record of climate change in the Cavi Unit with SHARAD. *Geophysical Research Letters, 46*(13), 7278-7286. https://doi.org/10.1029/2019GL082114

Ojha, L., Karimi, S., Buffo, J., Nerozzi, S., Holt, J. W., Smrekar, S., & Chevrier, V. (2020). Martian Mantle Heat Flow Estimate from the Lack of Lithospheric Flexure in the South Pole of Mars: Implications for Planetary Evolution and Basal Melting. *Geophysical Research Letters*, e2020GL091409. https://doi.org/10.1029/2020GL091409

Orosei, R., Lauro, S., Pettinelli, E., Cicchetti, A., Coradini, M., Cosciotti, B., et al. (2018). Radar evidence of subglacial liquid water on Mars. *Science, 361*(6401), 490-493.

Phillips, R. J., Davis, B. J., Tanaka, K. L., Byrne, S., Mellon, M. T., Putzig, N. E., et al. (2011). Massive CO2 ice deposits sequestered in the south polar layered deposits of Mars. *Science, 332*(6031), 838-841.

Phillips, R. J., Zuber, M. T., Smrekar, S. E., Mellon, M. T., Head, J. W., Tanaka, K. L., et al. (2008). Mars north polar deposits: Stratigraphy, age, and geodynamical response. *Science, 320*(5880), 1182-1185.

Picardi, G., Biccari, D., Seu, R., Marinangeli, L., Johnson, W., Jordan, R., et al. (2004). Performance and surface scattering models for the Mars Advanced Radar for Subsurface and Ionosphere Sounding (MARSIS). *Planetary and Space Science, 52*(1-3), 149-156.

Plaut, J. (2005). *An inventory of impact craters on the Martian south polar layered deposits.* Paper presented at the Lunar and Planetary Science Conference.

Plaut, J. (2020). Topographic, Compositional, and Textural Variations in Basal Interfaces Beneath the South Polar Plateau of Mars from MARSIS Radar Sounding. *LPI Contributions, 2099*, 6048.

Plaut, J., Bellutta, D., & Gim, Y. (2018). New Insights into the Internal Structure of the Martian Polar Plateaus from MARSIS 3D Mapping. *Lunar and Planetary Science Conference, 49*(2083), 2252.

Plaut, J., Kahn, R., Guinness, E., & Arvidson, R. (1988). Accumulation of sedimentary debris in the south polar region of Mars and implications for climate history. *Icarus, 76*(2), 357-377.

Plaut, J. J., Picardi, G., Safaeinili, A., Ivanov, A. B., Milkovich, S. M., Cicchetti, A., et al. (2007). Subsurface radar sounding of the south polar layered deposits of Mars. *Science, 316*(5821), 92-95.

Putzig, N. E., Smith, I. B., Perry, M. R., Foss II, F. J., Campbell, B. A., Phillips, R. J., & Seu, R. (2018). Three-dimensional radar imaging of structures and craters in the Martian polar caps. *Icarus, 308*, 138-147.

Seidelmann, P., Abalakin, V., Bursa, M., Davies, M., De Bergh, C., Lieske, J., et al. (2002). Report of the IAU/IAG working group on cartographic coordinates and rotational elements of the planets and satellites: 2000. *Celestial Mechanics and Dynamical Astronomy, 82*(1), 83-111.

Selvans, M., Plaut, J., Aharonson, O., & Safaeinili, A. (2010). Internal structure of Planum Boreum, from Mars advanced radar for subsurface and ionospheric sounding data. *Journal of Geophysical Research: Planets, 115*(E9). https://doi.org/10.1029/2009JE003537

Seu, R., Phillips, R. J., Biccari, D., Orosei, R., Masdea, A., Picardi, G., et al. (2007). SHARAD sounding radar on the Mars Reconnaissance Orbiter. *Journal of Geophysical Research: Planets, 112*(E5). https://doi.org/10.1029/2006JE002745

Smith, D. E., Zuber, M. T., Frey, H. V., Garvin, J. B., Head, J. W., Muhleman, D. O., et al. (2001). Mars Orbiter Laser Altimeter: Experiment summary after the first year of global mapping of Mars. *Journal of Geophysical Research: Planets, 106*(E10), 23689-23722. https://doi.org/10.1029/2000JE001364

Sori, M. M., & Bramson, A. M. (2019). Water on Mars, with a grain of salt: Local heat anomalies are required for basal melting of ice at the south pole today. *Geophysical Research Letters, 46*(3), 1222-1231. https://doi.org/10.1029/2018GL080985

Tanaka, K. L., & Kolb, E. J. (2001). Geologic history of the polar regions of Mars based on Mars Global Surveyor Data: I. Noachian and Hesperian Periods. *Icarus, 154*(1), 3-21.

Tanaka, K. L., Robbins, S., Fortezzo, C., Skinner Jr, J., & Hare, T. M. (2014). The digital global geologic map of Mars: Chronostratigraphic ages, topographic and crater morphologic characteristics, and updated resurfacing history. *Planetary and Space Science, 95*, 11-24.

Whitten, J. L., Campbell, B. A., & Morgan, G. A. (2017). A subsurface depocenter in the South Polar Layered Deposits of Mars. *Geophysical Research Letters, 44*(16), 8188-8195. https://doi.org/10.1002/2017GL074069

Whitten, J. L., Campbell, B. A., & Plaut, J. J. (2020). The ice content of the Dorsa Argentea Formation from radar sounder data. *Geophysical Research Letters, 47*(23), e2020GL090705. https://doi.org/10.1029/2020GL090705

Chapter 6

IRREGULAR POLYGONAL RIDGE NETWORKS IN ARABIA TERRA, NILI FOSSAE AND NILOSYRTIS

Aditya R. Khuller[1,2*], Laura Kerber[2], Megan E. Schwamb[3,4], Sylvia Beer[5], Fernando E. Nogal[6], Ray Perry[7], William Hood[8], Klaus-Michael Aye[9], Ganna Portyankina[10], Candice J. Hansen[11]

[1]School of Earth and Space Exploration, Arizona State University, Tempe, AZ 85281, USA

[2]Jet Propulsion Laboratory, Caltech, Pasadena, CA 91109, USA

[3]Astrophysics Research Centre, School of Mathematics and Physics, Queen's University Belfast, Belfast BT7 1NN, UK

[4]Gemini Observatory, Northern Operations Center, 670 North A'ohoku Place, Hilo, HI 96720, USA

[5]Planet Four: Ridges Team

[5]Laboratory for Atmospheric and Space Physics, University of Colorado at Boulder, Boulder, CO 80303, USA

[7]Planetary Science Institute, 1700 E. Fort Lowell, Suite 106, Tucson, AZ 85719, USA

Abstract

Numerous irregular, polygonal ridge networks have been mapped in the Nilosyrtis and Nili Fossae regions on Mars. Hypotheses ranging from impact-induced breccia dikes to mineralized fractures have been proposed for their formation. In order to constrain the range of potential formation mechanisms, we mapped the distribution of 952 morphologically similar polygonal ridge networks in Arabia Terra, Terra Sabaea, Tyrrhena Terra, Nili Fossae and Nilosyrtis across an area of 2.8×10^7 km^2, representing a 100x larger mapping area in comparison with previous studies of these regions. Of these ridge networks, 864 out of 952 (91%) are confined to Noachian-aged 'etched', 'dissected' or 'cratered' terrain, suggesting that they represent ancient records of crustal fracture and fill processes. Previous spectral analyses of selected ridges in Nili Fossae revealed that both the ridges and their host units are phyllosilicate-rich, but found that the ridges might have larger grain sizes in comparison with their host units. Our thermophysical analysis of seven ridge networks studied previously using spectral data indicates that the ridges typically have lower average thermal inertias (409 ± 120 J m^{-2} s$^{-0.5}$ K^{-1}) than their host units (477 ± 138 J m^{-2} s$^{-0.5}$ K^{-1}). These lower ridge thermal inertias are contrary to what is expected, and could be due to sub-pixel mixing with nearby detrital material. While it is not possible to determine the precise formation mechanism of these polygonal ridge networks from our new data, their formation can be assessed in terms of three possibly separate processes: (1) polygonal fracture formation, (2) fracture filling and (3) exhumation. We find that polygonal fracture formation by impact cratering and/or desiccation of sedimentary host deposits is consistent with our results and previous

spectral studies. Once the polygonal fractures have formed, fracture filling by clastic dikes and/or mineral precipitation from aqueous circulation is most consistent with our results. Exhumation, probably by aeolian processes that eroded much of these ancient Noachian terrains where the ridges are present caused the filled fractures to lie in relief as ridges today. If these ridge networks represent ancient, fossilized remnants of aqueous circulation, then our new results suggest that groundwater processes were widespread across Noachian terrain. In-situ studies by the Perseverance rover in these regions might help shed light on this potential former groundwater activity, and better constrain the formation mechanisms and histories of these ridge networks.

6.1. Introduction

Numerous irregular, polygonal ridge networks have been mapped in the Nilosyrtis and Nili Fossae regions on Mars (centered near 23°N, 70°E and 24°N, 77°E, respectively) using Mars Reconnaissance Orbiter High Resolution Imaging Experiment (HiRISE; McEwen et al., 2007a) and Context Camera (CTX; Malin et al., 2007) data. These ridge networks are characterized by intersecting, sub-rectilinear ridges (Fig. 6.1) that are formed in polygonal networks, with the individual ridges making up the polygon sides often up to 500 meters in length (Head & Mustard, 2006; Saper & Mustard, 2013; Ebinger & Mustard, 2015; Kerber et al., 2017; Pascuzzo et al., 2019b)**.** The width of the ridges often changes along strike, and also from ridge to ridge. In addition, ridges also occasionally splinter along strike (Kerber et al., 2017). The ridges are not perfectly orthogonal, and commonly have an average intersecting angle of 68° ± 17°, with a mode of 89° (Pascuzzo et al., 2019).

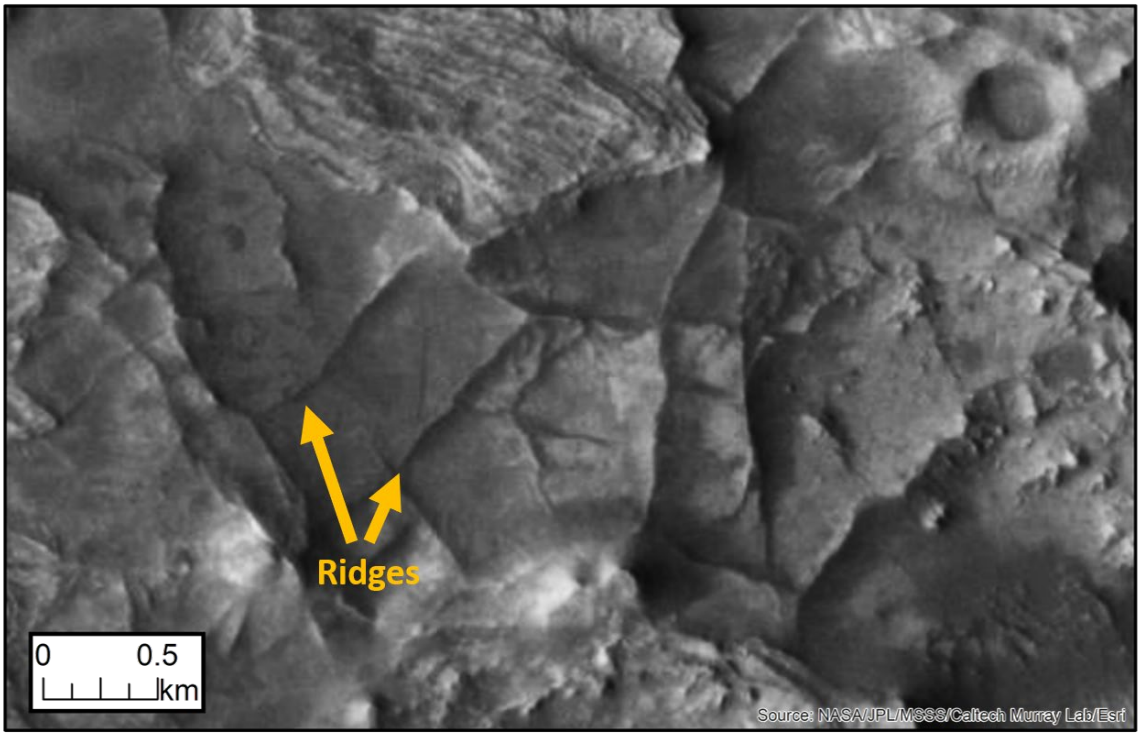

Figure 6.1. Example of a polygonal ridge network in Nili Fossae (21.8°N, 77.1°E) from CTX mosaic (Dickson et al., 2018), showing ~10-m thick, intersecting ridges enclosing irregular 100-200 m-sided polygons.

Where they have been mapped in Nili Fossae and Nilosyrtis, the polygonal ridge networks are confined to an altered, Fe/Mg-rich smectite unit that is often overlain by a stratigraphic sequence of an olivine-rich/mafic unit variably altered to carbonate, and a spectrally featureless capping unit (Mustard et al., 2009a; Ehlmann & Mustard, 2012; Goudge et al., 2015; Bramble et al., 2017; Kremer et al., 2019; Scheller & Ehlmann, 2020). [Note that in this work we refer to all units overlying the ridges stratigraphically as 'cap units', and correlate them to previously identified olivine-rich/mafic units and/or capping units (e.g., Bramble et al., 2017) when possible]. The ridges in these regions are

spectrally similar to their Noachian Mg-smectite host units, but with weaker H_2O and Fe/Mg-OH absorptions and lower spectral albedo in the Visible and Near-Infrared (VNIR) (Pascuzzo et al., 2019). The cause of the observed weaker absorptions over the ridges has been attributed to either: (1) a large grain size in the ridges versus their host units, or (2) the presence of a VNIR-featureless cementing mineral over the ridges, such as silica, some oxides, or an amorphous material that suppresses the spectral absorptions of the clay (Pascuzzo et al., 2019). Alternatively, it is possible that the ridges are composed of different minerals than their host units but are not being resolved accurately enough from orbit due to the ~18 m/pixel spatial resolution of the Compact Reconnaissance Imaging Spectrometer for Mars (CRISM; Murchie et al., 2007), or these minerals are present below the 5% detection limit of CRISM (Pascuzzo et al., 2019).

Numerous processes have been proposed for the formation of these ridge networks, such as: (1) impact-related fractures and breccia dikes (Head & Mustard, 2006; Mustard et al., 2007), (2) clastic dikes (Saper & Mustard, 2013; Pascuzzo et al., 2019b), and (3) mineralized fractures (Mangold et al., 2007; Mustard et al., 2009b; Saper & Mustard, 2013; Kerber et al., 2017; Pascuzzo et al., 2019b). In order to help constrain the ridge networks' formation mechanism, Pascuzzo et al. (2019) recently compiled ridge maps made by Saper and Mustard (2013); Ebinger and Mustard (2015, 2016) in Nili Fossae and Nilosyrtis. The resultant map, covering an area of 2.86×10^5 km^2, included ~16,000 individual ridges, although only 52% of these ridges were part of polygonal networks (Figures 2a – c and e in Pascuzzo et al. (2019) show examples of other ridges that were mapped by those authors that are not in polygonal networks). They found that

most of their mapped ridges were present outside of craters, and showed no preferential alignment to Isidis Planitia, which they interpreted to mean that the ridges were not likely to have formed as impact-breccia dikes as originally proposed by Head and Mustard (2006) and Mustard et al., (2007). Formation by magmatic dike was also ruled out by these authors, due to the ridge networks' polygonal geometry (compared to commonly parallel, en-echelon, or radial geometries for dikes) and the lack of mafic spectral signatures. Instead, they favored either cementation/lithification along fracture zones and fracture fill or shallow clastic diking into pre-existing subsurface fractures as more likely hypotheses for polygonal ridge formation.

Nili Fossae and Nilosyrtis are well studied areas of Mars, principally because a large number of mineral types have been identified in VNIR data (Bibring et al., 2006; Mangold et al., 2007; Mustard et al., 2009a; Ehlmann & Mustard, 2012), following which the region was considered as a potential landing site (Golombek et al., 2012). Thus, the polygonal ridges in this region have mostly been mapped within the context of the local area and with the purpose of understanding the region better. However, a coarse global survey conducted by Kerber et al. (2017) found instances of morphologically similar polygonal ridge networks well outside Nili Fossae and Nilosyrtis, which raised the question of whether the formation mechanism responsible for the ridges was specific to the region where they had been most extensively mapped, or more broadly applicable across the highlands. For this reason, this study was undertaken to map a much larger region, starting from previously mapped areas, and moving outwards across the highlands. In the course of this mapping, we investigated: (1) the broad regional extent of

morphologically similar polygonal ridge networks outside Nili Fossae and Nilosyrtis, (2) how the ridges relate to their regional geological and topographic context, (3) how their distribution informs us about potential formation mechanisms of the ridges, and (4) potential causes for weaker VNIR spectral absorption features over the ridges relative to their host unit. To help address these questions, we build on past surveys with detailed mapping of irregular, polygonal ridge networks (i.e., 'Nili-type' as classified by Kerber et al. (2017) and 'dense and polygonal' as classified by Pascuzzo et al. (2019)) across Arabia Terra, Terra Sabaea, Tyrrhena Terra, Nili Fossae and Nilosyrtis. Other types of ridge morphologies mapped by Kerber et al. (2017) and Pascuzzo et al. (2019) were not included in the present study. Additionally, we characterized the properties of ridge and ridge-hosting materials using thermal infrared data to independently investigate results from VNIR analyses of ridge networks (Pascuzzo et al., 2019).

6.2. Geological Setting: Arabia Terra, Terra Sabaea and Tyrrhena Terra, Nili Fossae and Nilosyrtis Regions

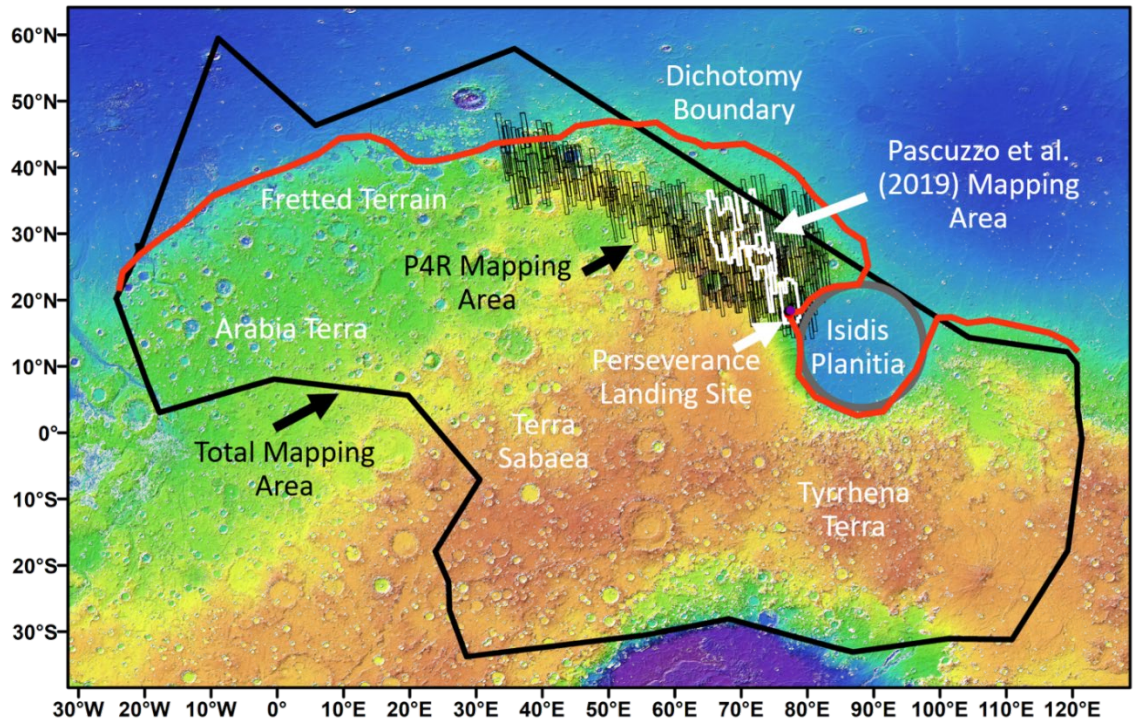

Figure 6.2. Mapped region of interest (black outline), highlighting the regions of fretted terrain in Arabia Terra, Terra Sabaea, Isidis Planitia, the dichotomy boundary (red line) and the Perseverance rover landing site (violet). The areas mapped by Planet Four: Ridges (P4R; black boxes) and Pascuzzo et al. (2019) (white boxes) are also shown for reference.

Arabia Terra (Fig. 6.2) is a region of Noachian terrain on the edge of the dichotomy boundary, encompassing an area of ~1.2×10^7 km^2 (Smith et al., 1999; McGill, 2000). The etched, dissected terrain in this region is characterized by its eroded appearance, pitted by infilled craters and depressions (Greeley & Guest, 1987; Fassett & Head, 2007). A 0.1 – 2 m thick mantle of dust is present throughout much of Arabia Terra, thought to have been deposited in the last ~10^5 years (Christensen, 1986; Fergason & Christensen, 2008). East of Arabia Terra lies Terra Sabaea, which also contains

rugged, eroded terrain with extensive faulting and degradation. This region is dominated by impact cratering and lava flows, along with erosion by fluvial and aeolian processes (Rogers & Nazarian, 2013; Irwin III et al., 2018). The dust cover in most of these two regions makes orbital spectroscopic analysis very challenging, because these techniques are only sensitive up to the upper few hundred microns of the surface in both the VNIR and the thermal infrared (TIR). Tyrrhena Terra lies further east of Terra Sabaea, and is primarily composed of etched and eroded Noachian terrain (Greeley and Guest, 1987). More recently, numerous detections of hydrated silicates have been made in Tyrrhena Terra, prompting discussion of the alteration history in the region and the hydrated minerals' possible correlation with the valley networks which are also present in and around this region (Mustard et al., 2008; Loizeau et al., 2012).

Numerous geologically distinct regions are present in the vicinity of Arabia Terra (Fig. 6.2). The northern edge of Arabia Terra (Deuteronilus Mensae, Protonilus Mensae, and Nilosyrtis Mensae) has been extensively modified by glacial processes (commonly termed fretted terrain; McGill, 2000; Levy et al., 2007). To the east of Arabia Terra is Isidis Planitia, formed by a massive impact event in the Noachian (Fassett & Head, 2011). Northeast of Isidis Planitia, near the Nilosyrtis highlands, are the Nili Fossae graben, which are likely to have formed contemporaneously or following the Isidis impact (Wichman & Schultz, 1989; Mustard et al., 2007; Scheller & Ehlmann, 2020). The Hesperian Syrtis Major volcanic complex is present in eastern Arabia Terra along the southwestern margin of Isidis Planitia (Hiesinger & Head, 2000; Bramble et al., 2017). In between Nili Fossae and Syrtis Major there are ~500 m thick layered sulfates and

Hesperian lavas in a region referred to as Northeast (NE) Syrtis (Bramble et al., 2017; Quinn & Ehlmann, 2019), which is adjacent to the landing site of the Perseverance rover (Jezero Crater). We mapped irregular polygonal ridge networks across the region outlined in Figure 6.2, encompassing large portions of Arabia Terra, Terra Sabaea and Tyrrhena Terra, including previously mapped regions in Nili Fossae, Nilosyrtis and Jezero Crater**.**

6.3. Methods

Following the discovery of additional morphologically similar ridge networks outside the well-studied regions of Nili Fossae and Nilosyrtis by Kerber et al. (2017), this project began as a citizen science project, where citizen scientist volunteers were asked to closely map Nili Fossae and Nilosyrtis, where the majority of ridges had been found previously. This original mapping area was extended to a much larger area by one volunteer (author Beer) and the results were organized by another (author Nogal). Author Khuller completed his own survey of the mapping area the following summer, validating and compiling the volunteer datasets to create one large dataset. The results were compared to each other and also to previous mapping efforts in overlapping areas to determine whether any ridge networks had been overlooked. Ridges were mapped if they matched the morphologies of previously identified ridges from Nili Fossae and Nilosyrtis Mensae/northern Terra Sabaea as described above (intersecting at sub-orthogonal angles, splintering, variable width along their length, found in a network with other similar ridges). For additional information on the citizen science project origin, see Supplementary Text 6.S1.

6.3.1. Mapping: Broad Surveys

The broad surveys were conducted over the entire mapping area by authors Khuller and Beer. Both mappers used images from CTX. Beer mapped ridge networks by accessing CTX images via Google Earth, that were then compiled into a point catalog of ridge networks by author Nogal. Khuller mapped ridge networks using a seamless global CTX mosaic (~6 m/pixel; Dickson et al., 2018) accessed using ArcGIS, creating polygons around patches of ridge networks (e.g., Fig. 6.3). Because we are interested in the process of polygonal ridge network formation, only ridge networks present in polygonal patterns were mapped, and locations where an isolated ridge (as mapped by Pascuzzo et al. (2019), for example) was present were ignored. No measurements of ridge orientations or ridge junction angles were made. The distribution of ridges was then assessed relative to local geography and geological maps of the region as mapped by Scott and Tanaka (1986); Greeley and Guest (1987), and the topographic characteristics (slope and elevation) of the ridge networks were determined by comparing mapped polygons to Mars Orbiter Laser Altimeter (MOLA) 128 pixel per degree data (Smith et al., 2001a), using the spatial intersection tools in ArcGIS and JMARS (Christensen et al., 2009b), respectively.

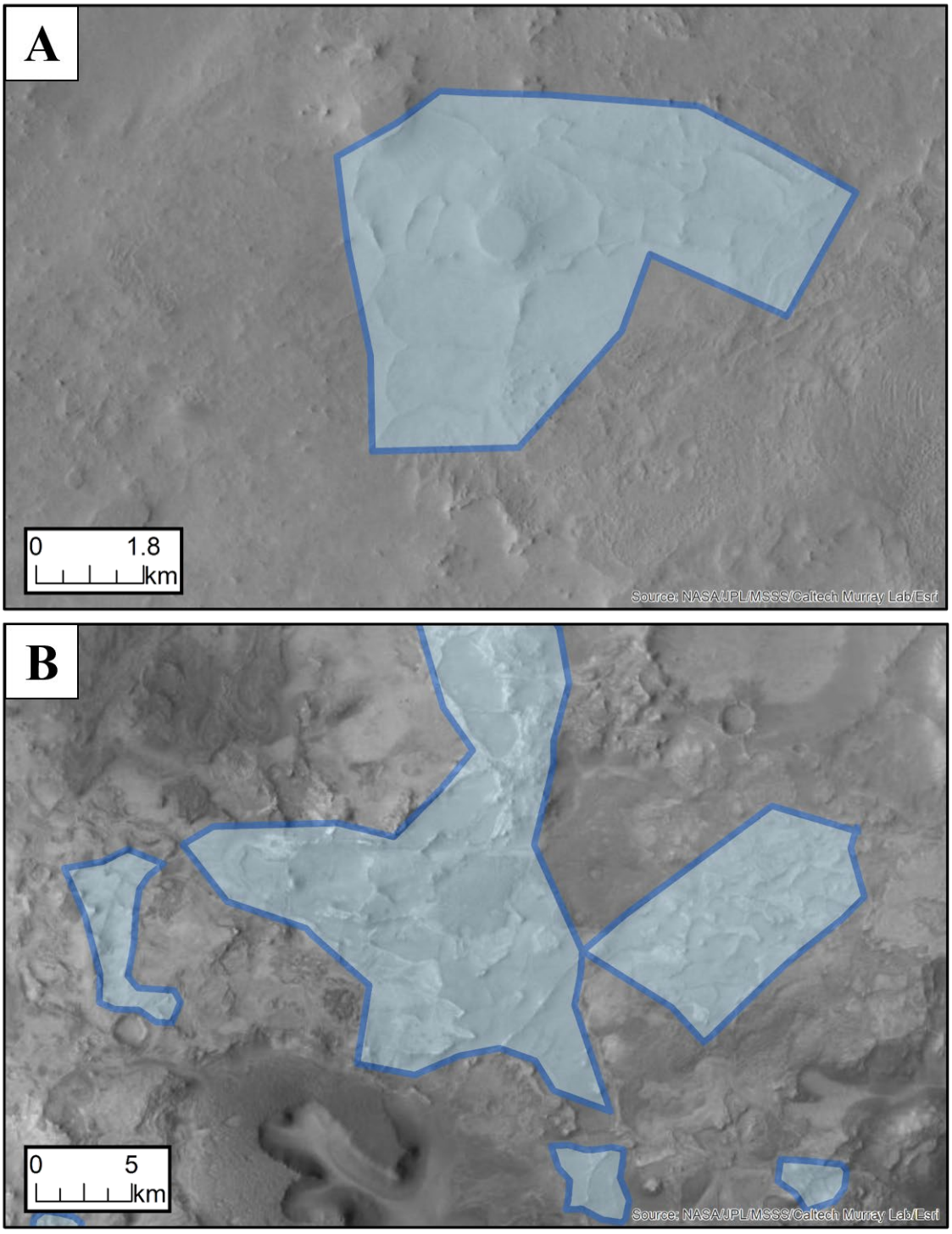
A
0 1.8
km
Source: NASA/JPL/MSSS/Caltech Murray Lab/Esri
B
0 5
km
Source: NASA/JPL/MSSS/Caltech Murray Lab/Esri

Figure 6.3. Examples of polygons (blue) drawn around ridge networks at a) 30.2°N, 69.3°E and b) 22.4°N, 77.1°E. Each polygon shown represents one polygonal ridge network in our dataset.

These two surveys were compared and combined by Khuller into one large broad survey output, from -24° to 120°E, 33°S to 60°N. This mapped region covers an approximate area of 2.8×10^7 km^2, representing a mapping area 100x larger than that of Pascuzzo et al. (2019). Ridges in the survey area that did not meet the criteria of polygonal networks (e.g., 'Meridiani-type ridges'; Kerber et al. (2017), or 'short anastomosing'; Pascuzzo et al. (2019)) were excluded.

6.3.2. Mapping: Planet Four: Ridges

The detailed, systematic citizen scientist ridge network survey was conducted on a subset of the larger mapping area in Nili Fossae and parts of Nilosyrtis/northern Terra Sabaea with the help of citizen scientist volunteers through the Planet Four: Ridges (P4R) project, which is hosted on the Zooniverse platform. The P4R project works by combining multiple non-expert assessments to identify polygonal ridge networks in images. In the following sections, we describe how the CTX images were prepared, the P4R classification interface, and our technique for combining responses from volunteer reviews to identify polygonal ridge networks.

6.3.2.1. CTX Image Preparation and P4R Subject Creation

Each CTX image used by the P4R project (Fig. 6.S1**)** was cut up into smaller subimages, which we refer to as 'subjects'. A P4R volunteer reviews one subject at a time on the P4R website. To create the P4R subjects from the CTX full frame images, we

use the same software and techniques as Zooniverse's Planet Four: Terrains project (Schwamb et al., 2018). First, raw CTX Experiment Data Record images were downloaded and processed (radiometric calibration and noise removal). These processed images were then map-projected using Pysis (http://pysis.readthedocs.io/en/latest) and ISIS3 (Becker et al., 2007). The resulting images were then cut into smaller, non-overlapping 800 × 600-pixel (~4.8 × 3.6 km) subimages that were subsequently uploaded to the P4R website, becoming P4R subjects. The full list of CTX images reviewed on the P4R website along with the number of subjects is given in Supplementary Material Table 1 (https://doi.org/10.1016/j.icarus.2021.114833).

6.3.2.2. Classification Interface

The P4R classification interface (Fig. 6.4) was built using Zooniverse's Project Builder platform (https://www.zooniverse.org/lab) to allow volunteers to identify polygonal ridge networks. This classification interface provides a tutorial and other help content, including examples of polygonal ridge networks to assist volunteers. A volunteer is shown a single image to visually inspect and confirms whether there are polygonal ridge networks visible within the image. To submit their response (which we refer to as a classification), the volunteer clicks on either the "Done & Talk" button, which takes the individual to a discussion tool, or "Done", which loads the next image to be reviewed. Classifications are stored in the Zooniverse database as described in Schwamb et al. (2018).

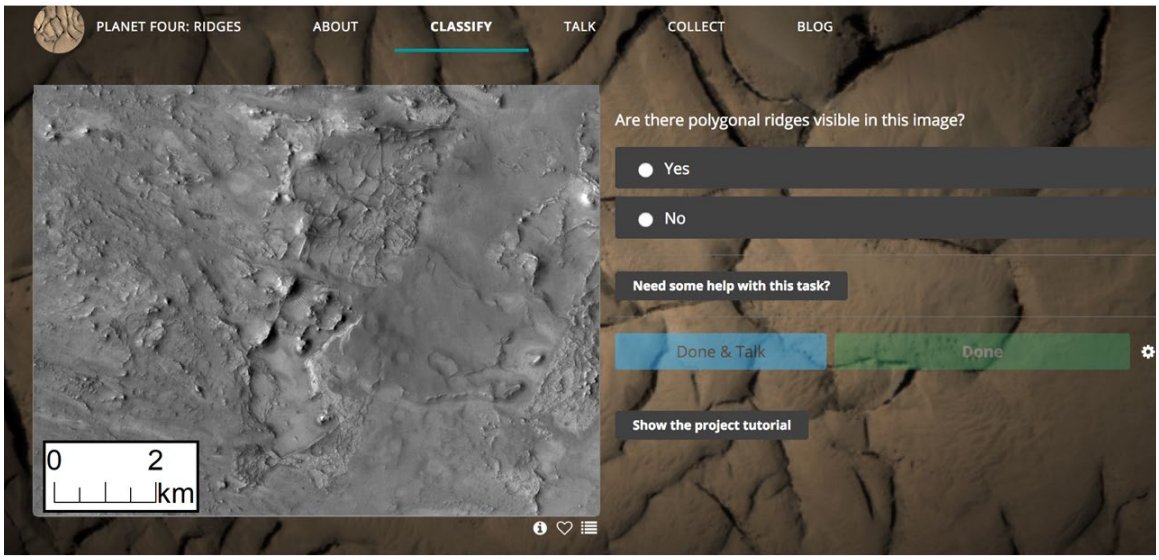

Figure 6.4. The Zooniverse user interface for classifying ridge network images. There is a polygonal ridge network in this sample image (27.9°N, 73°E).

6.3.2.3. Polygonal Ridge Network Identification and P4R Validation

Ten independent volunteers are presented with each P4R subject and assess if there are polygonal ridge networks present. We combine the equally weighted assessments together, taking the majority vote, i.e., if 70% of the P4R volunteers reviewing a given subject image identified polygonal ridges, then this is counted as a positive detection. Author Kerber examined all these positive detections and filtered out any images without at least one ridge in them. The remaining positive detections were compiled as points on a map. These ridge network location points were then further analyzed, validated, and combined with the broad surveys by Khuller using the global CTX mosaic.

6.3.3. Thermophysical analysis of selected ridge networks

To independently investigate the results from VNIR analyses of ridge networks in the well-studied regions of Nili Fossae and Niloysrtis (Pascuzzo et al., 2019), seven ridge networks were analyzed using Mars Odyssey's Thermal Emission Imaging System (THEMIS; Christensen et al., 2004) data (100 m/pixel) in JMARS. We used THEMIS nighttime thermal infrared temperature data (band 9; 3 – 5 Local Solar Time (LST)), which are primarily indicative of a material's thermophysical properties, when the effects of surface albedo and topography are greatly reduced (Christensen et al., 2003). The absolute temperature error of these data range from 0.4 K at 245 K to 1.1 K at 180 K. THEMIS nighttime thermal infrared data is sensitive to a few diurnal thermal skin depths, i.e., on the order of ~20 centimeters for most geologic materials (Christensen et al., 2003). We selected ridge networks that were previously analyzed using CRISM data by Pascuzzo et al. (2019) to independently assess their thermophysical properties. All selected THEMIS images were filtered (http://viewer.mars.asu.edu/viewer/themis#T=0) by the IR calibration flag parameter (a value of 0 indicates a useable image) to ensure that no artifacts were present in the image.

We used a one-dimensional planetary thermal model (KRC; Kieffer, 2013) to derive the thermal inertia from representative nighttime temperature pixels from ridge and ridge-hosting units. Note that only locations where the "fractured, bright-toned host" unit (Pascuzzo et al., 2019) was exposed at THEMIS temperature pixel spatial scale (100 m/pixel) were analyzed to facilitate a fair comparison with their VNIR results. As inputs for the thermal model, topography data was obtained from the KRC layer in JMARS, albedo values were taken from 18 m/pixel THEMIS visible Lambert albedo products

(Edwards et al., 2011) over the same pixel locations. Three ridge networks did not have THEMIS albedo data available, so we assumed albedos of 0.23 and 0.24 (i.e., the average values derived from other observations used) for the ridges and the host unit in those cases, respectively (Table 6.1). Local atmospheric dust opacity values were derived from the online Mars Climate Database under average Mars Year conditions (http://www-mars.lmd.jussieu.fr/mcd_python/) (Forget et al., 1999; Millour et al., 2018). Input parameters used are summarized in Supplementary Material Table 2 (https://doi.org/10.1016/j.icarus.2021.114833). The resultant thermal inertia uncertainty using this method is about 15 – 20%, primarily depending on how different the true albedo of the surface is from the THEMIS visible albedo values (see Figure 1 in Fergason et al., 2006b for additional details on thermal inertia uncertainties).

The derived thermal inertia is primarily affected by the material's particle size and/or degree of cementation, and it is not possible to separate the two effects without in-situ studies. A material's effective particle size can be derived from its thermal inertia quantitatively if the thermal inertia is less than 350 $J\ m^{-2}\ s^{-0.5}\ K^{-1}$ (Presley & Christensen, 1997a; Fergason et al., 2006b). When doing so, it is assumed that the surface is not indurated, and unconsolidated to depths of several diurnal skin depths (Presley & Christensen, 1997a). For values of thermal inertia > 350 $J\ m^{-2}\ s^{-0.5}\ K^{-1}$, the effective particle size cannot be uniquely determined (Presley and Christensen, 1997). In the presence of cement, numerical models have shown that < 3% cement can raise the thermal inertia of martian soil from 260 to 650 – 750 $J\ m^{-2}\ s^{-0.5}\ K^{-1}$ (Piqueux & Christensen, 2009). These relatively small fractions of cement, which might be in the

form of salts, oxides, etc. may be undetectable using VNIR CRISM data, because CRISM's detection limit for distinct minerals is 5% by volume (Pascuzzo et al., 2019). In any case, if the ridges either have a larger grain size, and/or are cemented compared to their host unit, we would expect them to have a higher thermal inertia.

6.4. Observations

6.4.1. Ridge Network Distribution and Comparison with Previous Studies

6.4.1.1. Overall Distribution and P4R Validation

Ridge networks were found to be concentrated in the Nili Fossae and Nilosyrtis/northern Terra Sabaea regions (Fig. 6.5). New, previously undetected ridge networks were also found across Arabia Terra, Terra Sabaea and Tyrrhena Terra, with the total area covered by ridge networks equal to ~11,960 km^2 (total polygon area calculated using ArcGIS). Almost all the ridge networks identified are either west or south of Isidis Planitia, with only one group of ridge networks mapped east of 80°E.

Comparing P4R (white dots) and Kerber et al. (2017) results (orange) indicates that 66% of all final polygonal ridge networks identified by P4R were not detected by Kerber et al. (2017). Conversely, 30% of the ridge networks mapped by Kerber et al. (2017) were not marked as ridge networks by P4R within the P4R mapping region (Fig. 6.5b), partly because Kerber et al.'s (2017) survey focused on HiRISE images and therefore found smaller ridge networks that could be missed in CTX images by P4R. Additionally, Kerber et al.'s (2017) survey mapped ridge network clusters (combining many groups of polygonal ridge networks that were separated by a few kilometers into one cluster) rather than individual ridge networks (as shown in Fig. 6.3, for example), meaning that empty

terrain between ridge clusters was also included into mapping polygons. Note that all comparisons with the P4R points were buffered by 3 km because these points represent the centers of the CTX images analyzed i.e., 3 km represents the distance from the P4R center points to the diagonal edges of the CTX subimages analyzed.

Comparing the final map results (blue) with the P4R points shows that 813 out of 1,016 (80%) of all P4R points were included in the final map results (Fig. 6.5a), i.e., 203 (20%) of all P4R points were false positives where ridges (in networks) were not present. Most (64%; 23 out of 36) ridge networks identified by Kerber et al. (2017) also correspond to the final map results. However, whereas Kerber et al. (2017) only identified 36 clusters of ridge networks within our overall mapping area, 952 ridge networks were mapped in this work (final map results).

6.4.1.2. Comparison with Previous Studies

A comparison between the final map results and all the ridge types mapped by Pascuzzo et al. (2019) (black lines) is shown in Figure 6.4c. 40% of all the ridge types mapped by Pascuzzo et al. (2019) overlap with our final map results. However, only 52% of all the ridges mapped by Pascuzzo et al. (2019) were “dense and polygonal”. Thus, at least 12% of their “dense and polygonal” ridges did not meet our mapping criteria because they appeared to be present in mostly isolated segments, rather than in a polygonal ridge network. Meanwhile, some of our final map results (14%) did not overlap with any of their ridges, meaning that they were considered to be polygonal by us but not mapped by them. The variations in results between mappers and mapping approaches reflect the nature of the polygonal ridge networks: a broad view (the scale of

an entire CTX image) is needed to assess whether or not the largest ridges are part of polygonal networks, but full HiRISE resolution or better is sometimes needed to identify the very smallest networks (indeed, clay-rich ridge polygonal networks similar to those mapped here have even been found at the rover scale at Gale Crater (Léveillé et al., 2014)). A significant proportion of morphologically similar ridges in the mapped regions are not actually part of polygonal networks, and the choice to include or exclude such ridges can lead to local discrepancies in mapped extent between workers. However, while differing in details, the general regions where ridges can be found match well between maps.

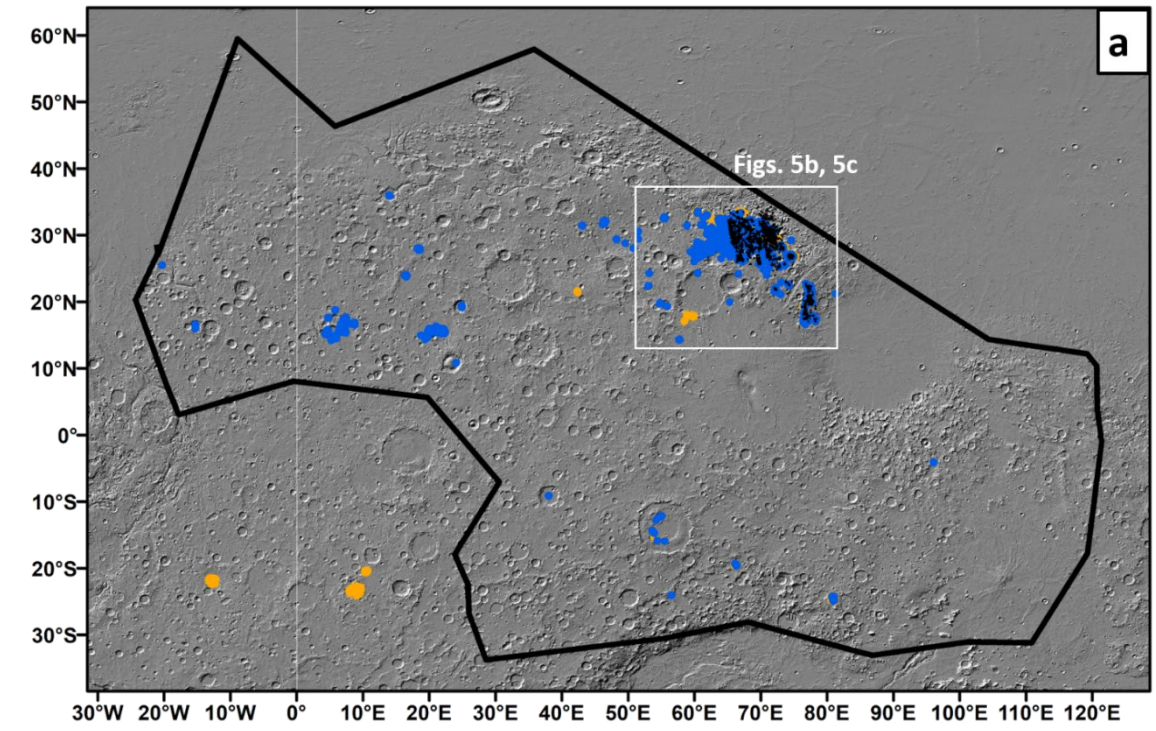
a
Figs. 5b, 5c
60°N
50°N
40°N
30°N
20°N
10°N
0°
10°S
20°S
30°S
30°W 20°W 10°W 0° 10°E 20°E 30°E 40°E 50°E 60°E 70°E 80°E 90°E 100°E 110°E 120°E

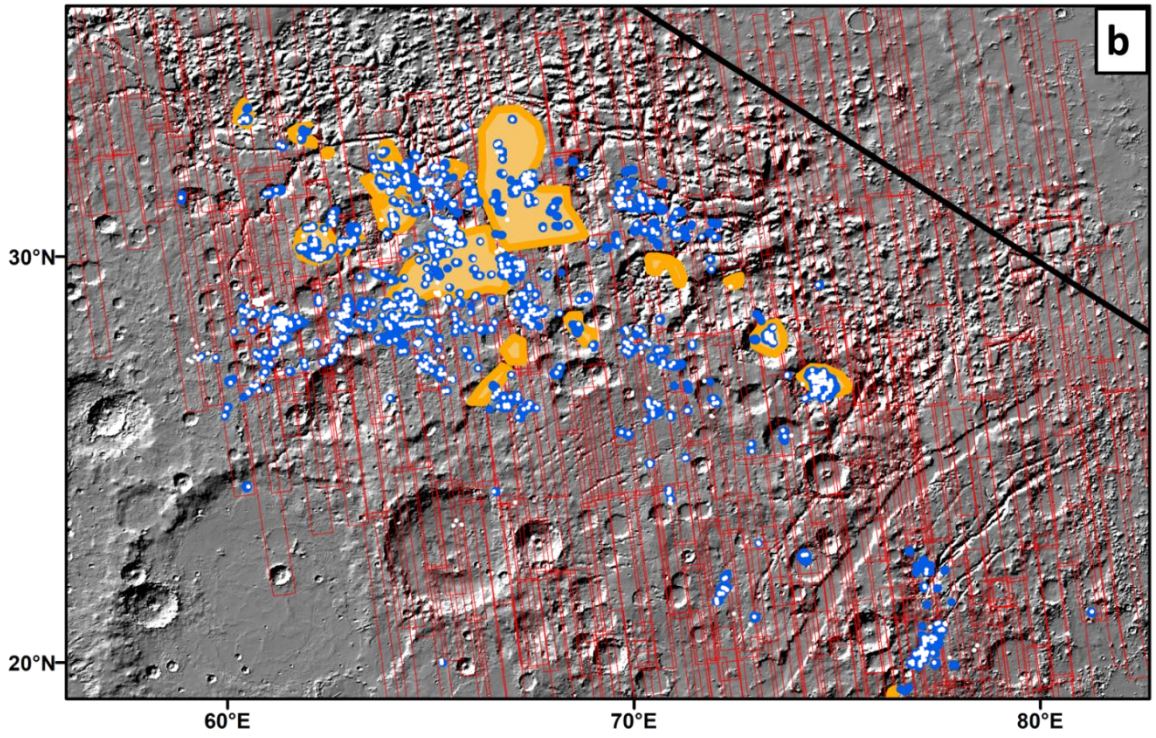
b
30°N
20°N
60°E
70°E
80°E

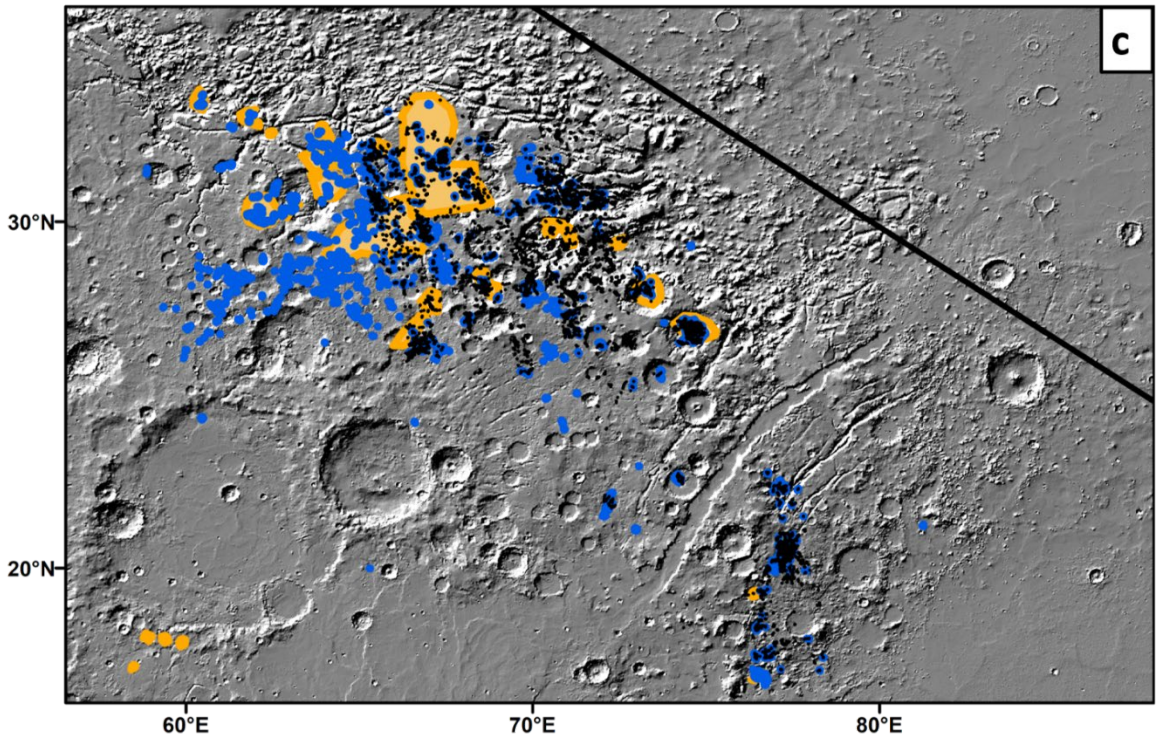

Figure 6.5. (a) The distribution of polygonal ridge networks found in the mapping region (black outline), including results from the two broad surveys and detailed Planet Four: Ridges survey (blue). Orange polygons show ridge networks previously identified by Kerber et al. (2017) within the mapping region. Black lines show all ridges mapped by Pascuzzo et al. (2019). (b) Comparison between ridge networks identified by P4R (white), Kerber et al. (2017) (orange) and the final map results (blue) within a portion of the mapped extent (black line). Areas (CTX images) studied by P4R are shown in red boxes. (c) A close-up of a subset of the mapping region, showing details of the differences between mapping techniques (ridges west of 65° E are outside the Pascuzzo mapping area).

6.4.1.3. Relation with Local Geological Maps

Figure 6.6a shows the relationship between polygonal ridge networks and geologic maps of this region, simplified to highlight major units/materials and corresponding epochs (Scott & Tanaka, 1986; Greeley & Guest, 1987; Skinner Jr & Hare, 2006). Although there are a few exceptions (e.g., Fig. 6.6c), most (91%) polygonal ridge networks (e.g., Fig. 6.7**)** were found in Noachian 'etched', 'dissected' or 'cratered' terrain (Fig. 6.6b) as mapped by Scott and Tanaka (1986) and Greeley and Guest (1987) using the spatial intersection tool in ArcGIS. However, while most of the region is covered with these Noachian terrains (green areas in Fig. 6.6), polygonal ridge networks are visible only in patches in these areas, apart from the dense cluster around Nili Fossae. One unusual polygonal ridge network that borders Noachian 'dissected' terrain is present within a Hesperian 'ridged' unit in the global geologic map and displays groups of junctions that are more regular and orthogonal than typical ridge networks, based on their morphology (see Fig. 6.8a).

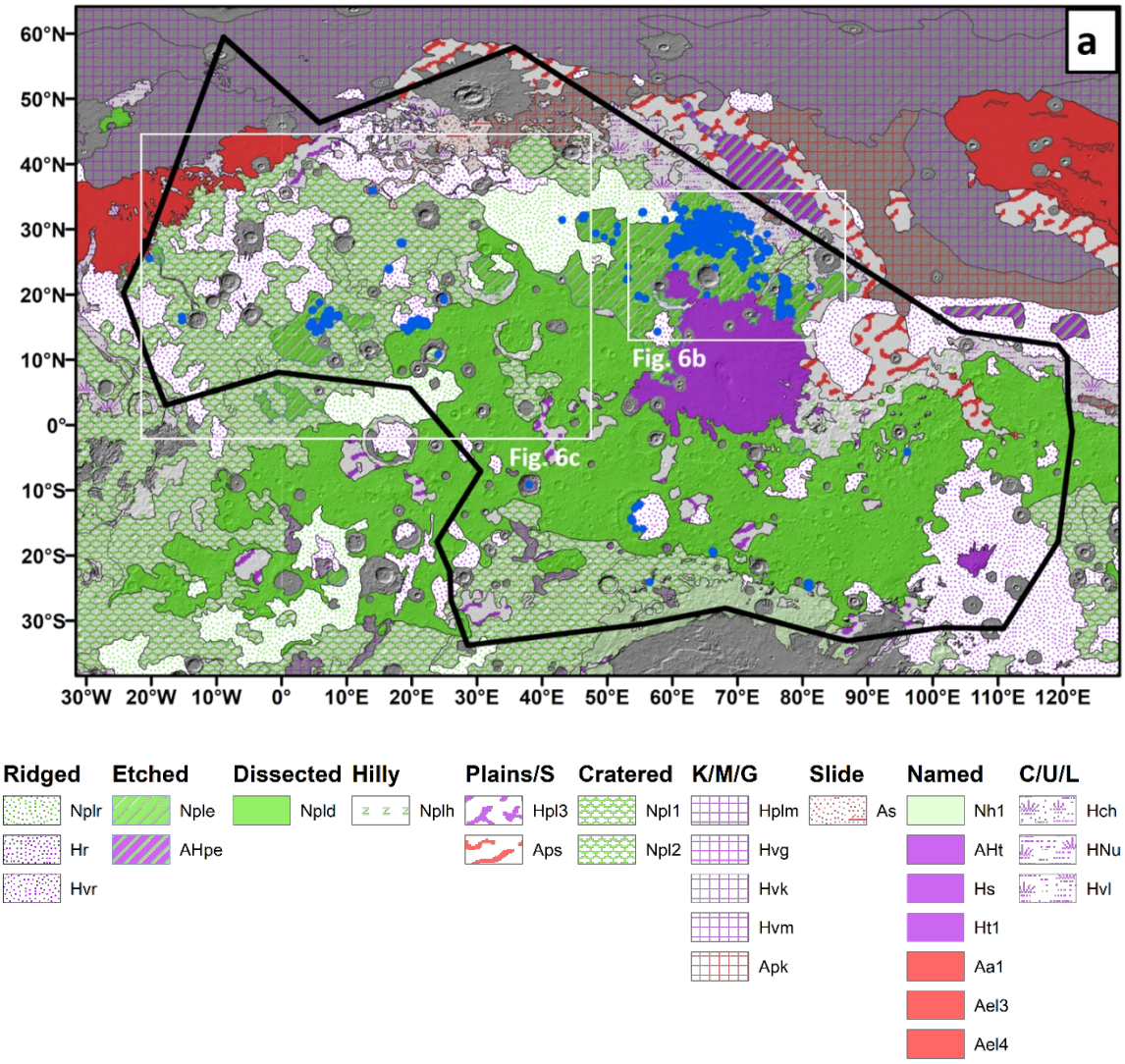
a
Fig. 6b
Fig. 6c
60°N
50°N
40°N
30°N
20°N
10°N
0°
10°S
20°S
30°S
30°W 20°W 10°W 0° 10°E 20°E 30°E 40°E 50°E 60°E 70°E 80°E 90°E 100°E 110°E 120°E
Ridged
Nplr
Hr
Hvr
Etched
Nple
AHpe
Dissected
Npld
Hilly
Nplh
Plains/S
Hpl3
Aps
Cratered
Npl1
Npl2
K/M/G
Hplm
Hvg
Hvk
Hvm
Apk
Slide
As
Named
Nh1
AHt
Hs
Ht1
Aa1
Ael3
Ael4
C/U/L
Hch
HNu
Hvl

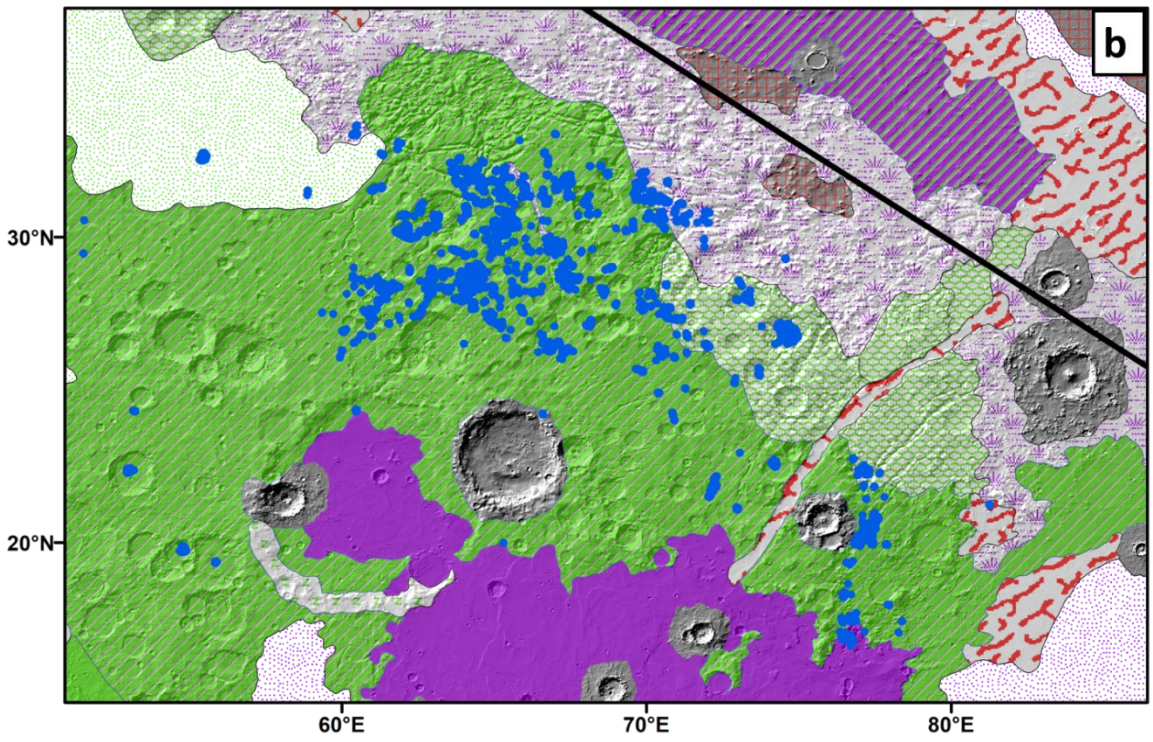
b
30°N
20°N
60°E
70°E
80°E

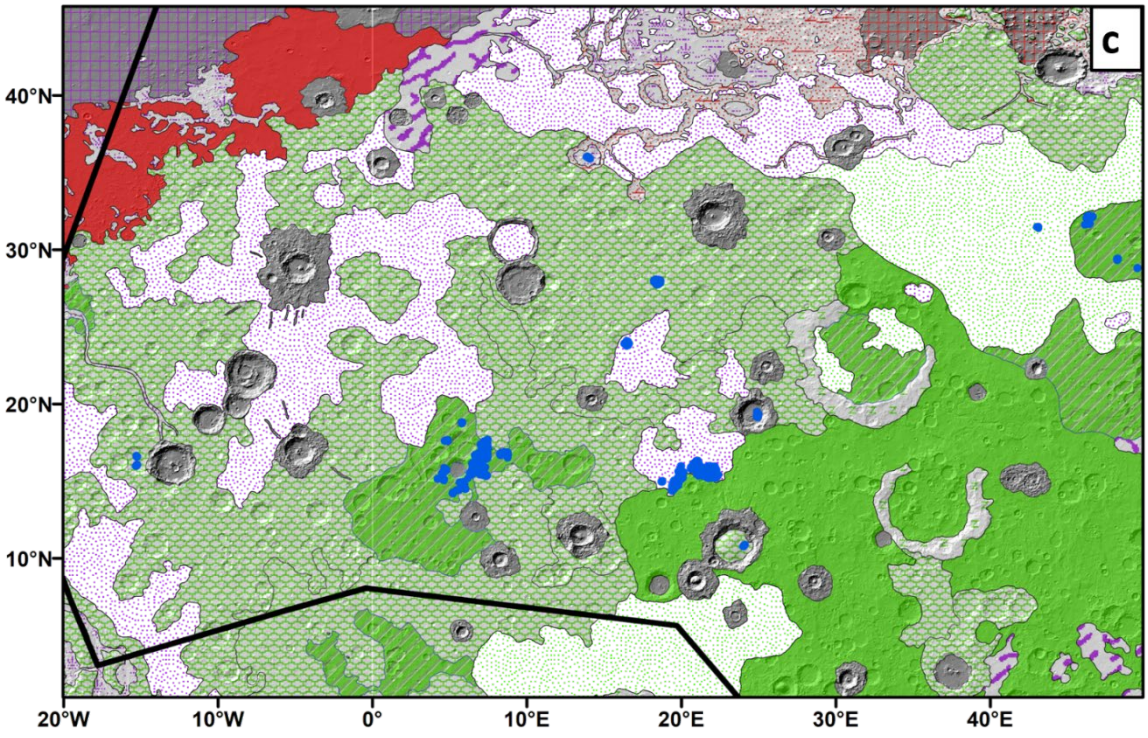
c
40°N
30°N
20°N
10°N
20°W
10°W
0°
10°E
20°E
30°E
40°E

Figure 6.6. Polygonal ridge networks (blue) within mapped extent (black line) shown on geologic map based on Scott and Tanaka (1986); Greeley and Guest (1987) overlaid on Mars Orbiting Laser Altimeter (MOLA) shaded topography. Noachian, Hesperian and Amazonian-aged units are marked in green, violet and red patterns respectively (Legend: **Ridged**: Hr: Ridged plains, Hvr: Ridged member, Nplr: Ridged unit; **Etched:** Ahpe: etched plains, Nple: Etched unit; **Dissected:** Npld: Dissected unit; **Hilly:** Nplh: Hilly unit; **Plains/Smooth:** Aps: Smooth plains, Hpl3: Smooth unit; **Cratered:** Npl1: Cratered unit, Npl2: Subdued cratered unit; **Knobby/Mottled/Grooved:** Apk: Knobby plains, Hplm: Mottled plains, Hvg: Grooved, Hvk: Knobby, Hvm: Mottled; **Slide:** As: Slide; **Named:** Nh1: Basin-rim, Aht: Tyrrhena Patera, Hs: Syrtis Major, Ht1: Tharsis montes member 1, Aa1: Arcadia Formation members 1, Ael3, 4: Elysium Formation members 3, 4; **Older Channel/Undivided/Layered:** HNu: Undivided, Hch: Older channel, Hvl: Layered). Polygonal ridge networks appear almost exclusively in 'etched', 'dissected' or 'cratered' terrain.

6.4.2. Morphology and Relation to Surrounding Units

While all of the ridge networks mapped in this work meet the mapping criteria (intersecting at sub-orthogonal angles, splintering, variable width along their length, found in a network with other like ridges), there are qualitative differences in polygonal patterns, and the scale of erosion and exhumation that has exposed them (Fig. 6.7). The size of individual polygonal cells enclosed by ridge networks vary between different ridge networks, and the mean ridge network area (13 km^2) calculated using ArcGIS geometry tools has a large standard deviation of ± 44 km^2 (n = 952 samples). Evidence

for aeolian activity (e.g., dunes, transverse aeolian ridges (TARs), etc.) that could be related to the formation of the etched/dissected terrain where most of these ridge networks are present (Fassett & Head, 2007; Fergason & Christensen, 2008; Ivanov et al., 2012) is common near most ridge networks.

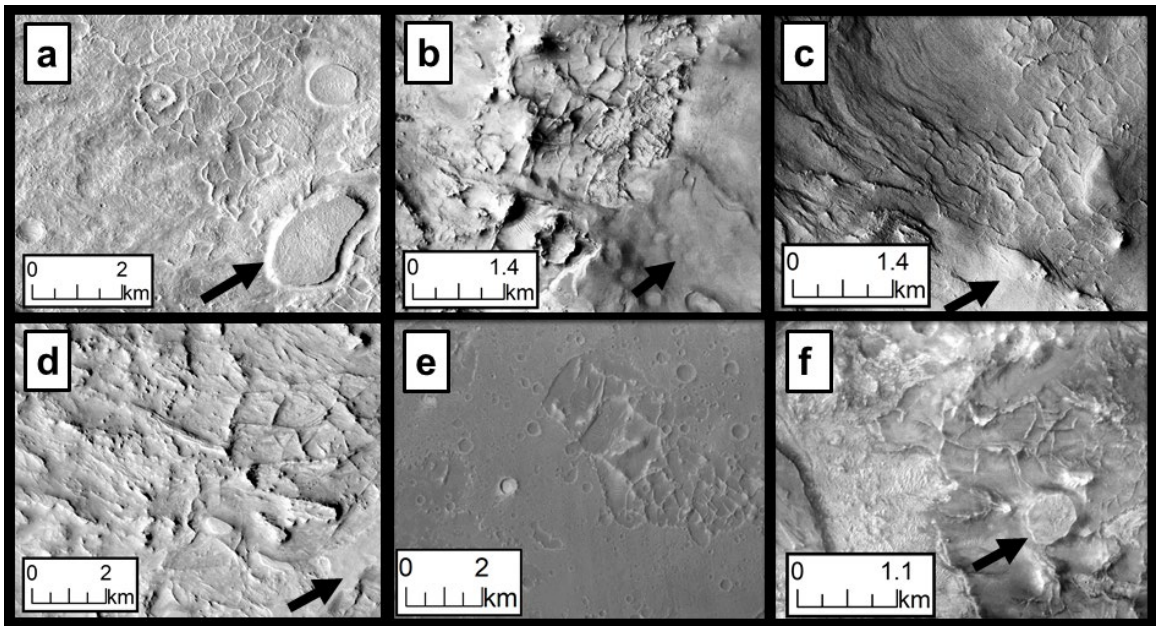

Figure 6.7. Typical polygonal networks observed in this survey. (a) Ridge network in Nilosyrtis adjacent to mesa (centered at 31.4°N, 69.6°E), (b) Ridge network in Nili Fossae exhumed from under mantling unit in etched Noachian terrain (centered at 20.2°N, 76.9°E), (c) Partially exhumed ridge network in a crater in Arabia Terra (centered at 15°N, 18.7°E), (d) Ridge network, mantling unit and mesas in North East (NE) Syrtis (centered at 27.9°N, 73°E), (e) Ridge network being exhumed within cratered terrain in Arabia Terra (centered at 16.6°N, -15.3°E) and (f) Nearest (~26 km) observed ridge network (centered at 18.2°N, 76.5°E) to the Perseverance rover landing site. All

images are portions from the global CTX mosaic (Dickson et al., 2018). Arrows indicate observations of mantling unit near ridge networks.

In a few cases (Fig. 6.8)**,** the mapped ridge networks appear morphologically distinct in terms of geometry and tone (relative reflectance at CTX wavelength, i.e., 611 nm). For example, a group of particularly orthogonal ridges are present at 15.6°N, 21.6°E (Fig 6.8a). These ridges appear in a densely cratered region that is mapped as a Hesperian unit by Greeley and Guest (1987). Distinct variations in tone are also observed. Figures 6.8b-d show ridge networks adjacent to unusually light and dark-toned materials that might indicate compositional differences. In one case (Fig. 6.8d), these light-toned materials have been identified as sulfate-rich deposits using CRISM data (Quinn & Ehlmann, 2019).

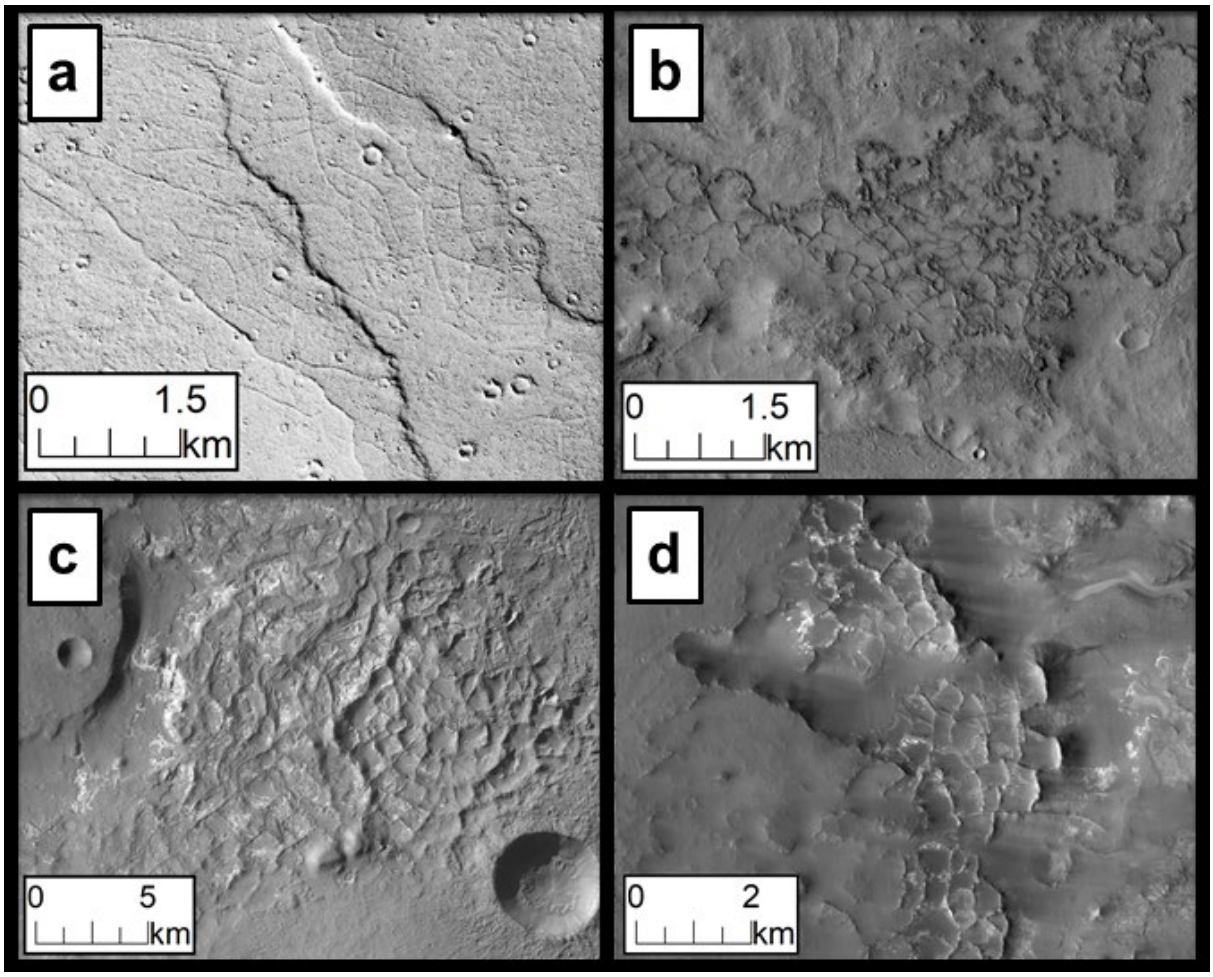

Figure 6.8. Unusual polygonal ridge networks observed in this survey. (a) Ridge network with unusually orthogonal junctures observed in a Hesperian unit (Hr) (Scott and Tanaka, 1986; Greeley and Guest, 1987), centered at 15.6°N, 21.6°E, (b) Atypical dark material adjacent to partially exhumed ridge network, centered at 32°N, 46.5°E, (c) Network with anomalously wide ridges and lighter toned materials, centered at 24.8°S, 80.9°E and (d) Jarosite-rich ridges present within layered sulfate deposits (Quinn and Ehlmann, 2019) in NE Syrtis, centered at 17.4°N, 76.4°E. All images are portions from the global CTX mosaic (Dickson et al., 2018).

We find that 123 (13% of total) of the ridge networks are present within impact craters with discernable rims at CTX resolution. Erosional mesas and buttes with irregular edges are often present near most polygonal ridge networks. Much of the surrounding regions near the ridge networks appear relatively smooth and featureless, likely due to mantling by dust. In some cases, it is possible to identify previously mapped units (e.g., olivine-rich unit) near ridge networks in Nili Fossae that are stratigraphically higher than the ridges. However, without the use of spectral data throughout the mapped extent in the dust-covered regions of Arabia Terra and Terra Sabaea, it is difficult to confirm whether morphologically similar units that lie stratigraphically above the polygonal ridge networks are the same as those around Nili Fossae.

6.4.3. Topographic Characteristics

Ridge networks are found in a wide range of differing elevations and slopes (~ -3,700 m within crater floors, up to ~2,200 m in Syrtis Major; Fig. 6.9a), based on Mars Orbiting Laser Altimeter (MOLA) data (Smith et al., 2001a). The mean ridge network elevation is ~ -860 ± 990 m (n = 68,643 MOLA data points lying within our mapped ridge network polygons), with a median of about -1,080 m. Most ridge networks are found at low (< 7°) slope angles (Fig. 6.9b), with a mean slope angle of ~2.1 ± 2.4° (n = 68,643 MOLA data points lying within our mapped ridge network polygons) and a median of 1.2°.

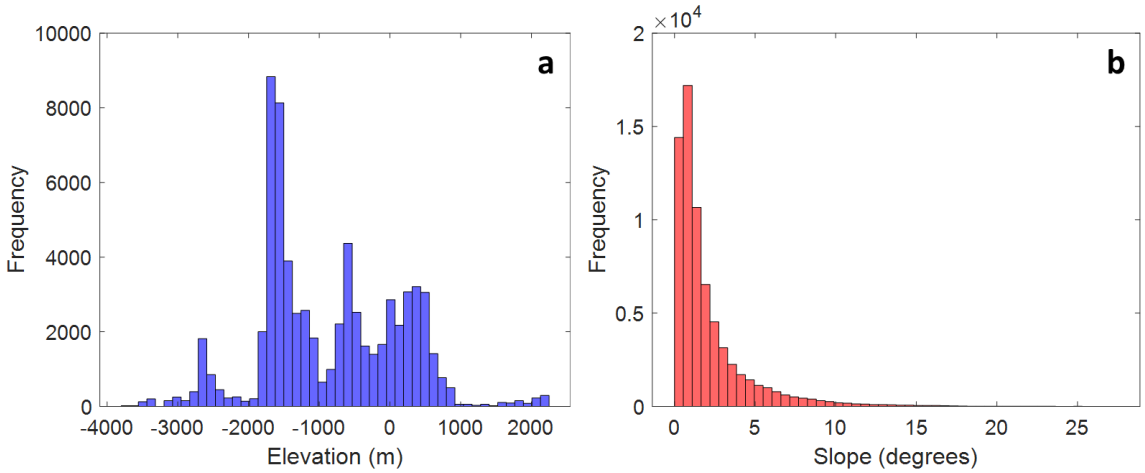

Figure 6.9. Histograms showing (a) Elevation and (b) Slope of mapped polygonal ridge networks derived from Mars Orbiter Laser Altimeter 128 pixels per degree data (Smith et al., 2001a).

The ridges are often confined to a stratigraphically lower unit with respect to the local environment. In Nili Fossae, this stratigraphically lower host unit has been found to be phyllosilicate-rich based on VNIR spectral data (Mustard et al., 2007; Pascuzzo et al., 2019b). A HiRISE Digital Terrain Model (DTM; ~1 m/pixel) of an area of ridges where phyllosilicates have been identified previously (e.g., Mustard et al., 2007) is shown in Figure 6.10. The ridges are ~10 m high relative to their immediate surroundings, with the phyllosilicate-rich unit ~100 m lower than the neighboring olivine-rich (Mustard et al., 2007) cap unit. This result suggests that at least ~100 meters of material was removed to expose the ridges at the surface. Alternatively, the ridges could have formed on a local slope, indicating less erosion. However, most ridge networks are present on relatively flat surfaces (Fig. 6.9), including at this location (slope angles < 2°).

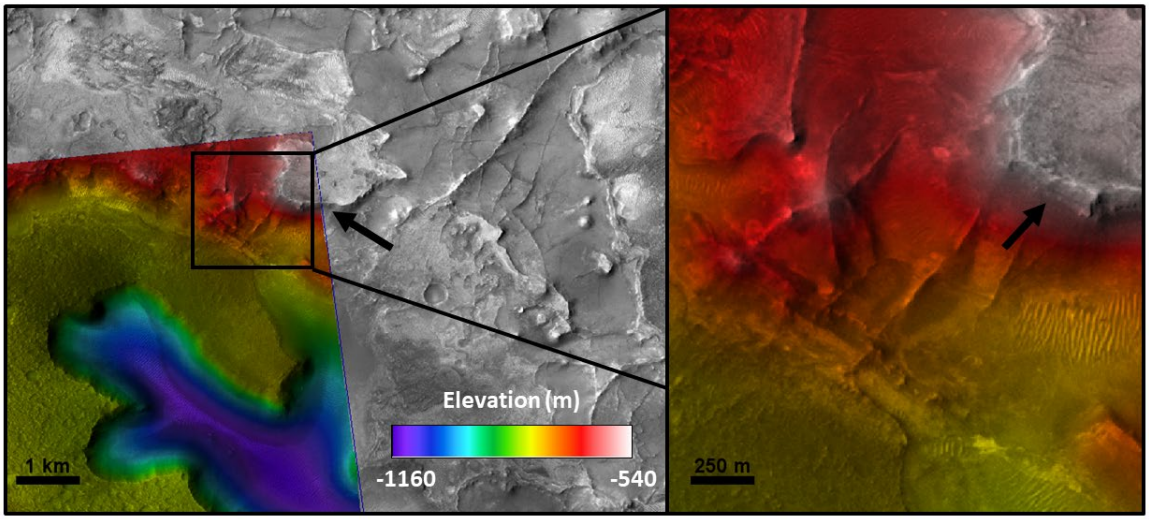

Figure 6.10. (Left) Context from grayscale CTX image D01_027691_2025 for (black box; right) colorized HiRISE DTM DTEEC_002888_2025_002176_2025_A01, centered at 22.2°N, 77°E. Ridges are ~10 m higher than their host units, while the host units are ~100 m lower than neighboring mafic cap rock (arrows).

6.4.4. Thermophysical Properties

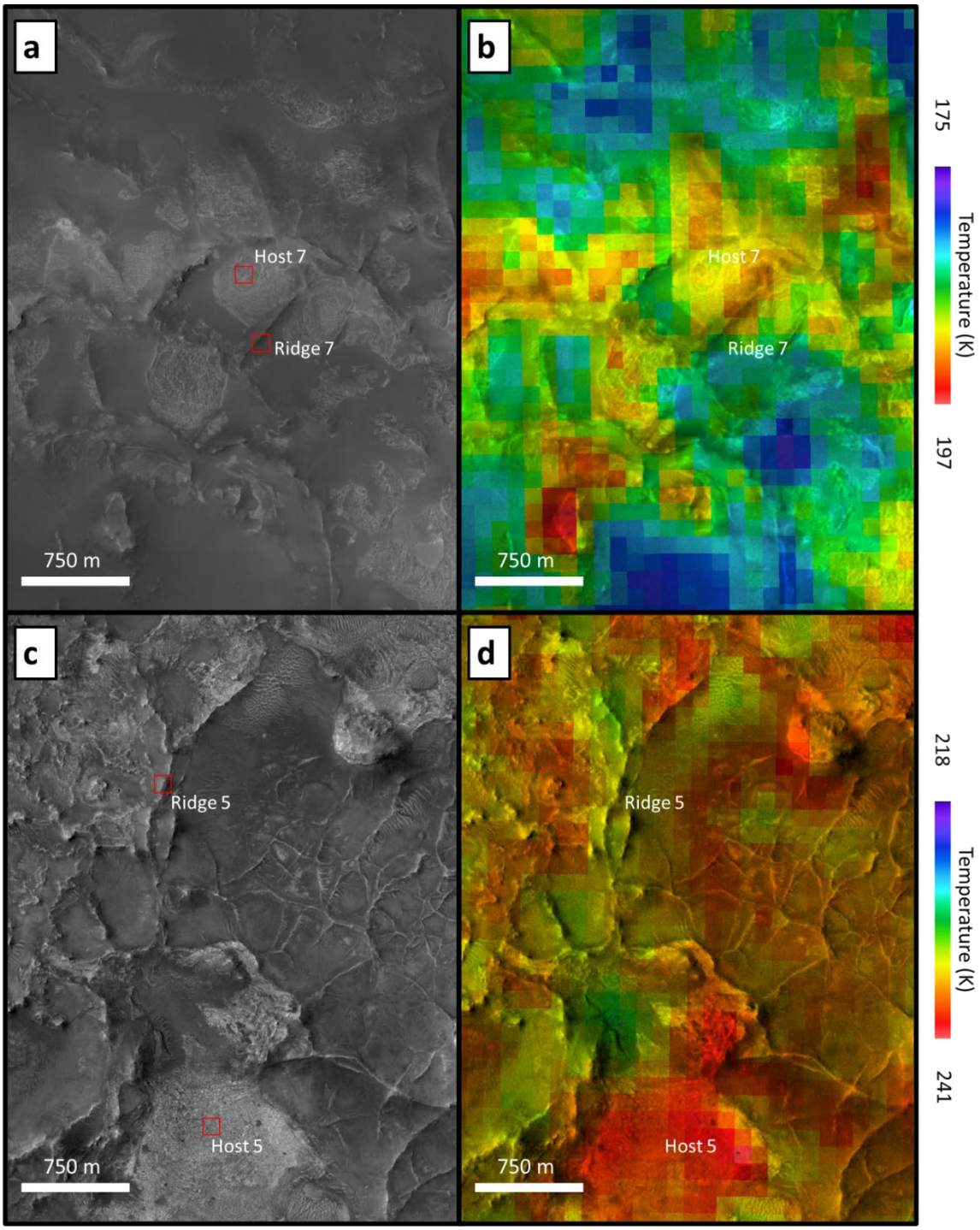

Figure 6.11. Visible wavelength HiRISE images (left) and nighttime thermal infrared images overlaid on the CTX visible mosaic (right) showing locations (red boxes) chosen

to analyze thermophysical properties of ridge and ridge-hosting materials. See **Table 6.1** for image details.

Figure 6.11 shows two examples of variations in nighttime temperature between ridge-hosting and ridge units. In both cases, the host unit is warmer than the ridge, by 2 K (Fig. 6.11b) and 7 K (Fig. 6.11d). Only a few ridges span 1-2 complete THEMIS pixels, so sub-pixel mixing is likely to occur. Sub-pixel mixing with nearby cooler detrital materials would cause ridge temperatures to be underestimated, although the presence of boulders on top of ridges (Pascuzzo et al., 2019) can result in elevated temperatures. Variations in THEMIS temperature and visible wavelength reflectance (e.g., in HiRISE images) are observed along ridge lengths in most cases.

Table 6.1 THEMIS observations along with measured ridge and host temperatures (T; K) and derived thermal inertias (TI; units of $J\ m^{-2}\ s^{-0.5}\ K^{-1}$). Locations analyzed are shown in Figure 6.S2. When available, HiRISE images were analyzed to ensure that the "fractured, bright-toned host" unit (Pascuzzo et al., 2019) was being measured.

No.	**Type**	**Latitude (°N)**	**Longitude (°E)**	**T (K)**	**TI**	**THEMIS Image**	**HiRISE Image**
1	Host	22.2	77.19	201	608	I01327002	ESP_027691_2025
	Ridge	22.24	77.18	196	475		
2	Host	21.88	77.13	200	627		PSP_005855_2020
	Ridge	21.88	77.13	199	567		
3	Host	22.3	77.1	198	555		PSP_002888_2025
	Ridge	22.28	77.1	194	392		

4	Host	22.29	77.15	198	571		N/A
	Ridge	22.32	77.16	198	550		
5	Host	20.81	77.57	198	377		ESP_044662_2010
	Ridge	20.84	77.57	191	299		
6	Host	17.48	76.6	194	351	I18264010	ESP_018988_1980
	Ridge	17.49	76.58	195	365		
7	Host	17.44	76.81	189	249	I17952011	ESP_026280_1975
	Ridge	17.43	76.81	187	215		

The other ridge networks analyzed by Pascuzzo et al. (2019) also show similar variations in nighttime temperatures (Fig. 6.S3) with respect to their local environment (see Table 6.1 for details). In all cases, except for location 6, the ridges are cooler than their host materials (Table 6.1). Average, derived ridge thermal inertia is 409 ± 120 $J\ m^{-2}\ s^{-0.5}\ K^{-1}$. The average host thermal inertia is higher: 477 ± 138 $J\ m^{-2}\ s^{-0.5}\ K^{-1}$. Because both types of materials have average thermal inertia values > 350 $J\ m^{-2}\ s^{-0.5}\ K^{-1}$, their average effective particle diameters cannot be determined with confidence (Presley and Christensen, 1997). Alternatively, it is possible for the host materials to contain < 3% cement to raise their thermal inertia relative to the ridges (see Figure 5b in Piqueux and Christensen, 2009), which would imply lower effective particle diameters. However, without in-situ data it is not possible to uniquely determine whether the higher thermal inertia values of the host unit are caused by larger grains or cementation (e.g., Edwards et al., 2018). We deem it likely that sub-pixel mixing with

nearby detrital material leads to reduced thermal inertia values for the ridges, which are expected to have higher thermal inertia values than their host units.

6.5. Interpretation and Discussion

6.5.1. Correlation with Noachian Terrains

The main finding of the mapping project is that while ridges are in fact heavily concentrated in Nili Fossae and Nilosyrtis/northern Terra Sabaea, polygonal ridge networks can also be found in widely spread regions of the mapping area, meaning that their formation is not unique to these areas. Ninety one percent of all the polygonal ridge networks identified here are found in 'etched', 'dissected' or 'cratered' Noachian terrain, which often contain phyllosilicates in the places where their composition can be determined from orbit (Mangold et al., 2007; Mustard et al., 2007). These clay minerals have been proposed to form during the Noachian era from subsurface aqueous activity (Poulet et al., 2005; Bibring et al., 2006; Ehlmann et al., 2011), or possibly even during pre-Noachian times from atmospheric-crust interactions (Cannon et al., 2017). The ridge networks' correlation with Noachian terrain thus might be suggestive of an aqueous influence.

Near Nili Fossae, the ridge networks are typically present in a regional stratigraphic unit of Noachian-aged Fe/Mg smectites that are thought to have formed after the Isidis impact, and before the Hesperian-aged Syrtis Major lavas (Bramble et al., 2017; Pascuzzo et al., 2019b; Scheller & Ehlmann, 2020). Surface dust cover precludes the spectral analysis of the ridge-hosting units in the newly mapped areas, so it remains possible that ridge networks outside of Nili Fossae also formed in clay-rich units. The

correlation between ridge networks and Noachian-aged units suggests that ridge formation mostly ceased before the start of the Hesperian. A small fraction (84 out of 952 total ridge networks; 9%) polygonal ridge networks are present in Hesperian regions, but (with the exception of the jarosite-rich ridges shown in Figure 6.8d) they appear morphologically distinct from typical networks (e.g., Fig. 6.8a). This result suggests that they may not be related to the majority of the ridges found in Noachian terrains, and could have formed from different combinations of fracture and fill processes (reviewed below).

6.5.2. Implications for Polygonal Ridge Network Formation Mechanisms

In the following section we will discuss potential formation mechanisms for the polygonal ridge networks mapped in this work. We assume that their morphological similarities imply that they form from similar processes. To interpret their formation mechanisms, we combined our results from mapping their distribution and characterizing their thermophysical properties with compositional and orientation results from previous work (e.g., Pascuzzo et al., 2019). It is not necessary for all the ridges to have formed from similar processes and it is entirely possible for some combination of these processes to be at work. In addition, it is also possible that the major control on our mapped polygonal ridge network distribution is exhumation, rather than formation, because a few locations where ridges continue under overlying strata have been observed in Nili Fossae (Pascuzzo et al., 2019). Regardless, the formation of these polygonal ridge networks involves three potentially separate processes: (1) polygonal fracturing, (2) fracture filling, and (3) exhumation, which we discuss below.

6.5.2.1. Polygonal Fracture Mechanisms

Several processes can cause fractures to form in polygonal patterns, such as columnar jointing, thermal contraction caused by subsurface ice, impacts, and desiccation of salts/mud.

In the case of columnar jointing, cracks form due to thermal contraction caused by rapid cooling of lava, with cracks typically growing perpendicular to local isothermal surfaces at the time of cooling (Mallet, 1875). This rapid cooling usually occurs when lava interacts with ice or water, and columnar joints can form in flows, sills, dikes, plugs and welded tuffs (DeGraff & Aydin, 1987). Evidence for columnar jointing has been observed in the walls of fresh craters on Mars in the regions of Elysium and Amazonis Planitae (Milazzo et al., 2009), but at a scale much smaller than the polygonal networks seen here, and in volcanic rather than phyllosilicate units. Thus, it is likely that columnar jointing did not play a key role in forming precursor polygonal fractures.

Another process that can cause polygonal fractures to form is thermal contraction caused by the presence of shallow subsurface ice, which expands and contracts in response to solar heating. This type of thermal contraction polygon has been identified poleward of 30° latitude in both hemispheres on Mars, where shallow subsurface ice (and polygonal patterns) is present (Levy et al., 2009a). However, 679 (71% of total) polygonal ridge networks are found equatorward of 30° latitude where ice has not been stable for long periods in Mars' history, disfavoring ice-related processes for fracture formation.

Polygonal fractures can also be caused by impact bombardment (see Cooper et al., 1974 for evidence of this process on the Moon; Carr, 1996; Rodríguez et al., 2005). Impact-related fractures are usually concentric to a given impact basin (e.g., Senft & Stewart, 2009). Given that there was widespread impact cratering during the Noachian, these fractures may be common across the Noachian highlands (Rodríguez et al., 2005). We find that only 123 (13% of total) of our mapped polygonal ridge networks are found in impact craters, and their overall distribution suggests that they are not concentric around an impact basin. However, many successive generations of impacts could have obscured any potential concentricity around past impact craters and basins (Rodríguez et al., 2005). Thus, it is possible that impacts could have led to the formation of some precursor polygonal fractures.

Patterns of polygonal fractures similar in polygon-size and morphology to the ridges mapped here are commonly found in shallow marine basins on Earth, within fine-grained sedimentary units such as smectite claystones and chalk deposits (Cartwright & Dewhurst, 1998; Cartwright, 2011; Tewksbury et al., 2014). In these deposits, pressure on the strata causes the clay to dewater, producing the fracture system (Cartwright, 2011). The ridges' host units have similar mineralogical characteristics to these terrestrial locations (Cartwright, 2011), suggesting that this process might be applicable to Mars. Our mapping area covers a large area along the dichotomy boundary that could have been at the edge of a possible ancient Noachian sea (Perron et al., 2007), but there is not a clear decrease in ridges with elevation above the dichotomy boundary as might be expected if the networks were limited to a shallow marine environment (though any

ridges north of the boundary would have been obscured by glacial activity in those regions). The appearance of ridge networks at a variety of elevations and throughout the mapping region serves as additional evidence against a simple shallow marine hypothesis.

Desiccation within mud and salts also leads to the formation of polygonal fractures. For example, areas rich in salts on Mars are commonly fractured in polygonal patterns (Osterloo et al., 2008). Most of these units are fractured on a much smaller scale than seen here, though some polygons interpreted to be desiccation-related which are of similar scale to the polygonal ridge networks we observe have been found in crater floors across Mars (El Maarry et al., 2010; El Maarry et al., 2012).

6.5.2.2. Polygonal Fracture Filling Mechanisms

Once the polygonal fractures are in place, some process must fill in the fracture with relatively erosion-resistant material. In the case of dikes formed by igneous processes, impact breccias, or clastic dikes, filling occurs simultaneously with polygonal fracture formation whereas fractures not immediately filled can provide a pathway for later fluids to circulate, resulting in mineral vein deposition (Osinski et al., 2001). Igneous dikes form when magma flows into a fracture and solidifies. These dikes often form in swarms that are concentric or radial around volcanic centers (Delaney et al., 1986), The phyllosilicate-rich mineralogy of the ridges analyzed thus far makes ridge formation by igneous processes less likely (Pascuzzo et al., 2019). Polygonal patterns are not common for dike networks, which usually outcrop as parallel, en-echelon, or radial

lines. Our distribution results also do not show a correlation with any mapped volcanic center.

Impact breccia dikes form from impacts when impacted material is injected into fractures when the impact excavates material. These dikes are usually of similar composition to their host rock, and concentric/radial to impact craters (Head & Mustard, 2006). However, as discussed above, there is not a clear correlation between impact craters and the majority of mapped ridge networks (87% of total are not associated with impact craters), which suggests that breccia dikes may not be the primary formation mechanism for the ridges.

Clastic dikes form in a variety of environments, such as underneath glaciers or as salt diapirs (Boulton & Caban, 1995; Marco et al., 2002). Fluidized sediment flows into fractures before solidifying; on Earth these dikes are commonly some form of sandstone (Winslow, 1983). The ridges we observe could represent a form of clastic dikes, and their polygonal nature is similar to a clastic dike network in the Badlands National Park, South Dakota (Madison, 2010), as discussed by Pascuzzo et al. (2019).

The ridges could represent fossilized remnants of mineral precipitation in the form of large-scale veins from aqueous circulation. The Noachian basement around the Isidis Basin holds an ancient record of aqueous activity, with unique identifiable events of hydrated mineral formation (e.g., Ehlmann et al., 2009; Ehlmann et al., 2011; Ehlmann & Mustard, 2012; Scheller & Ehlmann, 2020). However, the large variation in observed elevation in the mapped ridge networks (Fig. 6.9) suggests that potential subsurface groundwater systems in the region (Andrews-Hanna et al., 2010) may not be

interconnected, which might mean there were multiple regional upwellings of groundwater that led to ridge formation in that scenario.

6.5.2.3. Exhumation

Noachian-aged areas in Arabia Terra are thought to have experienced large amounts of erosion (on the order of ~20,000 km3; Fergason & Christensen, 2008). Erosion from wind could have exhumed the ridges to expose them at the surface today. However, it is difficult to determine why the ridge networks are most densely populated around Nili Fossae in particular. One possibility is that these types of polygonal ridge networks are prevalent across ancient martian surfaces, but are only exposed in certain regions today (e.g., Saper and Mustard, 2013). In that scenario, the dense clustering of these ridge networks around Nili Fossae could be because they are preferentially exposed due to structural faulting associated with the Nili Fossae graben (Pascuzzo et al., 2019).

6.5.3. Assessing Proposed VNIR Spectral Hypotheses from Thermophysical Analyses

The ridge networks' thermophysical properties suggest that the ridges are either finer-grained or less cemented than their host units, which is inconsistent with VNIR spectral analyses (Pascuzzo et al., 2019) and with the fact that ridges are left in relief after erosion. However, this result could be due to sub-pixel mixing with nearby detrital material causing the ridges to have lower thermal inertia values. It is difficult to separate these possibilities from the available orbital data, and future studies would benefit greatly from potential in-situ studies by the Perseverance rover to study the mineralogical and physical properties (grain size, hardness, cement fraction, etc.) of these types of

polygonal ridge networks to help constrain their formation mechanism (and compare with orbital results).

6.6. Conclusions

We mapped 952 irregular, polygonal ridge networks across Arabia Terra, Terra Sabaea, Tyrrhena Terra, Nili Fossae and Nilosyrtis using a global CTX mosaic (aided by citizen scientist volunteers). Our mapping area spanned approximately 2.8×10^7 km^2, representing a 100x larger mapping area than that of previous studies (e.g., Saper and Mustard, 2013; Ebinger and Mustard, 2015, 2016; Pascuzzo et al. 2019). In addition, we used thermal infrared data from THEMIS to characterize ridge, host and local environmental thermophysical properties. Our observations led to the following conclusions:

1. 864 out of 952 (91%) of these polygonal ridge networks are confined to Noachian terrain within these regions. The ridge networks are most densely clustered around Nili Fossae, although morphologically similar ridge networks are scattered across Arabia Terra, Terra Sabaea and Tyrrhena Terra. If polygonal ridge networks are widespread across Noachian terrain and only exposed in certain regions today, their dense clustering around Nili Fossae and Nilosyrtis could be due to preferential exposure.
2. Ridges have lower average thermal inertias ($409 \pm 120\ J\ m^{-2}\ s^{-0.5}\ K^{-1}$) than their host units ($477 \pm 138\ J\ m^{-2}\ s^{-0.5}\ K^{-1}$), although this result is likely due to sub-pixel mixing in the case of the ridges with nearby detrital material. Potential in-situ studies by the Perseverance rover or future, high-resolution

thermal infrared instruments are required in order to accurately characterize the mineralogical and physical properties (grain size, hardness, cement fraction, etc.) of the ridges and compare them with VNIR analyses (Pascuzzo et al., 2019b).

3. The formation of these polygonal ridge networks can be assessed in terms of three possibly separate processes: (1) polygonal fracture formation, (2) fracture filling and (3) exhumation. Based on our results and previous spectral studies, polygonal fracture formation is likely to have occurred by impact cratering and/or desiccation of likely sedimentary host deposits. Additionally, our results do not contradict the finding of previous authors that favor an origin by fracture filling by clastic dikes and/or mineral precipitation from aqueous circulation. The ridge networks are found in areas with varying elevations (-3,700 m to 2,200 m) that typically have relatively low slope angles (< 7°). If groundwater upwelling led to mineral precipitation and ridge formation, then the large variation in ridge network elevation suggests that these groundwater systems may not be interconnected in the subsurface. These processes were then followed by exhumation, probably by aeolian processes that eroded much of these ancient Noachian terrains where the ridges are present.
4. Considering the widespread distribution of our mapped ridges, an aqueous origin for the ridges would imply widespread groundwater processes in the Noachian. In-situ studies by the Perseverance rover in these regions might

help shed light on potential former aqueous activity, and better constrain the formation mechanisms and histories of these ridge networks.

6.7. Acknowledgements

The authors would like to thank Debra Buczkowski, Eva Scheller, Chris Haberle and an anonymous reviewer for constructive and helpful formal reviews that greatly improved the manuscript. Additionally, we are very grateful to Alyssa Pascuzzo for providing us with ridge mapping data from Pascuzzo et al. (2019) for us to make comparisons. Informal reviews and discussions with Kathryn Powell, Sean Peters, Jay Serla, Alex Huff and Anmol Lal are also greatly appreciated. The P4R data presented in this paper are the result of the efforts of the P4R volunteers, without whom this work would not have been possible. Their contributions are individually acknowledged at: https://www.zooniverse.org/projects/mschwamb/planet-four-ridges/about/results. This publication uses data generated via the Zooniverse.org platform, development of which is funded by generous support, including a Global Impact Award from Google, and by a grant from the Alfred P. Sloan Foundation. This research made use of Astropy, a community-developed core Python package for Astronomy (The Astropy Collaboration et al., 2013; Price-Whelan et al., 2018) and NASA's Astrophysics Data System Bibliographic Services. ARK's work was supported by the ASU Fulton Undergraduate Research Initiative. In addition, ARK's and LK's work was supported through the NASA Mars Odyssey project. LK's work and a part of ARK's work were carried out at the Jet Propulsion Laboratory/California Institute of Technology under a contract with NASA.

MES was supported in part by the international Gemini Observatory, a program of NSF's OIR Lab, which is managed by the Association of Universities for Research in Astronomy (AURA) under a cooperative agreement with the National Science Foundation, on behalf of the Gemini partnership of Argentina, Brazil, Canada, Chile, the Republic of Korea, and the United States of America.

6.8. Data Availability

The CTX, THEMIS and HiRISE data used in this work is accessible through JMARS (https://jmars.asu.edu/). The 1-D numerical model KRC is available at: http://krc.mars.asu.edu. MOLA elevation data is available through the PDS at: http://pds-geosciences.wustl.edu/missions/mgs/megdr.htm. ArcGIS is accessible at: http://desktop.arcgis.com/en/arcmap/. Map datasets related to this article can be found at https://doi.org/10.5281/zenodo.4441387 (Khuller et al., 2021c).

6.9. Supplementary Material

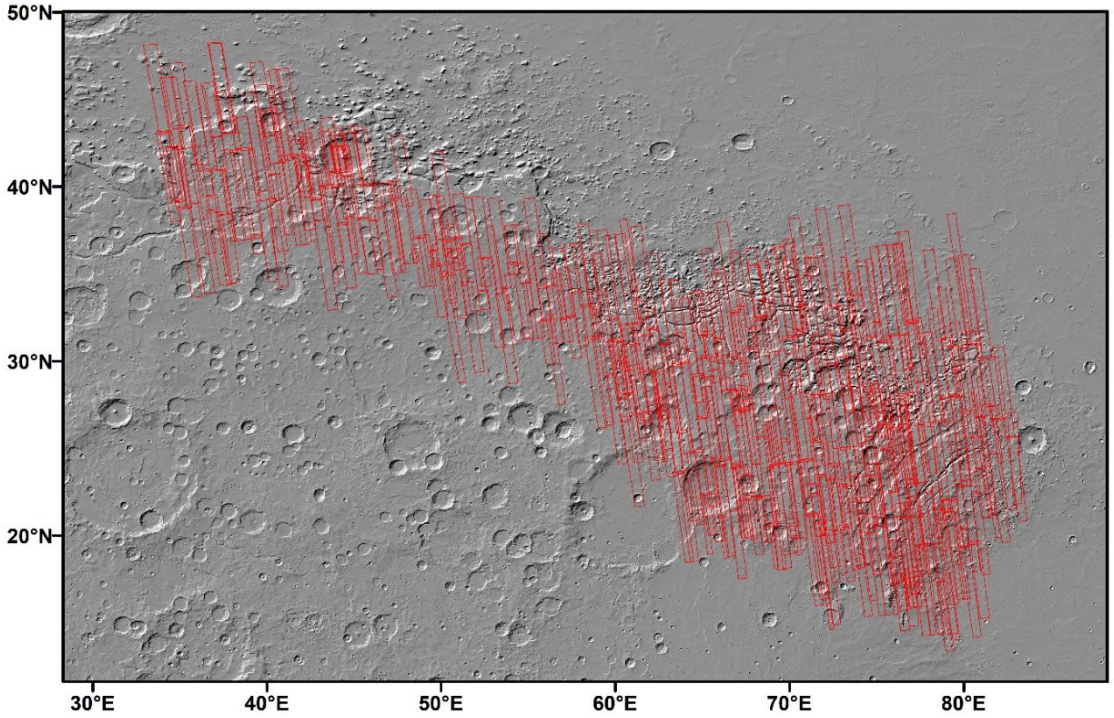

Figure 6.S1. Map of CTX image footprints (red boxes) analyzed by P4R.

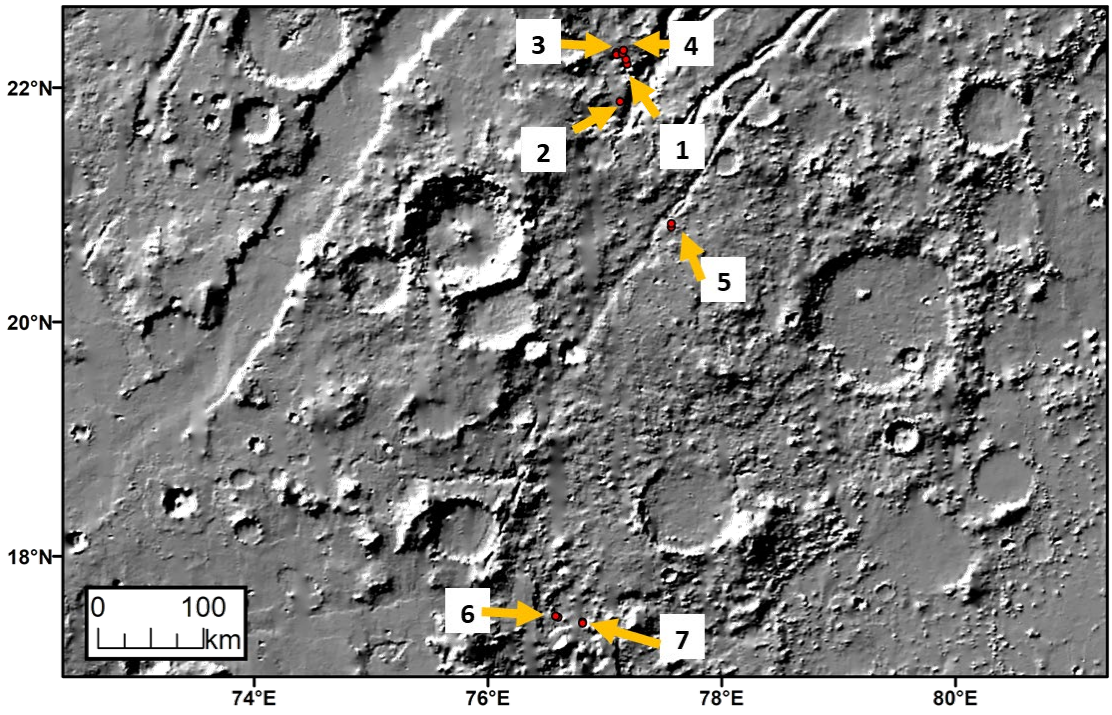

Figure 6.S2. Locations of ridge networks analyzed using THEMIS in Figures 6.11 and 6.S3. See **Table 6.1** for additional details.

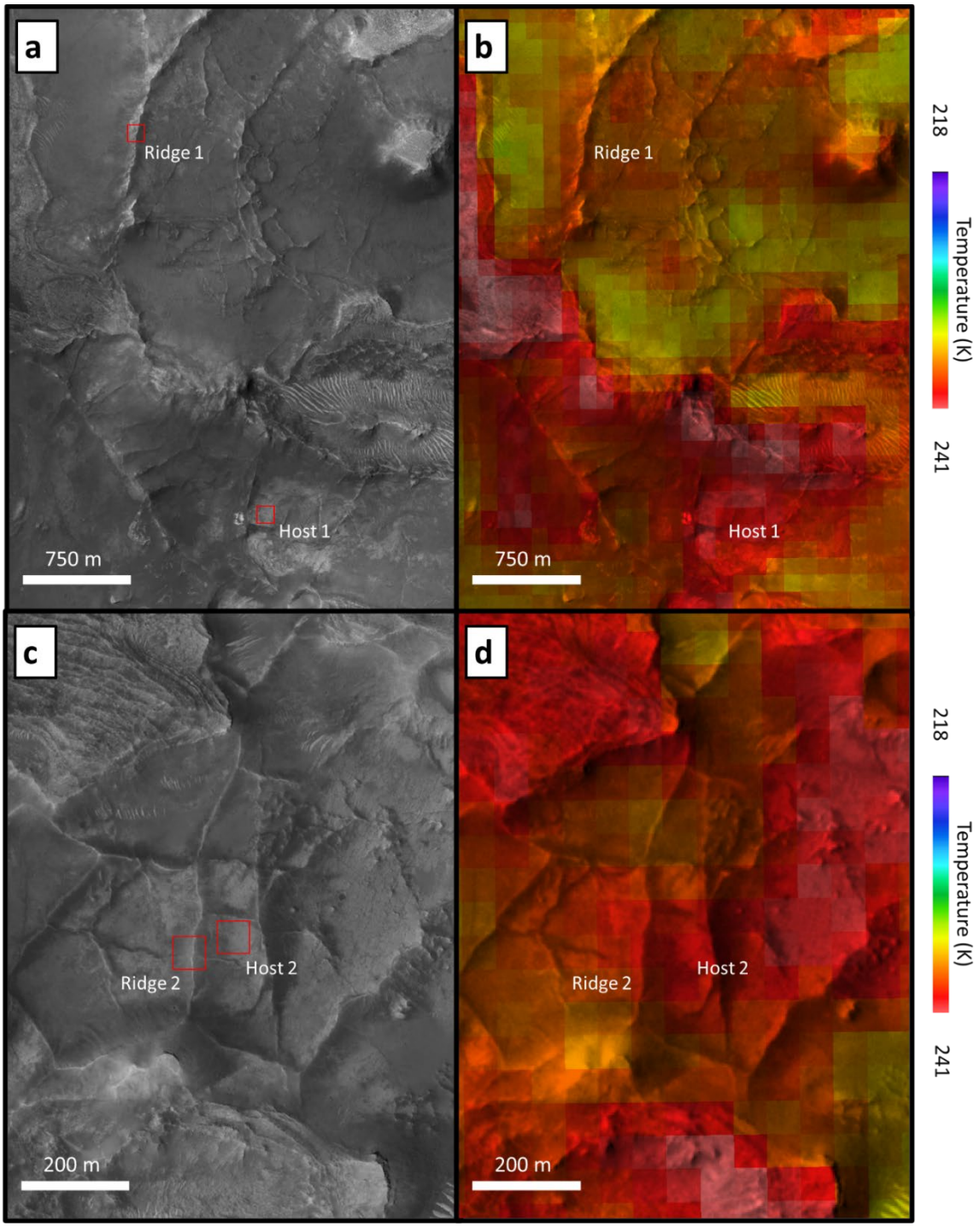
a
Ridge 1
Host 1
750 m
b
Ridge 1
Host 1
750 m
218
Temperature (K)
241
c
Ridge 2
Host 2
200 m
d
Ridge 2
Host 2
200 m
218
Temperature (K)
241

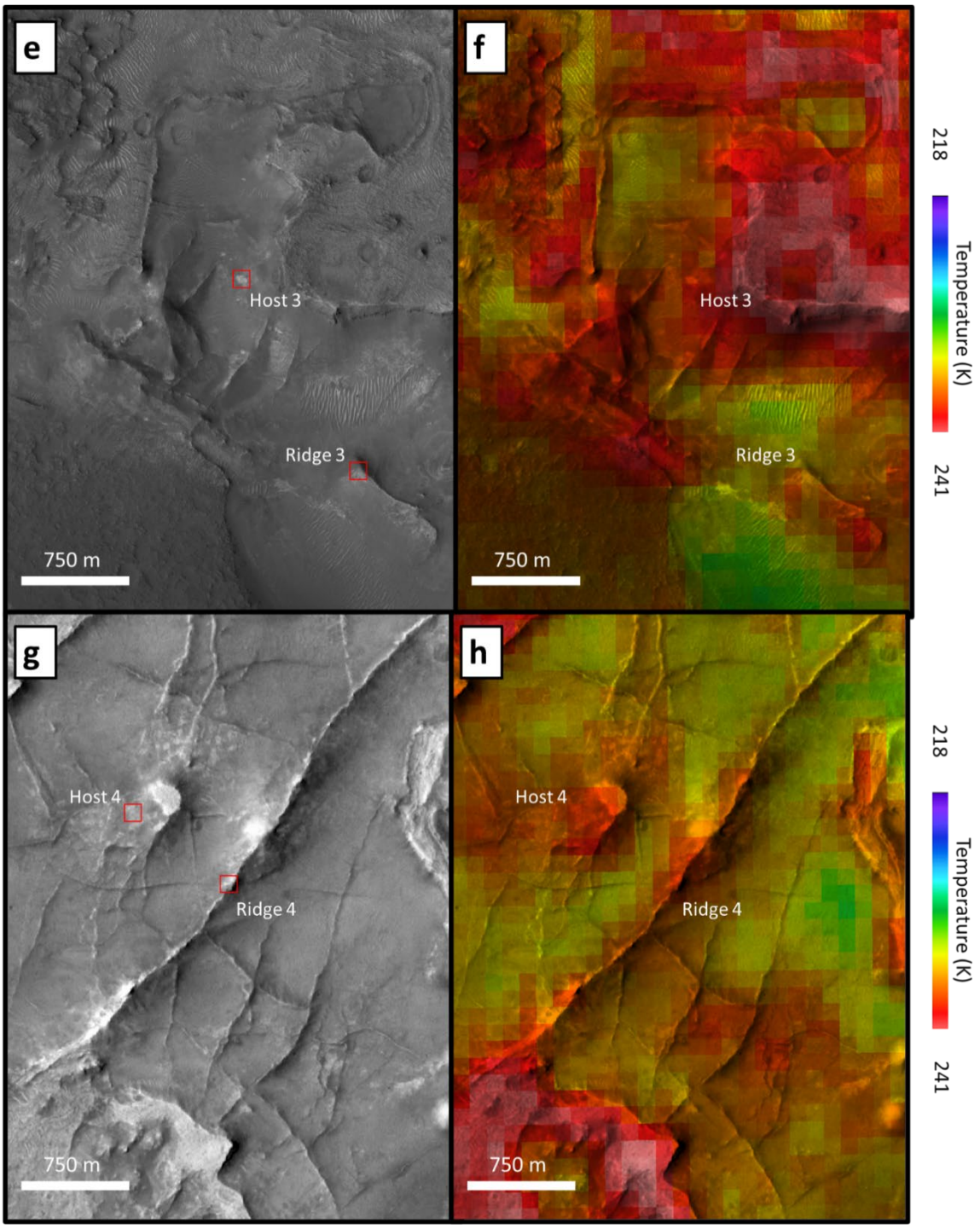
e
Host 3
Ridge 3
750 m
f
Host 3
Ridge 3
750 m
218
Temperature (K)
241
g
Host 4
Ridge 4
750 m
h
Host 4
Ridge 4
750 m
218
Temperature (K)
241

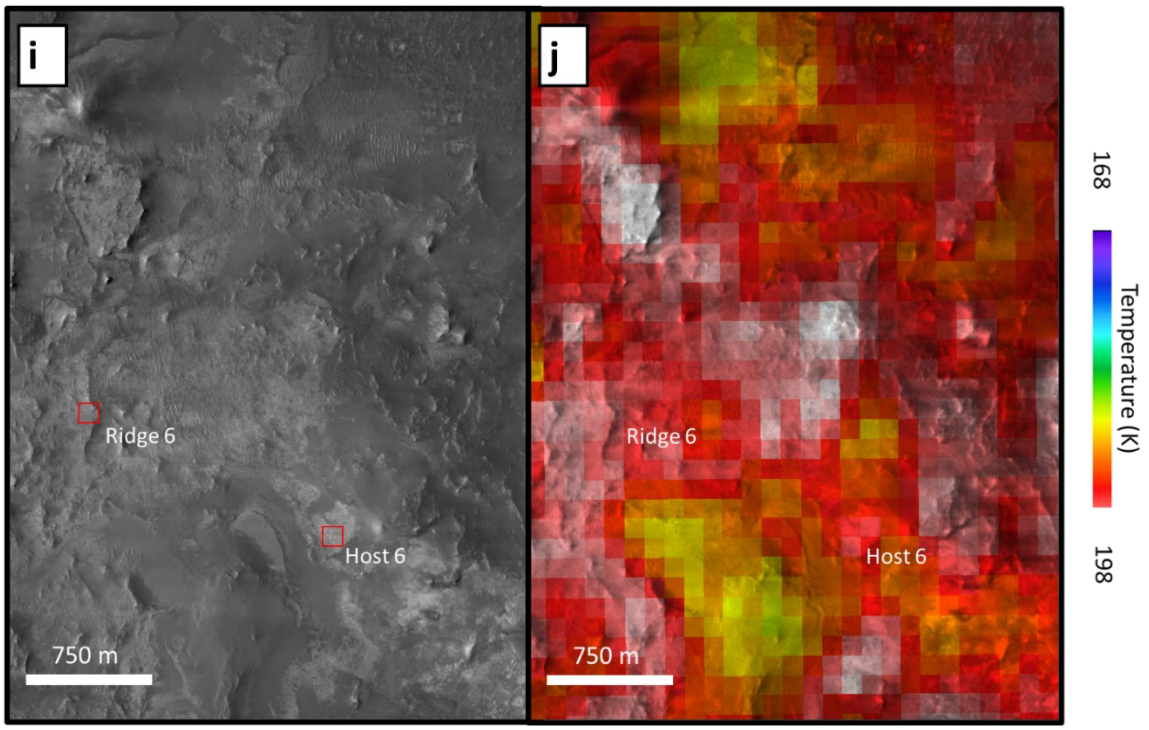

Figure 6.S3. Visible wavelength HiRISE/CTX images (left) and nighttime thermal infrared images overlaid on the CTX visible mosaic (right) showing locations (red boxes) chosen to analyze thermophysical properties of ridge and ridge-hosting materials. See **Table 6.1** for image details.

REFERENCES

Andrews-Hanna, J. C., Zuber, M. T., Arvidson, R. E., & Wiseman, S. M. (2010). Early Mars hydrology: Meridiani playa deposits and the sedimentary record of Arabia Terra. *Journal of Geophysical Research: Planets, 115*(E6).

Becker, K., Anderson, J., Sides, S., Miller, E., Eliason, E., & Keszthelyi, L. (2007). *Processing HiRISE images using ISIS3.* Paper presented at the Lunar and Planetary Science Conference.

Bibring, J.-P., Langevin, Y., Mustard, J. F., Poulet, F., Arvidson, R., Gendrin, A., et al. (2006). Global mineralogical and aqueous Mars history derived from OMEGA/Mars Express Data. *Science, 312*, 400-404.

Boulton, G., & Caban, P. (1995). Groundwater flow beneath ice sheets: Part II—Its impact on glacier tectonic structures and moraine formation. *Quaternary Science Reviews, 14*(6), 563-587.

Bramble, M. S., Mustard, J. F., & Salvatore, M. R. (2017). The geological history of northeast Syrtis Major, Mars. *Icarus, 293*, 66-93.

Cannon, K. M., Parman, S. W., & Mustard, J. F. (2017). Primordial clays on Mars formed beneath a steam or supercritical atmosphere. *Nature, 552*(7683), 88.

Carr, M. H. (1996). Water erosion on Mars and its biologic implications. *Endeavour, 20*(2), 56-60.

Cartwright, J. (2011). Diagenetically induced shear failure of fine-grained sediments and the development of polygonal fault systems. *Marine and Petroleum Geology, 28*(9), 1593-1610.

Cartwright, J., & Dewhurst, D. (1998). Layer-bound compaction faults in fine-grained sediments. *Geological Society of America Bulletin, 110*(10), 1242-1257.

Christensen, P. R. (1986). Regional dust deposits on Mars: Physical properties, age, and history. *Journal of Geophysical Research: Solid Earth, 91*(B3), 3533-3545.

Christensen, P. R., Bandfield, J. L., Bell III, J. F., Gorelick, N., Hamilton, V. E., Ivanov, A., et al. (2003). Morphology and composition of the surface of Mars: Mars Odyssey THEMIS results. *Science, 300*(5628), 2056-2061.

Christensen, P. R., Engle, E., Anwar, S., Dickenshied, S., Noss, D., Gorelick, N., & Weiss-Malik, M. (2009). JMARS - A Planetary GIS. *AGU 2009 Fall Meeting, abstract id.IN22A-06*.

Christensen, P. R., Jakosky, B. M., Kieffer, H. H., Malin, M. C., McSween, H. Y., Nealson, K., et al. (2004). The Thermal Emission Imaging System (THEMIS) for the Mars 2001 Odyssey Mission. *Space Science Reviews, 110*(1-2), 85-130.

Collaboration, A., Robitaille, T. P., Tollerud, E. J., Greenfield, P., Droettboom, M., Bray, E., et al. (2013). Astropy: A community Python package for astronomy. *Astron. Astrophys., 558*, A33. https://ui.adsabs.harvard.edu/abs/2013A&A...558A..33Adoi:

Cooper, M. R., Kovach, R. L., & Watkins, J. S. (1974). Lunar near-surface structure. *Reviews of Geophysics, 12*(3), 291-308.

DeGraff, J. M., & Aydin, A. (1987). Surface morphology of columnar joints and its significance to mechanics and direction of joint growth. *Geological Society of America Bulletin, 99*(5), 605-617.

Delaney, P. T., Pollard, D. D., Ziony, J. I., & McKee, E. H. (1986). Field relations between dikes and joints: Emplacement processes and paleostress analysis. *Journal of Geophysical Research: Solid Earth, 91*(B5), 4920-4938.

Dickson, J., Kerber, L., Fassett, C., & Ehlmann, B. (2018). *A Global, Blended CTX Mosaic of Mars with Vectorized Seam Mapping: A New Mosaicking Pipeline Using Principles of Non-Destructive Image Editing.* Paper presented at the Lunar and Planetary Science Conference.

Ebinger, E., & Mustard, J. (2015). *Linear ridges in the Nilosyrtis region of Mars: implications for subsurface fluid flow.* Paper presented at the Lunar and Planetary Science Conference.

Ebinger, E., & Mustard, J. (2016). Classification of Curvilinear Ridges in the Nilosyrtis Highlands of Mars. *LPI*(1903), 2731.

Edwards, C., Christensen, P., & Hill, J. (2011). Mosaicking of global planetary image datasets: 2. Modeling of wind streak thicknesses observed in Thermal Emission Imaging System (THEMIS) daytime and nighttime infrared data. *Journal of Geophysical Research: Planets, 116*(E10).

Edwards, C. S., Piqueux, S., Hamilton, V. E., Fergason, R. L., Herkenhoff, K. E., Vasavada, A. R., et al. (2018). The thermophysical properties of the Bagnold Dunes, Mars: Ground-truthing orbital data. *Journal of Geophysical Research: Planets, 123*(5), 1307-1326.

Ehlmann, B. L., & Mustard, J. F. (2012). An in-situ record of major environmental transitions on early Mars at Northeast Syrtis Major. *Geophysical Research Letters, 39*(11).

Ehlmann, B. L., Mustard, J. F., Murchie, S. L., Bibring, J.-P., Meunier, A., Fraeman, A. A., & Langevin, Y. (2011). Subsurface water and clay mineral formation during the early history of Mars. *Nature, 479*, 53-60. 10.1038/nature10582

Ehlmann, B. L., Mustard, J. F., Swayze, G. A., Clark, R. N., Bishop, J. L., Poulet, F., et al. (2009). Identification of hydrated silicate minerals on Mars using MRO-CRISM: Geologic context near Nili Fossae and implications for aqueous alteration. *Journal of Geophysical Research, 114*(E00D08). 10.1029/2009JE003339

El Maarry, M., Markiewicz, W., Mellon, M., Goetz, W., Dohm, J., & Pack, A. (2010). Crater floor polygons: Desiccation patterns of ancient lakes on Mars? *Journal of Geophysical Research: Planets, 115*(E10).

El Maarry, M. R., Kodikara, J., Wijessoriya, S., Markiewicz, W. J., & Thomas, N. (2012). Desiccation mechanism for formation of giant polygons on Earth and intermediate-sized polygons on Mars: Results from a pre-fracture model. *Earth and Planetary Science Letters, 323*, 19-26.

Fassett, C. I., & Head, J. W. (2007). Layered mantling deposits in northeast Arabia Terra, Mars: Noachian-Hesperian sedimentation, erosion, and terrain inversion. *Journal of Geophysical Research: Planets, 112*(E8).

Fassett, C. I., & Head, J. W. (2011). Sequence and timing of conditions on early Mars. *Icarus, 211*(2), 1204-1214.

Fergason, R., & Christensen, P. (2008). Formation and erosion of layered materials: Geologic and dust cycle history of eastern Arabia Terra, Mars. *Journal of Geophysical Research: Planets, 113*(E12).

Fergason, R. L., Christensen, P. R., & Kieffer, H. H. (2006). High-resolution thermal inertia derived from the Thermal Emission Imaging System (THEMIS): Thermal model and applications. *Journal of Geophysical Research: Planets, 111*(E12).

Forget, F., Hourdin, F., Fournier, R., Hourdin, C., Talagrand, O., Collins, M., et al. (1999). Improved general circulation models of the Martian atmosphere from the surface to above 80 km. *Journal of Geophysical Research: Planets, 104*(E10), 24155-24175.

Golombek, M., Grant, J., Kipp, D., Vasavada, A., Kirk, R., Fergason, R., et al. (2012). Selection of the Mars Science Laboratory landing site. *Space Science Reviews, 170*(1-4), 641-737.

Goudge, T. A., Mustard, J. F., Head III, J. W., Fassett, C. I., & Wiseman, S. M. (2015). Assessing the mineralogy of the watershed and fan deposits of the Jezero crater

paleolake system, Mars. *Journal of Geophysical Research*, 775-808. 10.1002/2014JE004782

Greeley, R., & Guest, J. (1987). Geologic map of the eastern equatorial region of Mars.

Head, J. W., & Mustard, J. F. (2006). Breccia dikes and crater-related faults in impact craters on Mars: Erosion and exposure on the floor of a crater 75 km in diameter at the dichotomy boundary. *Meteoritics & Planetary Science, 41*(10), 1675-1690.

Hiesinger, H., & Head, J. W. (2000). Characteristics and origin of polygonal terrain in southern Utopia Planitia, Mars: results from Mars Orbiter Laser Altimeter and Mars Orbiter Camera data. *Journal of Geophysical Research: Planets, 105*(E5), 11999-12022.

Irwin III, R. P., Wray, J. J., Mest, S. C., & Maxwell, T. A. (2018). Wind-eroded crater floors and intercrater plains, Terra Sabaea, Mars. *Journal of Geophysical Research: Planets, 123*(2), 445-467.

Ivanov, M., Hiesinger, H., Erkeling, G., Hielscher, F., & Reiss, D. (2012). Major episodes of geologic history of Isidis Planitia on Mars. *Icarus, 218*(1), 24-46.

Kerber, L., Dickson, J. L., Head, J. W., & Grosfils, E. B. (2017). Polygonal ridge networks on Mars: Diversity of morphologies and the special case of the Eastern Medusae Fossae Formation. *Icarus, 281*, 200-219.

Khuller, A. R., Kerber, L., Schwamb, M. E., Beer, S., Nogal, F. E., Perry, R., et al. (2021). *Repository: Irregular Polygonal Ridge Networks in Ancient Noachian Terrain on Mars*. Retrieved from: https://doi.org/10.5281/zenodo.4441387

Kieffer, H. H. (2013). Thermal model for analysis of Mars infrared mapping. *Journal of Geophysical Research: Planets, 118*(3), 451-470.

Kremer, C. H., Mustard, J. F., & Bramble, M. S. (2019). A widespread olivine-rich ash deposit on Mars. *Geology*. https://doi.org/10.1130/G45563.1doi:10.1130/g45563.1

Léveillé, R. J., Bridges, J., Wiens, R. C., Mangold, N., Cousin, A., Lanza, N., et al. (2014). Chemistry of fracture-filling raised ridges in Yellowknife Bay, Gale Crater: Window into past aqueous activity and habitability on Mars. *Journal of Geophysical Research: Planets, 119*(11), 2398-2415.

Levy, J. S., Head, J. W., & Marchant, D. R. (2007). Lineated valley fill and lobate debris apron stratigraphy in Nilosyrtis Mensae, Mars: Evidence for phases of glacial modification of the dichotomy boundary. *Journal of Geophysical Research: Planets, 112*(E8).

Levy, J. S., Head, J. W., & Marchant, D. R. (2009). Thermal contraction crack polygons on Earth and Mars; classification, distribution, and implications for recent cold desert processes. In (Vol. 90). Washington, DC: Washington, DC, United States: American Geophysical Union.

Loizeau, D., Carter, J., Bouley, S., Mangold, N., Poulet, F., Bibring, J.-P., et al. (2012). Characterization of hydrated silicate-bearing outcrops in Tyrrhena Terra, Mars: Implications to the alteration history of Mars. *Icarus, 219*(1), 476-497.

Madison, M. P. (2010). *Origins and characteristics of clastic dikes in the Sage Creek area of Badlands National Park.* Northern Illinois University,

Malin, M. C., Bell III, J. F., Cantor, B. A., Caplinger, M. A., Calvin, W. M., Clancy, R. T., et al. (2007). Context Camera Investigation on board the Mars Reconnaissance Orbiter. *Journal of Geophysical Research: Planets, 112*(E5). https://agupubs.onlinelibrary.wiley.com/doi/abs/10.1029/2006JE002808doi:doi:10.1029/2006JE002808

Mallet, R. (1875). I. On the origin and mechanism of production of the prismatic (or columnar) structure of basalt. *Proceedings of the Royal Society of London, 23*(156-163), 180-184.

Mangold, N., Poulet, F., Mustard, J., Bibring, J. P., Gondet, B., Langevin, Y., et al. (2007). Mineralogy of the Nili Fossae region with OMEGA/Mars Express data: 2. Aqueous alteration of the crust. *Journal of Geophysical Research: Planets, 112*(E8).

Marco, S., Weinberger, R., & Agnon, A. (2002). Radial clastic dykes formed by a salt diapir in the Dead Sea Rift, Israel. *Terra Nova, 14*(4), 288-294.

McEwen, A. S., Eliason, E. M., Bergstrom, J. W., Bridges, N. T., Hansen, C. J., Delamere, W. A., et al. (2007). Mars Reconnaissance Orbiter's High Resolution Imaging Science Experiment (HiRISE). *Journal of Geophysical Research: Planets, 112*(E5). https://agupubs.onlinelibrary.wiley.com/doi/abs/10.1029/2005JE002605doi:doi:10.1029/2005JE002605

McGill, G. E. (2000). Crustal history of north central Arabia Terra, Mars. *Journal of Geophysical Research: Planets, 105*(E3), 6945-6959.

Milazzo, M. P., Keszthelyi, L. P., Jaeger, W. L., Rosiek, M., Mattson, S., Verba, C., et al. (2009). Discovery of columnar jointing on Mars. *Geology, 37*(2), 171-174.

Millour, E., Forget, F., Spiga, A., Vals, M., Zakharov, V., Montabone, L., et al. (2018). The Mars Climate Database (version 5.3). *From Mars Express to ExoMars*.

Murchie, S., Arvidson, R., Bedini, P., Beisser, K., Bibring, J.-P., Bishop, J. L., et al. (2007). Compact Reconnaissance Imaging Spectrometer for Mars (CRISM) on Mars Reconnaissance Orbiter (MRO). *Journal of Geophysical Research, 112*(E05S03). 10.1029/2006JE002682

Mustard, J., Ehlmann, B., Murchie, S., Poulet, F., Mangold, N., Head, J., et al. (2009a). Composition, morphology, and stratigraphy of Noachian crust around the Isidis basin. *Journal of Geophysical Research: Planets, 114*(E2).

Mustard, J., Poulet, F., Head, J., Mangold, N., Bibring, J. P., Pelkey, S., et al. (2007). Mineralogy of the Nili Fossae region with OMEGA/Mars Express data: 1. Ancient impact melt in the Isidis Basin and implications for the transition from the Noachian to Hesperian. *Journal of Geophysical Research: Planets, 112*(E8).

Mustard, J. F., Ehlmann, B. L., Murchie, S. L., Poulet, F., Mangold, N., Head, J. W., et al. (2009b). Composition, Morphology, and Stratigraphy of Noachian Crust around the Isidis basin. *Journal of Geophysical Research, 114*(E00D12). 10.1029/2009JE003349

Mustard, J. F., Murchie, S. L., Pelkey, S. M., Ehlmann, B. L., Milliken, R. E., Grant, J. A., et al. (2008). Hydrated silicate minerals on Mars observed by the Mars Reconnaissance Orbiter CRISM instrument. *Nature, 7097*, 305-309.

Osinski, G. R., Spray, J. G., & Lee, P. (2001). Impact-induced hydrothermal activity within the Haughton impact structure, arctic Canada: Generation of a transient, warm, wet oasis. *Meteoritics & Planetary Science, 36*(5), 731-745.

Osterloo, M. M., Hamilton, V. E., Bandfield, J. L., Glotch, T. D., Baldridge, A. M., Christensen, P. R., et al. (2008). Chloride-bearing materials in the southern highlands of Mars. *Science, 319*, 1651-1654. 10.1126/science.1150690

Pascuzzo, A. C., Mustard, J. F., Kremer, C. H., & Ebinger, E. (2019). The formation of irregular polygonal ridge networks, Nili Fossae, Mars: Implications for extensive subsurface channelized fluid flow in the Noachian. *Icarus, 319*, 852-868.

Piqueux, S., & Christensen, P. (2009). A model of thermal conductivity for planetary soils: 2. Theory for cemented soils. *Journal of Geophysical Research: Planets, 114*(E9).

Poulet, F., Bibring, J.-P., Mustard, J. F., Gendrin, A., Mangold, N., Langevin, Y., et al. (2005). Phyllosilicates on Mars and implications for early martian climate. *Nature, 438*(623-627).

Presley, M. A., & Christensen, P. R. (1997). Thermal conductivity measurements of particulate materials 2. Results. *Journal of Geophysical Research: Planets, 102*(E3), 6551-6566.

Price-Whelan, A. M., Sipőcz, B., Günther, H., Lim, P., Crawford, S., Conseil, S., et al. (2018). The Astropy project: Building an open-science project and status of the v2. 0 core package. *The Astronomical Journal, 156*(3), 123.

Quinn, D. P., & Ehlmann, B. (2019). The deposition and alteration history of the northeast Syrtis Major layered sulfates. *Journal of Geophysical Research. Planets*.

Rodríguez, J. A. P., Sasaki, S., Dohm, J. M., Tanaka, K. L., Strom, B., Kargel, J., et al. (2005). Control of impact crater fracture systems on subsurface hydrology, ground subsidence, and collapse, Mars. *Journal of Geophysical Research: Planets, 110*(E6).

Rogers, A., & Nazarian, A. (2013). Evidence for Noachian flood volcanism in Noachis Terra, Mars, and the possible role of Hellas impact basin tectonics. *Journal of Geophysical Research: Planets, 118*(5), 1094-1113.

Saper, L., & Mustard, J. F. (2013). Extensive linear ridge networks in Nili Fossae and Nilosyrtis, Mars: implications for fluid flow in the ancient crust. *Geophysical Research Letters, 40*(2), 245-249.

Scheller, E. L., & Ehlmann, B. L. (2020). Composition, Stratigraphy, and Geological History of the Noachian Basement Surrounding the Isidis Impact Basin. *Journal of Geophysical Research: Planets*, e2019JE006190.

Schwamb, M. E., Aye, K.-M., Portyankina, G., Hansen, C. J., Allen, C., Allen, S., et al. (2018). Planet Four: Terrains–Discovery of araneiforms outside of the south polar layered deposits. *Icarus, 308*, 148-187.

Scott, D. H., & Tanaka, K. L. (1986). Geologic map of the western equatorial region of Mars.

Senft, L. E., & Stewart, S. T. (2009). Dynamic fault weakening and the formation of large impact craters. *Earth and Planetary Science Letters, 287*(3-4), 471-482.

Skinner Jr, J., & Hare, T. (2006). Digital renovation of the atlas of Mars 1: 15,000,000-scale global geologic series maps.

Smith, D. E., Zuber, M. T., Frey, H. V., Garvin, J. B., Head, J. W., Muhleman, D. O., et al. (2001). Mars Orbiter Laser Altimeter: Experiment summary after the first year of global mapping of Mars. *Journal of Geophysical Research: Planets, 106*(E10), 23689-23722.

Smith, D. E., Zuber, M. T., Solomon, S. C., Phillips, R. J., Head, J. W., Garvin, J. B., et al. (1999). The global topography of Mars and implications for surface evolution. *Science, 284*(5419), 1495-1503.

Tewksbury, B. J., Hogan, J. P., Kattenhorn, S. A., Mehrtens, C. J., & Tarabees, E. A. (2014). Polygonal faults in chalk: Insights from extensive exposures of the Khoman Formation, Western Desert, Egypt. *Geology, 42*(6), 479-482.

Wichman, R. W., & Schultz, P. H. (1989). Sequence and mechanisms of deformation around the Hellas and Isidis impact basins on Mars. *Journal of Geophysical Research, 94*, 17,333-317,357. 10.1029/JB094iB12p17333

Winslow, M. A. (1983). Clastic dike swarms and the structural evolution of the foreland fold and thrust belt of the southern Andes. *Geological Society of America Bulletin, 94*(9), 1073-1080.

Chapter 7

LOOKING BEYOND: CONCLUSIONS & FUTURE WORK

In this dissertation, I have investigated the characteristics of martian ices and liquid water, and the landscapes they have shaped through time. My discovery of the lowest latitude detection of H_2O ice on Mars at 32.9°S in Chapter 2 confirms previous theoretical and observational predictions for stable subsurface H_2O ice within the top meter of the martian mid-latitudes. While most of this shallow, mid-latitude H_2O ice is buried on pole-facing slopes, should the slope landing/mobility hazards be circumvented, this ice represents a key resource for future robotic and human missions to Mars. Furthermore, as I propose in Chapter 2, this ice could be melting in the shallow subsurface, providing liquid water for any potential extant martian life.

I am currently working on an improved martian H_2O ice energy balance model that will better quantify the conditions under which ice can melt on Mars (Fig. 7.1). Because solar radiation and atmospheric turbulence represent the two biggest sources/sinks of energy in ice, this new energy balance model I am working on will incorporate the validated snow/ice radiative transfer model described in Chapter 3 and a validated turbulent flux model that I have developed with Gary Clow (Khuller & Clow, 2022).

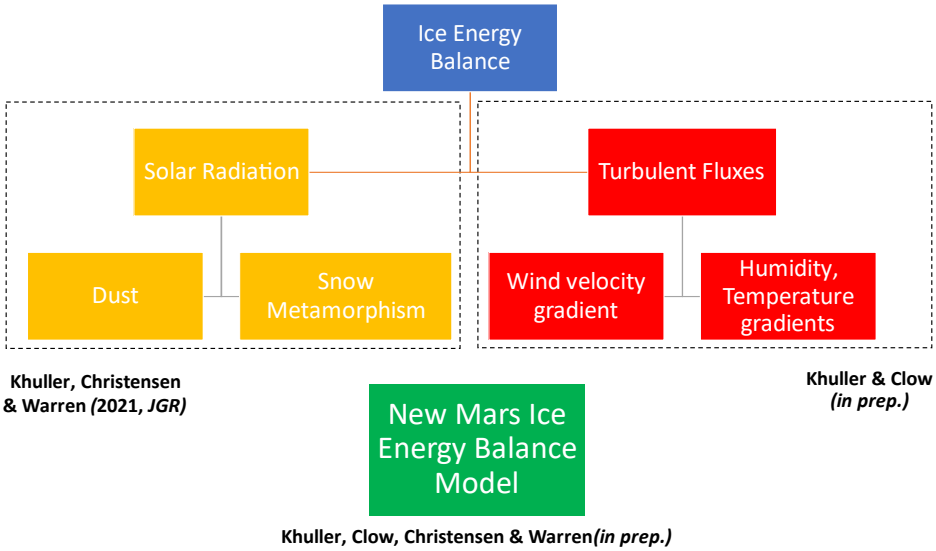

Figure 7.1. Schematic showing the two major sources/sinks of H_2O ice energy balance: solar radiation (yellow boxes) and turbulent fluxes (red boxes), along with key factors that influence them. Accounting for the effects of dust and snow metamorphism can lead to ~10x increased heating. I am in the process of combining the solar radiation and turbulent flux modeling work into a new, and improved ice energy balance model (green box) that will be validated using available terrestrial and martian measurements to better determine the conditions under which H_2O ice can melt on Mars.

In addition to the results presented in Chapters 2 and 3, I have validated the solar radiation model using terrestrial measurements of solar irradiances within glacier ice (Fig. 7.2). Figure 7.2 highlights the importance of explicitly calculating these fluxes, due to the significant amount of subsurface heating (up to ~10 K) that will not be accounted for if it is assumed that all the solar radiation is absorbed at the surface (as is commonly done by existing martian ice models). This improved solar radiation model can be used to calculate radiative fluxes and albedos of vertically inhomogeneous layers of clean/dusty

snow, dust and clean/dusty glacier ice. Thus, this model can be applied to evaluate the solar energy balance of all exposed ice observed on Mars, at the mid-latitudes and at the poles.

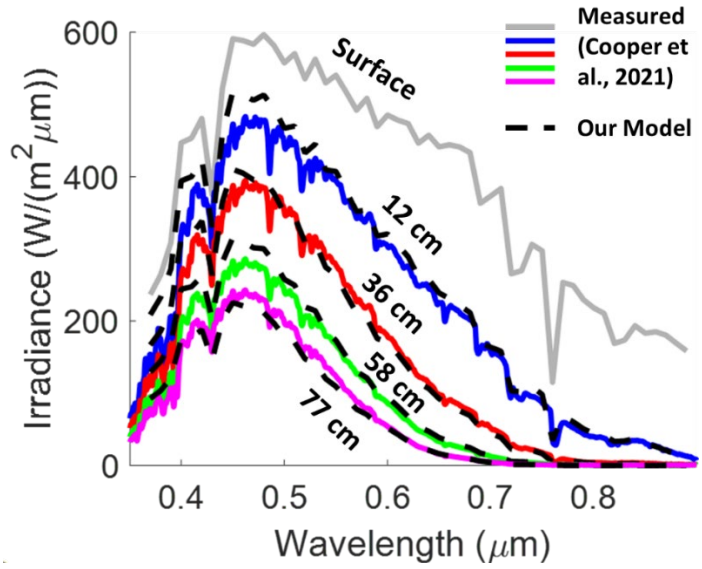

Figure 7.2. Comparison of the solar radiation spectral ice model (dashed lines) based on Khuller et al. (2021b); Whicker et al. (2022), with measured in-ice radiances in Greenland glacier ice at various depths (solid lines) (Cooper et al., 2021). Existing martian ice models assume that the irradiances below the surface (blue, red, green and pink curves) are zero, which can lead to a <~10 K underestimation in subsurface heating.

As mentioned above, I, along with Gary Clow, have developed a model of the atmospheric surface layer (lowest ~10% of the atmospheric boundary layer, where the surface interacts with the atmosphere) that is based on validated work on the terrestrial atmospheric surface layer. This model accounts for atmospheric stability, surface roughness, molecular diffusion, etc. Gary and I have validated this model using turbulent flux, wind/temperature/volatile profiles and sublimation/evaporation data from Earth,

Mars and Titan. A comparison of the Khuller & Clow (2022) model, the commonly used Dundas & Byrne (2010) model against measured sublimation rates at a Mars analog site (Lake Hoare, Antarctica), is shown in Figure 7.3. The Dundas & Byrne (2010) severely overestimates the sublimation rate by up to a factor of ~9, because of simplifying assumptions used in that model. Thus, the use of the improved Khuller & Clow (2022) model, coupled with the solar radiation work I have completed already will help provide a much better constrained answer as to whether and how H_2O ice can melt on Mars.

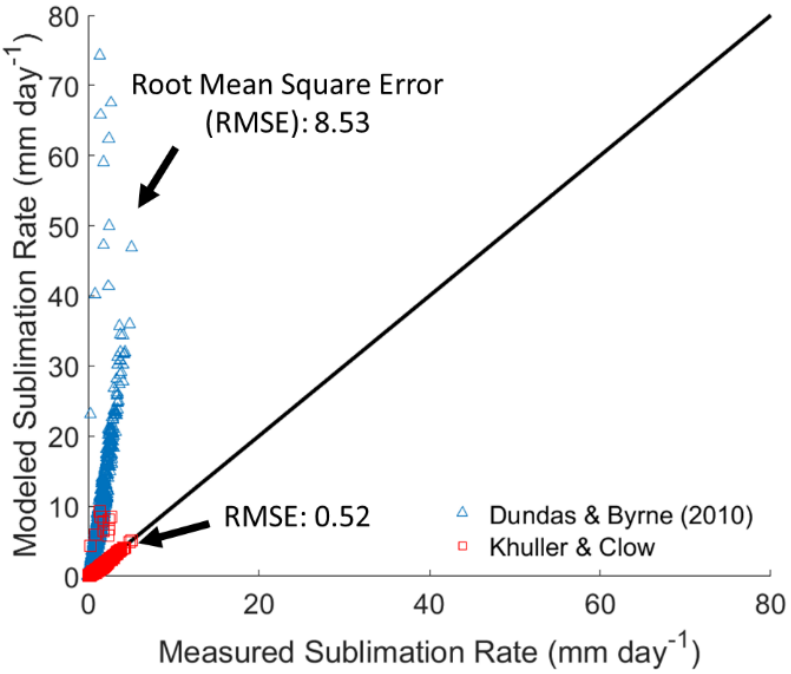

Figure 7.3. Cross-plot of the measured H_2O ice sublimation rate (mm day^{-1}) measured at Lake Hoare, Antarctica, a Mars analog (Clow et al., 1988), along with predictions from the Khuller & Clow (2022) model (red boxes), and the commonly used Dundas & Byrne (2010) model (blue triangles). Values along the diagonal 1:1 line indicate perfect agreement between measured and modeled values. The Root Mean Square Error (RMSE)

of the Dundas and Byrne (2010) model results is 8.53, about 17x higher than the Khuller & Clow (2022) model RMSE of 0.52, indicating a severe overestimation in sublimation rates by the Dundas & Byrne (2010) model.

In Chapter 4, I presented a model for how CO_2 frosts might form and sublimate in the shallow subsurface (top few millimeters/centimeters) in loose, unconsolidated materials to trigger new gully channel formation in these materials. However, whether it is possible to truly radiatively cool down to even this shallow depth is currently unknown. I hope to continue to investigate this process in more detail, by completing the development of a radiative transfer model I wrote during my undergraduate thesis for this purpose.

In Chapter 5, I discovered that there are, at some locations below the South Polar Layered Deposit basal interface, a set of deeper subsurface radar reflectors. I hope to continue investigating the nature of these deeper reflectors and assess whether they are part of the enigmatic Dorsa Argentea Formation thought to underlie the southern polar region of Mars.

Finally, in Chapter 6, I mapped a large fraction of Mars to find irregular polygonal ridge networks. I hope to one day map all of Mars with their help for these features, as they could hold a global record of ancient groundwater flowing within the ancient martian crust.

REFERENCES

Aharonson, O., & Schorghofer, N. (2006). Subsurface ice on Mars with rough topography. *Journal of Geophysical Research: Planets, 111*(E11).

Aharonson, O., Schorghofer, N., & Gerstell, M. F. (2003). Slope streak formation and dust deposition rates on Mars. *Journal of Geophysical Research: Planets, 108*(E12).

Allen, C. C., Morris, R. V., Jager, K. M., Golden, D., Lindstrom, D. J., Lindstrom, M. M., & Lockwood, J. P. (1998). Martian regolith simulant JSC Mars-1. *LPI*(1690), 1690.

Andrews-Hanna, J. C., Zuber, M. T., Arvidson, R. E., & Wiseman, S. M. (2010). Early Mars hydrology: Meridiani playa deposits and the sedimentary record of Arabia Terra. *Journal of Geophysical Research: Planets, 115*(E6).

Arfstrom, J., & Hartmann, W. K. (2005). Martian flow features, moraine-like ridges, and gullies: Terrestrial analogs and interrelationships. *Icarus, 174*(2), 321-335.

Arnold, N. S., Conway, S. J., Butcher, F. E., & Balme, M. R. (2019). Modeled subglacial water flow routing supports localized intrusive heating as a possible cause of basal melting of Mars' south polar ice cap. *Journal of Geophysical Research: Planets, 124*(8), 2101-2116. https://doi.org/10.1029/2019JE006061

Arvidson, R. E., Anderson, R. C., Bartlett, P., Bell, J. F., III, Blaney, D., Christensen, P. R., et al. (2004). Localization and physical properties experiments conducted by Spirit at Gusev Crater. *Science, 305*, 821-824.

Baker, V. (1985). *Problems in the paleohydrologic and hydroclimatologic interpretation of valley networks.* Paper presented at the Water on Mars Conference, Moffett Field, California.

Balme, M., Mangold, N., Baratoux, D., Costard, F., Gosselin, M., Masson, P., et al. (2006). Orientation and distribution of recent gullies in the southern hemisphere of Mars: observations from High Resolution Stereo Camera/Mars Express (HRSC/MEX) and Mars Orbiter Camera/Mars Global Surveyor (MOC/MGS) data. *Journal of Geophysical Research: Planets, 111*(E5).

Bapst, J., Bandfield, J. L., & Wood, S. E. (2015). Hemispheric asymmetry in martian seasonal surface water ice from MGS TES. *Icarus, 260*, 396-408.

Becerra, P., Sori, M. M., Thomas, N., Pommerol, A., Simioni, E., Sutton, S. S., et al. (2019). Timescales of the climate record in the south polar ice cap of Mars.

Geophysical Research Letters, 46(13), 7268-7277. https://doi.org/10.1029/2019GL083588

Becker, K., Anderson, J., Sides, S., Miller, E., Eliason, E., & Keszthelyi, L. (2007). *Processing HiRISE images using ISIS3.* Paper presented at the Lunar and Planetary Science Conference.

Bell III, J., Malin, M., Caplinger, M., Fahle, J., Wolff, M., Cantor, B., et al. (2013). Calibration and performance of the mars reconnaissance orbiter context camera (CTX). *International Journal of Mars Science and Exploration, 8*, 1-14.

Bell III, J., Rice, M., Johnson, J., & Hare, T. (2008). Surface albedo observations at Gusev crater and Meridiani Planum, Mars. *Journal of Geophysical Research: Planets, 113*(E6).

Berman, D. C., Hartmann, W. K., Crown, D. A., & Baker, V. R. (2005). The role of arcuate ridges and gullies in the degradation of craters in the Newton Basin region of Mars. *Icarus, 178*(2), 465-486.

Bibring, J.-P., Langevin, Y., Gendrin, A., Gondet, B., Poulet, F., Berthe, M., et al. (2005). Mars Surface Diversity as Revealed by the OMEGA/Mars Express Observations. *Science, 307*, 1576-1581.

Bibring, J.-P., Langevin, Y., Mustard, J. F., Poulet, F., Arvidson, R., Gendrin, A., et al. (2006). Global mineralogical and aqueous Mars history derived from OMEGA/Mars Express Data. *Science, 312*, 400-404.

Bibring, J.-P., Langevin, Y., Poulet, F., Gendrin, A., Gondet, B., Berthé, M., et al. (2004). Perennial water ice identified in the south polar cap of Mars. *Nature, 428*(6983), 627-630.

Bierson, C., Phillips, R., Smith, I., Wood, S., Putzig, N., Nunes, D., & Byrne, S. (2016). Stratigraphy and evolution of the buried CO2 deposit in the Martian south polar cap. *Geophysical Research Letters, 43*(9), 4172-4179.

Blackburn, D. G., Bryson, K. L., Chevrier, V. F., Roe, L. A., & White, K. F. (2010). Sublimation kinetics of CO2 ice on Mars. *Planetary and Space Science, 58*(5), 780-791.

Blaney, D., Archer, D., Arvidson, R., Cull, S., Ellehøj, M., Fisher, D., et al. (2009). Multi-spectral imaging of the Phoenix landing site: Characteristics of surface and subsurface ice, rocks, and soils. *LPI*, 2047.

Bleamaster III, L. F., & Crown, D. A. (2005). Mantle and gully associations along the walls of Dao and Harmakhis Valles, Mars. *Geophysical Research Letters, 32*(20).

Bohren, C. F. (1983). Colors of snow, frozen waterfalls, and icebergs. *JOSA, 73*(12), 1646-1652.

Bohren, C. F., & Barkstrom, B. R. (1974). Theory of the optical properties of snow. *Journal of Geophysical Research, 79*(30), 4527-4535. https://doi.org/10.1029/JC079i030p04527

Boulton, G. (1978). Boulder shapes and grain-size distributions of debris as indicators of transport paths through a glacier and till genesis. *Sedimentology, 25*(6), 773-799.

Boulton, G., & Caban, P. (1995). Groundwater flow beneath ice sheets: Part II—Its impact on glacier tectonic structures and moraine formation. *Quaternary Science Reviews, 14*(6), 563-587.

Boynton, W. V., Feldman, W. C., Mitrofanov, I. G., Evans, L. G., Reedy, R. C., Squyres, S. W., et al. (2004). The Mars Odyssey Gamma-Ray Spectrometer instrument suite. *Space Science Reviews, 110*, 37-83.

Brailsford, A., & Major, K. (1964). The thermal conductivity of aggregates of several phases, including porous materials. *British Journal of Applied Physics, 15*(3), 313.

Bramble, M. S., Mustard, J. F., & Salvatore, M. R. (2017). The geological history of northeast Syrtis Major, Mars. *Icarus, 293*, 66-93.

Bramson, A., Byrne, S., & Bapst, J. (2017). Preservation of midlatitude ice sheets on Mars. *Journal of Geophysical Research: Planets, 122*(11), 2250-2266.

Bramson, A. M., Byrne, S., Putzig, N. E., Sutton, S., Plaut, J. J., Brothers, T. C., & Holt, J. W. (2015). Widespread excess ice in Arcadia Planitia, Mars. *Geophysical Research Letters, 42*(16), 6566-6574.

Brandt, R. E., & Warren, S. G. (1993). Solar-heating rates and temperature profiles in Antarctic snow and ice. *J. Glaciol., 39*(131), 99-110.

Broquet, A., Wieczorek, M. A., & Fa, W. (2020). Flexure of the Lithosphere Beneath the North Polar Cap of Mars: Implications for Ice Composition and Heat Flow. *Geophysical Research Letters, 47*(5), e2019GL086746. https://doi.org/10.1029/2019GL086746

Brown, A. J., Byrne, S., Tornabene, L. L., & Roush, T. (2008). Louth crater: Evolution of a layered water ice mound. *Icarus, 196*(2), 433-445.

Büdel, J., Fischer, L., & Busche, D. (1982). *Climatic geomorphology* (Vol. 443): Princeton University Press Princeton.

Byrne, S. (2009). The polar deposits of Mars. *Annual Review of Earth and Planetary Sciences, 37*, 535-560.

Byrne, S., Dundas, C. M., Kennedy, M. R., Mellon, M. T., McEwen, A. S., Cull, S. C., et al. (2009). Distribution of mid-latitude ground ice on Mars from new impact craters. *Science, 325*(5948), 1674-1676.

Byrne, S., & Ingersoll, A. P. (2003). A sublimation model for Martian south polar ice features. *Science, 299*(5609), 1051-1053.

Byrne, S., & Ivanov, A. (2004). Internal structure of the Martian south polar layered deposits. *Journal of Geophysical Research: Planets, 109*(E11). https://doi.org/10.1029/2004JE002267

Cannon, K. M., Parman, S. W., & Mustard, J. F. (2017). Primordial clays on Mars formed beneath a steam or supercritical atmosphere. *Nature, 552*(7683), 88.

Cao, C., & Shao, X. (2013). Planck Calculator for Infrared Remote Sensing. Retrieved from https://ncc.nesdis.noaa.gov/data/planck.html

Carr, M. H. (1996). Water erosion on Mars and its biologic implications. *Endeavour, 20*(2), 56-60.

Carr, M. H. (2001). Mars Global Surveyor observations of Martian fretted terrain. *Journal of Geophysical Research: Planets, 106*(E10), 23571-23593.

Carrozzo, F., Bellucci, G., Altieri, F., D'aversa, E., & Bibring, J.-P. (2009). Mapping of water frost and ice at low latitudes on Mars. *Icarus, 203*(2), 406-420.

Cartwright, J. (2011). Diagenetically induced shear failure of fine-grained sediments and the development of polygonal fault systems. *Marine and Petroleum Geology, 28*(9), 1593-1610.

Cartwright, J., & Dewhurst, D. (1998). Layer-bound compaction faults in fine-grained sediments. *Geological Society of America Bulletin, 110*(10), 1242-1257.

Cedillo-Flores, Y., Treiman, A. H., Lasue, J., & Clifford, S. M. (2011). CO2 gas fluidization in the initiation and formation of Martian polar gullies. *Geophysical Research Letters, 38*(21).

Childs, C. (2004). Interpolating surfaces in ArcGIS spatial analyst. *ArcUser, July-September, 3235*(569), 32-35.

Chinnery, H. E., Hagermann, A., Kaufmann, E., & Lewis, S. R. (2020). The penetration of solar radiation into granular carbon dioxide and water ices of varying grain

sizes on Mars. *Journal of Geophysical Research: Planets, 125*(4), e2019JE006097.

Christensen, P. (2003a). Formation of recent martian gullies through melting of extensive water-rich snow deposits. *Nature, 422*(6927), 45-48. 10.1038/nature01436

Christensen, P., Engle, E., Anwar, S., Dickenshied, S., Noss, D., Gorelick, N., & Weiss-Malik, M. (2009a). *JMARS-a planetary GIS.* Paper presented at the AGU Fall Meeting Abstracts.

Christensen, P. R. (1986). Regional dust deposits on Mars: Physical properties, age, and history. *Journal of Geophysical Research: Solid Earth, 91*(B3), 3533-3545.

Christensen, P. R. (2003b). Formation of recent Martian gullies through melting of extensive water-rich snow deposits. *Nature, 422*(6927), 45.

Christensen, P. R., Bandfield, J. L., Bell III, J. F., Gorelick, N., Hamilton, V. E., Ivanov, A., et al. (2003). Morphology and composition of the surface of Mars: Mars Odyssey THEMIS results. *Science, 300*(5628), 2056-2061.

Christensen, P. R., Bandfield, J. L., Hamilton, V. E., Ruff, S. W., Kieffer, H. H., Titus, T. N., et al. (2001). Mars Global Surveyor Thermal Emission Spectrometer experiment: Investigation description and surface science results. *J. Geophys. Res., 106*, 23,823-823,871.

Christensen, P. R., Engle, E., Anwar, S., Dickenshied, S., Noss, D., Gorelick, N., & Weiss-Malik, M. (2009b). JMARS - A Planetary GIS. *AGU 2009 Fall Meeting, abstract id.IN22A-06*.

Christensen, P. R., Jakosky, B. M., Kieffer, H. H., Malin, M. C., McSween, H. Y., Nealson, K., et al. (2004). The Thermal Emission Imaging System (THEMIS) for the Mars 2001 Odyssey Mission. *Space Science Reviews, 110*(1-2), 85-130.

Clow, G., & Haberle, R. (1990). Characteristics of the martian atmospheric surface layer. *Scientific Results of the NASA-Sponsored Study Project on Mars: Evolution of Volcanism, Techtonics, and Volatiles.*, 111.

Clow, G., & Haberle, R. (1991). Free convection in the Martian atmosphere. *Reports of Planetary Geology and Geophysics Program*.

Clow, G. D. (1987). Generation of liquid water on Mars through the melting of a dusty snowpack. *Icarus, 72*(1), 95-127.

Clow, G. D., McKay, C. P., Simmons Jr, G. M., & Wharton Jr, R. A. (1988). Climatological observations and predicted sublimation rates at Lake Hoare, Antarctica. *Journal of Climate, 1*(7), 715-728.

Collaboration, A., Robitaille, T. P., Tollerud, E. J., Greenfield, P., Droettboom, M., Bray, E., et al. (2013). Astropy: A community Python package for astronomy. *Astron. Astrophys., 558*, A33. https://ui.adsabs.harvard.edu/abs/2013A&A...558A..33Adoi:

Conway, S., Harrison, T., Soare, R., Britton, A., & Steele, L. (2019). New slope-normalized global gully density and orientation maps for Mars. *Geological Society, London, Special Publications, 467*(1), 187-197.

Conway, S. J., & Balme, M. R. (2014). Decameter thick remnant glacial ice deposits on Mars. *Geophysical Research Letters, 41*(15), 5402-5409. 10.1002/2014GL060314

Conway, S. J., Butcher, F. E., de Haas, T., Deijns, A. A., Grindrod, P. M., & Davis, J. M. (2018). Glacial and gully erosion on Mars: A terrestrial perspective. *Geomorphology, 318*, 26-57.

Cooper, M. G., Smith, L. C., Rennermalm, A. K., Tedesco, M., Muthyala, R., Leidman, S. Z., et al. (2021). Spectral attenuation coefficients from measurements of light transmission in bare ice on the Greenland Ice Sheet. *15*(4), 1931-1953.

Cooper, M. R., Kovach, R. L., & Watkins, J. S. (1974). Lunar near-surface structure. *Reviews of Geophysics, 12*(3), 291-308.

Costard, F., Forget, F., Mangold, N., & Peulvast, J. P. (2002). Formation of recent martian debris flows by melting of near-surface ground ice at high obliquity. (Reports).(geophysical research on Mars). *Science, 295*(5552), 110. 10.1126/science.1066698

Cuffey, K. M., & Paterson, W. S. B. (2010). *The physics of glaciers*: Academic Press.

Cull, S., Arvidson, R., Morris, R., Wolff, M., Mellon, M., & Lemmon, M. (2010a). Seasonal ice cycle at the Mars Phoenix landing site: 2. Postlanding CRISM and ground observations. *Journal of Geophysical Research: Planets, 115*(E5).

Cull, S., Arvidson, R. E., Mellon, M. T., Skemer, P., Shaw, A., & Morris, R. V. (2010b). Compositions of subsurface ices at the Mars Phoenix landing site. *Geophysical Research Letters, 37*(24).

Cushing, G. E., Okubo, C. H., & Titus, T. N. (2015). Atypical pit craters on Mars: New insights from THEMIS, CTX, and HiRISE observations. *Journal of Geophysical Research: Planets, 120*(6), 1023-1043.

Cushing, G. E., & Titus, T. N. (2008). MGS-TES thermal inertia study of the Arsia Mons Caldera. *Journal of Geophysical Research: Planets, 113*(E6).

Cutts, J. A. (1973). Nature and origin of layered dust deposits of the dartian polar regions. *J. Geophys. Res., 78*(No. 20), 4231-4249.

Dadic, R., Mullen, P. C., Schneebeli, M., Brandt, R. E., & Warren, S. G. (2013). Effects of bubbles, cracks, and volcanic tephra on the spectral albedo of bare ice near the Transantarctic Mountains: Implications for sea glaciers on Snowball Earth. *Journal of Geophysical Research: Earth Surface, 118*(3), 1658-1676. https://doi.org/10.1002/jgrf.20098

Dang, C., Brandt, R. E., & Warren, S. G. (2015). Parameterizations for narrowband and broadband albedo of pure snow and snow containing mineral dust and black carbon. *Journal of Geophysical Research: Atmospheres, 120*(11), 5446-5468.

Daubar, I. J., Dundas, C. M., Byrne, S., Geissler, P., Bart, G., McEwen, A. S., et al. (2016). Changes in blast zone albedo patterns around new martian impact craters. *Icarus, 267*, 86-105.

Davies, D. W. (1979). The relative humidity of Mars' atmosphere. *J. Geophys. Res., 84*, 8335-8340.

DeGraff, J. M., & Aydin, A. (1987). Surface morphology of columnar joints and its significance to mechanics and direction of joint growth. *Geological Society of America Bulletin, 99*(5), 605-617.

Delamere, W. A., Tornabene, L. L., McEwen, A. S., Becker, K., Bergstrom, J. W., Bridges, N. T., et al. (2010). Color imaging of Mars by the high resolution imaging science experiment (HiRISE). *Icarus, 205*(1), 38-52.

Delaney, P. T., Pollard, D. D., Ziony, J. I., & McKee, E. H. (1986). Field relations between dikes and joints: Emplacement processes and paleostress analysis. *Journal of Geophysical Research: Solid Earth, 91*(B5), 4920-4938.

Dickson, J., Kerber, L., Fassett, C., & Ehlmann, B. (2018). *A Global, Blended CTX Mosaic of Mars with Vectorized Seam Mapping: A New Mosaicking Pipeline Using Principles of Non-Destructive Image Editing.* Paper presented at the Lunar and Planetary Science Conference.

Dickson, J. L., Head, J. W., & Fassett, C. I. (2012). Patterns of accumulation and flow of ice in the mid-latitudes of Mars during the Amazonian. *Icarus, 219*(2), 723-732.

Dickson, J. L., Head, J. W., Goudge, T. A., & Barbieri, L. (2015). Recent climate cycles on Mars: Stratigraphic relationships between multiple generations of gullies and the latitude dependent mantle. *Icarus, 252*, 83-94.

Dickson, J. L., Head, J. W., & Kreslavsky, M. (2007). Martian gullies in the southern mid-latitudes of Mars: Evidence for climate-controlled formation of young fluvial features based upon local and global topography. *Icarus, 188*(2), 315-323.

Dickson, J. L., Head, J. W., & Marchant, D. R. (2010). Kilometer-thick ice accumulation and glaciation in the northern mid-latitudes of Mars: Evidence for crater-filling events in the Late Amazonian at the Phlegra Montes. *Earth and Planetary Science Letters, 294*(3-4), 332-342.

Diniega, S., Byrne, S., Bridges, N. T., Dundas, C. M., & McEwen, A. S. (2010). Seasonality of present-day Martian dune-gully activity. *Geology, 38*(11), 1047-1050.

Diniega, S., Widmer, J., Hansen, C., & Portyankina, G. (2018). Present-Day (and Amazonian) Frost-Driven Geomorphic Changes on Martian Sandy Slopes. *LPI Contributions, 2086*.

Dozier, J., Green, R. O., Nolin, A. W., & Painter, T. H. (2009). Interpretation of snow properties from imaging spectrometry. *Remote Sensing of Environment, 113*, S25-S37.

Drube, L., Leer, K., Goetz, W., Gunnlaugsson, H., Haspang, M., Lauritsen, N., et al. (2010). Magnetic and optical properties of airborne dust and settling rates of dust at the Phoenix landing site. *Journal of Geophysical Research: Planets, 115*(E5). https://doi.org/10.1029/2009JE003419

Dundas, C. M. (2020). Geomorphological evidence for a dry dust avalanche origin of slope streaks on Mars. *Nature Geoscience, 13*(7), 473-476.

Dundas, C. M., Bramson, A. M., Ojha, L., Wray, J. J., Mellon, M. T., Byrne, S., et al. (2018). Exposed subsurface ice sheets in the Martian mid-latitudes. *Science (New York, N.Y.), 359*(6372), 199. 10.1126/science.aao1619

Dundas, C. M., & Byrne, S. (2010). Modeling sublimation of ice exposed by new impacts in the martian mid-latitudes. *Icarus, 206*(2), 716-728.

Dundas, C. M., Byrne, S., & McEwen, A. S. (2015a). Modeling the development of Martian sublimation thermokarst landforms. *Icarus, 262*, 154-169.

Dundas, C. M., Diniega, S., Hansen, C. J., Byrne, S., & McEwen, A. S. (2012). Seasonal activity and morphological changes in Martian gullies. *Icarus, 220*(1), 124-143.

Dundas, C. M., Diniega, S., & McEwen, A. S. (2015b). Long-term monitoring of martian gully formation and evolution with MRO/HiRISE. *Icarus, 251*, 244-263.

Dundas, C. M., McEwen, A. S., Diniega, S., Byrne, S., & Martinez-Alonso, S. (2010). New and recent gully activity on Mars as seen by HiRISE. *Geophysical Research Letters, 37*(7).

Dundas, C. M., McEwen, A. S., Diniega, S., Hansen, C. J., Byrne, S., & McElwaine, J. N. (2019). The formation of gullies on Mars today. *Geological Society, London, Special Publications, 467*(1), 67-94.

Dundas, C. M., Mellon, M. T., Conway, S. J., Daubar, I. J., Williams, K. E., Ojha, L., et al. (2021). Widespread Exposures of Extensive Clean Shallow Ice in the Mid-Latitudes of Mars. *Journal of Geophysical Research: Planets*, e2020JE006617. https://doi.org/10.1029/2020JE006617

Ebinger, E., & Mustard, J. (2015). *Linear ridges in the Nilosyrtis region of Mars: implications for subsurface fluid flow.* Paper presented at the Lunar and Planetary Science Conference.

Ebinger, E., & Mustard, J. (2016). Classification of Curvilinear Ridges in the Nilosyrtis Highlands of Mars. *LPI*(1903), 2731.

Edwards, C., Christensen, P., & Hill, J. (2011). Mosaicking of global planetary image datasets: 2. Modeling of wind streak thicknesses observed in Thermal Emission Imaging System (THEMIS) daytime and nighttime infrared data. *Journal of Geophysical Research: Planets, 116*(E10).

Edwards, C. S., Piqueux, S., Hamilton, V. E., Fergason, R. L., Herkenhoff, K. E., Vasavada, A. R., et al. (2018). The thermophysical properties of the Bagnold Dunes, Mars: Ground-truthing orbital data. *Journal of Geophysical Research: Planets, 123*(5), 1307-1326.

Ehlmann, B. L., & Mustard, J. F. (2012). An in-situ record of major environmental transitions on early Mars at Northeast Syrtis Major. *Geophysical Research Letters, 39*(11).

Ehlmann, B. L., Mustard, J. F., Murchie, S. L., Bibring, J.-P., Meunier, A., Fraeman, A. A., & Langevin, Y. (2011). Subsurface water and clay mineral formation during the early history of Mars. *Nature, 479*, 53-60. 10.1038/nature10582

Ehlmann, B. L., Mustard, J. F., Swayze, G. A., Clark, R. N., Bishop, J. L., Poulet, F., et al. (2009). Identification of hydrated silicate minerals on Mars using MRO-CRISM: Geologic context near Nili Fossae and implications for aqueous alteration. *Journal of Geophysical Research, 114*(E00D08). 10.1029/2009JE003339

El Maarry, M., Markiewicz, W., Mellon, M., Goetz, W., Dohm, J., & Pack, A. (2010). Crater floor polygons: Desiccation patterns of ancient lakes on Mars? *Journal of Geophysical Research: Planets, 115*(E10).

El Maarry, M. R., Kodikara, J., Wijessoriya, S., Markiewicz, W. J., & Thomas, N. (2012). Desiccation mechanism for formation of giant polygons on Earth and intermediate-sized polygons on Mars: Results from a pre-fracture model. *Earth and Planetary Science Letters, 323*, 19-26.

Eppes, M.-C., Willis, A., Molaro, J., Abernathy, S., & Zhou, B. (2015). Cracks in Martian boulders exhibit preferred orientations that point to solar-induced thermal stress. *Nature Communications, 6*(1), 1-11.

Farmer, C. B. (1976). Liquid water on Mars. *Icarus, 28*(2), 279-289.

Farmer, C. B., Davies, D. W., & LaPorte, D. D. (1976). Mars: Northern summer ice cap—Water vapor observations from Viking 2. *Science, 194*(4271), 1339-1341.

Fassett, C. I., & Head, J. W. (2007). Layered mantling deposits in northeast Arabia Terra, Mars: Noachian-Hesperian sedimentation, erosion, and terrain inversion. *Journal of Geophysical Research: Planets, 112*(E8).

Fassett, C. I., & Head, J. W. (2011). Sequence and timing of conditions on early Mars. *Icarus, 211*(2), 1204-1214.

Feldman, W. C., Boynton, W. V., Tokar, R. L., Prettyman, T. H., Gasnault, O., Squyres, S. W., et al. (2002). Global distribution of neutrons from Mars: Results from Mars Odyssey. *Science, 297*, 75-78.

Fergason, R., & Christensen, P. (2008). Formation and erosion of layered materials: Geologic and dust cycle history of eastern Arabia Terra, Mars. *Journal of Geophysical Research: Planets, 113*(E12).

Fergason, R. L., Christensen, P. R., Bell, J. F., III, Golombek, M. P., Herkenhoff, K. E., & Kieffer, H. H. (2006a). Physical properties of the Mars Exploration Rover landing sites as inferred from Mini-TES–derived thermal inertia. *Journal of Geophysical Research, 111*(E02S21), doi:10.1029/2005JE002583.

Fergason, R. L., Christensen, P. R., & Kieffer, H. H. (2006b). High-resolution thermal inertia derived from the Thermal Emission Imaging System (THEMIS): Thermal model and applications. *Journal of Geophysical Research: Planets, 111*(E12).

Fishbaugh, K. E., & Head, J. W. (2005). Origin and characteristics of the Mars north polar basal unit and implications for polar geologic history. *Icarus, 174*(2), 444-474.

Fisher, D. A. (2005). A process to make massive ice in the martian regolith using long-term diffusion and thermal cracking. *Icarus, 179*(2), 387-397.

Forget, F., Hourdin, F., Fournier, R., Hourdin, C., Talagrand, O., Collins, M., et al. (1999). Improved general circulation models of the Martian atmosphere from the surface to above 80 km. *Journal of Geophysical Research: Planets, 104*(E10), 24155-24175.

Forget, F., Pilorget, C., Pottier, A., & Meslin, P. (2016). *Deep incision of the Latitude Dependent Mantle in Martian gullies formed by CO 2 sublimation processes.* Paper presented at the Unnumbered abstract presented at the Workshop on Martian Gullies and their Earth Analogs.

Gaddis, L., Anderson, J., Becker, K., Becker, T., Cook, D., Edwards, K., et al. (1997). *An overview of the integrated software for imaging spectrometers (ISIS).* Paper presented at the Lunar and Planetary Science Conference.

Gaidos, E. J. (2001). Cryovolcanism and the recent flow of liquid water on Mars. *Icarus, 153*(1), 218-223.

Gilmore, M. S., & Phillips, E. L. (2002). Role of aquicludes in formation of Martian gullies. *Geology, 30*(12), 1107-1110.

Gim, Y., Bellutta, D., & Plaut, J. (2018). Construction of MARSIS 3D Radar Maps of the Martian Polar Regions. *Lunar and Planetary Science Conference, 49*(2083), 1793.

Goetz, W., Pike, W., Hviid, S., Madsen, M. B., Morris, R., Hecht, M., et al. (2010). Microscopy analysis of soils at the Phoenix landing site, Mars: Classification of soil particles and description of their optical and magnetic properties. *Journal of Geophysical Research: Planets, 115*(E8). https://doi.org/10.1029/2009JE003437

Golombek, M., Grant, J., Kipp, D., Vasavada, A., Kirk, R., Fergason, R., et al. (2012). Selection of the Mars Science Laboratory landing site. *Space Science Reviews, 170*(1-4), 641-737.

Golombek, M. P., Crumpler, L. S., Grant, J. A., Greeley, R., Cabrol, N. A., Parker, T., et al. (2006). Geology of the Gusev cratered plains from the Spirit rover transverse. *Journal of Geophysical Research: Planets, 111*(E2).

Goudge, T. A., Mustard, J. F., Head III, J. W., Fassett, C. I., & Wiseman, S. M. (2015). Assessing the mineralogy of the watershed and fan deposits of the Jezero crater paleolake system, Mars. *Journal of Geophysical Research*, 775-808. 10.1002/2014JE004782

Gow, A. J. (1969). On the rates of growth of grains and crystals in South Polar firn. *J. Glaciol., 8*(53), 241-252.

Greeley, R., & Guest, J. (1987). Geologic map of the eastern equatorial region of Mars.

Gulick, V. C., Glines, N., Hart, S., & Freeman, P. (2019). Geomorphological analysis of gullies on the central peak of Lyot Crater, Mars. *Geological Society, London, Special Publications, 467*(1), 233-265.

Gyalay, S., Dobrea, E. Z. N., Chu, K., & Pitman, K. M. (2019). Nonlinear spectral mixture modeling to estimate water-ice abundance of martian regolith. *Icarus, 329*, 79-87.

Haberle, R. M., Clancy, R. T., Forget, F., Smith, M. D., & Zurek, R. W. (2017). *The atmosphere and climate of Mars*: Cambridge University Press.

Hapke, B. (2012). *Theory of reflectance and emittance spectroscopy*: Cambridge university press.

Harrison, T., Stuurman, C., Osinski, G., & Tornabene, L. (2017). *Deposition and erosion of the scalloped depression bearing terrain in western Utopia Planitia, Mars.* Paper presented at the Lunar and Planetary Science Conference.

Harrison, T. N., Malin, M., & Edgett, K. (2009). *Present-day gully activity observed by the Mars Reconnaissance Orbiter (MRO) Context Camera (CTX).* Paper presented at the AAS/Division for Planetary Sciences Meeting Abstracts# 41.

Harrison, T. N., Osinski, G. R., Tornabene, L. L., & Jones, E. (2015). Global documentation of gullies with the Mars Reconnaissance Orbiter Context Camera and implications for their formation. *Icarus, 252*, 236-254.

Hart, H. M., & Jakosky, B. M. (1986). Composition and stability of the condensate observed at the Viking Lander 2 site on Mars. *Icarus, 66*(1), 134-142.

Head, J., Neukum, G., Jaumann, R., Hiesinger, H., Hauber, E., Carr, M., et al. (2005). Tropical to mid-latitude snow and ice accumulation, flow and glaciation on Mars. *Nature, 434*(7031), 346-351.

Head, J. W., & Mustard, J. F. (2006). Breccia dikes and crater-related faults in impact craters on Mars: Erosion and exposure on the floor of a crater 75 km in diameter at the dichotomy boundary. *Meteoritics & Planetary Science, 41*(10), 1675-1690.

Head, J. W., Mustard, J. F., Kreslavsky, M. A., Milliken, R. E., & Marchant, D. R. (2003). Recent ice ages on Mars. *Nature, 426*(6968), 797-802.

Hecht, M., Fisher, D., Catling, D. C., & Kounaves, S. P. (2018). RE: Radar evidence of subglacial liquid water on Mars (Orosei et al.).

Hecht, M. H. (2002). Metastability of liquid water on Mars. *Icarus, 156*, 373-386. 10.1006/icar.2001.6794

Heldmann, J. L., Carlsson, E., Johansson, H., Mellon, M. T., & Toon, O. B. (2007). Observations of Martian gullies and constraints on potential formation mechanisms: II. The northern hemisphere. *Icarus, 188*(2), 324-344.

Heldmann, J. L., & Mellon, M. T. (2004). Observations of martian gullies and constraints on potential formation mechanisms. *Icarus, 168*(2), 285-304. 10.1016/j.icarus.2003.11.024

Herkenhoff, K. E., & Plaut, J. J. (2000). Surface ages and resurfacing rates of the polar layered deposits on Mars. *Icarus, 144*(2), 243-253.

Hess, S., Ryan, J., Tillman, J., Henry, R., & Leovy, C. (1980). The annual cycle of pressure on Mars measured by Viking Landers 1 and 2. *Geophysical Research Letters, 7*(3), 197-200.

Hiesinger, H., & Head, J. W. (2000). Characteristics and origin of polygonal terrain in southern Utopia Planitia, Mars: results from Mars Orbiter Laser Altimeter and Mars Orbiter Camera data. *Journal of Geophysical Research: Planets, 105*(E5), 11999-12022.

Higuchi, K., & Nagoshi, A. (1977). Effect of particulate matter in surface snow layers on the albedo of perennial snow patches. *IAHS AISH Publication, 118*, 95-97.

Hoffman, N. (2002). Active Polar Gullies on Mars and the Role of Carbon Dioxide. *Astrobiology, 2*(3), 313-323. 10.1089/153110702762027899

Holt, J. W., Safaeinili, A., Plaut, J. J., Head, J. W., Phillips, R. J., Seu, R., et al. (2008). Radar sounding evidence for buried glaciers in the southern mid-latitudes of Mars. *Science, 322*(5905), 1235-1238.

Hourdin, F., Le Van, P., Forget, F., & Talagrand, O. (1993). Meteorological variability and the annual surface pressure cycle on Mars. *J. Atmos. Sci., 50*(21), 3625-3640.

Hudson, T. L., Aharonson, O., Schorghofer, N., Farmer, C. B., Hecht, M. H., & Bridges, N. T. (2007). Water vapor diffusion in Mars subsurface environments. *Journal of Geophysical Research: Planets, 112*(E5).

Hugenholtz, C. H. (2008). Frosted granular flow: A new hypothesis for mass wasting in martian gullies. *Icarus, 197*(1), 65-72.

Ingersoll, A. P. (1970). Mars: Occurrence of liquid water. *Science, 168*(3934), 972-973.

Irwin III, R. P., Wray, J. J., Mest, S. C., & Maxwell, T. A. (2018). Wind-eroded crater floors and intercrater plains, Terra Sabaea, Mars. *Journal of Geophysical Research: Planets, 123*(2), 445-467.

Ivanov, M., Hiesinger, H., Erkeling, G., Hielscher, F., & Reiss, D. (2012). Major episodes of geologic history of Isidis Planitia on Mars. *Icarus, 218*(1), 24-46.

Jakosky, B. M., & Carr, M. A. (1985). Possible precipitation of ice at low latitudes of Mars during periods of high obliquity. *Nature, 315*, 559-561.

Jakosky, B. M., & Farmer, C. B. (1982). The seasonal and global behavior of water vapor in the Mars atmosphere: Complete global results of the Viking atmospheric water detector experiment. *Journal of Geophysical Research: Solid Earth, 87*(B4), 2999-3019.

Jakosky, B. M., Henderson, B. G., & Mellon, M. T. (1995). Chaotic obliquity and the nature of the Martian climate. *Journal of Geophysical Research: Planets, 100*(E1), 1579-1584.

Jordan, R., Picardi, G., Plaut, J., Wheeler, K., Kirchner, D., Safaeinili, A., et al. (2009). The Mars express MARSIS sounder instrument. *Planetary and Space Science, 57*(14-15), 1975-1986.

Joseph, J. H., Wiscombe, W., & Weinman, J. (1976). The delta-Eddington approximation for radiative flux transfer. *J. Atmos. Sci., 33*(12), 2452-2459.

Kaempfer, T. U., & Schneebeli, M. J. J. o. G. R. A. (2007). Observation of isothermal metamorphism of new snow and interpretation as a sintering process. *112*(D24).

Kayetha, V. K., Prasad, A. K., Cervone, G., & Singh, R. P. (2007). Effect of dust storm on ocean color and snow parameters. *Journal of the Indian Society of Remote Sensing, 35*(1), 1.

Kerber, L., Dickson, J. L., Head, J. W., & Grosfils, E. B. (2017). Polygonal ridge networks on Mars: Diversity of morphologies and the special case of the Eastern Medusae Fossae Formation. *Icarus, 281*, 200-219.

Khuller, A. R., & Christensen, P. R. (2020). *Repository: Evidence of Exposed Dusty Water Ice within Martian Gullies. https://doi.org/10.5281/zenodo.4356920*.

Khuller, A. R., & Christensen, P. R. (2021). Evidence of Exposed Dusty Water Ice within Martian Gullies. *Journal of Geophysical Reasearch: Planets*. https://doi.org/10.1029/2020JE006539

Khuller, A. R., Christensen, P. R., Harrison, T. N., & Diniega, S. (2020). *Repository: The Distribution of Frosts on Mars: Links to Present-Day Gully Activity*. Retrieved from: https://doi.org/10.5281/zenodo.4446319

Khuller, A. R., Christensen, P. R., & Warren, S. G. (2021a). *Repository: Spectral Albedo of Dusty Martian H2O Snow and Ice*. Retrieved from: https://doi.org/10.5281/zenodo.4653768

Khuller, A. R., Christensen, P. R., & Warren, S. G. (2021b). Spectral albedo of dusty martian H2O snow and ice. *Journal of Geophysical Research: Planets, 126*(9), e2021JE006910.

Khuller, A. R., & Clow, G. (2022). *An Improved Model for H2O Ice Sublimation on Mars: Implications for Martian Ice Stability and Evolution.* Paper presented at the Fall Meeting 2022.

Khuller, A. R., Kerber, L., Schwamb, M. E., Beer, S., Nogal, F. E., Perry, R., et al. (2021c). *Repository: Irregular Polygonal Ridge Networks in Ancient Noachian Terrain on Mars*. Retrieved from: https://doi.org/10.5281/zenodo.4441387

Khuller, A. R., & Plaut, J. J. (2021). *Repository: Characteristics of the Basal Interface of the Martian South Polar Layered Deposits*. Retrieved from: https://doi.org/10.5281/zenodo.4653741

Kieffer, H. H. (1968). *Near infrared spectral reflectance of simulated Martian frosts.* California Institute of Technology,

Kieffer, H. H. (1979). Mars south polar spring and summer temperatures: A residual CO2 frost. *J. Geophys. Res., 84*, 8263-8289.

Kieffer, H. H. (1990). H2O grain size and the amount of dust in Mars' residual north polar cap. *Journal of Geophysical Research: Solid Earth, 95*(B2), 1481-1493.

Kieffer, H. H. (2013). Thermal model for analysis of Mars infrared mapping. *Journal of Geophysical Research: Planets, 118*(3), 451-470.

Kieffer, H. H., Christensen, P. R., & Titus, T. N. (2006). CO2 jets formed by sublimation beneath translucent slab ice in Mars' seasonal south polar ice cap. *Nature, 442*(7104), 793.

Kieffer, H. H., Martin, T. Z., Peterfreund, A. R., Jakosky, B. M., Miner, E. D., & Palluconi, F. D. (1977). Thermal and albedo mapping of Mars during the Viking primary mission. *J. Geophys. Res., 82*, 4249-4292.

Kieffer, H. H., S.C. Chase, J., Martin, T. Z., Miner, E. D., & Palluconi, F. D. (1976). Martian North Pole summer temperatures: Dirty water ice. *Science, 194*, 1341-1344.

Kieffer, H. H., Titus, T. N., Mullins, K. F., & Christensen, P. R. (2000). Mars south polar spring and summer behavior observed by TES: Seasonal cap evolution controlled by frost grain size. *Journal of Geophysical Research: Planets, 105*(E4), 9653-9699.

Kite, E. S., Michaels, T. I., Rafkin, S., Manga, M., & Dietrich, W. E. (2011). Localized precipitation and runoff on Mars. *Journal of Geophysical Research: Planets, 116*(E7).

Klimczak, C., Kling, C. L., & Byrne, P. K. (2018). Topographic expressions of large thrust faults on Mars. *Journal of Geophysical Research: Planets, 123*(8), 1973-1995. https://doi.org/10.1029/2017JE005448

Kolb, K. J., Pelletier, J. D., & McEwen, A. S. (2010). Modeling the formation of bright slope deposits associated with gullies in Hale Crater, Mars: Implications for recent liquid water. *Icarus, 205*(1), 113-137.

Kossacki, K. J., & Markiewicz, W. J. (2004). Seasonal melting of surface water ice condensing in martian gullies. *Icarus, 171*(2), 272-283. 10.1016/j.icarus.2004.05.018

Koutnik, M., Byrne, S., & Murray, B. (2002). South polar layered deposits of Mars: The cratering record. *Journal of Geophysical Research: Planets, 107*(E11), 10-11-10-10. https://doi.org/10.1029/2001JE001805

Kremer, C. H., Mustard, J. F., & Bramble, M. S. (2019). A widespread olivine-rich ash deposit on Mars. *Geology*. https://doi.org/10.1130/G45563.1doi:10.1130/g45563.1

Kreslavsky, M. A., & Head, J. W. (2002). Mars: Nature and evolution of young latitude-dependent water-ice-rich mantle. *Geophysical Research Letters, 29*(15), 14-11-14-14. 10.1029/2002GL015392

Kress, A. M., & Head, J. W. (2015). Late Noachian and early Hesperian ridge systems in the south circumpolar Dorsa Argentea Formation, Mars: Evidence for two stages of melting of an extensive late Noachian ice sheet. *Planetary and Space Science, 109*, 1-20.

Landis, G. (2007). *Observation of frost at the equator of Mars by the Opportunity rover.* Paper presented at the Lunar and Planetary Science Conference.

Langevin, Y., Poulet, F., Bibring, J.-P., Schmitt, B., Douté, S., & Gondet, B. (2005). Summer evolution of the north polar cap of Mars as observed by OMEGA/Mars express. *Science, 307*(5715), 1581-1584.

Lauro, S. E., Mattei, E., Pettinelli, E., Soldovieri, F., Orosei, R., Cartacci, M., et al. (2010). Permittivity estimation of layers beneath the northern polar layered deposits, Mars. *Geophysical Research Letters, 37*(14). https://doi.org/10.1029/2010GL043015

Lauro, S. E., Pettinelli, E., Caprarelli, G., Guallini, L., Rossi, A. P., Mattei, E., et al. (2021). Multiple subglacial water bodies below the south pole of Mars unveiled by new MARSIS data. *Nature Astronomy*, 1-8.

Law, J., & Van Dijk, D. (1994). Sublimation as a geomorphic process: a review. *Permafrost and Periglacial Processes, 5*(4), 237-249.

Leighton, R. B., & Murray, B. C. (1966). Behavior of carbon dioxide and other volatiles on Mars. *Science, 153*, 136-144.

Lemmon, M. T., Wolff, M. J., Smith, M. D., Clancy, R. T., Banfield, D., Landis, G. A., et al. (2004). Atmospheric imaging results from the Mars Exploration Rovers: Spirit and Opportunity. *Science, 306*, 1753-1756.

Léveillé, R. J., Bridges, J., Wiens, R. C., Mangold, N., Cousin, A., Lanza, N., et al. (2014). Chemistry of fracture-filling raised ridges in Yellowknife Bay, Gale Crater: Window into past aqueous activity and habitability on Mars. *Journal of Geophysical Research: Planets, 119*(11), 2398-2415.

Levy, J., Head, J. W., & Marchant, D. R. (2010). Concentric crater fill in the northern mid-latitudes of Mars: Formation processes and relationships to similar landforms of glacial origin. *Icarus, 209*(2), 390-404.

Levy, J. S., Head, J. W., & Marchant, D. R. (2007). Lineated valley fill and lobate debris apron stratigraphy in Nilosyrtis Mensae, Mars: Evidence for phases of glacial modification of the dichotomy boundary. *Journal of Geophysical Research: Planets, 112*(E8).

Levy, J. S., Head, J. W., & Marchant, D. R. (2009a). Thermal contraction crack polygons on Earth and Mars; classification, distribution, and implications for recent cold desert processes. In (Vol. 90). Washington, DC: Washington, DC, United States: American Geophysical Union.

Levy, J. S., Head, J. W., Marchant, D. R., Dickson, J. L., & Morgan, G. A. (2009b). Geologically recent gully–polygon relationships on Mars: Insights from the

Antarctic Dry Valleys on the roles of permafrost, microclimates, and water sources for surface flow. *Icarus, 201*(1), 113-126. 10.1016/j.icarus.2008.12.043

Linow, S., Hörhold, M. W., & Freitag, J. (2012). Grain-size evolution of polar firn: a new empirical grain growth parameterization based on X-ray microcomputer tomography measurements. *J. Glaciol., 58*(212), 1245-1252.

Liston, G. E., & Winther, J.-G. (2005). Antarctic surface and subsurface snow and ice melt fluxes. *Journal of Climate, 18*(10), 1469-1481.

Liston, G. E., Winther, J.-G., Bruland, O., Elvehøy, H., & Sand, K. (1999). Below-surface ice melt on the coastal Antarctic ice sheet. *J. Glaciol., 45*(150), 273-285.

Loizeau, D., Carter, J., Bouley, S., Mangold, N., Poulet, F., Bibring, J.-P., et al. (2012). Characterization of hydrated silicate-bearing outcrops in Tyrrhena Terra, Mars: Implications to the alteration history of Mars. *Icarus, 219*(1), 476-497.

Luikov, A., & Lebedev, D. (1973). Study of the ice sublimation process. *International Journal of Heat and Mass Transfer, 16*(6), 1087-1096.

Madeleine, J. B., Head, J. W., Forget, F., Navarro, T., Millour, E., Spiga, A., et al. (2014). Recent ice ages on Mars: the role of radiatively active clouds and cloud microphysics. *Geophysical Research Letters, 41*(14), 4873-4879.

Madison, M. P. (2010). *Origins and characteristics of clastic dikes in the Sage Creek area of Badlands National Park.* Northern Illinois University,

Malin, M., & Edgett, K. S. (2001). Mars global surveyor Mars orbiter camera: interplanetary cruise through primary mission. *Journal of Geophysical Research: Planets, 106*(E10), 23429-23570.

Malin, M. C., Bell III, J. F., Cantor, B. A., Caplinger, M. A., Calvin, W. M., Clancy, R. T., et al. (2007). Context Camera Investigation on board the Mars Reconnaissance Orbiter. *Journal of Geophysical Research: Planets, 112*(E5). https://agupubs.onlinelibrary.wiley.com/doi/abs/10.1029/2006JE002808doi:doi:10.1029/2006JE002808

Malin, M. C., & Edgett, K. S. (2000). Evidence for recent groundwater seepage and surface runoff on Mars. *Science, 288*, 2330-2335.

Malin, M. C., Edgett, K. S., Posiolova, L. V., McColley, S. M., & Dobrea, E. Z. N. (2006). Present-day impact cratering rate and contemporary gully activity on Mars. *Science, 314*(5805), 1573-1577.

Mallet, R. (1875). I. On the origin and mechanism of production of the prismatic (or columnar) structure of basalt. *Proceedings of the Royal Society of London, 23*(156-163), 180-184.

Mangold, N. (2003). Geomorphic analysis of lobate debris aprons on Mars at Mars Orbiter Camera scale: Evidence for ice sublimation initiated by fractures. *Journal of Geophysical Research: Planets, 108*(E4).

Mangold, N. (2011a). Ice sublimation as a geomorphic process: A planetary perspective. *Geomorphology, 126*(1-2), 1-17.

Mangold, N. (2011b). Water ice sublimation-related landforms on Mars. *Geological Society, London, Special Publications, 356*(1), 133-149.

Mangold, N., Poulet, F., Mustard, J., Bibring, J. P., Gondet, B., Langevin, Y., et al. (2007). Mineralogy of the Nili Fossae region with OMEGA/Mars Express data: 2. Aqueous alteration of the crust. *Journal of Geophysical Research: Planets, 112*(E8).

Marco, S., Weinberger, R., & Agnon, A. (2002). Radial clastic dykes formed by a salt diapir in the Dead Sea Rift, Israel. *Terra Nova, 14*(4), 288-294.

Matzler, C. (2002). Matzler's Matlab Code For Mie Theory.

McCleese, D., Schofield, J., Taylor, F., Calcutt, S., Foote, M., Kass, D., et al. (2007). Mars Climate Sounder: An investigation of thermal and water vapor structure, dust and condensate distributions in the atmosphere, and energy balance of the polar regions. *Journal of Geophysical Research: Planets, 112*(E5).

McEwen, A. S., Dundas, C. M., Mattson, S. S., Toigo, A. D., Ojha, L., Wray, J. J., et al. (2014). Recurring slope lineae in equatorial regions of Mars. *Nature Geoscience, 7*(1), 53.

McEwen, A. S., Eliason, E. M., Bergstrom, J. W., Bridges, N. T., Hansen, C. J., Delamere, W. A., et al. (2007a). Mars Reconnaissance Orbiter's High Resolution Imaging Science Experiment (HiRISE). *Journal of Geophysical Research: Planets, 112*(E5). https://agupubs.onlinelibrary.wiley.com/doi/abs/10.1029/2005JE002605doi:doi:10.1029/2005JE002605

McEwen, A. S., Hansen, C., Delamere, W. A., Eliason, E., Herkenhoff, K. E., Keszthelyi, L., et al. (2007b). A closer look at water-related geologic activity on Mars. *Science, 317*(5845), 1706-1709.

McEwen, A. S., Thomas, M., & Dundas, C. M. (2018). *Active gullies and mass wasting on equatorial Mars.* Paper presented at the European Planetary Science Congress.

McGill, G. E. (2000). Crustal history of north central Arabia Terra, Mars. *Journal of Geophysical Research: Planets, 105*(E3), 6945-6959.

McMichael, J. G., Gim, Y., Arumugam, D. D., & Plaut, J. J. (2017). *Radar autofocus algorithm incorporating terrain knowledge for correction of Mars' ionospheric distortion in MARSIS observations.* Paper presented at the 2017 IEEE Radar Conference (RadarConf).

Mellon, M. T., Arvidson, R. E., Sizemore, H. G., Searls, M. L., Blaney, D. L., Cull, S., et al. (2009). Ground ice at the Phoenix landing site: Stability state and origin. *Journal of Geophysical Research: Planets, 114*(E1). https://doi.org/10.1029/2009JE003417

Mellon, M. T., Feldman, W. C., & Prettyman, T. H. (2004). The presence and stability of ground ice in the southern hemisphere of Mars. *Icarus, 169*(2), 324-340.

Mellon, M. T., & Jakosky, B. M. (1995). The distribution and behavior of Martian ground ice during past and present epochs. *Journal of Geophysical Research: Planets, 100*(E6), 11781-11799.

Mellon, M. T., & Phillips, R. J. (2001). Recent gullies on Mars and the source of liquid water. *Journal of Geophysical Research: Planets, 106*(E10), 23165-23179.

Milazzo, M., Herkenhoff, K., Becker, K., Russell, P., Delamere, A., & McEwen, A. (2015). MRO/HiRISE Radiometric Calibration Update. *LPI*(1832), 1498.

Milazzo, M. P., Keszthelyi, L. P., Jaeger, W. L., Rosiek, M., Mattson, S., Verba, C., et al. (2009). Discovery of columnar jointing on Mars. *Geology, 37*(2), 171-174.

Milliken, R., Mustard, J., & Goldsby, D. (2003). Viscous flow features on the surface of Mars: Observations from high-resolution Mars Orbiter Camera (MOC) images. *Journal of Geophysical Research: Planets, 108*(E6).

Millour, E., Forget, F., Spiga, A., Vals, M., Zakharov, V., Montabone, L., et al. (2018). The Mars Climate Database (version 5.3). *From Mars Express to ExoMars*.

Mitrofanov, I., Anfimov, D., Kozyrev, A., Litvak, M., Sanin, A., Tret'yakov, V., et al. (2002). Maps of subsurface hydrogen from the high energy neutron detector, Mars Odyssey. *Science, 297*(5578), 78-81.

Moore, H. J., Bickler, D. B., Crisp, J. A., Eisen, H. J., Gensler, J. A., Haldemann, A. F. C., et al. (1999). Soil-like deposits observed by Sojourner, and Pathfinder Rover. *Journal of Geophysical Research, 104*(E4), 8729-8746.

Moore, H. J., & Jakosky, B. M. (1989). Viking landing sites, remote-sensing observations, and physical properties of Martian surface materials. *Icarus, 81*(1), 164-184.

Mullen, P. C., & Warren, S. G. (1988). Theory of the optical properties of lake ice. *Journal of Geophysical Research: Atmospheres, 93*(D7), 8403-8414. https://doi.org/10.1029/JD093iD07p08403

Murchie, S., Arvidson, R., Bedini, P., Beisser, K., Bibring, J.-P., Bishop, J. L., et al. (2007). Compact Reconnaissance Imaging Spectrometer for Mars (CRISM) on Mars Reconnaissance Orbiter (MRO). *Journal of Geophysical Research, 112*(E05S03). 10.1029/2006JE002682

Musselwhite, D. S., Swindle, T. D., & Lunine, J. I. (2001). Liquid CO2 breakout and the formation of recent small gullies on Mars. *Geophysical Research Letters, 28*(7), 1283-1285. 10.1029/2000GL012496

Mustard, J., Ehlmann, B., Murchie, S., Poulet, F., Mangold, N., Head, J., et al. (2009a). Composition, morphology, and stratigraphy of Noachian crust around the Isidis basin. *Journal of Geophysical Research: Planets, 114*(E2).

Mustard, J., Poulet, F., Head, J., Mangold, N., Bibring, J. P., Pelkey, S., et al. (2007). Mineralogy of the Nili Fossae region with OMEGA/Mars Express data: 1. Ancient impact melt in the Isidis Basin and implications for the transition from the Noachian to Hesperian. *Journal of Geophysical Research: Planets, 112*(E8).

Mustard, J. F., Christopher, D. C., & Moses, K. R. (2001). Evidence for recent climate change on Mars from the identification of youthful near-surface ground ice. *Nature, 412*(6845), 411. 10.1038/35086515

Mustard, J. F., Ehlmann, B. L., Murchie, S. L., Poulet, F., Mangold, N., Head, J. W., et al. (2009b). Composition, Morphology, and Stratigraphy of Noachian Crust around the Isidis basin. *Journal of Geophysical Research, 114*(E00D12). 10.1029/2009JE003349

Mustard, J. F., Murchie, S. L., Pelkey, S. M., Ehlmann, B. L., Milliken, R. E., Grant, J. A., et al. (2008). Hydrated silicate minerals on Mars observed by the Mars Reconnaissance Orbiter CRISM instrument. *Nature, 7097*, 305-309.

Naar, J., Forget, F., Madeleine, J.-B., Millour, E., Spiga, A., Vals, M., et al. (2020). Recent Formation of Ice-Rich Latitude-Dependent Mantle from Polar Ice Reservoirs. *LPI Contributions, 2099*, 6041.

Nerozzi, S., & Holt, J. (2019). Buried ice and sand caps at the North Pole of Mars: revealing a record of climate change in the Cavi Unit with SHARAD.

Geophysical Research Letters, 46(13), 7278-7286. https://doi.org/10.1029/2019GL082114

Neumann, T. A., Albert, M. R., Engel, C., Courville, Z., & Perron, F. (2009). Sublimation rate and the mass-transfer coefficient for snow sublimation. *International Journal of Heat and Mass Transfer, 52*(1-2), 309-315.

Núñez, J., Barnouin, O., Murchie, S., Seelos, F., McGovern, J., Seelos, K., & Buczkowski, D. (2016). New insights into gully formation on Mars: Constraints from composition as seen by MRO/CRISM. *Geophysical Research Letters, 43*(17), 8893-8902.

Ojha, L., Karimi, S., Buffo, J., Nerozzi, S., Holt, J. W., Smrekar, S., & Chevrier, V. (2020). Martian Mantle Heat Flow Estimate from the Lack of Lithospheric Flexure in the South Pole of Mars: Implications for Planetary Evolution and Basal Melting. *Geophysical Research Letters*, e2020GL091409. https://doi.org/10.1029/2020GL091409

Orosei, R., Lauro, S., Pettinelli, E., Cicchetti, A., Coradini, M., Cosciotti, B., et al. (2018). Radar evidence of subglacial liquid water on Mars. *Science, 361*(6401), 490-493.

Osinski, G. R., Spray, J. G., & Lee, P. (2001). Impact-induced hydrothermal activity within the Haughton impact structure, arctic Canada: Generation of a transient, warm, wet oasis. *Meteoritics & Planetary Science, 36*(5), 731-745.

Osterloo, M. M., Hamilton, V. E., Bandfield, J. L., Glotch, T. D., Baldridge, A. M., Christensen, P. R., et al. (2008). Chloride-bearing materials in the southern highlands of Mars. *Science, 319*, 1651-1654. 10.1126/science.1150690

Painter, T. H., Seidel, F. C., Bryant, A. C., McKenzie Skiles, S., & Rittger, K. (2013). Imaging spectroscopy of albedo and radiative forcing by light-absorbing impurities in mountain snow. *Journal of Geophysical Research: Atmospheres, 118*(17), 9511-9523. https://doi.org/10.1002/jgrd.50520

Pascuzzo, A., Condus, T., Mustard, J., & Arvidson, R. (2019a). The Effects of Ice and Dust Aerosols, and Surface Scattering on the Interpretation of the Martian North Polar Ice Cap Surface Characteristics Using CRISM VNIR-SWIR Data. *LPI Contributions, 2089*, 6380.

Pascuzzo, A. C., Mustard, J. F., Kremer, C. H., & Ebinger, E. (2019b). The formation of irregular polygonal ridge networks, Nili Fossae, Mars: Implications for extensive subsurface channelized fluid flow in the Noachian. *Icarus, 319*, 852-868.

Paterson, W. S. B. (1994). *Physics of glaciers*: Butterworth-Heinemann.

Pelletier, J. D., Kolb, K. J., McEwen, A. S., & Kirk, R. L. (2008). Recent bright gully deposits on Mars: Wet or dry flow? *Geology, 36*(3), 211-214.

Phillips, R. J., Davis, B. J., Tanaka, K. L., Byrne, S., Mellon, M. T., Putzig, N. E., et al. (2011). Massive CO2 ice deposits sequestered in the south polar layered deposits of Mars. *Science, 332*(6031), 838-841.

Phillips, R. J., Zuber, M. T., Smrekar, S. E., Mellon, M. T., Head, J. W., Tanaka, K. L., et al. (2008). Mars north polar deposits: Stratigraphy, age, and geodynamical response. *Science, 320*(5880), 1182-1185.

Picardi, G., Biccari, D., Seu, R., Marinangeli, L., Johnson, W., Jordan, R., et al. (2004). Performance and surface scattering models for the Mars Advanced Radar for Subsurface and Ionosphere Sounding (MARSIS). *Planetary and Space Science, 52*(1-3), 149-156.

Pierce, T. L., & Crown, D. A. (2003). Morphologic and topographic analyses of debris aprons in the eastern Hellas region, Mars. *Icarus, 163*(1), 46-65.

Pilorget, C., & Forget, F. (2016). Formation of gullies on Mars by debris flows triggered by CO 2 sublimation. *Nature Geoscience, 9*(1), 65.

Piqueux, S., Byrne, S., & Richardson, M. I. (2003). Sublimation of Mars's southern seasonal CO2 ice cap and the formation of spiders. *Journal of Geophysical Research: Planets, 108*(E8).

Piqueux, S., & Christensen, P. (2009). A model of thermal conductivity for planetary soils: 2. Theory for cemented soils. *Journal of Geophysical Research: Planets, 114*(E9).

Piqueux, S., Kleinböhl, A., Hayne, P. O., Heavens, N. G., Kass, D. M., McCleese, D. J., et al. (2016). Discovery of a widespread low-latitude diurnal CO2 frost cycle on Mars. *Journal of Geophysical Research: Planets, 121*(7), 1174-1189.

Piqueux, S., Kleinböhl, A., Hayne, P. O., Kass, D. M., Schofield, J. T., & McCleese, D. J. (2015). Variability of the Martian seasonal CO2 cap extent over eight Mars Years. *Icarus, 251*, 164-180.

Plaut, J. (2005). *An inventory of impact craters on the Martian south polar layered deposits.* Paper presented at the Lunar and Planetary Science Conference.

Plaut, J. (2020). Topographic, Compositional, and Textural Variations in Basal Interfaces Beneath the South Polar Plateau of Mars from MARSIS Radar Sounding. *LPI Contributions, 2099*, 6048.

Plaut, J., Bellutta, D., & Gim, Y. (2018). New Insights into the Internal Structure of the Martian Polar Plateaus from MARSIS 3D Mapping. *Lunar and Planetary Science Conference, 49*(2083), 2252.

Plaut, J., Kahn, R., Guinness, E., & Arvidson, R. (1988). Accumulation of sedimentary debris in the south polar region of Mars and implications for climate history. *Icarus, 76*(2), 357-377.

Plaut, J. J., Picardi, G., Safaeinili, A., Ivanov, A. B., Milkovich, S. M., Cicchetti, A., et al. (2007). Subsurface radar sounding of the south polar layered deposits of Mars. *Science, 316*(5821), 92-95.

Plaut, J. J., Safaeinili, A., Holt, J. W., Phillips, R. J., Head, J. W., Seu, R., et al. (2009). Radar evidence for ice in lobate debris aprons in the mid-northern latitudes of Mars. *Geophysical Research Letters, 36*(2).

Portyankina, G., Hansen, C. J., & Aye, K.-M. (2017). Present-day erosion of Martian polar terrain by the seasonal CO2 jets. *Icarus, 282*, 93-103.

Poulet, F., Bibring, J.-P., Mustard, J. F., Gendrin, A., Mangold, N., Langevin, Y., et al. (2005). Phyllosilicates on Mars and implications for early martian climate. *Nature, 438*(623-627).

Presley, M. A., & Christensen, P. R. (1997a). Thermal conductivity measurements of particulate materials 2. Results. *Journal of Geophysical Research: Planets, 102*(E3), 6551-6566.

Presley, M. A., & Christensen, P. R. (1997b). Thermal conductivity measurements of particulate materials, Part II: Results. *J. Geophys. Res., 102*, 6651-6566.

Price-Whelan, A. M., Sipőcz, B., Günther, H., Lim, P., Crawford, S., Conseil, S., et al. (2018). The Astropy project: Building an open-science project and status of the v2. 0 core package. *The Astronomical Journal, 156*(3), 123.

Putzig, N. E., Phillips, R. J., Campbell, B. A., Mellon, M. T., Holt, J. W., & Brothers, T. C. (2014). SHARAD soundings and surface roughness at past, present, and proposed landing sites on Mars: Reflections at Phoenix may be attributable to deep ground ice. *Journal of Geophysical Research: Planets, 119*(8), 1936-1949. https://doi.org/10.1002/2014JE004646

Putzig, N. E., Smith, I. B., Perry, M. R., Foss II, F. J., Campbell, B. A., Phillips, R. J., & Seu, R. (2018). Three-dimensional radar imaging of structures and craters in the Martian polar caps. *Icarus, 308*, 138-147.

Quinn, D. P., & Ehlmann, B. (2019). The deposition and alteration history of the northeast Syrtis Major layered sulfates. *Journal of Geophysical Research. Planets*.

Rice, M. S., Reynolds, M., Studer-Ellis, G., Bell III, J. F., Johnson, J. R., Herkenhoff, K. E., et al. (2018). The albedo of Mars: Six Mars years of observations from Pancam on the Mars Exploration Rovers and comparisons to MOC, CTX and HiRISE. *Icarus, 314*, 159-174.

Richardson, M. I., & Mischna, M. A. (2005). Long-term evolution of transient liquid water on Mars. *Journal of Geophysical Research: Planets, 110*(E3).

Robbins, S. J., & Hynek, B. M. (2012). A new global database of Mars impact craters≥ 1 km: 2. Global crater properties and regional variations of the simple-to-complex transition diameter. *Journal of Geophysical Research: Planets, 117*(E6).

Rodríguez, J. A. P., Sasaki, S., Dohm, J. M., Tanaka, K. L., Strom, B., Kargel, J., et al. (2005). Control of impact crater fracture systems on subsurface hydrology, ground subsidence, and collapse, Mars. *Journal of Geophysical Research: Planets, 110*(E6).

Rogers, A., & Nazarian, A. (2013). Evidence for Noachian flood volcanism in Noachis Terra, Mars, and the possible role of Hellas impact basin tectonics. *Journal of Geophysical Research: Planets, 118*(5), 1094-1113.

Ryan, J., & Sharman, R. (1981). H2O frost point detection on Mars? *Journal of Geophysical Research: Oceans, 86*(C1), 503-511.

Ryan, J., Sharman, R., & Lucich, R. (1982). Mars water vapor, near-surface. *Journal of Geophysical Research: Oceans, 87*(C9), 7279-7284.

Saper, L., & Mustard, J. F. (2013). Extensive linear ridge networks in Nili Fossae and Nilosyrtis, Mars: implications for fluid flow in the ancient crust. *Geophysical Research Letters, 40*(2), 245-249.

Scheller, E. L., & Ehlmann, B. L. (2020). Composition, Stratigraphy, and Geological History of the Noachian Basement Surrounding the Isidis Impact Basin. *Journal of Geophysical Research: Planets*, e2019JE006190.

Schon, S. C., Head, J. W., & Milliken, R. E. (2009). A recent ice age on Mars: Evidence for climate oscillations from regional layering in mid-latitude mantling deposits. *Geophysical Research Letters, 36*(15).

Schorghofer, N. (2010). Fast numerical method for growth and retreat of subsurface ice on Mars. *Icarus, 208*(2), 598-607.

Schorghofer, N., & Aharonson, O. (2005). Stability and exchange of subsurface ice on Mars. *Journal of Geophysical Research: Planets, 110*(E5).

Schorghofer, N., & Edgett, K. S. (2006). Seasonal surface frost at low latitudes on Mars. *Icarus, 180*(2), 321-334.

Schorghofer, N., & Forget, F. (2012). History and anatomy of subsurface ice on Mars. *Icarus, 220*(2), 1112-1120.

Schorghofer, N., Levy, J., & Goudge, T. (2019). High-Resolution Thermal Environment of Recurring Slope Lineae in Palikir Crater, Mars, and Its Implications for Volatiles. *Journal of Geophysical Research: Planets*.

Schwamb, M. E., Aye, K.-M., Portyankina, G., Hansen, C. J., Allen, C., Allen, S., et al. (2018). Planet Four: Terrains–Discovery of araneiforms outside of the south polar layered deposits. *Icarus, 308*, 148-187.

Schwerdtfeger, P. (1969). Absorption, scattering and extinction of light in ice and snow. *Nature, 222*(5191), 378-379.

Schwerdtfeger, P., & Weller, G. (1967). The measurement of radiative and conductive heat transfer in ice and snow. *Archiv für Meteorologie, Geophysik und Bioklimatologie, Serie B, 15*(1-2), 24-38.

Scott, D. H., & Tanaka, K. L. (1986). Geologic map of the western equatorial region of Mars.

Sears, D. W., & Moore, S. R. (2005). On laboratory simulation and the evaporation rate of water on Mars. *Geophysical Research Letters, 32*(16).

Seidelmann, P., Abalakin, V., Bursa, M., Davies, M., De Bergh, C., Lieske, J., et al. (2002). Report of the IAU/IAG working group on cartographic coordinates and rotational elements of the planets and satellites: 2000. *Celestial Mechanics and Dynamical Astronomy, 82*(1), 83-111.

Selvans, M., Plaut, J., Aharonson, O., & Safaeinili, A. (2010). Internal structure of Planum Boreum, from Mars advanced radar for subsurface and ionospheric sounding data. *Journal of Geophysical Research: Planets, 115*(E9). https://doi.org/10.1029/2009JE003537

Senft, L. E., & Stewart, S. T. (2009). Dynamic fault weakening and the formation of large impact craters. *Earth and Planetary Science Letters, 287*(3-4), 471-482.

Seu, R., Phillips, R. J., Biccari, D., Orosei, R., Masdea, A., Picardi, G., et al. (2007). SHARAD sounding radar on the Mars Reconnaissance Orbiter. *Journal of Geophysical Research: Planets, 112*(E5). https://doi.org/10.1029/2006JE002745

Shinbrot, T., Duong, N.-H., Kwan, L., & Alvarez, M. M. (2004). Dry granular flows can generate surface features resembling those seen in Martian gullies. *Proceedings of the National Academy of Sciences, 101*(23), 8542-8546.

Singh, D., Flanner, M., & Millour, E. (2018). Improvement of Mars surface snow albedo modeling in LMD Mars GCM with SNICAR. *Journal of Geophysical Research: Planets, 123*(3), 780-791. https://doi.org/10.1002/2017JE005368

Sizemore, H. G., Zent, A. P., & Rempel, A. W. (2015). Initiation and growth of Martian ice lenses. *Icarus, 251*, 191-210.

Skinner Jr, J., & Hare, T. (2006). Digital renovation of the atlas of Mars 1: 15,000,000-scale global geologic series maps.

Smith, D. E., Zuber, M. T., Frey, H. V., Garvin, J. B., Head, J. W., Muhleman, D. O., et al. (2001a). Mars Orbiter Laser Altimeter: Experiment summary after the first year of global mapping of Mars. *Journal of Geophysical Research: Planets, 106*(E10), 23689-23722.

Smith, D. E., Zuber, M. T., & Neumann, G. A. (2001b). Seasonal variations of snow depth on Mars. *Science, 294*(5549), 2141-2146.

Smith, D. E., Zuber, M. T., Solomon, S. C., Phillips, R. J., Head, J. W., Garvin, J. B., et al. (1999). The global topography of Mars and implications for surface evolution. *Science, 284*(5419), 1495-1503.

Smith, M. D. (2002). The annual cycle of water vapor on Mars as observed by the Thermal Emission Spectrometer. *Journal of Geophysical Research: Planets, 107*(E11), 25-21-25-19.

Smith, M. D. (2004). Interannual variability in TES atmospheric observations of Mars during 1999–2003. *Icarus, 167*(1), 148-165.

Smith, M. D. (2009). THEMIS observations of Mars aerosol optical depth from 2002–2008. *Icarus, 202*(2), 444-452.

Smith, M. D. (2019). *THEMIS observations during MY 33 and 34*. Retrieved from: https://data.mendeley.com/datasets/8sv44gs4k5/2

Smith, P. H., Tamppari, L., Arvidson, R., Bass, D., Blaney, D., Boynton, W. V., et al. (2009). H2O at the Phoenix landing site. *Science, 325*(5936), 58-61.

Soderblom, J. M., Bell III, J. F., Hubbard, M. Y., & Wolff, M. J. (2006). Martian phase function: Modeling the visible to near-infrared surface photometric function using HST-WFPC2 data. *Icarus, 184*(2), 401-423.

Sori, M. M., & Bramson, A. M. (2019). Water on Mars, with a grain of salt: Local heat anomalies are required for basal melting of ice at the south pole today. *Geophysical Research Letters, 46*(3), 1222-1231. https://doi.org/10.1029/2018GL080985

Spiga, A., Hinson, D. P., Madeleine, J.-B., Navarro, T., Millour, E., Forget, F., & Montmessin, F. (2017). Snow precipitation on Mars driven by cloud-induced night-time convection. *Nature Geoscience, 10*(9), 652-657.

Squyres, S. W. (1979). The distribution of lobate debris aprons and similar flows on Mars. *J. Geophys. Res., 84*(No. B14), 8087-8096.

Squyres, S. W., & Carr, M. H. (1986). Geomorphic evidence for the distribution of ground ice on Mars. *Science, 231*, 249-252.

Stephenson, P. (1967). Some considerations of snow metamorphism in the Antarctic ice sheet in the light of ice crystal studies. *Physics of Snow and Ice: proceedings, 1*(2), 725-740.

Stull, R. (2000). *Meteorology for scientists and engineers*: Brooks/Cole.

Stuurman, C., Osinski, G., Holt, J., Levy, J., Brothers, T., Kerrigan, M., & Campbell, B. (2016). SHARAD detection and characterization of subsurface water ice deposits in Utopia Planitia, Mars. *Geophysical Research Letters, 43*(18), 9484-9491.

Sullivan, R., Thomas, P., Veverka, J., Malin, M., & Edgett, K. S. (2001). Mass movement slope streaks imaged by the Mars Orbiter Camera. *Journal of Geophysical Research, 106*, 23,607-623,633.

Svitek, T., & Murray, B. (1990). Winter frost at Viking Lander 2 site. *Journal of Geophysical Research: Solid Earth, 95*(B2), 1495-1510.

Sylvest, M. E., Conway, S. J., Patel, M. R., Dixon, J. C., & Barnes, A. (2016). Mass wasting triggered by seasonal CO2 sublimation under Martian atmospheric conditions: Laboratory experiments. *Geophysical Research Letters, 43*(24), 12,363-312,370.

Sylvest, M. E., Dixon, J. C., Conway, S. J., Patel, M. R., McElwaine, J. N., Hagermann, A., & Barnes, A. (2019). CO2 sublimation in Martian gullies: laboratory experiments at varied slope angle and regolith grain sizes. *Geological Society, London, Special Publications, 467*(1), 343-371.

Tamppari, L. K., & Lemmon, M. T. (2020). Near-surface atmospheric water vapor enhancement at the Mars Phoenix lander site. *Icarus*, 113624.

Tanaka, K. L., Robbins, S., Fortezzo, C., Skinner Jr, J., & Hare, T. M. (2014). The digital global geologic map of Mars: Chronostratigraphic ages, topographic and crater morphologic characteristics, and updated resurfacing history. *Planetary and Space Science, 95*, 11-24.

Tewksbury, B. J., Hogan, J. P., Kattenhorn, S. A., Mehrtens, C. J., & Tarabees, E. A. (2014). Polygonal faults in chalk: Insights from extensive exposures of the Khoman Formation, Western Desert, Egypt. *Geology, 42*(6), 479-482.

Titus, T. N., & Cushing, G. E. (2014). The Mars Diurnal CO 2 Cycle as Observed in the Tharsis Region. *AGUFM, 2014*, P51C-3957.

Titus, T. N., Kieffer, H. H., & Christensen, P. R. (2003). Exposed water ice discovered near the south pole of Mars. *Science, 299*(5609), 1048-1051.

Treiman, A. H. (2003). Geologic settings of Martian gullies: Implications for their origins. *Journal of Geophysical Research: Planets, 108*(E4).

van de Hulst, H. (1957). Light Scattering by Small Particles. In: New York: John Wiley & Sons.

Viles, H., Ehlmann, B., Wilson, C. F., Cebula, T., Page, M., & Bourke, M. (2010). Simulating weathering of basalt on Mars and Earth by thermal cycling. *Geophysical Research Letters, 37*(18).

Vincendon, M. (2015). Identification of Mars gully activity types associated with ice composition. *Journal of Geophysical Research: Planets, 120*(11), 1859-1879.

Vincendon, M., Forget, F., & Mustard, J. (2010a). Water ice at low to midlatitudes on Mars. *Journal of Geophysical Research: Planets, 115*(E10).

Vincendon, M., Mustard, J., Forget, F., Kreslavsky, M., Spiga, A., Murchie, S., & Bibring, J. P. (2010b). Near-tropical subsurface ice on Mars. *Geophysical Research Letters, 37*(1).

Viola, D., & McEwen, A. S. (2018). Geomorphological Evidence for Shallow Ice in the Southern Hemisphere of Mars. *Journal of Geophysical Research: Planets, 123*(1), 262-277. 10.1002/2017JE005366

Viviano-Beck, C. E., Seelos, F. P., Murchie, S. L., Kahn, E. G., Seelos, K. D., Taylor, H. W., et al. (2014). Revised CRISM spectral parameters and summary products based on the currently detected mineral diversity on Mars. *Journal of Geophysical Research: Planets, 119*(6), 1403-1431. 10.1002/2014JE004627

Warren, S. G. (1984). Impurities in snow: Effects on albedo and snowmelt. *Annals of Glaciology, 5*, 177-179.

Warren, S. G. (2019). Optical properties of ice and snow. *Philosophical Transactions of the Royal Society A, 377*(2146), 20180161.

Warren, S. G., & Brandt, R. E. (2008). Optical constants of ice from the ultraviolet to the microwave: A revised compilation. *Journal of Geophysical Research: Atmospheres, 113*(D14).

Warren, S. G., & Wiscombe, W. J. (1980). A model for the spectral albedo of snow.2. Snow containing atmospheric aerosols. *J. Atmos. Sci., 37*(No. 12), 2734-2745.

Weidelt, H.-J. (1976). Manual of reforestation and erosion control for the Philippines.

Wellen, E. W. (1979). *Sublimation of ice from permafrost silt at the CRREL tunnel.* University of Alaska, Fairbanks,

Weller, G. E. (1969). Radiation diffusion in Antarctic ice media. *Nature, 221*(5178), 355-356.

Wells, E. N., Veverka, J., & Thomas, P. (1984). Experimental study of albedo changes caused by dust fallout. *Icarus, 58*, 331-338.

Whicker, C. A., Flanner, M. G., Dang, C., Zender, C. S., Cook, J. M., & Gardner, A. S. J. T. C. (2022). SNICAR-ADv4: a physically based radiative transfer model to represent the spectral albedo of glacier ice. *16*(4), 1197-1220.

Whiteway, J., Komguem, L., Dickinson, C., Cook, C., Illnicki, M., Seabrook, J., et al. (2009). Mars water-ice clouds and precipitation. *Science, 325*(5936), 68-70.

Whitten, J. L., Campbell, B. A., & Morgan, G. A. (2017). A subsurface depocenter in the South Polar Layered Deposits of Mars. *Geophysical Research Letters, 44*(16), 8188-8195. https://doi.org/10.1002/2017GL074069

Whitten, J. L., Campbell, B. A., & Plaut, J. J. (2020). The ice content of the Dorsa Argentea Formation from radar sounder data. *Geophysical Research Letters, 47*(23), e2020GL090705. https://doi.org/10.1029/2020GL090705

Wichman, R. W., & Schultz, P. H. (1989). Sequence and mechanisms of deformation around the Hellas and Isidis impact basins on Mars. *Journal of Geophysical Research, 94*, 17,333-317,357. 10.1029/JB094iB12p17333

Williams, K. E., Toon, O. B., Heldmann, J. L., McKay, C., & Mellon, M. T. (2008). Stability of mid-latitude snowpacks on Mars. *Icarus, 196*(2), 565-577. 10.1016/j.icarus.2008.03.017

Winslow, M. A. (1983). Clastic dike swarms and the structural evolution of the foreland fold and thrust belt of the southern Andes. *Geological Society of America Bulletin, 94*(9), 1073-1080.

Wiscombe, W. J., & Warren, S. G. (1980). A model for the spectral albedo of snow.1. Pure snow. *J. Atmos. Sci., 37*(No. 12), 2712-2733.

Wolff, M., Smith, M., Clancy, R., Arvidson, R., Kahre, M., Seelos, F., et al. (2009). Wavelength dependence of dust aerosol single scattering albedo as observed by the Compact Reconnaissance Imaging Spectrometer. *Journal of Geophysical Research: Planets, 114*(E2). https://doi.org/10.1029/2009JE003350

Yen, Y.-C. (1981). *Review of thermal properties of snow, ice, and sea ice* (Vol. 81): US Army, Corps of Engineers, Cold Regions Research and Engineering Laboratory.

Zamani, P., Tamppari, L., Lemmon, M., Keller, U., Hecht, M., Cooper, B., et al. (2009). *Phoenix Software Interface Specification*. Retrieved from https://pds-imaging.jpl.nasa.gov/data/phoenix/phxsci_0xxx/document/cam_edr_rdr_sis.pdf

Zanetti, M., Hiesinger, H., Reiss, D., Hauber, E., & Neukum, G. (2010). Distribution and evolution of scalloped terrain in the southern hemisphere, Mars. *Icarus, 206*(2), 691-706.

Zent, A., Hecht, M., Hudson, T., Wood, S., & Chevrier, V. (2016). A revised calibration function and results for the Phoenix mission TECP relative humidity sensor. *Journal of Geophysical Research: Planets, 121*(4), 626-651.

APPENDIX A

CO-AUTHOR PERMISSION STATEMENT

All co-authors have granted their permission to include the published papers as chapters 2-6 in this dissertation.